



TECHNISCHE
UNIVERSITÄT
WIEN

D I S S E R T A T I O N

**Statistical analysis of
biomolecular clustering
and oligomerization**

ausgeführt zum Zwecke der Erlangung des akademischen Grades
eines Doktors der technischen Wissenschaften unter der Leitung von

Univ.Prof. Dipl.-Ing. Dr.techn. Gerhard J. Schütz

E134 – Institut für Angewandte Physik, TU Wien

eingereicht an der Technischen Universität Wien

Fakultät für Physik

von

Dipl.-Ing. Magdalena Schneider, BSc

Matrikelnummer: 01227037

L'essentiel est invisible pour les yeux.

Antoine de Saint-Exupéry

Dem Anwenden muss das Erkennen vorausgehen.

Max Planck

Kurzfassung

Einzelmolekül-Lokalisationsmikroskopie (Single Molecule Localization Microscopy, SMLM) umgeht die Auflösungsgrenze herkömmlicher Lichtmikroskopie indem die Signale einzelner Fluorophore zeitlich separiert werden, sodass die entsprechenden Punktbildfunktionen nicht mehr überlappen. Durch Fitten der Einzelmolekül-Signale kann die Position jedes einzelnen Emitters mit Nanometer-Genauigkeit bestimmt werden. Die erhaltenen Koordinaten von tausenden aufgenommenen Einzelbildern werden kombiniert und ergeben eine rekonstruierte Lokalisationskarte. Dies ermöglicht es, die Anordnung von Biomolekülen in deren nativer Umgebung, der Zelle, in bisher unvorstellbarem Detail zu erforschen.

Bei SMLM-Methoden wird die erreichbare Auflösung durch die Lokalisierungsgenauigkeit bestimmt. In den letzten Jahren lag der Fokus einiger Forschungsgruppen darauf, SMLM unter Tieftemperaturen durchzuführen (cryo-SMLM). Durch die höhere Anzahl an Photonen per Fluorophor, die dabei erreicht werden kann, sowie die Unterbindung von residualer Diffusion der Moleküle kann die Lokalisierungsgenauigkeit noch weiter verbessert werden. Eine Herausforderung besteht jedoch darin, dass dabei auch die Fluorophor-Dipole fixiert sind: Eine laterale Verschiebung der Intensitätsmaxima führt zu einer Verzerrung der Lokalisierung. In dieser Dissertation zeige ich wie ein einfacher astigmatischer Bildgebungsansatz diese Verzerrung vermeiden kann, während die Lokalisierungsgenauigkeit die Cramér-Rao-Schranke erreicht.

Das bisherige Hauptaugenmerk von SMLM-Analysen lag auf der genauen Lokalisierung von Fluorophoren. Der natürliche nächste Schritt betrifft die qualitative und quantitative Interpretation der Lokalisationskarten und deren biologische Relevanz. Solch eine Interpretation ist herausfordernd, da durch Fluorophor-Blinken dasselbe Molekül öfters detektiert werden kann, was zu scheinbaren Lokalisations-Clustern führt. Andere Moleküle wiederum werden aufgrund unzureichender Markierungs- oder Detektionseffizienz übersehen. Als Konsequenz erscheint die erhaltene Lokalisationskarte entstellt.

In dieser Dissertation stelle ich zwei verschiedene Methoden vor, die es ermöglichen echtes molekulares Clustering von Artefakten durch Mehrfachdetektion zu unterscheiden. Als Erstes erlaubt eine umfassende Charakterisierung des Fluorophor-Blinkverhaltens kombiniert mit Monte-Carlo-Simulationen eine robuste Evaluierung von Lokalisationskarten bezüglich molekularem Clustering. Zweitens erreicht ein neuer Ansatz, welcher ein Molekül kompetitiv mit zwei verschiedenen Farbstoffen markiert, eine Beurteilung des molekularen Clustering komplett unabhängig vom Fluorophor-Blinkverhalten. Dies ermöglicht es, biomolekulares Clustering bis hinunter auf das Niveau von Dimeren zuverlässig und mit hoher Sensitivität zu detektieren.

Im Falle von cryo-SMLM besteht eine weitere Möglichkeit Artefakte durch Mehrfachdetektion zu umgehen: Bei Tieftemperaturen stellen die fixierten Dipolorientierungen ein einzigartiges Merkmal dar, welches ausgenützt werden kann, um Lokalisationen den jeweiligen Fluorophoren zuzuordnen. Gemeinsam mit Ansätzen zur Mittelung von Eigenschaften über viele Partikeln (particle averaging) kann die exakte Anordnung von Molekülen in Oligomer-Komplexen mit einer Größe von wenigen Nanometern bestimmt werden. Hier wird eine Methode für präzises Bestimmen der Größe von Oligomer-Strukturen vorgestellt. Insgesamt kann somit eine umfassende Analyse und Bestimmung von biomolekularen Verteilungen und Anordnungen in der Zelle erreicht werden.

Abstract

Single molecule localization microscopy (SMLM) circumvents the diffraction limit of light by separating the signals from individual fluorophores in time, so that the corresponding point spread functions do not overlap anymore. Fitting the single molecule signals allows to determine the position of each emitter with nanometer precision. The obtained coordinates from thousands of recorded frames are combined, yielding a reconstructed localization map. Thus, the arrangement of biomolecules in their native environment can be investigated in unprecedented detail.

In SMLM, the localization precision limits the achievable resolution. In the recent years, several research groups focused their interest onto SMLM performed under cryogenic conditions (cryo-SMLM). In cryo-SMLM, a higher photon yield per fluorophore and the prevention of residual diffusion allow to improve the localization precision beyond previous limits. One challenge, however, are fixed fluorophore dipole orientations: A lateral shift of the intensity peak easily leads to a localization bias. Here, I show how a simple astigmatic imaging approach avoids this bias, while achieving a precision at the Cramér–Rao bound.

While the main focus of SMLM analysis up to now has been the precise localization of the fluorophores, the natural next step concerns qualitative and quantitative interpretation of the localization maps and their biological relevance. Such an interpretation is challenging, as the same molecule of interest may be detected multiple times due to blinking, leading to apparent localization clusters. On the other hand, molecules may be missed due to insufficient labeling or detection efficiency. In consequence, the determined localization map appears distorted.

In this thesis, I present two different methods for distinguishing true molecular clustering from overcounting artifacts. First, a comprehensive characterization of fluorophore blinking behavior combined with Monte Carlo simulations allows for robust evaluation of localization maps with respect to true molecular clustering. Second, a novel approach based on targeting the same molecule of interest with two different labels competitively achieves an assessment of molecular clustering completely independent of fluorophore blinking. Thus, biomolecular clustering can be reliably detected with high sensitivity down to the level of dimers.

In case of cryo-SMLM, another possibility for circumventing overcounting artifacts arises: At cryogenic temperatures, the fixed fluorophore dipole orientations present a unique characteristic, which can be exploited in order to assign localizations to individual fluorophores. Combined with particle averaging approaches, the exact arrangement of molecules in oligomeric complexes of a few nanometers in size can be determined. A method for precise sizing of oligomeric structures is presented in this thesis. Taken together, a comprehensive analysis and description of biomolecular distributions and arrangements in the cell can be achieved.

Acknowledgments

First, I want to acknowledge the support by the Austrian Science Fund (FWF) through the SFB project F68 (Tomography Across the Scales), in particular subproject F6809-N36 (Ultra-high Resolution Microscopy).

Above all, I would like to express my sincere gratitude to my supervisor Gerhard Schütz, for your invaluable support and belief in me. Thank you for your persistent encouragement and for giving me the opportunity and freedom to pursue all my research interest. I am very grateful for the amicable work atmosphere that you have created throughout all the years and for many inspiring discussions, which have allowed me to grow both scientifically and personally. In addition, I sincerely appreciate the possibilities you gave me to attend many inspiring conferences already early in my PhD, which I could not have done later due to the Covid situation.

This thesis would not have been possible without the support of numerous people, without whom I would not stand where I am today. I wish to thank all my colleagues and co-authors who have worked together with me all these years. In particular, I want to express my gratitude to Mario Brameshuber and Eva Sevcsik who gave me opportunities to pursue an even wider variety of intriguing research topics. Moreover, I owe great thanks to Andreas Arnold for being a great colleague and friend and for all the research we had the opportunity to do together. I always admired your enthusiasm and cheerfulness. In addition, I appreciate Florian Baumgart, Joschka Hellmeier, Montse López-Martinez, René Platzer, Benedikt Rossboth and Tímea Váradi for our joint work throughout the years. I truly enjoyed working with you. I would like to extend my thanks to all colleagues from the SFB project; particularly, to Fabian Hinterer, Gwenael Mercier and Roger Telschow for the close collaboration.

Especially, I whole-heartedly appreciate all my colleagues of the Biophysics group (many of whom were already mentioned above) I had the great pleasure to be with. Thanks to all of you for the wonderful work atmosphere and all the fun we have had together! Many of you have not only been colleagues to me but became dear friends. I want to express special thanks to Clara and Montse, who are always a source of joy and were the best room mates at several conferences and meetings. Thanks also to Clara, Lukas S., and Lukas V. for our unforgettable road trip in the US! I also want to sincerely appreciate Elena, you have always provided an open door and ear for me.

Further, I would like to extend my thanks to all my study colleagues and friends who have accompanied me on my way. Thank you for the wonderful time we have spent together!

I am very grateful for the constant and unlimited support I have received from my family throughout all the years of my studies. This especially applies to my parents, but also to my siblings, for your emotional support and welcome diversions from work.

Most importantly, I want to express my deepest gratitude to my beloved Michael, first and foremost, for your unconditional and enduring love, for your understanding, and for being always there for me. In addition, I want to sincerely appreciate your invaluable personal and professional support in any situation. And last but not least, thank you for being the best home office colleague I could have wished for during lockdowns in Covid times.

Eidesstattliche Erklärung

Ich erkläre an Eides statt, dass ich die vorliegende Dissertation selbstständig und ohne fremde Hilfe verfasst, andere als die angegebenen Quellen und Hilfsmittel nicht benutzt bzw. die wörtlich oder sinngemäß entnommenen Stellen als solche kenntlich gemacht habe.

Wien, am 10. September 2021

Unterschrift

Contents

1. Preface	1
1.1 Motivation and research question	1
1.2 Published articles and contributions	3
1.3 Published software	4
2. Background	5
2.1 Cell biology	6
2.2 Basics of microscopy	10
2.3 Single molecule localization microscopy	15
 I Verifying molecular clusters	
3. Introduction	35
3.1 Methods for cluster analysis	36
3.2 The p-value and statistical significance	47
4. Monte Carlo simulations based on blinking statistics	55
4.1 Introduction	56
4.2 Results	56
4.3 Discussion	65
4.4 Methods	67
5. 2-CLASTA	69
5.1 Introduction	70
5.2 Results	70
5.3 Discussion	90
5.4 Methods	94
 II Particle averaging in cryo-SMLM	
6. Introduction	101
6.1 PSF for fixed dipole emitters	102
6.2 Particle averaging	107

7. Localization of fixed dipole emitters	113
7.1 Introduction	114
7.2 Results	118
7.3 Discussion	125
7.4 Methods	128
7.5 Appendix	132
8. Sizing of oligomers via cryo-SMLM	133
8.1 Introduction	134
8.2 Results	136
8.3 Discussion	146
8.4 Methods	149
8.5 Appendix	154
9. Conclusion and outlook	155
References	157
List of figures	171
Curriculum vitae	175

1. Preface

1.1. Motivation and research question

The development of superresolution microscopy in the last decades has allowed to circumvent the diffraction limit of light and study the structural arrangement of cells in unprecedented detail. One major group of superresolution techniques is single molecule localization microscopy (SMLM), which achieves superior spatial resolution by stochastic separation of the signals of different fluorophores in time.

Quite surprisingly, various studies based on these SMLM techniques consistently reported the presence of nanoclustering to various degrees for virtually any investigated membrane protein. Therefore, nanoclustering has been thought to be a prevalent feature of cell plasma membrane organization [1,2]. More recently, however, concerns about the notion of ubiquitous nanoclustering have been raised: Multiple detections of the same molecule lead to localization clusters, which can be easily mistaken for true molecular clustering at the nanoscale [3,4]. It is essential to note that it is the distribution of molecules of interest instead of the mere distribution of localizations, which is of biological relevance. Several methods have been developed in order to account for overcounting and determine whether a localization map shows features of true molecular clustering which differ from spatial randomness. All previously proposed methods rely on at least some knowledge or assumption about fluorophore blinking statistics—either explicitly or implicitly [4–7]. Often, complex blinking behavior and long-lived dark states hamper the analysis [5]. Moreover, fluorophore blinking statistics are affected by the imaging parameters and the local molecular nanoenvironment of the dye [8].

In the first part of my thesis, I present two different approaches, which allow to distinguish true molecular clustering from overcounting-induced clustering artifacts. In this part I address the following research questions:

Part I — *Verifying Molecular Clusters*

- *How is a reliable characterization of fluorophore blinking statistics possible? How can Monte Carlo simulations based on the recorded blinking statistics help to distinguish true molecular clustering from overcounting artifacts?*
- *Is it possible to distinguish true molecular clustering from overcounting artifacts independently of fluorophore blinking statistics?*

Once one has verified that the observed nanoclusters are in fact true molecule clusters, their structural organization can be studied in greater detail. Ultimately, the resolution of SMLM is limited by two factors: First, the available photon budget limits the localization precision that can be achieved. Second, the resolution is affected by the quality of the sample fixation. Thorough sample fixation is essential as SMLM image acquisition may take several minutes up to hours. Common chemical fixatives show residual diffusion of molecules, deteriorating the apparent localization precision [9]. In addition, chemical fixatives may distort the ultrastruc-

tural organization of the cell during the fixation process, which itself takes several minutes [10]. SMLM performed at cryogenic temperatures (cryo-SMLM) promises to address these issues: First, the photophysics of fluorophores is slowed down, allowing to achieve a higher photon yield per fluorophore and, thus, a better localization precision. Second, cryo-fixation offers supreme fixation and preservation of the sample's ultrastructure [11]. Performing SMLM under cryogenic temperatures promises advantages, but also poses challenges. Most evidently, the dipole orientation of fluorophores is fixed, leading to a more complex PSF shape. The intensity peak of the PSF is shifted laterally, which leads to a localization bias if not accounted for correctly [12, 13].

In the second part of this thesis I describe methods to determine the exact arrangement of proteins within an oligomer via cryo-SMLM. I address the following points:

Part II — *Particle averaging in cryo-SMLM*

- *How can one achieve bias-free localization of fixed dipole emitters?*
- *How can the features of cryo-SMLM be used in order to assign localizations to individual fluorophores? How precisely can the size of oligomers be determined with cryo-SMLM?*

The content of this thesis is based on several publications, which are listed in section 1.2.

1.2. Published articles and contributions

This thesis is based on the following publications (* denotes equal contribution):

- **M. C. Schneider** and G. J. Schütz. *Single-Molecule Localization Microscopy (SMLM)*. In: *Imaging modalities for biological and preclinical research: A compendium*, IOP Publishing, 2021. doi: 10.1088/978-0-7503-3059-6ch18
- R. Platzer*, B. K. Rossboth*, **M. C. Schneider**, E. Sevcsik, F. Baumgart, H. Stockinger, G. J. Schütz, J. B. Huppa, M. Brameshuber. *Unscrambling Fluorophore Blinking for Comprehensive Cluster Detection via PALM*. *Nature Communications*, 11, 2020. doi: 10.1038/s41467-020-18726-9
- A. M. Arnold*, **M. C. Schneider***, C. Hüsson, R. Sablatnig, M. Brameshuber, F. Baumgart, G. J. Schütz. *Verifying molecular clusters by 2-color localization microscopy and significance testing*. *Scientific Reports*, 10, 2020. doi: 10.1038/s41598-020-60
- F. Hinterer*, **M. C. Schneider***, S. Hubmer, M. López-Martinez, P. Zelger, A. Jesacher, R. Ramlau, G. J. Schütz. *Robust and bias-free localization of individual fixed dipole emitters achieving the Cramér Rao bound*. arXiv, 2021. arXiv-ID: 2104.02449
- **M. C. Schneider***, R. Telschow*, G. Mercier, M. López-Martinez, O. Scherzer, G. J. Schütz. *A workflow for sizing oligomeric biomolecules based on cryo single molecule localization microscopy*. *PLoS One*, 16(1), 2021. doi: 10.1371/journal.pone.0245693

Further, during my time as a PhD student I contributed to the following publications, which are not covered in this thesis:

- T. Váradi, **M. Schneider**, E. Sevcsik, D. Kiesenhofer, F. Baumgart, G. Batta, T. Kovács, R. Platzer, J. Huppa, J. Szöllösi, G. Schütz, M. Brameshuber, P. Nagy. *Homo- and heteroassociations drive activation of ErbB3*. *Biophysical Journal*, 117(10), 2019. doi: 10.1016/j.bpj.2019.10.001
- F. Baumgart, **M. Schneider**, and G. J. Schütz. *How T-cells do the “search for the needle in the haystack”*. *Frontiers in Physics*, 7(11), 2019. doi: 10.3389/fphy.2019.00011
- J. Hellmeier, R. Platzer, V. Mühlgrabner, **M. C. Schneider**, E. Kurz, G. J. Schütz, J. B. Huppa, E. Sevcsik. *Strategies for the site-specific decoration of DNA origami nanostructures with functionally intact proteins*. *ACS Nano*, 2021. doi: 10.1021/acsnano.1c05411
- J. Hellmeier, R. Platzer, A. S. Eklund, T. Schlichthaerle, A. Karner, V. Motsch, **M. C. Schneider**, E. Kurz, V. Bamieh, M. Brameshuber, J. Preiner, R. Jungmann, H. Stockinger, G. J. Schütz, J. B. Huppa, E. Sevcsik. *DNA origami demonstrate the unique stimulatory power of single pMHCs as T-cell antigens*. *PNAS*, 118(4), 2021. doi: 10.1073/pnas.2016857118
- M. López-Martinez, G. Mercier, K. Sadiq, O. Scherzer, **M. Schneider**, J. C. Schotland, G. J. Schütz, R. Telschow. *Inverse Problems of Single Molecule Localization Microscopy*. In: *Time-dependent Problems in Imaging and Parameter Identification*, Springer International Publishing, 2021. doi: 10.1007/978-3-030-57784-1.

1.3. Published software

I contributed to the following software packages, which were published along with the according articles:

- **Blinking statistics analysis for cluster detection**

Code package: <https://zenodo.org/record/4003734#.YG8ceD9CRPY>

According publication:

R. Platzer*, B. K. Rossboth*, **M. C. Schneider**, E. Sevcsik, F. Baumgart, H. Stockinger, G. J. Schütz, J. B. Huppa, M. Brameshuber. *Unscrambling Fluorophore Blinking for Comprehensive Cluster Detection via PALM*. Nature Communications, 11, 2020. doi: 10.1038/s41467-020-18726-9

- **2-CLASTA ImageJ plugin**

Code package: <https://github.com/schuetzgroup/2-CLASTA>

According publication:

A. M. Arnold*, **M. C. Schneider***, C. Hüsson, R. Sablatnig, M. Brameshuber, F. Baumgart, G. J. Schütz. *Verifying molecular clusters by 2-color localization microscopy and significance testing*. Scientific Reports, 10, 2020. doi: 10.1038/s41598-020-60

- **Bias-free localization of fixed dipole emitters**

Code package: <https://github.com/schuetzgroup/localizationFixedDipoles>

According publication:

F. Hinterer*, **M. C. Schneider***, S. Hubmer, M. López-Martinez, P. Zelger, A. Jesacher, R. Ramlau, G. J. Schütz. *Robust and bias-free localization of individual fixed dipole emitters achieving the Cramér Rao bound*. arXiv, 2021. arXiv-ID: 2104.02449

- **Sizing Oligomers with Cryo-SMLM**

Code package: <https://github.com/schuetzgroup/sizingOligomersCryoSMLM>

According publication:

M. C. Schneider*, R. Telschow*, G. Mercier, M. López-Martinez, O. Scherzer, G. J. Schütz. *A workflow for sizing oligomeric biomolecules based on cryo single molecule localization microscopy*. PLoS One, 16(1), 2021. doi: 10.1371/journal.pone.0245693

2. Background

Every living organism is composed of cells, which are often referred to as the fundamental units of life. A crucial prerequisite for the discovery of cells was the invention of the microscope in the 17th century. The term *cell* was coined by Robert Hooke in 1665, who first described the cell-like structure of a piece of cork [14]. The existence of living cells was first observed by Anton Van Leeuwenhoek in 1674.

Cell biology is the study of the structure, function and behavior of cells. Although cells exhibit an astonishing variety, from unicellular organisms to human cells, their mechanism is built on the same fundamental concepts. All living organisms are comprised of cells, and all cells origin from the division of pre-existing cells. A schematic structure of an animal cell is depicted in Fig. 2.1. With a size typically ranging from $1\ \mu\text{m}$ to $100\ \mu\text{m}$, most animal cells are only visible under the microscope.

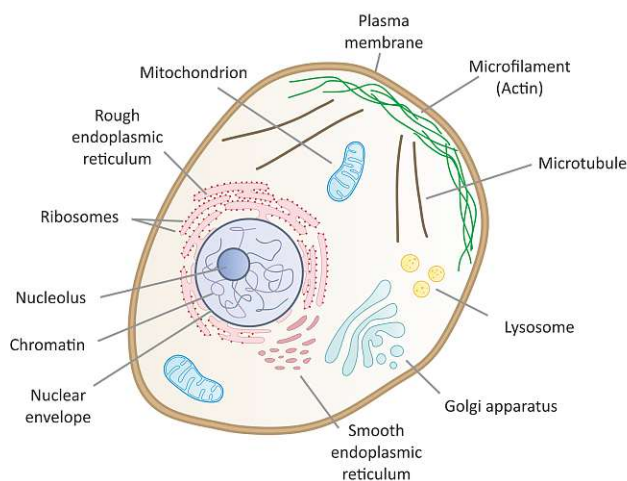


Figure 2.1.: The cell. A schematic cross section of an animal cell. The cytoplasm is enclosed within the cellular plasma membrane. The cell comprises a nucleus and various cell organelles. It is composed of molecules including proteins, lipids and nucleic acids.

Optical microscopy has played a key role in the discovery and study of cells in the last centuries, but until recently was thought to be fundamentally limited to structures above $200\ \text{nm}$ due to diffraction of light. While this resolution is sufficient for visualizing most cell organelles, individual protein molecules at a scale below $10\ \text{nm}$ cannot be resolved. Remarkably, the advent of superresolution microscopy in the last decade has allowed to circumvent the diffraction limit of conventional microscopy [15, 16]. Thus, superresolution techniques offer the possibility to study cellular structures in unprecedented detail and to gain even deeper understanding of all forms of life.

For this thesis, I developed approaches and analysis methods for single molecule localization microscopy (SMLM) which allow to investigate the distribution and arrangement of biomolecules, in particular proteins, within the cellular plasma membrane. In section 2.1, I will give a short

introduction to the relevant aspects of cell biology, in particular the plasma membrane and membrane proteins. Basic concepts of microscopy and details of the SMLM imaging technique will be covered by sections 2.2 and 2.3, respectively.

2.1. Cell biology

2.1.1. Cell plasma membrane

A cell is enclosed by the cellular plasma membrane, which separates the cytosolic interior from the extracellular environment. The plasma membrane is crucial for the communication of the cell with its environment and for the transport of substances between the in- and outside of the cell. The plasma membrane is composed of a lipid bilayer with a thickness of approximately 5 nm (Fig. 2.2). This bilayer is stabilized by hydrophobic interactions: the hydrophobic fatty acid chains are oriented towards the inside of the bilayer, while the hydrophilic headgroups of the lipids face towards the aqueous environment. Thus, the membrane constitutes a barrier, which is highly impermeable to water-soluble molecules.

Besides lipids, the plasma membrane contains proteins, which are embedded in the lipid bilayer and serve a variety of functions [17]. For example, ion channels transfer ions across the membrane and thus, can establish ion gradients needed for transmitting electrical signals; receptor proteins sense external signals and changes in the cellular environment and thus, allow the cell to respond accordingly. It is estimated that around 20–30 percent of all proteins in the human genome encode membrane proteins [18].

Previously, the membrane was thought to be a 2D fluid structure with proteins being present at low concentrations only. The *fluid mosaic model* suggested that proteins are mainly present in their monomeric form, freely diffusing and dispersed randomly throughout the membrane [19]. Nowadays, a different model of membrane organization prevails: The plasma membrane is densely populated by proteins and characterized by heterogeneous structure and composition [20]. Interactions between lipids and proteins lead to grouping of molecules, often yielding the formation of large functional complexes.

Notably, the plasma membrane is not necessarily a flat 2D surface, but a cell may form membrane undulations and protrusions such as microvilli [22]. In this thesis, I assume adhered cells which are well attached to the microscope coverslip and, hence, can be regarded as a flat 2D plane. Yet, also sample preparation and excitation schemes exist which allow to visualize thin sections of a cell which exhibits more complex membrane shapes (see section 2.3.4).

Both lipids and proteins can diffuse laterally within the plasma membrane. Therefore, thorough sample fixation is necessary for SMLM in order to prevent a distortion of the resulting image during the acquisition time of several minutes up to hours [9, 11]. Common chemical fixatives cross-link the proteins [23], while the lipids are virtually unaffected. Possible fixation procedures and their effect on SMLM imaging will be discussed in more detail in section 2.3.3.

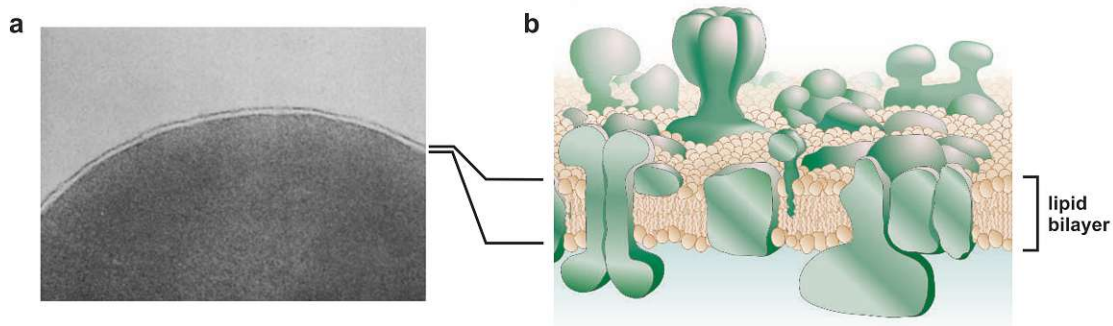


Figure 2.2.: Cellular plasma membrane. An image of the cross section of a cell acquired by electron microscopy is shown in panel **a**. The plasma membrane of the cell is clearly discernible at the top rim of the cell. A schematic structure of the plasma membrane is illustrated in panel **b**: The plasma membrane consists of a double layer of lipids (brown) with proteins (green) embedded in or associated with the bilayer. Figure from [21] (panel **a**) and [20] (panel **b**).

2.1.2. Proteins

Proteins constitute more than half of a cell's dry mass and fulfill a broad variety of functions [17]. Membrane proteins, in particular, can serve as channels, pumps, enzymes or receptors [18] and, hence, play important roles in transport and signaling. The function of proteins is directly linked to their structure: Proteins are composed out of amino acids—organic compounds consisting of an amino (NH_2) and carboxyl (COOH) functional group, together with a side chain (R group). The side group is specific to each type of amino acid; the general amino acid structure is shown in Fig. 2.3a. In eukaryotic cells, 21 different side groups can be found, each having its own characteristic chemical properties. For example, some amino acids are nonpolar and hydrophobic, while others are negatively or positively charged. These properties of different amino acids directly affect the conformation of a protein.

A protein molecule is a chain of amino acids, which are linked through covalent peptide bonds. Therefore, proteins are also referred to as polypeptides. Each type of protein has its unique sequence of amino acids, which is termed the *primary structure* of a protein (Fig. 2.3b). The peptide backbone of the amino acid chain can form hydrogen bonds, leading to the folding of the chain into either an α -helix or a β -pleated sheet. These repeating patterns are referred to as the *secondary structure* of the protein (Fig. 2.3c). The *tertiary structure* of the protein describes the further folding of the protein into a three-dimensional structure (Fig. 2.3d). This folding is determined by the interactions of the amino acid side chains, including hydrogen bonds, electrostatic interactions and van der Waals forces. In addition, hydrophobic interactions cause amino acids with nonpolar, hydrophobic groups to arrange towards the inside of the protein, while hydrophilic amino acids preferentially face towards the outside. Further, covalent disulfide bonds may connect adjacent cysteine side chains. Several polypeptide chains may associate and form a protein complex. This assembly of multiple polypeptide chains with a specific number and arrangement of protein subunits is termed the *quaternary structure* of a protein (Fig. 2.3e). The individual polypeptide chains are held together by the same interactions as responsible for the tertiary structure, thus forming a larger protein with precisely

defined geometry. Typical examples for proteins with a quaternary structure are ion channels, which facilitate the passive flux of specific ions across the cell membrane [24]. As an example, the structure of the KcsA potassium channel is depicted in Fig. 2.3e.

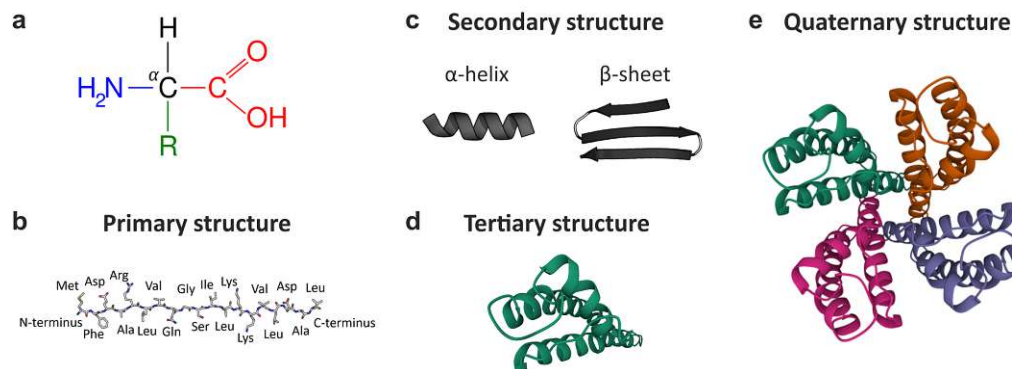


Figure 2.3.: Protein structure. (a) Molecular structure of an amino acid, consisting of an amino (NH₂) and carboxyl (COOH) functional group, and a side chain (R group). (b) *Primary protein structure.* The primary structure is given by the sequence of amino acids in the polypeptide chain. Here, a representative sequence is illustrated. (c) *Secondary protein structure.* Hydrogen bonds of the peptide backbone lead to folding of the polypeptide chain into either α-helices or β-pleated sheets. (d) *Tertiary protein structure.* Interactions of the amino acid side chains determine the folding of the protein into a 3D structure. (e) *Quaternary protein structure.* Several polypeptide chains may associate and form a larger functional protein complex with a specific number and arrangement of the protein subunits. Here, the structure of the KcsA potassium channel is depicted [25]. Figure adapted from [26] (a) and [27] (b,c). Images of the KcsA structure (PDB ID: 1BL8) were created via the protein data bank [28,29].

Overall, the specific 3D structure of a particular protein is determined by its amino acid sequence and the resulting interactions due to the characteristics of the amino acid side chains. The final conformation of the protein in general is the one that minimizes the free energy of the polypeptide chain. Most proteins exhibit a single stable conformation, but slight changes in their structure may occur, for instance upon interaction with other molecules. For many proteins, these structural changes are part of their proper function, for example the opening and closing of an ion channel [24]. The correct structure of proteins is essential for their functionality; a change in the structure typically causes the loss of protein function. Mutations in the amino acid sequence, improper folding of proteins or aberrant protein-protein interactions are the cause of many severe diseases [30,31].

Oligomerization. An oligomer (Greek: *oligo*-, 'a few'; *-mer*, 'part, subunit') is a protein that is composed of more than one polypeptide subunit and thus, possesses a quaternary structure. If all polypeptide subunits are identical, the protein complex is referred to as homo-oligomer, otherwise as hetero-oligomer. The basic subunit of an oligomer is also termed monomer. The oligomerization degree describes the number of subunits of an oligomer; a dimer, trimer or tetramer is an assembly of two, three or four subunits, respectively. For example, the potassium channel shown in Fig. 2.3e is comprised of four identical subunits and thus, a homo-

tetramer [25]. For some proteins, it makes sense to conceptually combine polypeptide chains into subgroups. For this, the term protomer was introduced: A protomer is a structural unit of an oligomeric protein, which may be composed of a single or multiple polypeptide chains that form a structural and functional subgroup. A complex of several protomers again forms an oligomer. The individual subunits of an oligomer are connected primarily by noncovalent bonds and forces, including hydrogen bonds and electrostatic interactions. These weak interactions may also be disrupted, allowing the protein complex to change its oligomeric state and undergo conformational changes that affect its biological function. Interestingly, changes of the oligomerization states have been associated with many diseases, including Parkinson's disease [32] and cancer [33]. Notably, many protein oligomers have a size of a few nanometers only and thus, cannot be directly resolved using conventional SMLM techniques with a localization precision of around 10 nm. In chapter 8 I describe a workflow which allows precise sizing of oligomeric structures via SMLM performed at cryogenic temperatures.

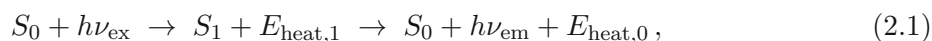
Nanoclustering. Oligomerization describes protein complexes of a specific number of subunits and precisely defined shapes. In contrast, proteins may aggregate in the cell and form loosely assembled clusters. These clusters do not show any distinct quaternary structure and may be of varying occupation and extent. Still, it is usually assumed that the clusters are not formed by random chance alone, but some underlying force or mechanism causes the formation of the clusters. Clusters with a size below the diffraction limit of about 200 nm are typically referred to as nanoclusters. Of note, this term has been used in the literature in various ways and thus, is rather ambiguous as no common distinct definition of a nanocluster exists. In this thesis, I resort to the definition of a nanocluster as given by Feher et al., who characterized a nanocluster as *'points that are grouped on a subdiffraction-limit scale [...] to a greater extent than would be expected for a random distribution'* [34]. This description encompasses both oligomers of precisely defined geometry, as well as loose assemblies of varying protein numbers. Interestingly, virtually all membrane proteins investigated with SMLM techniques were reported to exhibit nanoclustering [1]. However, overcounting in SMLM leads to localization clusters which can be easily mistaken for biomolecule nanoclusters. This issue will be discussed in more detail in section 2.3.8. In the chapters 4 and 5 of this thesis, I propose two methods which allow to distinguish true biomolecular nanoclustering from overcounting artifacts.

2.2. Basics of microscopy

Microscopy has played a crucial role in the discovery and study of biological cells. The first microscopy techniques relied on scattering, reflection, attenuation, absorption or phase shift of the illumination light by the sample in order to acquire an image of the specimen. One important development in microscopy was fluorescence microscopy. The use of fluorescent labels allows to specifically target molecules of interest and to collect the light emitted from these labels, while the contribution of other molecules to the signal is minimized. In the following section, I will give a short introduction to some basic concepts in fluorescence microscopy, including the phenomenon of fluorescence itself, the diffraction limit of light, and methods for sample illumination.

2.2.1. Fluorescence

Fluorescence is the process of absorption and subsequent emission of electromagnetic radiation occurring in specific molecules, which are referred to as fluorophores [35]. A comprehensive characterization of the process can only be given by quantum mechanics; in the following, I will describe a simplified model (Fig. 2.4a). A fluorescent molecule can be excited from its ground state S_0 to a state S_1 of higher energy via the absorption of a photon. Some of the photon energy may be stored in vibrational sub-states and is dissipated as heat. After a short time delay of usually less than a microsecond, the fluorophore emits a photon and thus, relaxes back to its ground state. Again, some energy may be lost as heat due to dissipative processes. Taken together, the process of fluorescence can be described by the following transitions:



where h is the Planck constant, ν_{ex} and ν_{em} the frequency of the exciting and emitted photon, respectively, and E_{heat} the energy dissipated as heat.

As some of the energy is lost in dissipative processes, it holds that the energy of the emitted photon is lower than the energy of the absorbed photon, i.e. $h\nu_{\text{em}} < h\nu_{\text{ex}}$. Therefore, the wavelength of the emitted photon is longer than the wavelength of the absorbed photon. This shift of the emission towards higher wavelength is the so-called Stokes shift (Fig. 2.4b).

Each type of fluorophore possesses a specific absorption and emission spectrum. For excitation of a fluorophore, the wavelength of the excitation laser needs to be chosen according to the absorption spectrum. The Stokes shift allows to separate the excitation from the emission light via suitable filters, although slight overlap between the excitation and emission spectrum has to be considered.

One important aspect for the use of fluorophores in microscopy is the transition of fluorophores into dark states, in which the molecules cannot be excited. Fluorophores may repeatedly transition between the bright and dark states. This property is exploited in SMLM techniques (see section 2.3). Further, the fluorescent property of a fluorophore can be lost permanently, which is referred to as photobleaching.

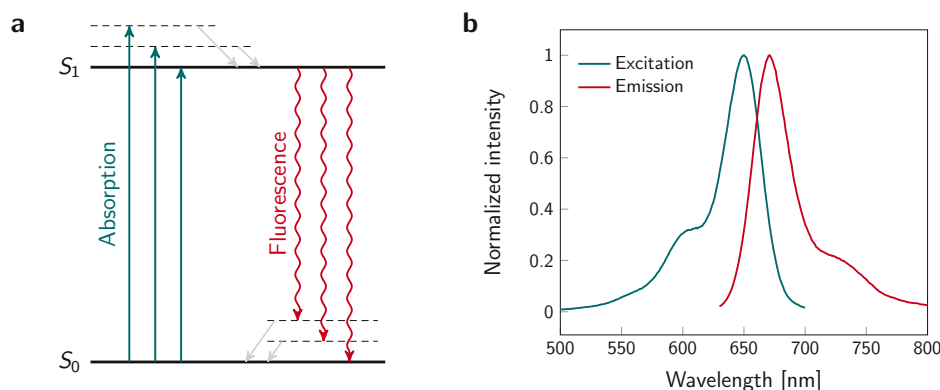


Figure 2.4.: Fluorescence. (a) Jablonski diagram depicting a simplified model of fluorescence. A fluorescent molecule can be excited from its ground state S_0 into a state of higher energy S_1 via absorption of a photon (green arrows). The molecule relaxes back to its ground state by the emission of a photon (red arrows). A part of the energy may be stored in vibrational sub-states (dashed lines) and is dissipated as heat (gray arrows). (b) Stokes shift. Shown are the excitation and emission spectra of the dye Alexa Fluor 647. As some of the excitation energy is lost in dissipative processes, the wavelength of the emitted photon is longer than the wavelength of the absorbed photon. Hence, the emission spectrum is shifted towards higher wavelengths compared to the excitation spectrum. Spectral data from [36].

2.2.2. Diffraction limit and point spread function

The phenomenon of diffraction describes the interaction of an electromagnetic wave with an object, in particular an obstacle or opening. Due to bending of the waves, the light spreads into the geometrical shadow of the object. The theory behind diffraction is given by the Huygens-Fresnel principle and wave interference [37].

Diffraction is central to optical microscopy: Due to diffraction, a point object is not imaged as a point, but as the diffraction pattern of this point. The response of an optical system to a point object or point source is referred to as the *point spread function* (PSF). The PSF incorporates the effect of diffraction as well as any optical imperfections in the imaging system. The obtained microscopy image of an object can be described as a convolution of the true object with the PSF of the optical system.

For an ideal optical system without any aberrations, the PSF (i.e. the diffraction pattern of a point) can be well described by the Airy pattern, which is shown in Fig. 2.5 and given by

$$I(\theta) = I_0 \left(\frac{2 J_1(ka \sin(\theta))}{ka \sin(\theta)} \right)^2, \quad (2.2)$$

where I_0 is the maximum intensity of the Airy disc center, J_1 the Bessel function of first kind and order one, $k = 2\pi/\lambda$ the angular wavenumber (with λ being the wavelength), a the aperture radius, and θ the observation angle. The Airy pattern shows a central diffraction disk, also referred to as the 0th order spot, which is surround by diffraction rings (referred to as 1st, 2nd, 3rd order diffraction ring, etc.). In case of perfect focus, the intensity minima between the rings are zero. The size of the central spot depends on the wavelength of light

2. Background

and the aperture angle of the objective. The central spot directly determines the resolution of the microscope, which will be discussed in the following.

In 1873, Ernst Abbe studied the resolution of a microscope based on an illuminated optical grating [38]. He found that the grating can be resolved if the objective lens can capture at least the 0th and 1st order diffraction maxima, which is the case if the spacing d between the grating lines is at least

$$d = \frac{\lambda}{2n \sin(\alpha)} = \frac{\lambda}{2 \text{NA}}, \quad (2.3)$$

where λ is the wavelength of light, n the refractive index of the imaging medium, α the angular aperture, and $\text{NA} = n \sin(\alpha)$ the numerical aperture of the objective.

Another approach for defining the resolution limit of a microscope is the Rayleigh criterion. According to this criterion, two points are resolvable if their mutual distance d is larger than the radius of the central disk of the Airy pattern. The radius of the central disk is defined as the distance between the 0th order maximum and the first minimum of the Airy pattern and calculated as

$$d = \frac{1.22 \lambda}{2 \text{NA}}. \quad (2.4)$$

Fig. 2.5 shows the Airy patterns of two points separated by different distances, which are clearly resolvable (b), just resolvable (c) and not resolvable anymore (d). According to Eq. (2.3) and (2.4), the resolution can be increased by decreasing the wavelength of the imaging light or increasing the numerical aperture of the objective. The highest angular aperture that could theoretically be achieved with a standard objective is 180°, corresponding to a half-angle $\alpha = 90^\circ$. As $\sin(90^\circ)$ is equal to 1, the numerical aperture would consequently only depend on the imaging medium. Assuming an immersion objective with oil of high refractive index $n = 1.52$ and a low imaging wavelength of 450 nm, the achievable resolution according to the Rayleigh criterion is limited by 180 nm.

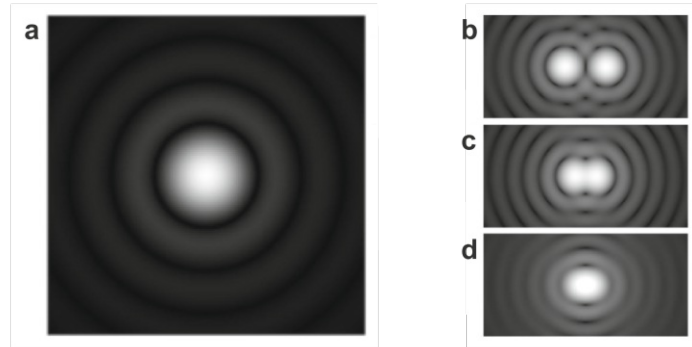


Figure 2.5.: Airy pattern and resolution. (a) Airy pattern describing the PSF of an isotropic single point emitter. (b-d) Resolution according to the Rayleigh criterion. In panel **b** the emitters are sufficiently separated in order to be easily distinguishable. In panel **b**, the maximum of the Airy pattern arising from the first point coincides with the first minimum of the Airy pattern arising from the second point. Thus, the points are still resolvable. In panel **d** the distance between the two points is below the diffraction limit and thus, the points cannot be resolved anymore. Figure adapted from [39, 40].

In fluorescence microscopy, the molecules of interest are labeled with fluorescent molecules, which act as point emitters. The emission characteristics of a fluorophore can be described as an ideal oscillating dipole. If the fluorophore can freely rotate, which is typically the case for experiments performed at room temperature, the emission of the fluorophore is isotropic and its PSF can be described well by the Airy pattern introduced above in Eq. (2.2). In an experiment, the detected photons are integrated over the pixels of the camera chip. In addition, background noise typically obscures the secondary maxima of the Airy pattern. Thus, the resulting PSF image can in practice be well approximated by a simple Gaussian function [41]. If a fluorophore is linked rigidly to a stationary structure, however, it is rotationally immobile. Also imaging at cryogenic temperature prohibits the rotational diffusion of a fluorophore. In these cases, the dipole orientation of the fluorophore is fixed and its emission is anisotropic. Hence, the PSF cannot be described by the Airy pattern anymore, but more sophisticated models accounting for the emission characteristics of a dipole emitter are required [42, 43]. The shape of the resulting PSF highly depends on the orientation of the dipole moment, the numerical aperture of the objective and the position of the emitter with respect to the focal plane. The PSF may exhibit a complex, asymmetric shape deviating strongly from a Gaussian function [12, 41]. Further, it has to be noted that the assumptions used in the derivation of Eq. (2.3) and (2.4) are not valid in the case of fixed dipole emitters. If two points are resolvable now depends strongly on the specific shape of the respective PSFs.

Diffraction poses a fundamental limit on the resolution of conventional optical microscopy. Structural information about an object can only be obtained if the spatial structure of interest is larger than this resolution limit. A resolution of around 200 nm is sufficient for identifying most cellular organelles, including the nucleus and mitochondria. Many biological structures in the cell, however, are smaller than the diffraction limit. Protein complexes show a lateral diameter of around 100 nm (e.g. the nuclear pore complex, [44]) down to a few nanometers only (e.g. ion channels, [24]). Consequently, these structures cannot be resolved with conventional optical microscopy methods, but more advanced and sophisticated approaches are required to investigate them in detail—one such approach is provided by SMLM.

2.2.3. TIRF microscopy

For achieving optimal resolution in fluorescence microscopy a high signal-to-noise ratio is crucial. Background signal includes camera noise, but also cellular autofluorescence or other fluorophores outside the focal plane. Total internal reflection fluorescence (TIRF) microscopy is an excitation scheme, which excites only fluorophores close to the coverslip, while reducing the contribution of fluorescent background signals [45, 46]. The illumination schemes for epi-illumination and TIRF microscopy are illustrated in Fig. 2.6.

The principle of TIRF is based on Snell's law of refraction, which describes the relation between the incidence and refraction angle of an electromagnetic wave when passing the boundary between two isotropic media:

$$n_1 \sin(\theta_1) = n_2 \sin(\theta_2), \quad (2.5)$$

where n_1, n_2 are the refractive indices of the two media, and θ_1, θ_2 are the angle of incidence and refraction, respectively. According to Eq. (2.5), for an increasing angle of incidence θ_1 , also

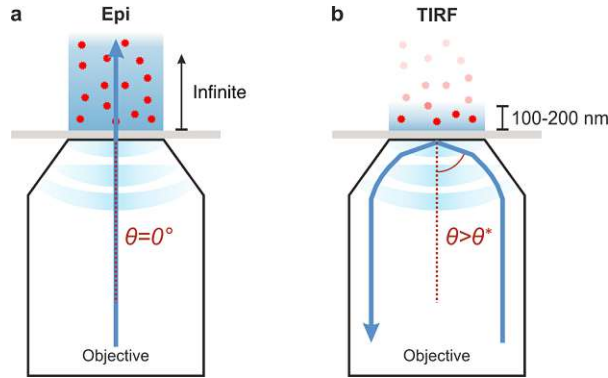


Figure 2.6.: Illumination. (a) Epifluorescence. An excitation beam parallel to the optical axis ($\theta = 0^\circ$) passes directly through the whole sample, with theoretically infinite penetration depth. (b) TIRF. The sample is excited with a laser at an angle above the critical angle ($\theta > \theta^*$). The beam is totally reflected at the interface between the microscope slide and the specimen. Some of the incident energy passes the interface as an evanescent wave, with exponentially decaying intensity and a characteristic penetration depth of around 100 nm to 200 nm. Thus, fluorophores close to the glass slide (gray) are excited, while the background fluorescence is highly reduced. Figure recreated and adapted from [47].

the refraction angle θ_2 increases. The incidence angle for which the refraction angle reaches $\theta_2 = 90^\circ$ is referred to as the critical angle θ^* , i.e. $n_1 \sin(\theta^*) = n_2 \sin(90^\circ)$. Solving this equation for the critical angle yields

$$\theta^* = \arcsin\left(\frac{n_2}{n_1}\right). \quad (2.6)$$

Of note, a real-valued solution to this equation only exists if $n_1 > n_2$, which means for light passing from the medium of higher optical density to a medium of lower optical density.

If the angle of incidence exceeds the critical angle, i.e. $\theta_1 > \theta^*$, the incident light gets totally reflected. Nevertheless, at the interface of the two media some of the incident energy passes into the second medium. The resulting electromagnetic field in the second medium is referred to as evanescent wave, which decays exponentially according to

$$I(z) = I_0 e^{-z/d}, \quad \text{with } d = \frac{\lambda}{4\pi} \left(n_1^2 \sin^2(\theta_1) - n_2^2 \right)^{-1/2}, \quad (2.7)$$

where $I(z)$ describes the intensity at distance z from the interface, and d is the characteristic penetration depth, which depends on the wavelength of light λ , the incidence angle θ_1 , and the refractive indices n_1, n_2 of the two media. With increasing incidence angle θ_1 , the penetration depth decreases.

In TIRF microscopy, the excitation light is reflected at the interface between the microscope glass slide ($n_1 \approx 1.5$) and the aqueous specimen ($n_2 \approx 1.33$). Hence, according to Eq. 2.6 the critical angle θ^* calculates to around 60° . For light in the visible spectrum, the penetration depth ranges from approximately 100 nm to 200 nm. The evanescent wave excites fluorophores close to the glass slide, while preventing background signal from autofluorescence or out-of-focus fluorophores. Therefore, TIRF is well suited for studying molecules in the cellular plasma membrane at the bottom of adhered cells. This excitation scheme can be combined with many fluorescence microscopy techniques, in particular SMLM (see section 2.3).

2.3. Single molecule localization microscopy

This chapter contains content from the following published book chapter:

M. C. Schneider and G. J. Schütz. *Single-Molecule Localization Microscopy (SMLM)*.

In: *Imaging modalities for biological and preclinical research: A compendium*, IOP Publishing, 2021. doi: 10.1088/978-0-7503-3059-6ch18

The diffraction limit of light (see section 2.2.2) has long been thought to set an inevitable barrier to the resolution of light microscopy. In the last decades, however, the development of superresolution microscopy techniques has achieved to circumvent the diffraction limit and thus, has enabled the study of cellular structures in unprecedented detail. The two major types of superresolution microscopy are stimulated emission depletion (STED) microscopy [48] and single molecule localization microscopy (SMLM) [16]. Since this thesis builds up on SMLM techniques, I provide in the following an introduction to the basic principles behind SMLM and its imaging parameters, which are key for achieving optimal resolution and crucial for appropriate interpretation of the obtained super-resolution images.

2.3.1. Principle

In 2006, different realizations of SMLM were published in parallel: photoactivated localization microscopy (PALM) [49], fluorescence photoactivation localization microscopy (fPALM) [50] and stochastic optical reconstruction microscopy (STORM) [51]. Further approaches include direct stochastic optical reconstruction microscopy (dSTORM) [52] and point accumulation for imaging in nanoscale topography (PAINT) [53], including DNA-PAINT [54].

All variants of SMLM rely on the same basic idea: to separate the signal of individual emitters in time, which allows to determine their positions with nanometer precision. An illustration of the principle behind SMLM is depicted in Fig. 2.7. Here, the scale of the structure of interest is too small to be resolved by diffraction-limited microscopy. If all labels emit a signal at the same time, their PSFs will overlap, resulting in a blurry spot with no discernible structure (Fig. 2.7a). In SMLM, the signals of individual emitters are separated in time. In each frame, only a sparse subset of all labels are in the bright state, so that their individual signals are well separated (Fig. 2.7b). This is typically achieved by exploiting stochastic blinking or binding phenomena (see section 2.3.2), leaving only a sparse subset of molecules visible at a certain time point. Hence, for image acquisition thousands of individual frames need to be recorded until most labels have been detected at least once.

Subsequently, the raw data is analyzed: For each detected signal, a localization coordinate is determined, which describes the position of the emitter (see section 2.3.5). Decisively, the position of an individual emitter can be estimated with a precision at the nanometer scale which is well below the diffraction limit of light. This can be achieved, for example, by simply determining the center of the fluorescence signal or by fitting a PSF model to the recorded data [55]. Finally, the obtained localizations from all frames are combined to yield a reconstructed image. Thereby, the resolution of the image is not limited by the diffraction of light anymore, but instead by the precision and accuracy of the position estimation for individual emitters.

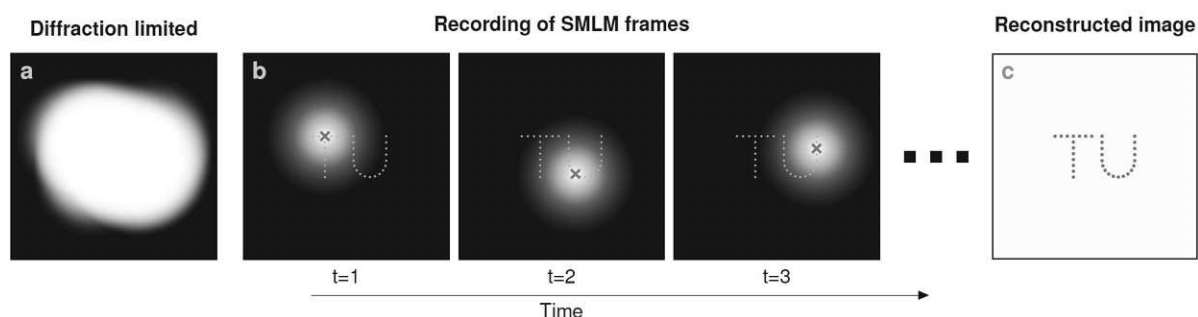


Figure 2.7.: Principle of single molecule localization microscopy (SMLM). The structure of interest is labeled with fluorophores. In the diffraction-limited image (a), the PSFs of individual emitters overlap and the structure cannot be determined. For SMLM, the fluorophores switch stochastically between a bright (fluorescent) on-state and a dark (non-fluorescent) off-state (b). In each frame, only a small subset of all labels is in the bright state, so that their fluorescence signals are well separated and the position of the molecules can be determined with high precision. Finally, the obtained localizations from all acquired frames are combined to yield a reconstructed super-resolution image (c). Figure adapted from [56].

2.3.2. Methods for separating signals in time

The stochastic separation of fluorescence signals of individual emitters in time can be achieved in several ways, which can be broadly distinguished into stochastic blinking of fluorophores and transient binding events. In the following, an overview of different methods will be given, which are also depicted in Fig. 2.8.

Switching. *Switching methods* are based on transitions of fluorescent labels between a bright on- and a dark off-state. The on-state is fluorescent and the label can be detected as a signal on the camera chip, whereas the off-state is non-fluorescent and does not emit any signal. Stochastic transitions between the bright and dark state are achieved by irradiation with light of appropriate wavelength. The main mechanisms are the following [35, 52, 57–59]:

- **(Photo-)Activation:** An initially non-fluorescent molecule acquires fluorescent properties. This process can either be induced by irradiation with light of appropriate wavelength (photoactivation) or occur spontaneously by oxidation of the fluorophore.
- **Photodeactivation:** Irradiation with light of appropriate wavelength causes the loss of fluorescent properties of the molecule.
- **Photoconversion:** Irradiation with light of appropriate wavelength leads to a photoinduced shift of the excitation and/or emission spectrum.

Commonly, a combination of these mechanisms is used for imaging. A variety of underlying physical or chemical processes have been described, resulting in varying nature of the dark state and degree of reversibility to the bright state. Reversible transitions between the bright and dark state are usually referred to as *photoswitching*, whereas the permanent transition into the dark state is termed *photobleaching*. A broad range of physicochemical mechanisms are

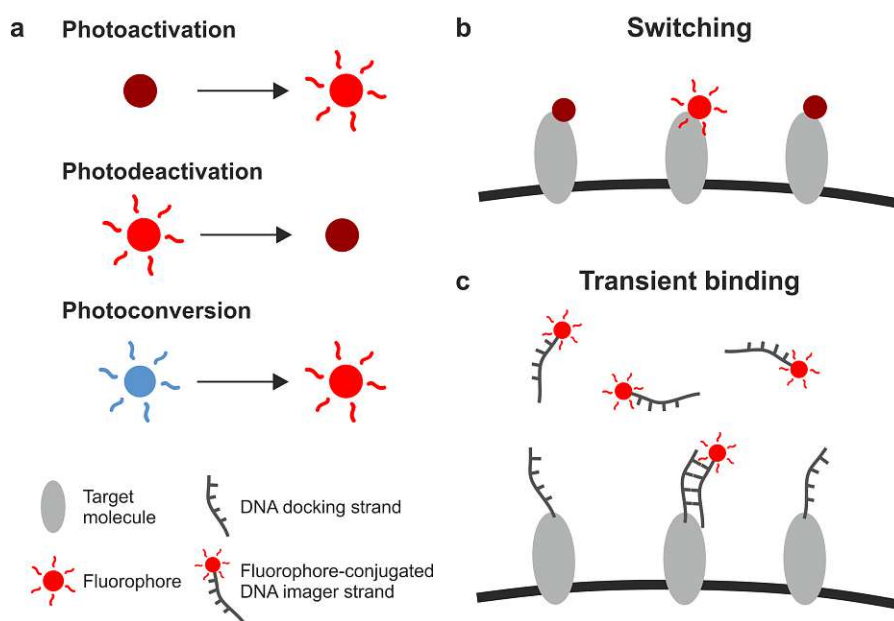


Figure 2.8.: Methods for separating fluorescence signals in time. (a) Depiction of (photo)activation, photodeactivation and photoconversion. In photoactivation and -deactivation the fluorophore is transferred from a dark into a bright state, or vice versa, upon irradiation with light. Activation can also occur spontaneously by oxidation of the fluorophore. In photoconversion, the fluorophore is transferred from one bright state into a second spectrally distinct bright state upon irradiation with light. (b) Switching methods are exploited in STORM and PALM. Here, fluorophores are conjugated to the target molecules. Stochastic switching of the fluorescent labels between a bright and a dark state allows to separate signals in time. (c) Transient binding methods, including PAINT and variants of it, rely on the transient binding of the fluorescent labels to the target of interest. Here, DNA-PAINT is shown: The molecule of interest is labeled with a short DNA docking strand. The complementary imager strands carry the fluorophore and diffuse freely in solution, smearing out their fluorescence signal over the whole camera chip. Upon binding of an imager strand to a docking strand, the fluorophore is immobilized for a certain time and can be detected as fluorescence spot on the detector. Figure adapted from [56].

responsible for inducing the switching behavior. Photoactivation and photoconversion typically involve a bond cleavage. Possible underlying processes for photoswitching include cis-trans isomerization steps, proton transfer or chemical reactions with extrinsic additives, e.g. redox reactions. The methods PALM [49] and fPALM [50] apply photoactivatable, photoswitchable or photoconvertible fluorescent proteins to achieve switching, while STORM [51] and dSTORM [52] rely on chemically induced blinking of organic dyes.

Transient binding. A different approach for separating the emission of fluorescent labels in time is based on *transient binding events*. This principle is exploited in PAINT [53] and various adaptations of it. Here, fluorophores diffuse freely in the imaging solution. The diffusion times exceed the illumination time for one frame, which leads to spreading of the signal over the camera chip. Hence, unbound fluorophores can only be observed as background fluorescence.

Additionally, quenching of fluorophores in the unbound state may suppress their emission. Upon spontaneous binding to the target, the fluorophore is immobilized for at least a few milliseconds and can be detected as a bright spot. Due to the stochastic nature of the binding process, the fluorophores in solution bind to the target structures at different times; thus, their signal is separated in time. The binding rate can be adjusted by changing the concentration of the fluorophore in solution, while the duration of a binding event can be adjusted via the binding affinity of the label to its target. The original PAINT approach has been generalized under the acronym uPAINT (universal points accumulation for imaging in nanoscale topography) [60]. A main advancement of the principle is DNA-PAINT [54,61]. Here, short fluorescently labeled oligonucleotides (imager strands) diffuse in solution and transiently bind to complementary DNA docking strands that are attached to the target of interest. Altering the specific oligonucleotide sequence and its length offers the possibility to conveniently adjust binding strengths. In combination with the adjustment of imager strand concentration, DNA-PAINT thus allows for programmable binding and unbinding kinetics.

In each frame of the SMLM acquisition, only a sparse subset of fluorophores is supposed to be in the fluorescent on-state, whereas all others are required to be in the off-state. Imaging conditions need to be adjusted in order to achieve an optimal density of active emitters. If this density is too high, the signals of individual emitters will overlap and impede accurate localization. On the other hand, too few active emitters will reduce the obtained number of localizations per frame and thus, either require a high number of recorded frames or result in a low detection efficiency. On- and off-rates depend on the illumination protocol, in particular illumination time and power, but are also influenced by buffer conditions and the fluorophore's particular nanoenvironment [8,62,63]. These parameters need to be optimized according to the requirements of the specific fluorescent probe used for labeling. One important aspect which has to be kept in mind is that repeated transitions between the on- and off-state lead to multiple detections of the very same label [59]. The issue of overcounting will be discussed in section 2.3.8.

2.3.3. Sample preparation

Appropriate sample preparation is a key aspect in SMLM imaging. First, sample fixation is crucial for preserving the structure of interest over the whole image acquisition time. Second, the selected label is required to be suited for SMLM purposes, in particular it has to enable the transition between a bright and dark state. Third, the buffer conditions need to be adjusted in order to achieve suitable on-off switching rates. In the following, I will give an overview of these aspects.

Sample fixation. As the image acquisition in SMLM requires several minutes up to hours, SMLM is typically performed in fixed cells. Fixation is commonly achieved by means of chemical fixatives, typically paraformaldehyde and/or glutaraldehyde, which cross-link cellular proteins by covalent chemical bonds [23]. Of note, only proteins are cross-linked, whereas lipids in the cellular plasma membrane are virtually unaffected by chemical fixation, i.e. they

can still diffuse in-between the interconnected proteins. Crucial for any fixation method is the preservation of structural organization at the nanoscale. Applied fixation protocols should be optimized in order to reduce any induced structural artifacts. However, for chemical fixatives the fixation process takes several seconds up to minutes. During this time, the cellular structures necessarily rearrange due to diffusion, thus distorting the original structural organization [10]. Further, SMLM requires the acquisition of thousands of individual frames for obtaining a final reconstructed image. For achieving reliable images, it needs to be ensured that the sample stays as static as possible during the imaging procedure. Yet, residual diffusion of molecules after chemical fixation was reported [9], which distorts the recorded SMLM localization maps.

An alternative to chemical fixation methods is provided by cryogenic approaches: Imaging at cryogenic temperatures immobilizes all the molecules of the cell and offers the advantage of superior structural preservation [11]. In addition, the photophysics of fluorophores is affected by temperature. In particular, the photostability of fluorophores is increased at low temperatures, leading to a higher photon yield and thus, improved localization precision. However, performing experiments at cryogenic temperatures is demanding and fluorophore dipoles are fixed, which complicates the localization procedure [12, 55]. A further introduction to cryo-SMLM approaches will be given in chapter 6 of this thesis.

Labeling. For SMLM applications, a critical feature of any labeling technique is its ability to switch between a bright and a dark state. The labeling of choice further needs to fit to the chosen target structure. Importantly, the original properties of the biomolecules of interest should not be affected, in particular, if labeling is performed prior to fixation. Overall requirements demanded from any fluorescent probe include high labeling efficiency and binding specificity in order to ensure that the labeling correctly represents the structural organization of the biomolecules of interest. Moreover, the size of the label needs to be small with regard to the structure of interest and the desired localization precision. Otherwise, the introduced localization bias (see section 2.3.5) will lead to a distortion of the structure. Furthermore, labels need to exhibit favorable fluorescent properties: particularly, the on-off switching contrast and the number of switching cycles influence the quality of the obtained image. Most importantly, a high photon budget, i.e. brightness, is a prerequisite for achieving high localization precision in SMLM (compare section 2.3.5). In the following, I will give a short overview of different types of labeling methods [64]. In Fig. 2.9 the molecular structures of a few commonly used labels are shown.

Photoactivatable fluorescent proteins (FPs) fused to the protein of interest ensure specific targeting. Commonly, FPs are derivatives of the green fluorescent protein (GFP, Fig. 2.9b) originally extracted from the jellyfish *Aequorea victoria* [67]. FPs are genetically fused to the protein of interest. Photoactivatable, photoswitchable or photoconvertible FPs allow for SMLM applications. However, with a size around 2 nm to 5 nm FPs are rather larger and it has to be ensured that the FP does not perturb the functionality of the original protein. Moreover, detection efficiency can be reduced by the presence of not fully matured FPs as well as photobleaching before the actual detection step. Notably, the brightness of FPs is generally worse compared to organic fluorophores, which affects localization precision. Furthermore, an

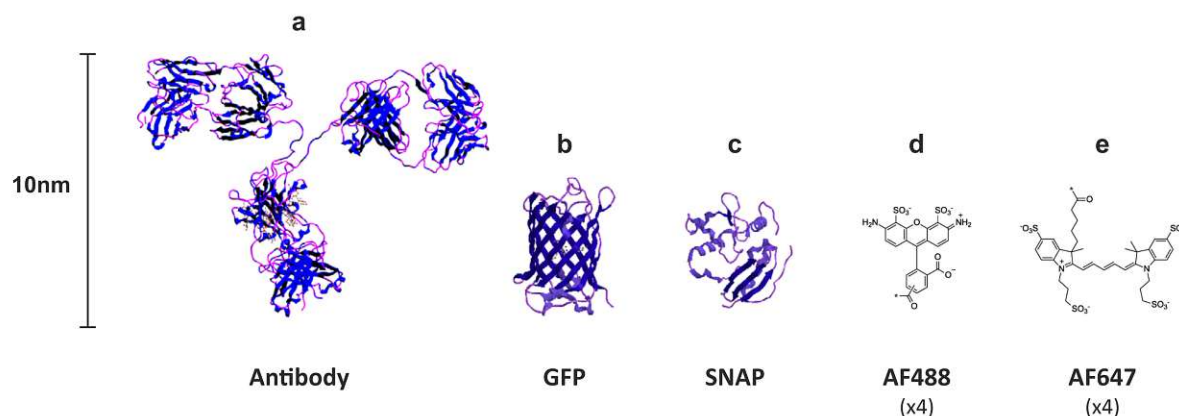


Figure 2.9.: Structure and size of various labels. (a) Immunoglobulin G (IgG) antibody. (b) Green fluorescent protein (GFP). (c) SNAP-tag. (d) Alexa Fluor 488. (e) Alexa Fluor 647. Note that the scale for the Alexa Fluor dyes is different ($\times 4$). Figure adapted from [65, 66].

obvious disadvantage of FPs is the exclusive applicability to proteins.

Organic dyes (e.g. rhodamine and cyanine dyes) represent another group of fluorescent labels. Two commonly used families of dyes are the Alexa Fluor (Fig. 2.9d,e) and ATTO dyes, available at various excitation and emission spectra. These synthetic fluorophores have a rather small size of around 1 nm, high quantum yield and extinction coefficient. For application in SMLM, a stable off-state together with appropriate photoswitching rates of the dye are required. The probes typically cycle between their bright and dark state many times before photobleaching. A disadvantage of organic dyes compared to FPs is the need for a chemical labeling procedure. Organic dyes may be attached to the biomolecule of interest via immunofluorescence, enzymatic protein tags or click chemistry, explained in more detail below.

In immunofluorescence, the structure of interest is targeted via primary and optionally secondary antibodies conjugated to fluorophores. The main advantage of immunofluorescence labeling is its rather simple applicability. However, the comparably large size of antibodies of around 10 nm can cause steric hindrance, thus hampering target recognition. In addition, the fluorophores are displaced from the actual target structure; in particular, when labeling with secondary antibodies, the position of the label can be shifted up to 20 nm away from the biomolecule of interest. A smaller alternative is provided by nanobodies, which are camelid antibodies with a size around 2 nm.

Another labeling approach are enzymatic protein tags, which combine the advantage of genetic encoding with the favorable properties of fluorescent dyes, while being comparably small in size. Here, the polypeptide tag is fused to the protein of interest and labeled after translation with an organic fluorophore. Available tags include the SNAP, CLIP and Halo tags [68, 69]. The SNAP-tag, for example, relies on the human O⁶-alkylguanine-DNA alkyltransferase (hAGT)—a human DNA repair enzyme—as a protein tag, which can be fused to the protein of interest. Labeling of the tag is achieved via fluorophore-conjugated O⁶-benzylguanine (BG) derivatives: The hAGT protein cleaves off the BG subunit and covalently binds the fluorophore.

An emerging versatile labeling tool is click chemistry [70], which offers labeling of various cellular structures, including proteins, nucleic acids, glycans and lipids. For this, the fluorophore can be modified for example as azide and the targeted reaction partner as alkyne, or vice versa, which yields a selective and extremely stable covalent linkage between them. Modified amino acids, nucleotides, monosaccharides, or fatty acids can be incorporated by the cells due to the small size of the azide or alkyne tags, and subsequently be labeled with the fluorophore. In particular unnatural amino acids allow for site-specific labeling of proteins of interest [71].

For DNA-PAINT [54, 61], the structure of interest is not directly labeled with a fluorescent probe, but bound to a short oligonucleotide strand (the docking strand) via an antibody or an enzymatic protein tag, for example. The fluorophores are coupled to complementary oligonucleotide strands (the imager strands) as part of the imaging solution.

Imaging buffer. In a typical SMLM experiment, cells are seeded on a microscopy glass coverslip and immersed in imaging buffer. In general, the refractive index of the imaging buffer should be adjusted in order to minimize aberrations. Depending on the variant of SMLM that is performed, the imaging buffer needs to meet additional requirements: Imaging of organic dyes in dSTORM requires special buffers for inducing blinking and controlling the on-off switching rates; these buffers usually include thiols and an oxygen scavenging system [52, 72]. The presence of thiols leads to the formation of radical anions of the fluorophore, which provide a stable dark state for several seconds up to minutes; oxidation of the radical anion recovers the bright singlet state. Thus, the concentration of thiols and oxygen in the imaging buffer control the fluorophore switching rates between bright and dark states. For fluorescent proteins in contrast, cells can be embedded in standard water-based saline solutions without the need for additional ingredients. In the case of DNA-PAINT, the imaging solution is also based on a saline solution. However, it additionally needs to contain the fluorophore-conjugated imager strands, which diffuse freely in the solution [73]. Here, the concentration of imager strands and the salt concentration affect the imaging speed and quality. By optimizing the buffer conditions best imaging conditions can be achieved [62, 73, 74].

2.3.4. Setup

In this thesis, I will propose analysis methods both for conventional SMLM experiments performed at room temperature as well as cryo-SMLM approaches performed under cryogenic conditions. In Fig. 2.10 schematic illustrations of both considered setups are shown. For experiments at room temperature, SMLM imaging is typically performed on modified conventional inverted wide-field fluorescence microscopy systems (Fig. 2.10a).

In case of cryo-fixation, also the SMLM image acquisition needs to be performed under cryogenic temperature. Here, a setup as described in [75] is considered. For cryo-SMLM, the sample needs to be cooled via liquid nitrogen or liquid helium, and an additional vacuum chamber is required in order to prevent thermal conduction from room ambient temperature (Fig. 2.10b). This demands for a larger working distance of the objective, thus prohibiting the use of high numerical aperture (NA) oil-immersion objectives. Instead, the setup requires the use of an air-objective with a larger working distance, restricting the possible NA to much lower values

2. Background

of typically 0.7 to 0.8. An interesting alternative strategy to increase the NA also for large working distances is the use of a super-hemispherical solid immersion lens [76].

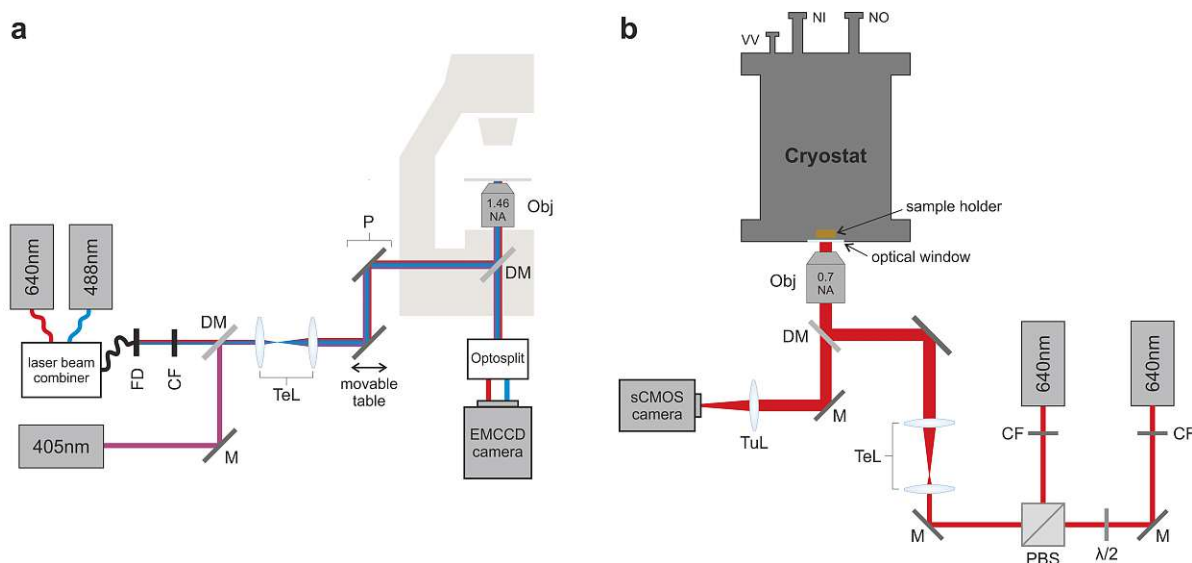


Figure 2.10.: Schematic outline of microscopy setups. (a) Setup for measurements at room temperature. Two laser lines (640 nm, 488 nm) are used for fluorophore excitation, the 405 nm laser for fluorophore activation. An oil-immersion objective with 1.46 NA and 100 \times magnification is used. (b) Cryo-setup. Two 640 nm laser lines with linearly polarized light are used for fluorophore excitation. The two laser lines show orthogonal polarization directions. The sample is cooled via liquid nitrogen in the cryostat tank. An air-objective with 0.7 NA and 60 \times magnification is used. Abbreviations: FD fibre decoupler, CF cleaning filter, M mirror, DM dichroic mirror, $\lambda/2$ wave plate, PBS polarizing beam splitter, TuL tube lens, P periscope, Obj objective, VV vacuum valve connection, NI nitrogen inlet, NO nitrogen outlet.

Sample illumination. The illumination light for activation and excitation of fluorophores needs to be ideally uniform in intensity and of well-defined wavelength. Typically, lasers are employed as light source, which are required to match the respective activation and excitation spectra of the used fluorophores. For example, commonly used laser lines are 488 nm and 640 nm for excitation of Alexa Fluor 488 and Alexa Fluor 647, respectively, and 405 nm for activation. Excitation filters and beam shapers are inserted into the excitation path for optimization of the laser beam. Emission filters separate excitation from emission light; careful selection of the filters helps to improve the signal-to-noise ratio. Illumination intensities are typically 0.5-5 kW/cm² for excitation and less than 0.1 kW/cm² for photoconversion or photoactivation. Excitation intensity and illumination time influence the localization precision and detection efficiency: In general, there is a trade-off between the time required for image acquisition and image quality [62]. For high intensities, a large fraction of fluorophores bleaches before being detected [62]; moreover, increased background signal leads to undesired false positive localizations [63]. Low intensities in combination with longer illumination times generally improve the detection efficiency and localization precision; however, the problem of overcounting increases [62]. For ideal results, it was proposed to perform the initial switch-

off phase for STORM experiments at low intensities to retain the effective labeling efficiency, while the actual image acquisition may be performed at higher intensities [62]. For experiments performed at cryogenic temperature, it has to be ensured that the laser power does not lead to heating of the sample; local heating leading to lateral diffusion of molecules would conflict with cryo-fixation and distort the resulting localization maps. In addition, the fixed orientation of fluorophore dipoles at cryogenic temperature offers valuable additional information which can be exploited in analysis approaches (see chapter 8). Slight rotations of fluorophore dipole orientations due to sample heating would confound such an analysis.

Several modes of sample illumination are available for SMLM. Ideally, all fluorophores bound to a biomolecule of interest get excited, while background contribution is avoided. Of note, background fluorescence may arise from cellular autofluorescence, dirt particles, unspecifically bound labels and residual unbound fluorophores. First, homogeneous background from any out-of-focus signal adds to the noise in the image and thus, deteriorates the localization precision. Second, background signals lead to spurious localizations which distort the analysis of localization maps. Specialized illumination approaches exist that suppress out-of-focus signal and thus, reduce background fluorescence: TIRF microscopy (see section 2.2.3) is ideally suited for imaging of the cellular plasma membrane of adhered cells; illumination at the critical angle causes an evanescent wave that excites only those fluorophores that are located within approximately hundred nanometers from the coverslip. Thus, TIRF allows for a confined excitation region and yields an increased signal-to-noise ratio and image contrast. However, the illumination power decreases exponentially with the fluorophores' z -position. This leads to inhomogeneous illumination of the fluorophores within the sample and thus, possibly different blinking behavior depending on the fluorophores' axial position. As TIRF imaging requires a high NA objective in order to achieve a laser inclination above the critical angle, it is infeasible for cryo-SMLM experiments with low NA, and one has to revert to a conventional epi-illumination scheme. In order to avoid out-of-focus fluorescence in this case, a thin cell section can be cut out of the frozen cell by focused-ion-beam milling [77].

Objective. A microscope objective is characterized by its magnification and numerical aperture. For SMLM at room temperature, oil-immersion objectives with high numerical aperture—typically with a NA higher than 1.4—achieve a high photon collection efficiency. Currently, the objective with the highest available NA achieves a value of 1.7 [78]. For cryo-SMLM, the larger working distance requires the use of air-objectives with low NA of 0.7 to 0.8. Notably, for emitters with fixed dipole orientation the numerical aperture greatly influences the obtained PSF, as will be discussed in chapter 6.1 of this thesis. High-quality objectives typically correct for common lens errors such as spherical aberration; for dual-color imaging apochromat objectives reduce chromatic aberrations.

Detection. Photons emitted from the fluorophores are detected and imaged on a sensitive camera chip. Apart from traditional charge-coupled device (CCD) cameras, further options are available. Electron-multiplying charge-coupled device (EMCCD) cameras amplify the signal in order to increase it above read-out noise and thus allows for imaging with high frame rates. The more recent development of scientific complementary metal-oxide-semiconductor

(sCMOS) cameras is an even faster alternative to EMCCDs. The image pixel size of the camera is typically chosen to be around 100 nm, which balances signal and noise and thus, optimizes localization precision (compare section 2.3.5).

Acquisition times for a single frame range from 1 ms to 20 ms for STORM or PALM, and up to 100 ms to 500 ms for PAINT approaches, due to the longer duration of transient binding events needed compared to fluorophore blinking. Typically, thousands of frames are recorded for one region of interest. Sample movement relative to the detector due to mechanical instabilities of the microscope stage and thermal drift may distort the image, especially for prolonged imaging times. This stage drift can be compensated for by means of fiducial markers or based on cross-correlation (see section 2.3.6). Furthermore, waiting times before the beginning of the measurement reduce the effect of initial mechanical relaxation.

3D setups. In conventional 2D microscopy, the PSF is axially symmetric. The signal of a fluorophore slightly above and below the focal plane cannot be distinguished and thus, the extraction of 3D information is limited. In order to enable localization in the third dimension, the axial symmetry has to be broken. This can be achieved by various methods that rely on recording the fluorescence of emitters in multiple channels simultaneously and/or modifying the shape of the PSF. Methods using multiple imaging channels include biplane imaging [79], interferometric approaches [80,81] and supercritical angle microscopy methods [82]. The shape of the PSF can be modified by introducing additional optical elements in the light path, as for example in astigmatic imaging [83] or for a double-helix PSF [84]. Various 3D methods primarily differ in their complexity, resolution along the optical axis and imaging depth. An overview of 3D techniques can be found in [55].

2.3.5. Localization

An essential part of SMLM is the post-processing of the recorded raw image data in order to obtain the reconstructed final image. Raw SMLM data typically consists of thousands of individual frames. For each frame, the blinking events have to be analyzed and the positions of active emitters need to be determined with high precision and accuracy. Difficulties that have to be faced in the analysis include background noise, uncertainties in the size and shape of the point spread function and possible aberrations. Localization algorithms need to process large amounts of data, typically in the range of gigabytes for a single image. Often, the demands for speed and precision of the localization compete.

As a first step in the analysis, active fluorophores have to be identified. For this, threshold and rejection parameters are set in order to distinguish fluorophores from background and avoid fitting of signals or peaks that do not arise from the fluorescent probes. Subsequently, the localization coordinates of the detected fluorophores have to be determined. In the simplest case, the centroid of the signal can be taken as an estimate for the emitter position. Another commonly applied method is Gaussian fitting of the signal with a least-squares or maximum likelihood approach [41]. More complex PSF models include theoretical ones based on the laws of diffraction [85], and experimentally acquired PSF models [86]. In case of imaging at cryogenic temperature, the fixed dipole orientation of fluorophores has to be taken into account

for determining an accurate PSF model [12, 13]. For 3D localization of fluorophores, the axial position can be extracted from the shape of the PSF or the recording of multiple channels simultaneously [55].

In general, the density of simultaneously active emitters should be low enough to ensure that individual signals are well separated. However, as blinking is stochastic, it may occur that neighboring fluorophores are active at the same time, leading to insufficient spatial separation of their signals. In cryo-SMLM, in particular, the issue of overlapping signals is abundant as the photophysics of fluorophores is slowed down [75, 87]. For measurements at room temperature, a high density of active emitters might be desired as it allows for faster acquisition and thus, higher temporal resolution in case of live-cell imaging. Specific algorithms exist that allow for multi-emitter fitting, i.e. the fitting of partially overlapping signals [88, 89]. Alternatively, those frames showing only a single signal in a certain region can be determined and analyzed, while frames with overlapping signals are neglected [90]. Of note, this procedure might distort the resulting localization map, as more signals will be discarded in dense regions compared to sparse ones. This is primarily an issue for the analysis of clusters with varying densities over the region of interest; the results for homogeneous oligomer distributions will be less affected.

An evaluation and comparison of a broad range of available localization software packages both for 2D and 3D SMLM was performed by Sage et al. [91, 92]. These software tests were mainly based on computer-simulated data sets, which provide knowledge of ground truth, and thus, allow to reliably assess the achieved localization precision, accuracy and detection rate.

Localization precision. The fundamental concept behind SMLM is to determine the position coordinates of isolated emitters from their PSF image. However, the position can only be estimated with limited certainty. The standard deviation of this error distribution is referred to as the localization precision. An estimate of the achieved precision may be acquired experimentally by repeatedly imaging and localizing the same emitter, and determining the spread of the position coordinates.

The localization precision is influenced by several parameters, including the shape and width of the PSF, shot and background noise, and defocus. Various formulas have been derived to describe the achievable localization precision based on these parameters [55]. Theoretically, the best possible precision is determined by the Cramér–Rao bound (CRB) [93]: The variance of any unbiased estimator $\hat{\xi}$ of a parameter ξ is bound from below by the inverse of the Fisher information matrix \mathcal{I} , in particular

$$\text{Var}(\hat{\xi}) \geq \mathcal{I}^{-1}(\xi), \quad \text{with } \mathcal{I}(\xi) = \mathbb{E} \left[\left(\frac{\partial \ln L(\xi)}{\partial \xi} \right)^2 \right], \quad (2.8)$$

where $L(\xi)$ is the likelihood of the observed data given a model generated by ξ . Hence, the Fisher information matrix depends on the statistical model of the underlying stochastic process of the data (see chapter 7.4.3 for a derivation of the Fisher information matrix for SMLM data). Commonly, the localization precision is defined as the standard deviation of the localizations; the lower limit for the localization precision of an unbiased estimator is hence given by the square root of $\mathcal{I}^{-1}(\xi)$ [94, 95].

Importantly, the maximum-likelihood estimator achieves the CRB [96]. Assuming a Gaussian PSF model and a maximum-likelihood fit, the localization errors can be well described by [97]

$$\langle (\Delta x)^2 \rangle = \frac{s^2 + a^2/12}{N} \left(1 + 4\tau + \sqrt{\frac{2\tau}{1 + 4\tau}} \right), \quad \text{with } \tau = \frac{2\pi b(s^2 + a^2/12)}{Na^2}, \quad (2.9)$$

where Δx is the error in localization, s is the width of the Gaussian PSF, a the pixel size and b the background noise, i.e. the standard deviation of the background signal. The localization precision σ_{loc} is given by the square root of $\langle (\Delta x)^2 \rangle$.

The main impact on localization precision arises from shot noise, which originates from the particle nature of light and scales with the square root of the number N of detected photons; hence, the localization precision is proportional to s/\sqrt{N} . The photon count depends on illumination time, wavelength of illumination and photophysical properties of the fluorophore, including extinction coefficient, quantum yield and photostability. Hence, fluorescent probes with high photon output are desired for SMLM applications.

Background signal primarily arises from residual cellular autofluorescence, and from Rayleigh or Raman-scattered light. Careful choice of emission filters, and selective excitation of the focal plane (see section 2.3.4) helps to reduce these contributions. Moreover, dark current due to thermic noise adds to the background. This type of noise causes a Poisson distributed background and increases with exposure time. Cameras are typically cooled in order to minimize dark current. A further source of noise is camera read-out noise, which arises from the electronics when reading out the image of a camera chip and is independent of the detected photon number. Read-out noise has been dramatically reduced by the introduction of EMCCDs and sCMOS cameras.

In addition, localization precision is influenced by the pixel size. On the one hand, smaller pixel size of the camera chip allows to better resolve the PSF. On the other hand, for a smaller pixel size, fewer photons are detected per pixel and the signal ultimately gets obscured by the detector noise. An optimal compromise was found to be given for a pixel size a fulfilling $(a/s)^4 = 96\pi b^2/N$ [98]. Typical pixel sizes correspond to 100 nm to 160 nm in the object plane.

For more complex PSF shapes, the formula given in Eq. 2.9, does not hold true and the CRB cannot be easily expressed analytically. However, the CRB may be calculated numerically based on Eq. 2.8.

Localization accuracy. The aim of the localization procedure is to correctly determine the position coordinates of the molecules of interest. Importantly, correct position estimation is not only affected by limited precision, but may also be impaired by a localization bias, which describes the deviation of the mean measured position from the true position coordinate of the target molecule. The effect of localization precision and accuracy is illustrated in Fig. 2.11.

In general, it is not the molecule of interest itself that is detected in SMLM techniques, but a fluorescent probe attached to it (see section 2.3.3). A bias in localization may arise from the finite size of fluorescent probes themselves, in particular for larger probes like fluorescent proteins. Moreover, linker moieties that connect the target to the fluorophore, e.g. primary

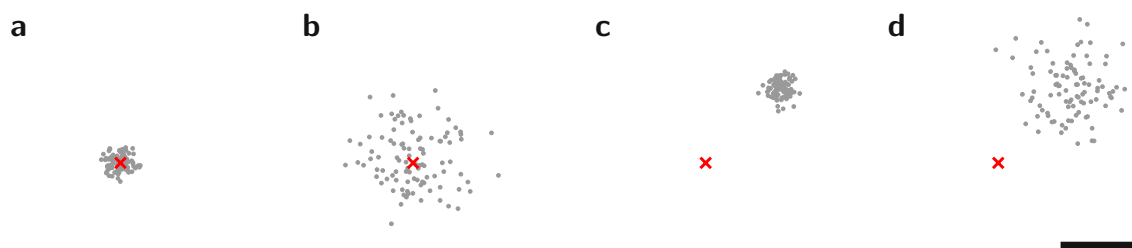


Figure 2.11.: Localization precision versus accuracy. The four panels show simulated repeated localizations of a target under the following conditions: **(a)** Precise and accurate. **(b)** Imprecise, but accurate. **(c)** Precise, but inaccurate. **(d)** Imprecise and inaccurate. The assumed position of the target is depicted as red cross. The localization precision was set to 5 nm and 20 nm for panels a,c and panels b,d, respectively. For panels c,d a bias of 50 nm in each direction was assumed. Scale bar: 50 nm.

and secondary antibodies, can lead to displacements of the fluorophore of up to 20 nm in a random direction.

Furthermore, fluorophores are dipole emitters and thus, exhibit asymmetric emission patterns. If a fluorophore's dipole orientation is fixed and cannot rotate freely, this will lead to distortions of the PSF. As a consequence, localization inaccuracies arise when using common estimators such as Gaussian approximation, in particular in case of imperfect focusing [12,13]. This aspect will be covered in detail in chapter 7 of this thesis.

2.3.6. Post-processing

After single molecule signals have been localized, the resulting list of localizations can be further processed. In order to minimize false positive localizations, the obtained localizations can be filtered. This allows to discard localizations that do not fulfill certain quality criteria. For example, localizations showing untypical characteristics for the used fluorescent probe, e.g. very high brightness values, large spread of the signal or enduring on-times, can be removed. As another post-processing step, localizations from the same emitter detected in different frames can be merged based on spatial and temporal proximity [5]. This reduces the problem of multiple detections of the same emitter (compare section 2.3.8).

The obtained localization coordinates further need to be corrected for drift, which occurs during the rather long acquisition times from minutes up to hours. Drift correction can either be achieved based on fiducial markers [99,100] or cross-correlation [101]. In the first case, fiducial markers such as fluorescent beads or gold nanoparticles are inserted into the sample and recorded together with it. The markers are tracked and their trajectories are used to retrieve the drift-corrected localizations. Drift correction based on cross-correlation is feasible if the target is highly structured. Partial images reconstructed from sub-sequences of the recorded data can then be cross-correlated in order to determine the drift.

For multi-channel imaging, additional corrections are required in order to account for the shift, stretch and possible distortion between the channels. Particularly, for multi-color imaging, chromatic aberration needs to be corrected for. Registration of the individual channels can be

performed based on multi-spectral fiducials, which are detectable in all channels [102].

For interpretation of the data, it is important to note that SMLM data substantially differs from conventional microscopy data: Conventional microscopy yields a pixelated image, with pixel values according to the recorded intensities. SMLM techniques, instead, yield a list of localization coordinates. For visual interpretation of the data, the localization list can be plotted as scatter plot or 2D histogram. Alternatively, each localization can be represented as a Gaussian, with a mean at the determined position coordinate and a width according to the localization precision. Notably, any visualization method is based on the determined localization coordinates, which do not correspond to the exact fluorophore positions, and due to linkage errors even less so to the true positions of the molecule of interest. Typically, SMLM data is not merely analyzed visually, but the localization map coordinates are the basis for more advanced analysis methods, in particular for quantitative analysis or structure determination [59, 103, 104].

2.3.7. Spatial, temporal and spectral resolution

A fundamental aspect of microscopy is resolution. In the following, I will shortly discuss spatial, temporal and spectral resolution with regard to SMLM.

Spatial resolution. For localization microscopy, the term resolution used in the conventional theory of Abbe and Rayleigh has to be redefined [105]. In the context of SMLM, spatial resolution is commonly reported as the precision achieved in the localization of a single emitter (see section 2.3.5). However, resolution is not only limited by localization precision, but also by labeling density and detection efficiency. In fluorescence microscopy in general, the sample is labeled at discrete sites, i.e. the molecules of interest. If the labeling is too sparse, structural details cannot be resolved, even in case of optimum localization precision. Here, often the Nyquist-Shannon sampling theorem is taken as a guideline, which states that neighboring localized emitters need to be closer than half of the smallest structural feature that can be resolved. However, for structures that do not show a continuous boundary, e.g. individual molecules in the cell membrane expressed at low levels, the final image will inherently be sparse. Thus, the reliability of the obtained information also depends on the specific features of the structure under investigation.

Temporal resolution. In SMLM, high spatial resolution is traded for temporal resolution. Typically, imaging is performed in fixed cells, i.e. at a single time point only. For live-cell imaging [57], the achievable temporal resolution mainly depends on the blinking behavior of the fluorescent probe and its photophysical properties, in particular quantum yield. Moreover, frame rates are limited by the camera read-out speed. The overall time required for obtaining an individual image results from the acquisition time for a single frame times the total number of frames that are recorded.

Multi-color imaging. In many biological questions, it is not sufficient to investigate a single type of biomolecule, but the interaction of several different ones. This aim can be achieved by multi-color imaging. Conventionally, multi-color imaging in SMLM is implemented by the use of spectrally distinct dyes, each of which targeting a specific molecule of interest. The different types of fluorophores can either be excited and imaged alternately in the same detection path, or their respective emission can be split into different color channels and imaged on separate regions of the camera chip. Color channels can be aligned by means of multi-color beads, which allows also to correct for chromatic aberrations. Spectral overlap limits the number of targets that can be imaged simultaneously to about three. In case of (d)STORM, buffer conditions have to be optimized dependent on the specific fluorophore [74], which further complicates the simultaneous imaging of multiple targets.

A major advancement towards multi-color imaging has been enabled by Exchange-PAINT [106]. Based on DNA-PAINT, this method allows for imaging a large number of different targets, only limited by the number of orthogonal DNA docking strand sequences. The idea is to repeatedly introduce and wash out imager strands specific for a single target until all desired targets have been imaged. The separated imaging steps allow to assign a pseudo-color to each target and obtain a multiplexed final image. A recent study showed the capability to differentiate up to 124 different colors based on this method [107]. For Exchange-PAINT, a single dye and a single laser source are sufficient. Hence, a dye with optimal photophysical properties can be selected for imaging of all targets. Moreover, the method circumvents the problem of chromatic aberrations.

2.3.8. Quantitative biology

As SMLM yields imaging information at the single molecule level, it seems ideally suited for quantitative biology studies [103, 104, 108]. Quantitative biology aims at characterizing and comparing highly complex biological structures, thus allowing to gain new insights into the functional mechanisms of cells. However, two issues—undercounting and overcounting—impede a direct assessment of biomolecular numbers and arrangements.

First of all, for a correct representation of the biomolecules of interest a well-defined stoichiometry of labeling is essential; ideally, each target molecule is labeled with exactly one dye molecule. Due to insufficient labeling efficiencies a certain fraction of the biomolecules of interest cannot be detected at all [109]. In contrast, for some labeling approaches—in particular antibody labeling—a biomolecule of interest may carry multiple fluorophores, and thus, can be detected multiple times, as illustrated in Fig. 2.12.

Surprisingly, even in the case of an ideal one-to-one labeling, a direct quantification of biomolecules via SMLM will be impeded: Ideally, every fluorophore or docking strand is in its on-state in exactly one frame during the whole acquisition procedure and thus, detected exactly once. However, fluorophores may bleach before being detected or never return from the dark state during the image acquisition time. In case of DNA-PAINT, a docking strand may never be reached by an imager strand, or only by imager strands carrying bleached fluorophores.

In contrast, if on-times exceed the acquisition time for a single frame, fluorophores will be

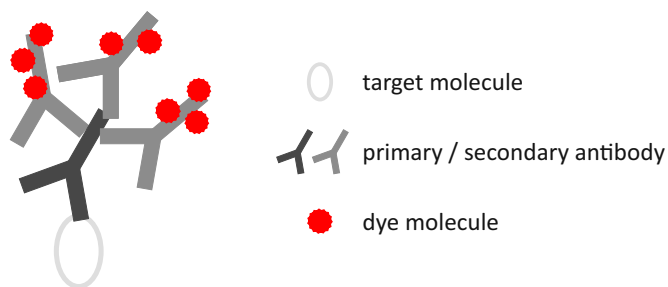


Figure 2.12.: Reasons for overcounting. A single molecule of interest—the target molecule (white)—is labeled with a primary antibody (dark gray), to which multiple secondary antibodies (light gray) may bind. Again, each of the secondary antibodies may carry multiple dye molecules (red). Additionally, each dye molecule may be observed multiple times due to repeated switching between the on- and the off-state. In combination, this leads to numerous detections of a single target molecule.

detected in multiple consecutive frames [3]. Further, fluorescent probes can switch repeatedly between the on- and the off-state, resulting in additional overcounting. While consecutive detections of the same fluorophore can be merged [5], prolonged dark times impede such a correction. Organic dyes typically show extensive and complex blinking behavior [110–112]. Blinking is less pronounced for photoactivatable fluorescent proteins, nevertheless, also FPs were observed to transition into prolonged dark states and subsequently return into the bright state [63]. In case of PAINT approaches, transient binding events to the same target molecule can occur repeatedly over the whole image acquisition time.

Both under- and overcounting have to be carefully considered, especially in quantitative analysis and interpretation of SMLM data. To this end, analysis methods tailored to the specific features of SMLM imaging are essential. The problem of overcounting, in particular, is central to this thesis, and possible solutions for circumventing the wrong interpretation of overcounting artifacts will be proposed.

2.3.9. Reference structures for avoiding imaging artifacts

As SMLM requires careful preparation of the sample as well as complex experimental procedures and data analysis, a wide range of parameters influence the final quality of the obtained images. Throughout this section, several issues distorting the resulting SMLM localization maps were pointed out which need to be considered for a correct interpretation of SMLM data. Fig. 2.13 shows a plot summarizing the influence of these aspects on the localization map.

First, localization precision and localization accuracy limit the achievable resolution in SMLM (Fig. 2.13a,b). The localization precision is mainly determined by the number of available photons in the signal, but also dependent on other parameters, including background noise (see section 2.3.5). The localization accuracy is directly influenced by the size of the linker used for labeling (section 2.3.3). In addition, localization bias may be caused by a spatially fixed dipole moment, if not accounted for in the localization procedure (section 2.3.5). A method for avoiding this localization bias in a cryo-SMLM setting will be proposed in chapter

7 of this thesis.

The localization map is further affected by undercounting: Due to insufficient labeling or detection efficiency some target molecules will not be detected, leading to misrepresentation of the imaged structure (Fig. 2.13c). Particle averaging approaches can often recover the underlying structure. An approach which allows to analyze only particles with at least one localization per target molecule and thus, yields precise estimates of oligomer sizes will be presented in chapter 8 of this thesis.

In contrast to undercounting, multiple detections of the same biomolecule of interest causes overcounting (Fig. 2.13d). Overcounting in combination with localization errors leads to clustering artifacts, which can be easily mistaken for true biomolecular clustering at the nanoscale (Fig. 2.13d). Clustering artifacts and methods which allow to distinguish these artifacts from true biomolecular nanoclustering will be the central topic of the first part of this thesis (chapters 4 and 5).

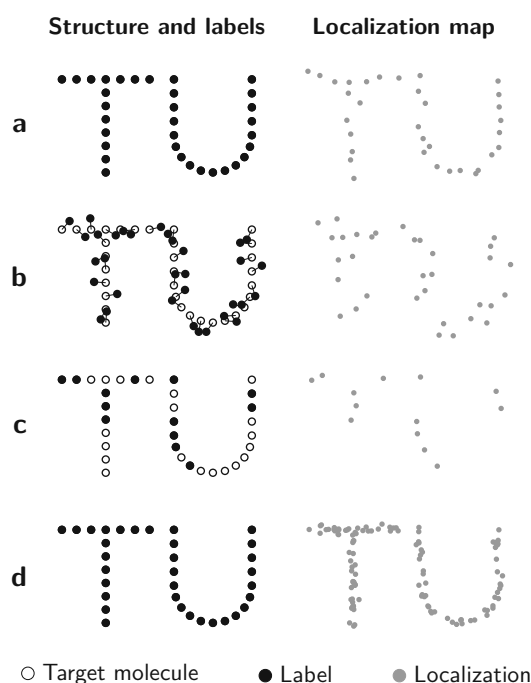


Figure 2.13.: Possible distortions of localization maps. The left column shows the actual position of the target molecules (circles); full and open circles indicate the presence or absence of a detectable label, respectively. In the right column, corresponding representative localization maps are depicted. Due to localization errors, the localizations are slightly displaced from the true molecule positions (a). The structure is distorted or misrepresented by label displacement (b), decreased labeling efficiency (c), or overcounting (d). Figure adapted from [56].

Directly assessing the quality of localization microscopy data has proven to be difficult, especially for imaging of *a priori* unknown structures. While the achievable localization precision can be estimated either via theoretical calculations or experimentally (see section 2.3.5), for other parameters, including the labeling and detection efficiency, a direct quality assessment

is challenging or even impossible. Therefore, robust test samples are commonly used as a reference in order to judge the quality of SMLM data and optimize the imaging conditions. Natural biological samples of a well-defined structure include the nuclear pore complex and cytoskeleton structures such as actin filaments and microtubules [109, 113]. Moreover, DNA origami provide artificial samples that can be arbitrarily designed to exhibit a specific structure of choice [114, 115]. As a major drawback, however, obtained results often cannot be transferred directly to the target of interest, as parameters like labeling efficiency and geometry of the structure may differ from the reference sample.

A comprehensive alternative to experimental reference structures are computer simulations. While they cannot directly assess parameters such as the labeling or detection efficiency in an experiment, they are ideally suited for developing, testing and advancing new experimental and analysis approaches [91, 92]. The major advantage of simulations is the availability of the ground truth: All input parameters are known and adjustable at will. Thus, simulations provide a valuable tool to assess the performance of methods and explore their limits over a wide range of parameters. Notably, if physical concepts are correctly implemented in the simulations, the performance of methods should directly be transferable to experiments. If experiments do not show the same results, the physical concepts should be reconsidered. Computer simulations provided the basis for validating all methods developed in this thesis, and for exploring their performance and possible limits.

Part I.

Verifying molecular clusters

3. Introduction

Molecular clusters are thought to play an important role in cellular signaling and behavior: Many SMLM studies performed at the cellular plasma membrane have reported clustering of proteins at the nanoscale [1]. As nanoclustering emerged to supposedly be a prevalent feature of plasma membrane organization, a broad variety of clustering algorithms and methods have been developed to characterize and quantify the clustering behavior of molecules in detail [59, 116, 117]. However, two issues confound the analysis of biomolecular clustering: First, the presence of more than one dye molecule per label leads to multiple detections of a single protein molecule of interest. Second, researchers became aware that the stochastic nature of photophysics frequently leads to severe overcounting in SMLM, even if label stoichiometry is one to one. The prevalence of nanoclusters has since been put into question [4, 118].

An important aspect for the analysis and interpretation of SMLM data is that they fundamentally differ from conventional pixelated images: The obtained localization maps are a list of position coordinates. Therefore, SMLM techniques have often been associated with the term *pointillism* [116, 119]. The localization map can be considered as a spatial point pattern; hence, point pattern analysis can be applied to characterize the data [120, 121]. An introduction to point patterns and clustering methods will be given in section 3.1.

Typically, the prevalent criterion for assessing the quality and informative value of a microscopy image is resolution—the ability to distinguish two points in spatial proximity. For SMLM images, resolution is often equated with localization precision. It has to be considered that the quality of an image does not only depend on the localization precision, but also crucially on the effective labeling efficiency and the presence of artifacts such as overcounting. In order to assess the ability to answer a given biological question, the achieved resolution by itself—characterized by a single number—is not meaningful anymore. Moreover, the resolution also becomes a question of the structure of interest itself, in particular whether the structure is continuous (e.g. actin, microtubules) or discrete (e.g. protein monomers in the plasma membrane), and dense or sparse. For example, if monomeric biomolecules present at low concentrations are to be studied quantitatively, the labeling efficiency will be more critical than the obtained localization precision. The informative value of an SMLM localization map is often difficult to assess, even more so, by a single number only. Therefore, it has been proposed to introduce hypothesis testing in SMLM for answering biological questions, in particular, for assessing the obtained data against a specified hypothesis [122]. For many biological questions, the microscopic resolution is not critical, but it is more important whether a difference between two experimental conditions can be detected or not. One pending question is whether specific biomolecules form nanoclusters or are randomly distributed—developing methods for answering this question will be the basic concern of chapters 4 and 5 of this thesis. An introduction to p-values and significance testing will be given in section 3.2.

3.1. Methods for cluster analysis

In the following, I will first give a short introduction into spatial point patterns (section 3.1.1). Further, I will present an overview of various methods used for cluster analysis (sections 3.1.2 and 3.1.3). Notably, many methods used for cluster analysis in SMLM were adopted from other fields, for example ecology or geoscience [123, 124]. One central assumption of these methods is that every molecule of interest is detected only once; the occurrence of overcounting—an issue specific to SMLM—is neglected. Researchers hence typically recommend to post-process the recorded SMLM data prior to cluster analysis, in order to fulfill the requirement of a single localization per biomolecule of interest. However, no pre-processing method exists that can reliably identify and correct for all possible artifacts. Therefore, besides the conventional cluster analysis methods, other approaches have been developed that allow to specifically address overcounting artifacts (sections 3.1.4). These methods aim at analyzing the true distribution of biomolecules of interest, which underlies the observed distribution of localizations.

3.1.1. Spatial point patterns, null models and complete spatial randomness

The main aim of cluster analysis methods is to describe the distribution of biomolecules within the cell. In this thesis, I will consider the cellular plasma membrane, in particular. The position of molecules within the plasma membrane can be described by a set of position coordinates \vec{x} . The position of these molecules constitute a *spatial point pattern*, i.e. a set of points $\{\vec{x} \in A\}$, where A is the region of interest. For molecules within the plasma membrane, the region of interest can be described by a 2D surface. For cells well-attached to a coverslip this surface can be considered as a flat plane and thus, A is a subset of \mathbb{R}^2 . As the point pattern of the molecules consists of one type of objects only, it is a *univariate* point pattern. The arrangement of molecules can be seen as a realization of a spatial point process, i.e. a stochastic process which generated the point pattern.

Due to random variations inherent to a stochastic process, it is often difficult to directly characterize local features of a point pattern: Those features may not be due to present molecular interactions, but may arise from mere noise. This aspect will be considered in more detail in section 3.2. In order not to study mere random noise only, it is therefore necessary to investigate the pattern globally prior to a local analysis. For a global analysis of a point pattern, the pattern is typically compared to a *null model*, which represents a specific spatial structure. Based on this null model, it is assessed whether a given point pattern shows a spatial structure which significantly deviates from the null model. For a univariate point pattern, the most basic null model is complete spatial randomness (CSR), which is described by a spatial Poisson process. Notably, CSR corresponds to the absence of any interactions of the points—in particular, neither attractive nor repulsive forces affect the spatial arrangement of the biomolecules. This null model can be used to assess whether the point pattern exhibits any spatial structure of interest which can be distinguished from pure stochastic effects. A realization of a random point pattern is shown in Fig. 3.1a. If, overall, points are in closer proximity to each other than can be expected by random chance, the resulting pattern is termed clustered (Fig. 3.1b). In this case, either an attractive force between the biomolecules

is present, or an external factor causes the molecules to aggregate in certain subregions. For a so-called dispersed distribution, the points are spread out and their mutual distances are larger than expected under randomness (Fig. 3.1c). This case corresponds to repulsive interactions between the biomolecules.

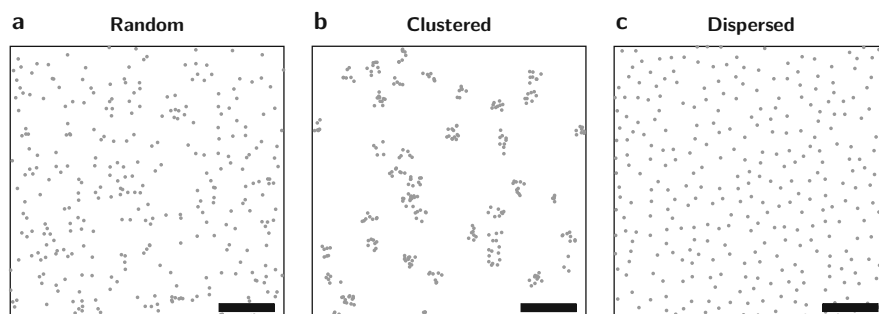


Figure 3.1.: Spatial distributions of point patterns. The panels show realizations of a random (a), clustered (b), and dispersed (c) spatial point process. For each scenario, the simulated density was set to 80 points per μm^2 . For the clustered scenario, the cluster density was set to 10 clusters per μm^2 with a cluster radius of 60 nm; the cluster center positions were distributed randomly within the whole region of interest. All points were distributed uniformly within the clusters. For the dispersed scenario, the minimum required distance between neighboring points was set to 70 nm. Scale bars: 400 nm.

For a spatial Poisson process, the points are distributed randomly and independently of each other. The spatial Poisson process is defined on the plane \mathbb{R}^2 and only depends on the parameter $\rho > 0$, the density of points. The number of points in an arbitrary region $A \subset \mathbb{R}^2$ is described by a random variable $N(A)$. The probability that the region A contains exactly n points is characterized by the Poisson distribution and given by

$$\mathbb{P}(N(A) = n) = \frac{(\rho |A|)^n}{n!} e^{-\rho |A|}, \quad \text{for } n \in \mathbb{N}, \quad (3.1)$$

where $|A|$ denotes the area of the region A . From the Poisson distribution it follows that the expected number of points for the region A is given by $\mathbb{E}(N(A)) = \rho |A|$.

3.1.2. Methods for comparison to CSR

In order to compare spatial point processes, summary statistics are used to describe certain characteristics of point patterns. The simplest characteristic of a spatial point process—the first-order property—is its intensity ρ , i.e. the expected number of points per area. The influence of points on one another is described by second-order properties. One widely used second-order statistic for point pattern analysis is Ripley's K function [123]. It is defined as the expected number $N(A_r(P))$ of points within a distance r of a typical point P in the pattern, divided by the intensity ρ of the pattern. For a spatial point pattern on a finite region, Ripley's K function can be calculated as

$$K(r) = \frac{\mathbb{E}(N(A_r(P)))}{\rho} \approx \frac{1}{\rho} \cdot \frac{1}{n} \sum_{i=1}^n N(A_r(P_i)), \quad (3.2)$$

where $N(A_r(P_i))$ is the number of points within a distance r around point i of the observed pattern, and n the number of points in the pattern (Fig. 3.2a).

Ripley's K function is typically used for comparing a given spatial distribution of points with a distribution as it would result from CSR, i.e. a homogeneous spatial Poisson process. For a spatial Poisson process, it holds that the expected number of points within a circle of radius r can be calculated by multiplying the density of the point process by the area of the circle, i.e. $\mathbb{E}(N(A_r(P))) = \rho\pi r^2$. Hence, for CSR it holds that $K(r) = \pi r^2$. Deviations from this expected value of the K-function indicate clustering of the points (if $K(r) > \pi r^2$) or dispersion (if $K(r) < \pi r^2$). As the K-function for a spatial Poisson process scales with r^2 , it is more convenient to use different versions of the function. The L-function is defined as

$$L(r) = \sqrt{K(r)/\pi}, \quad (3.3)$$

which can be further modified to the H-function defined as

$$H(r) = L(r) - r. \quad (3.4)$$

The expected values for the L- and H-function for a Poisson process are $L(r) = r$ and $H(r) = 0$, respectively; hence, positive values of $H(r)$ indicate clustering, whereas negative values indicate dispersion (Fig. 3.2a).

For the analysis of biomolecular distributions with Ripley's functions, one important assumption is that each biomolecule of interest is represented in the SMLM data by one single localization only. Ripley's functions directly analyze the point pattern of the localizations and thus, localization clusters arising from overcounting will be characterized as clustered. This problem and a solution to it will be discussed in detail in chapter 4 of this thesis.

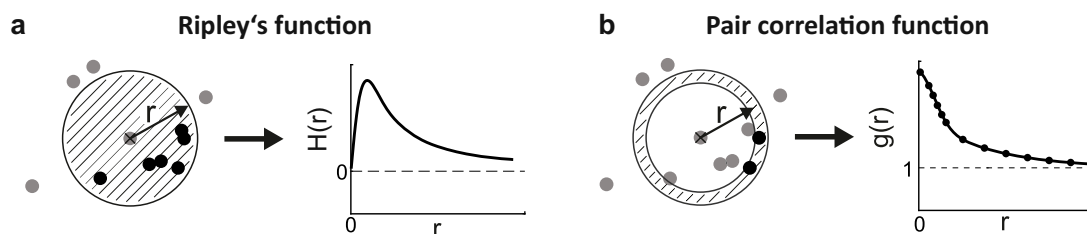


Figure 3.2.: Ripley's function and pair-correlation analysis. (a) Ripley's H function. For the calculation of Ripley's function, the average number of points within a circle of radius r around the points of the pattern is determined. For CSR it holds that $H(r) = 0$ for all values of r . Values of $H(r)$ greater or less than 0 indicate clustering or dispersion, respectively. (b) Pair correlation function (PCF). For the PCF, the number of neighboring points is not counted within a circle, but within rings of radius r centered on each point. For CSR it holds that $g(r) = 1$. Values of $g(r)$ greater or less than 1 indicate clustering or dispersion, respectively, at the corresponding scale. Figure adapted from [59].

One issue with Ripley's analysis is the fact that it is cumulative. Hence, pronounced clustering or depletion at short scales may obscure the analysis at larger scales. The pair-correlation function (PCF) is based on Ripley's function and offers a better assessment of clustering at individual scales. Instead of counting the number of neighboring points within a circle of radius

r , the PCF counts the number of points within rings of radius r and fixed width, centered on each point (Fig. 3.2b). Thereby, propagation of effects on a certain length scale to larger lengths scales is prohibited. Thus, it becomes possible to analyze true biomolecular clustering at scales larger than the localization precision, also if overcounting is present in the data.

The pair-correlation function describes the expected point density at distance r relative to the density of the whole point pattern. Hence, in case of complete spatial randomness it holds that the pair-correlation function is equal to 1. Values greater than 1 indicate clustering, whereas values smaller than 1 indicate dispersion at the given scale. Importantly, the pair-correlation function offers information about the range of the clustering as it declines to 1 if no clustering is present at larger scales anymore. Of note, the pair-correlation function is in practice slightly noisier than Ripley's K function, because its estimation is based on fewer points.

3.1.3. Segmentation of clusters

The Ripley's functions as defined above provide only a global assessment of potential clustering. In order to further analyze clustered localizations, several clustering algorithms can be applied to the recorded localization data that segment the data into individual clusters. The obtained individual clusters can further be analyzed to quantify the clustering and extract parameters of cluster description, including for instance the number of clusters, the number of localization per cluster and cluster radii.

Density-based spatial clustering of applications with noise (DBSCAN, [125]) counts the number of points within a neighborhood of radius r for each point (Fig. 3.3). If this number is equal to or exceeds a predefined threshold n , the point is considered as being part of a cluster. A point is regarded as edge or boundary point if the circle around this point contains less than n points, but at least one point which is itself a clustered point. Of note, not all points at the rim of clusters necessarily need to be edge points; if those points have enough neighbors, they are considered as core points. In case neither of the two criteria are fulfilled for a point, the point is classified as unclustered or noise. Of note, the choice of the two parameters r and n is user-dependent and strongly influences the cluster assignment.

A modified version of DBSCAN is provided by the method FOCAL (Fast Optimized Cluster Algorithm for Localizations) and its extension to 3D termed FOCAL3D [126,127]. The method is grid-based and creates a histogram of all localizations with bin size Δ (Fig. 3.4a). Based on this histogram a density map is generated and a density threshold $minL$ is applied (Fig. 3.4b,c). Regions which are larger than a specified minimum size $minC$ are defined as clusters (Fig. 3.4d). The method allows to evade overcounting artifacts by suitable choice of the three parameters Δ , $minL$ and $minC$. However, only clusters with an extent larger than the localization error can be detected in this way. In addition, the method is computationally less expensive than DBSCAN, in particular for very large numbers of localizations; a runtime comparison is given in [127].

Many clustering methods, including DBSCAN and FOCAL, depend on user-defined parameters, and their choice highly influences the outcome of the analysis. In order to overcome this problem, Bayesian approaches have been proposed [128–130]. They test a wide range of

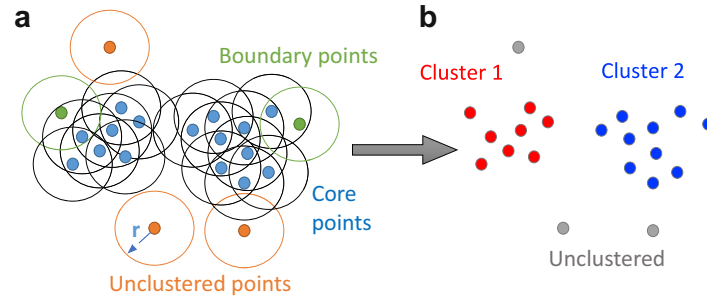


Figure 3.3.: DBSCAN. (a) For each point, the number of points within a radius r is counted. A point is considered as a core point (blue), if the circle around it contains at least $n = 3$ points. For boundary points (green), the circle around a point contains less than n points, but another core point. All other points are considered as unclustered (orange). (b) Resulting cluster assignment of the points. Figure adapted from [116].

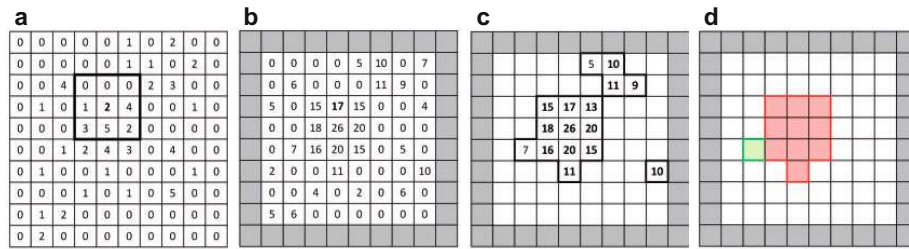


Figure 3.4.: FOCAL. (a) Histogram of the localization map. The bin size Δ of the histogram should be chosen according to the localization precision. (b) The density map is created by replacing each value with the sum of the 3×3 bin region around each bin. (c) Only points that exceed a set density threshold (here, $\min L = 9$) and their border points are kept. Core points are indicated in bold font. (d) Regions exceeding a certain size (here, $\min C = 10$) are defined as clustered. Figure adapted from [126].

different clustering parameters and finally assess, which of the thousands of resulting candidate cluster proposals scores best. Thus, the method becomes independent of an arbitrary choice of parameters by the user. However, Bayesian analysis is a model-based approach. It relies on a model of clustering, typically Gaussian-shaped clusters are assumed. Hence, it is restricted to the analysis of clusters which are in accordance with a predefined model, and cannot be applied to arbitrarily shaped clusters.

Another approach to segment localizations into clusters are tessellation-based methods, including Voronoi tessellation and Delaunay triangulation (Fig. 3.5), which divide a region into geometric shapes—the tiles—based on the points of a point pattern. In case of Voronoi tessellation, the analyzed region is split into tiles based on equidistant bisections between localizations (Fig. 3.5a). The localizations are positioned inside the tiles, with each tile containing exactly one localization. Delaunay triangulation is a straightforward approach, in which all points are

simply the vertices of triangular tiles (Fig. 3.5b). For both Voronoi tessellation and Delaunay triangulation, the area of the tiles indicates the degree of clustering, in particular, small tiles correspond to densely packed localizations belonging to a cluster. Subsequently, a threshold for the tile areas can be applied in order to distinguish clustered points from unclustered ones.

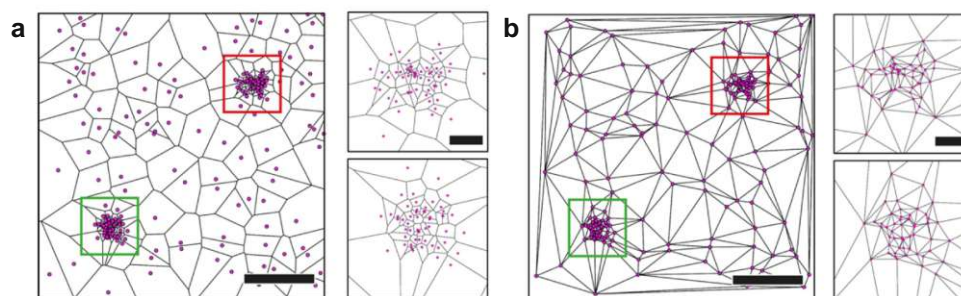


Figure 3.5.: Image tessellation. The panels show the results of Voronoi tessellation (a) and Delaunay triangulation (b). Enlarged views of the green and red regions are shown on the right of each panel. Figure adapted from [117].

Further types of clustering methods are based on graphs [131] or machine-learning [132]. SMLM localizations can be described as a mathematical graph, with its nodes representing the localizations and its edges representing their interactions. Based on this graph, cluster assignments may be deduced. Applying graph-based methods to SMLM data, however, has been rather infrequent up to now. Machine-learning approaches require large sets of data including knowledge of the ground truth for training of models. These prerequisites are fulfilled for simulated data, but difficult to obtain for real SMLM data recorded in experiments. Further, the performance of machine-learning approaches may strongly depend on the quality and adequacy of the training data.

3.1.4. Accounting for cluster artifacts

All of the methods and algorithms mentioned in the previous section analyze the distribution of the localizations obtained from an SMLM experiment. Importantly, it is not the localizations, which are biologically relevant, but the positions of the actual biomolecules. Various artifacts, however, may distort the localization map to different degrees [133]. With regard to clustering, the most severe artifact is overcounting due to both the presence of multiple fluorophores per biomolecule of interest and fluorophore blinking, leading to clustering artifacts. Notably, it is not biologically meaningful to analyze and characterize these artifacts.

Cluster analysis via the pair-correlation function and FOCAL(3D) may circumvent overcounting artifacts at length scales larger than the localization errors. However, clustering at length scales smaller than the localization error cannot be analyzed with these methods. Moreover, residual diffusion after chemical fixation may further increase the spread of localizations arising from the same biomolecule of interest [9]. If residual diffusion is not accounted for appropriately, this will lead to wrong results of the clustering algorithms.

Merging approaches. In order to analyze true molecular clustering at all length scales, in particular below the length scale of localization errors, it is often proposed to preprocess the localization data in order to eliminate clustering artifacts. One method for this task has been proposed by Annibale et al. [3,5]. In their approach, localizations are merged based on spatial and temporal proximity (Fig. 3.6). However, the method has two potential flaws: (i) The thresholds for spatial and temporal proximity are user-dependent. (ii) Fluorophores show complex blinking behavior and may exhibit long-lived dark states; this makes it impossible to distinguish a localization of a new dye molecule from a reappearance of a previously detected dye molecule.

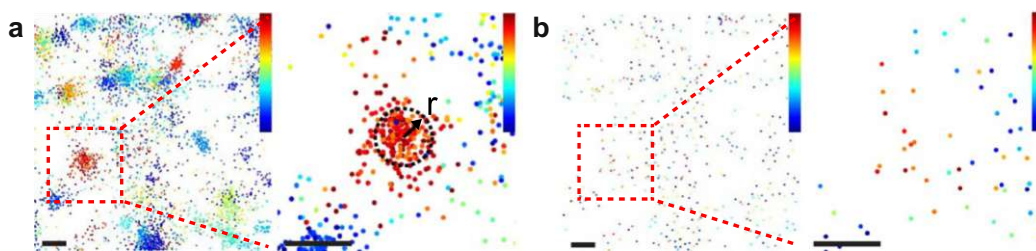


Figure 3.6.: Merging of localizations. Localization map before (a) and after merging of the localizations within a radius of $r = 35$ nm and 500 frames (b). Localizations are color-coded corresponding to their frame of appearance. In total, 5000 frames were recorded. The images on the right of each panel show an enlarged view of the region indicated by a red square on the left. Scale bars are $1\ \mu\text{m}$ and $100\ \text{nm}$ for the left and right image of each panel, respectively. Figure adapted from [134].

Recently, a more elaborate merging approach termed distance distribution correction (DDC) was proposed [135]. For this, the distribution of pairwise distances between individual fluorophores is obtained from the image sequence: Only those distances are taken into account which are separated by a time well exceeding the average survival time of a fluorophore; i.e. the time before it is being bleached. As an advantage, the method does neither require the setting of user-dependent parameters nor calibration measurements. Nevertheless, it is still not suitable if a single biomolecule may be detected repeatedly throughout the whole image acquisition time; in particular, this is the case for long-lived dark times, for PAINT imaging approaches, or antibody labeling, where multiple fluorophores per biomolecule of interest may be present.

Pair-correlation analysis. Sengupta et al. [6] proposed a pair correlation-based method which is not impacted by long dark times, but only depends on the mean number of observations of each biomolecule of interest. The pair-correlation function of an SMLM localization map has a contribution of both the distribution of biomolecules of interest and the spread of localizations due to localization errors. Therefore, the total pair-correlation function $g(r)^{\text{peaks}}$ can be represented as a convolution:

$$g(r)^{\text{peaks}} = \left(g(r)^{\text{centroid}} + g(r)^{\text{protein}} \right) * g(r)^{\text{PSF}} \quad (3.5)$$

$$= g(r)^{\text{centroid}} * g(r)^{\text{PSF}} + g(r)^{\text{protein}} * g(r)^{\text{PSF}}, \quad (3.6)$$

where $g(r)^{\text{centroid}}$ and $g(r)^{\text{protein}}$ are the correlation function of biomolecules at $r=0$ and $r>0$, respectively, and $g(r)^{\text{PSF}}$ is the correlation function of the localization uncertainty. The first term $g(r)^{\text{centroid}} * g(r)^{\text{PSF}}$ in Eq. (3.6) represents the correlation arising from multiple detections of the same biomolecule of interest. The second term $g(r)^{\text{protein}} * g(r)^{\text{PSF}}$ describes the correlation due to the spatial distribution of the biomolecules, which is equal to 1 for a random distribution (Fig. 3.7a). The localization error can be described by a normal distribution with mean 0 and standard deviation σ_{loc} . Hence, the correlation function of the localization uncertainty can be described by

$$g(r)^{\text{PSF}} = \frac{1}{4\pi\sigma_{\text{loc}}^2} \exp\left(\frac{-r^2}{4\sigma_{\text{loc}}^2}\right). \quad (3.7)$$

The correlation function $g(r)^{\text{centroid}}$ of the centroids is a delta function with amplitude equal to $1/\rho^{\text{average}}$, i.e. the inverse of the average density of biomolecules. This average density is given as $\rho^{\text{average}} = \rho^{\text{peaks}}/\bar{N}$, where ρ^{peaks} is the density of peaks present in the image and \bar{N} the average number of detections of a single biomolecule. Hence, together with Eq. (3.7) the total pair-correlation function from Eq. (3.6) can be expressed as

$$g(r)^{\text{peaks}} = \frac{1}{4\pi\sigma_{\text{loc}}^2\rho^{\text{average}}} \exp\left(\frac{-r^2}{4\sigma_{\text{loc}}^2}\right) + g(r)^{\text{protein}} * \frac{1}{4\pi\sigma_{\text{loc}}^2} \exp\left(\frac{-r^2}{4\sigma_{\text{loc}}^2}\right). \quad (3.8)$$

This function has two parameters, which are the localization precision σ_{loc} and the average density of biomolecules ρ^{average} , which is directly determined by \bar{N} . For determination whether biomolecules are randomly distributed, the total pair-correlation function obtained from an experiment is fitted to Eq. (3.8), yielding fit parameters $\sigma_{\text{loc}}^{\text{fit}}$ and \bar{N}^{fit} . Both parameters can also be estimated from an additional experiment recorded at sparse label densities, i.e. a recording of the blinking statistics. If the parameters obtained from both experimental approaches are consistent, the biomolecular distribution is assumed to be random (Fig. 3.7a), and clustered otherwise (Fig. 3.7b). In the clustered case, the experimentally obtained pair-correlation function may further be fitted with a specified model of $g(r)^{\text{protein}}$, which allows to extract parameters of cluster characterization, including cluster size and the average number of localizations per cluster. Notably, an analysis relying only on a single number describing the blinking statistics of the label, in particular the average number of detections \bar{N} , will not yield reliable results if the distribution of the number of blinks is very broad. Especially extreme outliers with a high number of localizations for a single biomolecule will confound the analysis.

Label titration. An experimental approach for distinguishing real biomolecular clustering from blinking artifacts was developed by Baumgart et al. [4]. It indirectly incorporates the blinking statistics of fluorophores into the analysis of spatial clustering. The deliberate variation of the labeling density leads to characteristic changes in the obtained localization maps (Fig. 3.8a). For each label density, the relative area η covered by localization clusters is plotted against the normalized density ρ of localizations inside the clustered area. Of note, the value of ρ directly depends on η . For an underlying random distribution of biomolecules, the relative clustered area η shows a linear increase for low label densities (Fig. 3.8b). At very high biomolecule and labeling densities, some of the randomly distributed labeled biomolecules

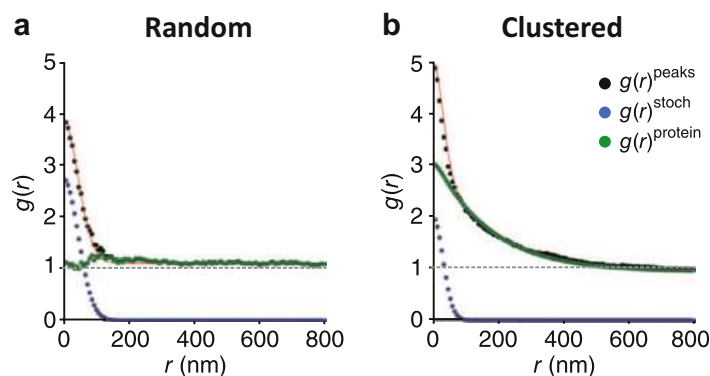


Figure 3.7.: Pair correlation analysis accounting for overcounting. Shown are the total pair-correlation function $g(r)^{\text{peaks}}$ (black), the contribution arising from overcounting $g(r)^{\text{stoch}} := g(r)^{\text{centroid}} * g(r)^{\text{PSF}}$ (blue), and the correlation function of the biomolecules $g(r)^{\text{protein}}$ (green). For a random biomolecular distribution (a) it holds that $g(r)^{\text{protein}} = 1$. For values of $g(r)^{\text{protein}}$ greater than 1, the biomolecular distribution is clustered (b). Figure adapted from [6].

will be close to each other and thus, their localization clusters due to blinking will partially overlap. Hence, the increase of η slightly declines and is not linear anymore for high labeling densities. Further, for a random distribution of biomolecules, the density of localizations ρ only depends on the blinking behavior of the fluorophore. The blinking statistics is independent of the labeling density and ρ in principle always stays the same. Hence, for a random biomolecular distribution the density is constant (Fig. 3.8c); after normalization this curve is constant to 1. However, at large biomolecule and labeling densities, the clustered area η does not increase linearly anymore, leading in turn to a slight increase in the density ρ . For an underlying clustered distribution of biomolecules, localization clusters of individual biomolecules overlap at higher labeling densities. The relative covered area η decreases, which in turn also increases the density ρ . In order to obtain a further pronounced difference between randomly distributed and clustered biomolecules, the normalized density ρ/ρ_0 is plotted against the relative covered area η (Fig. 3.8d). Deviations of the curve from the reference curve expected for random distributions indicate real molecular clustering. While being hardly affected by user-defined parameter settings or non-homogeneous photophysical behavior of dye molecules, the method lacks sensitivity in case of only faint molecular clusters since discrimination is difficult and rather subjective in this case. Moreover, it requires performing the same experiment at various label densities, which is laborious. Of note, the acquisition of experiments at low labeling densities is similar to the recording of a blinking statistics. Finally, the method is dependent on two parameters needed for the determination of the clustered area: The standard deviation σ of the Gaussian function used for representing a single localization and a cut off threshold. The parameter σ should be chosen in accordance with the localization precision of the experiment. A good choice for the cut off threshold was found to be 2.5; varying the threshold value between 0.5 and 4.5 was shown to have a negligible effect on the obtained results [4].

An adapted version of the labeling titration approach was proposed by Spahn et al. [7]. Regrouping the recorded SMLM frames of a single acquisition allows to circumvent the need

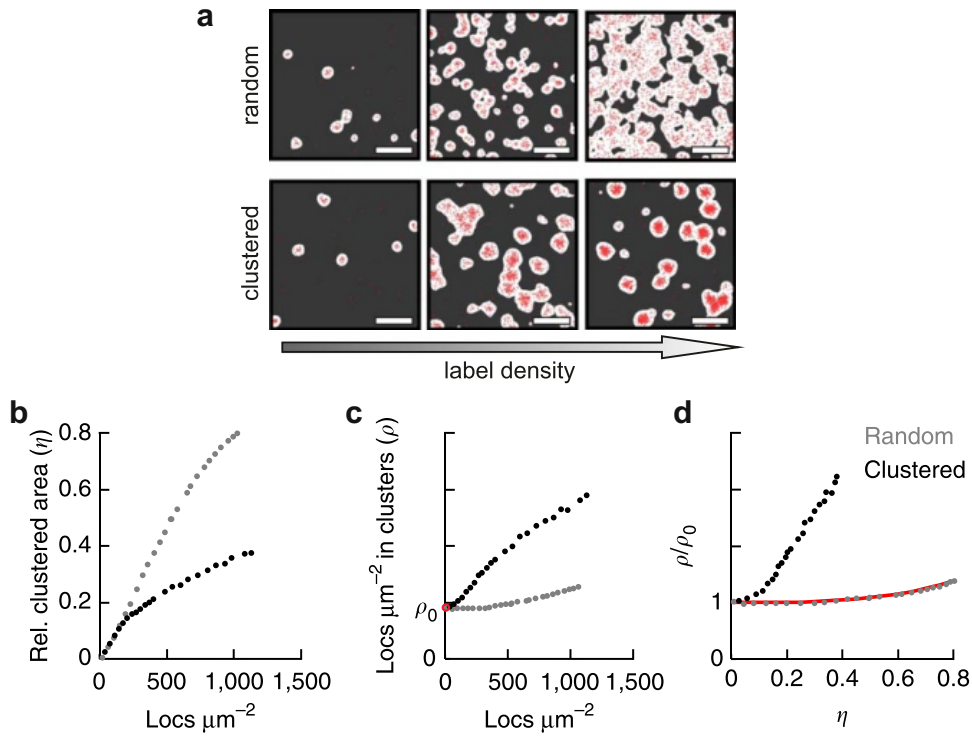


Figure 3.8.: Label titration method. (a) Variation of the labeling density leads to characteristic changes in the localization maps for random and clustered biomolecular distributions. (b) For random biomolecular distributions, the relative clustered area η increases approximately linearly with the number of localizations. For clustered biomolecular distributions, the increase in η is reduced. (c) The density ρ of localizations in the clustered areas is approximately constant for random biomolecular distributions. For clustered biomolecular distributions ρ increases with increased number of localizations. (d) Plotting the normalized density ρ/ρ_0 against η further pronounces the deviation between the curves for a clustered and random biomolecular distribution. Figure adapted from [4, 59].

for titration and thus, is supposedly more efficient. Both temporal accumulation and completely random splitting of localizations were shown to achieve comparable results. However, the principle underlying this method is quite different from the original approach proposed by Baumgart et al. [4]. It highly depends on the choice of the threshold used for determination of the clustered area. For temporal accumulation, this threshold is supposed to be set dependent on the blinking statistics; in particular, the average number of detections of a single biomolecule needs to be multiplied with the peak height of the Gaussian function representing an individual localization. Thus, clusters arising merely from multiple detections of the same biomolecule do not exceed the threshold and thus, are excluded from the cluster mask. Again, the knowledge of the average number of detections is an important prerequisite for this approach. Hence, the method strongly depends on parameters of fluorophore blinking statistics.

Counting of molecules. Instead of a global qualitative characterization of clustering, other approaches aim at a quantitative assessment of biomolecular aggregations. Quantitative PAINT (qPAINT) estimates integer numbers of biomolecules within observed localization clusters [136]. For this, the mean dark time τ_{d^*} and the influx rate ξ of image strands need to be determined. For each analyzed subregion, τ_{d^*} is obtained from the cumulative distribution function of all observed dark times. The influx rate ξ is calibrated based on a calibration sample with a known number of binding sites, e.g. from previous experiments under similar conditions, or DNA-origami. Subsequently, the number of binding sites N_b is calculated as $N_b = 1/(\tau_{d^*} \cdot \xi)$. While this approach allows to obtain the number of biomolecules in each subregion, large uncertainties arise due to stochastic variations if the analyzed subregions are too small or the imaging time too short. Further, multiple imager strand binding sites per biomolecule of interest may be present; in particular for imaging with primary and secondary antibodies, large labeling variabilities may be present, leading to higher uncertainties in the counts of biomolecules of interest. In addition, the approach does not account for unlabeled biomolecules which are not detected during the imaging time; thus, the actual number of present biomolecules will be underestimated. For reliable determination of molecule counts, the calibration of the influx rate ξ is crucial. Performing the calibration with inappropriate calibration samples which do not reflect the conditions of the actual experiment represents another source of error. For example, for biomolecules in the plasma membrane which are facing the coverslip, the accessibility for the image strand is low; in this case, a calibration with DNA origami on a coverslip without cells will be inappropriate.

Another approach for counting of molecules was proposed by Hummer et al. [137] and is an extension of a previous approach from Fricke et al. [138]. For this, obtained blinking statistics are fitted by a function with the four parameters p, p_0, q, m : The first two parameters p and p_0 describe the photophysics of the fluorophore, the parameter q quantifies the fraction of active labels, and $m + 1$ is equal to the oligomerization degree (i.e. $m = 0$ for monomers). An estimation \hat{p}, \hat{p}_0 for the parameters p, p_0 can be determined by recording blinking statistics of monomers, and fitting of the function with $q = 1$ (all observed fluorophores are inherently active) and $m = 0$ (monomers). The parameter q can be estimated by \hat{q} via imaging of dimers and fitting the obtained blinking statistics with \hat{p}, \hat{p}_0 , and $m = 1$ (dimers). Finally, a blinking statistics obtained for biomolecules of unknown oligomerization degree can be fitted with the previously estimated parameters \hat{p}, \hat{p}_0 and \hat{q} , while leaving the oligomerization degree m as a free fitting parameter; also a combination of different oligomerization degrees can be analyzed by fitting a weighted mixture of the functions with different values of the parameter m . The applied formula was shown to be appropriate for a variety of models of fluorophore photophysics, as long as there is only one single bright state, or multiple bright states but a single dark state only [137]. One main advantage of the method compared to others is that it becomes possible to account for missing labels via the parameter q . As a disadvantage, the approach is complex as two calibration experiments at different and well-defined oligomerization states are required. Creating such calibration samples which offer the same experimental conditions as given for the biomolecule of interest can be challenging.

3.2. The p-value and statistical significance

The informative value of an SMLM localization map is often difficult to assess: Due to insufficient labeling or detection efficiency only parts of the structure of interest are visible, while multiple detections of the same biomolecule of interest lead to overcounting and clustering artifacts. In addition, false positive localizations arising from cellular autofluorescence or background fluorescence may confound the proper analysis of localization maps. Another important fact to keep in mind is that biological cells exhibit a natural variation—each imaged cell will be slightly different than the previous one. On a smaller scale, this also applies to an individual cell itself, in particular the distribution of biomolecules within a cell: Due to purely random events, some biomolecules in the cell will be close to each other, although no attractive force nor interaction between them exists.

When analyzing biological data, in particular SMLM localization maps, one has to question whether observed patterns are of significance or just the outcome of random effects. Interestingly, humans tend to underestimate the natural scope of random processes; extreme events are often failed to be anticipated. At the same time, the human brain is remarkably capable of recognizing and detecting patterns. Taken together, humans easily misinterpret random events, recognizing patterns and attributing significance to them. Notably, also the use of computer algorithms may lead to wrong conclusions if not applied appropriately. As an example, let's consider a pattern generated by a spatial Poisson point process, i.e. complete spatial randomness. Very likely, several points will be in close spatial proximity due to random chance alone. This can be easily seen when analyzing realizations of CSR with clustering methods, e.g. DBSCAN, as shown in Fig. 3.9. Although the point pattern is purely random, multiple clusters were detected by the method. Importantly, a purely local analysis of clustering without assessing the global point pattern distribution would not yield valid but highly misleading results.

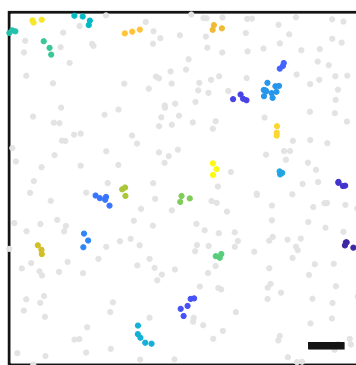


Figure 3.9.: Random spatial point pattern analyzed by DBSCAN. For the simulation, the density was set to 80 points per μm^2 . The analysis parameters were set to $r = 50\text{nm}$ for the search radius and $n = 3$ for the minimum number of points constituting a cluster. The color code represents the cluster assignment. Unclustered points are shown in gray. Although the point pattern was generated by a spatial Poisson process and thus is completely random, 22 clusters were identified by DBSCAN. Scale bar: 200 nm.

The p-value offers a way to assess whether data show any features which cannot be expected from random chance alone. Hence, it prevents researchers from being misled and attributing importance to purely random events. Statistical significance testing based on the obtained p-values allows for tests with a well-defined false positive rate. In the following, I will give a short introduction into the p-value and statistical significance testing. Further, I will discuss the validity of p-values and point out important issues for a correct interpretation of obtained results.

3.2.1. The sampling distribution

In statistics, the characteristics of a whole *population* are estimated based on a small subsample; for example, the general distribution of biomolecules is investigated based on a single or several imaged cells. The population follows an underlying unknown distribution. The *sample* is a data subset which should be representative of the population. It provides an empirical distribution, which is used to infer information about the whole population. A sample *summary statistic* is a metric describing the sample's characteristic; in the case of biomolecular distributions, for example, nearest neighbor distances or Ripley's H function. The summary statistics is calculated based on the data of a sample. Due to random effects the obtained value for a summary statistic varies from sample to sample, also if the samples are drawn from the same underlying population. Hence, the sample summary statistic is a random variable that follows a probability distribution. This probability distribution of the sample summary statistic over all possible random samples of given size n is called the *sampling distribution*, or also finite-sample distribution. The shape of the sampling distribution depends both on the underlying population and the sample size. For increasing sample sizes, the distribution becomes narrower (Fig. 3.10). For some statistics, the sampling distribution can be described by a theoretical formula. For example, the central limit theorem states that for a large enough sample size n , the distribution of the sample mean approximates a normal distribution. For other statistics, the sampling distribution takes on a more complicated form, and cannot be easily described by a mathematical formula. Nevertheless, Monte Carlo simulations or bootstrap methods can be applied in order to approximate the sampling distribution.

3.2.2. The null hypothesis and the p-value

The null hypothesis H_0 is a baseline assumption that is made about the population (for example, that the distribution of biomolecules is purely random). In particular, the sampling distribution of a summary statistic is assumed to take on a certain distribution. Based on this sampling distribution under the null hypothesis, we can calculate a p-value for a single sample drawn from the population. The p-value is the probability that, under the null hypothesis, a sample would yield a value of the summary statistics which is as extreme or more extreme than the observed value obtained from the sample. As the p-value is based on the sampling distribution, it not only depends on the population but also the sample size. Hence, the same outcome for a summary statistics may yield different p-values dependent on the sample size as the width of the sampling distribution varies.

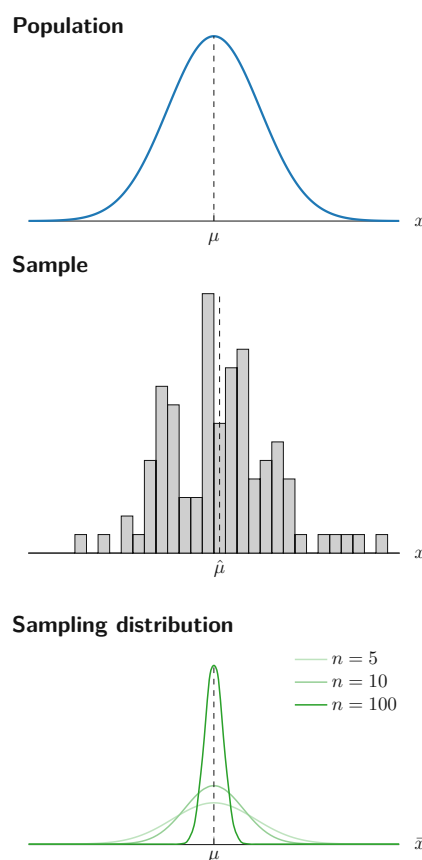


Figure 3.10.: Population, sample and sampling distribution. The distribution of the whole population (top) is estimated based on a subsample (middle) of the population. The population has a mean value of μ which is estimated by the value $\hat{\mu}$ obtained from the sample. The probability distribution of a summary statistic over many samples of given size n is the sampling distribution. It indicates the probability of obtaining certain values of the summary statistic for random samples of the population. The sampling distribution of μ is shown for the sample sizes $n = 5, 10, 100$ (bottom). The larger the sample size, the narrower is the sampling distribution. The ground truth value of μ is indicated by the dashed vertical line.

The p-value is a random variable in the interval $[0, 1]$ and describes how extreme the obtained value of a test statistic for an observed sample is. Which values are regarded as extreme depends on the choice of the alternative hypothesis (see Fig. 3.11). If we are interested whether the sample shows either only smaller values or only larger values compared to the null hypothesis, we calculate a one-sided p-value; left-sided (Fig. 3.11a) or right-sided (Fig. 3.11b), respectively. For a two-sided p-value, deviations in both directions are considered (Fig. 3.11c). As an example, for a null hypothesis of a random biomolecular distribution and the alternative hypothesis of nanoclustering, a one-sided p-value will be calculated. Whether a left- or right-sided p-value is appropriate depends on the chosen summary statistic.

A random variable P represents a valid p-value if the probability that $P \leq a$ under the null hypothesis is smaller or equal to the threshold a , in particular $\mathbb{P}(P \leq a \mid H_0) \leq a$ for every

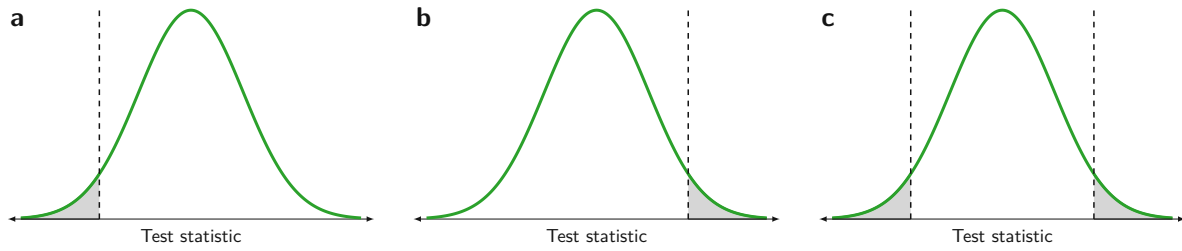


Figure 3.11.: The p-value. The green curves show the sampling distribution of a test statistic under the null hypothesis for a given sample size n . The value of the test statistic obtained for one specific sample is shown as dashed vertical line. The p-value is the probability that under the null hypothesis, the summary statistic would take on a value as or more extreme than the observed one. The p-value thus corresponds to the area indicated in gray, which is identical to the value of the cumulative distribution function (CDF) for the left-sided p-value (a). Depending on whether deviations in only one direction or both directions are of interest, a one-sided (a,b) or two-sided (c) p-value is calculated, respectively. The one-sided p-value can be either left- (a) or right-sided (b).

$0 \leq a \leq 1$. If equality holds true for all values of a , i.e. $\mathbb{P}(P \leq a \mid H_0) = a$, the p-value is exact. This definition implies that—under the null hypothesis—the p-value is uniformly distributed in the interval $[0, 1]$. In the following, I will take a closer look on the left-sided p-value and present a short prove of its uniformity under the null hypothesis. The cumulative distribution function of a continuous test statistic T under the null hypothesis is given by $F_T(t) = \mathbb{P}(T \leq t)$. The left-sided p-value is defined as $P = F_T(T)$. For the cumulative distribution function F_P of the p-value it holds that

$$F_P(p) = \mathbb{P}(P \leq p) = \mathbb{P}(F_T(T) \leq p) = \mathbb{P}(T \leq F_T^{-1}(p)) = F_T(F_T^{-1}(p)) = p. \quad (3.9)$$

As only the uniform distribution fulfills $F_P(p) = p$, the p-value follows a uniform distribution. Hence, it holds that $\mathbb{P}(P \leq a \mid H_0) = a$ and the p-value is exact. Of note, the proof only holds if F_T is invertible, which is not fulfilled in case of a discrete random variable T . If a test statistic T is discrete, the distribution of p-values will also be discrete. Hence, the p-value cannot be uniformly distributed over the whole interval $[0, 1]$, but can take on discrete values only. Nevertheless, the p-value will be distributed uniformly in the sense that $\mathbb{P}(p \leq a \mid H_0) = a$, if a is a value that can be taken on by the p-value, and $\mathbb{P}(p \leq a \mid H_0) < a$ otherwise. Hence, the p-value is valid. The validity of discrete p-values will be important for p-values based on Monte Carlo simulations or generated controls, which will be introduced in chapter 4 and 5. Notably, if the p-value is not distributed uniformly under the null hypothesis, the null hypothesis does not follow the assumed distribution and thus, the p-value is not valid.

3.2.3. Statistical significance and hypothesis testing

The p-value allows to asses statistical significance, i.e. whether a result for a test statistic is more extreme than what can be expected from random chance. It describes how incompatible the observed data are with a statistical model specified by the null hypothesis. In *hypothesis testing*, the null hypothesis H_0 is tested against the alternative hypothesis H_1 . Of note, the

union of H_0 and H_1 should cover the whole range of possibilities. For example, if we compare two groups characterized by a summary statistic with values A and B , respectively, we can conduct the following tests:

- Left-sided: $H_0: A \geq B$ vs. $H_1: A < B$,
- Right-sided: $H_0: A \leq B$ vs. $H_1: A > B$,
- Two-sided: $H_0: A = B$ vs. $H_1: A < B$ or $A > B$.

For the above tests, the left-sided, right-sided or two-sided p-value is calculated, respectively. The test decision, i.e. whether the null hypothesis is rejected or kept, is based on the p-value and a previously chosen threshold termed the level of significance α . The null hypothesis is rejected if the obtained p-value is lower than or equal to α . If the p-value is larger than α , the null hypothesis is kept.

For the interpretation of results it should be kept in mind that the outcome of any hypothesis test may be incorrect. There are two types of errors, which are described by the type I and type II error. The *type I error* corresponds to false positives: The null hypothesis is rejected and an observed effect is assumed to be real, although it is due to random chance alone. The probability of a type I error is directly determined by the level of significance. For a valid p-value it holds that $\mathbb{P}(p \leq \alpha \mid H_0) \leq \alpha$ for all $\alpha \in [0, 1]$. Hence, the probability of falsely rejecting the null hypothesis is smaller than or equal to α . Note that for an exact p-value the false positive rate is exactly α . A *type II error* occurs in case of false negatives: the null hypothesis is kept, although the alternative hypothesis is true. Of note, the probability of a type II error is dependent on the sample size; for increasing sample size the sampling variation decreases and even small differences in the summary statistics can be attributed to true existing effects instead of random noise.

3.2.4. Validity and interpretation of p-values

The p-value, and consequently also significance testing, has recently become an issue of dispute. A variety of articles and comments have been published, both arguing for and against the validity of p-values. This is mainly due to misinterpretations of how to correctly interpret p-values. In 2016, the American Statistical Association released a statement addressing several misconceptions about the p-value [139].

Firstly, the p-value is not the probability that the null hypothesis is true, but rather indicates how compatible the observed data are with the null hypothesis. Importantly, a rejection of the null hypothesis does not prove that the null hypothesis is false. The null hypothesis could still be true, but a very unlikely event occurred. Vice versa, not rejecting the null hypothesis does not prove its truth. The test decision always depends on the chosen level of significance, which usually affects the probabilities for a type I and type II error. Notably, lowering the chance for one error increases the other and a certain probability for either error always remains. Hence, an outcome of a test should never be taken as a sole source for *proving* a hypothesis.

One major issue is known as *fishing for p-values*. In case of a true null hypothesis, there is still a certain probability to obtain a significant p-value. For one hypothesis test, this

probability corresponds to the level of significance α . If one conducts multiple experiments and performs a hypothesis test for each, the probability to obtain a significant p-value is given by $1 - \alpha^n$, where n denotes the number of experiments. Evidently, $1 - \alpha^n$ approaches 1 for large values of n , i.e. for a large number of experiments, one will obtain a significant p-value with high probability. A closely related problem concerns publication bias. Significant results are considered as interesting and are much more likely to be published than observations which are non-significant. In this case, p-value fishing occurs at a much larger scale. For example, let's assume that 1000 different experiments—all following the null hypothesis—are conducted in 1000 different research groups. On average 50 of these observations will yield a significant p-value at a significance level of $\alpha = 0.05$ and thus, are likely to be published with the globally wrong assessment of being statistically significant.

Moreover, statistical significance does not directly relate to practical significance. Statistical significance is a measure of probability, which directly depends on the sampling distribution. The sampling distribution, in turn, depends on the sample size and reflects the natural variability of a summary statistics, which can be seen as noise. Statistical significance describes whether an observed effect could be due to noise inherent in small data sets only. For large data samples, the noise decreases and thus, even minor differences become statistically significant. However, this does not imply that such a difference will necessarily be of practical importance.

Calculating a p-value can be very useful for researchers in order not to be fooled by random chance. For small sample sizes in particular, random variations lead to outcomes that can easily be misinterpreted as interesting patterns. The p-value allows to quantitatively assess whether an observed effect could have been due to random chance alone and whether it is worth to study the effect in more detail.

As p-values have been controversial, the use of alternatives such as estimation statistics and confidence intervals have been encouraged. A confidence interval is an interval estimate for an unknown parameter. It is always associated with a certain confidence level, which corresponds to the percentage of confidence intervals containing the true parameter. Nevertheless, both p-values and confidence intervals are based on the same statistical theories. Inferences about statistical significance based on either are directly linked: If a p-value is smaller than the level of significance α , the $1 - \alpha$ confidence interval will not include the null hypothesis value. Vice versa, if the $1 - \alpha$ confidence interval does not include the null hypothesis value, the p-value will be smaller than α .

Finally, as long as random variability is involved, no effect can be strictly proven merely based on a (small) sample of observations alone. Scientific conclusions must not merely be based on whether a p-value passes a user-set threshold without any other supporting evidence or reasoning. Moreover, also a true but possibly small difference might be of no essential practical importance. In general, it is necessary that researchers are aware of what statistical significance testing really means in order not to misuse it. Merely replacing the p-value with other methods will not solve the problem, but rather only shift it. Most importantly, completely abolishing any assessment of statistical significance poses a great risk of everyone being fooled by random chance.

3.2.5. P-values for assessing biomolecular distributions

A direct interpretation of SMLM localization maps is often hampered by artifacts arising from overcounting or background detections. Interestingly, though, even in case of a localization map void of any artifacts a purely local analysis of features will yield misleading results as interesting subpatterns may arise due to random chance alone (compare Fig. 3.9). A global statistical assessment based on a p-value and statistical significance testing provides a means for a valid evaluation of biomolecular distributions.

In the following two chapters of this thesis, I will present two different methods to assess biomolecular distributions with regard to statistical significance. In particular, the null hypothesis of a random distribution of biomolecules in the cell plasma membrane will be tested against the alternative hypothesis of (nano-)clustering. The first method (chapter 4) relies on the recording of reliable blinking statistics which are the basis for generating realizations of the null hypothesis as controls via Monte Carlo simulations. For the evaluation of clustering, Ripley's H function is employed as a summary statistic. The second method (chapter 5) is based on competitive labeling of the same type of biomolecule with labels of two different colors. By investigating the correlations between the two color channels, clustering can be assessed completely independent of fluorophore blinking behavior. Most importantly, both methods allow to investigate the true distribution of biomolecules which underlies the observed distribution of SMLM localizations.

4. Monte Carlo simulations based on blinking statistics

This chapter contains data and figures from the following publication:

R. Platzer*, B. K. Rossboth*, **M. C. Schneider**, E. Sevcsik, F. Baumgart, H. Stockinger, G. J. Schütz, J. B. Huppa, M. Brameshuber. *Unscrambling Fluorophore Blinking for Comprehensive Cluster Detection via PALM*. Nature Communications, 11, 2020.

doi: 10.1038/s41467-020-18726-9

Aim

SMLM localization maps strongly depend on the blinking characteristics of fluorescent labels. In particular, multiple detections of the same biomolecule of interest lead to localization clusters, which can easily be misinterpreted as molecular nanoclusters. Methods trying to account and correct for overcounting typically rely on some assumption or knowledge about fluorophore blinking parameters. However, complex blinking behavior including long-lived dark states and broad distributions of the blinking statistics often impede a valid assessment of the spatial arrangement of biomolecules. In addition, recording of reliable blinking statistics is often challenging. Here, we aimed at developing methods for reliable and comprehensive characterization of fluorophore blinking behavior, which allows for an accurate assessment of biomolecular spatial distributions.

Contribution

Together with Benedikt Rossboth, I conceived and developed software tools for analytical methods and simulations for the study. For analysis of the blinking data, I implemented a software package for comprehensive characterization of fluorophore blinking statistics. Moreover, I contributed code for Monte Carlo simulations of localization maps and assessment of biomolecular distributions via Ripley's analysis. Further, I extended the content from the paper to allow for statistical significance testing with regard to biomolecular clustering. The linker system for the platform was developed by René Platzer, who also contributed all probes. Imaging experiments were performed by René Platzer and Benedikt Rossboth.

Outcome

A specially designed platform allowed for reliable recording and evaluation of fluorophore blinking statistics. This comprehensive characterization of the blinking behavior was the basis for Monte Carlo simulations of SMLM experiments. The resulting simulated localization maps were used for a robust evaluation of biomolecular distributions based on experimentally recorded SMLM localization maps and statistical significance testing.

4.1. Introduction

Fluorophore blinking statistics crucially affect the localization maps obtained via SMLM techniques. All methods for discrimination of true biomolecular clustering from clustering artifacts discussed in section 3.1 depend on fluorophore blinking behavior. Either the recording of the blinking statistics is incorporated in the method itself [4] or at least some parameters of the blinking statistics, in particular the mean number of detections of a single biomolecule, need to be known or estimated [5–7]. For the validity of these cluster analysis methods, it is hence crucial to characterize the blinking statistics accurately.

However, a reliable characterization of blinking behavior is challenging. First, the fluorophores need to be recorded at sparse densities in order to ensure that localizations from different fluorophores can be spatially distinguished. Further, the photophysical properties of fluorophores, including photobleaching and -blinking, have been shown to depend on their molecular nanoenvironment [8], in particular for organic dyes. In addition, the illumination protocol affects the resulting blinking statistics [62]. Therefore, the characterization of blinking behavior should be performed under the same imaging conditions and molecular environment as given for the experiment of interest. Employing a blinking statistics for correction and analysis of data recorded under different experimental conditions may lead to misleading results. One factor additionally impeding proper characterization of blinking behavior are spurious background signals. Any trace amounts of buffer- or lipid-derived dyes may distort the recorded blinking statistics of the fluorophores of interest. In case blinking statistics are recorded within the cellular environment, cellular autofluorescence may impede the proper characterization of fluorophore blinking.

In this chapter, I will present a method for comprehensive and reliable characterization of fluorophore blinking behavior based on a specially designed platform, which addresses the above-mentioned issues. Subsequently, the obtained blinking statistics can be used for Monte Carlo simulations of SMLM localization maps, which allow for a statistical assessment of true biomolecular distributions.

4.2. Results

4.2.1. Recording of blinking statistics

For the recording of fluorophore blinking statistics, we developed a specially designed platform (Fig. 4.1). The platform consists of monovalent and recombinant streptavidin (mSAv^{*}-3cHis₆), which is anchored via three histidine tags to a gel-phase planar glass-supported lipid bilayer (SLB). The fluorophore of interest is coupled to the platform site-specifically via a biotin modification. For localization of the platform itself, a spectrally complementary dye is site-specifically conjugated to an unpaired cysteine residue within the same streptavidin subunit. The use of the platform together with appropriate buffer conditions allows to mimic the environment of a cell, while minimizing false positive localizations, which are particularly prominent under strong illumination conditions. In addition, the platform not only ensures that just a single

fluorophore molecule is bound, but further can be diluted to arbitrarily low densities. Thus, localizations from different fluorophores are well separated from each other and can be spatially distinguished.

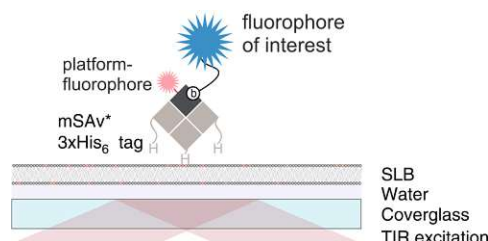


Figure 4.1.: Platform design for recording of blinking statistics. The platform consists of monovalent and recombinant streptavidin (mSAv*-3cHis₆) and is anchored to a glass-supported lipid bilayer (SLB) via three histidine tags. The fluorophore of interest (blue) is site-specifically bound to the platform via a biotin-modification. A spectrally complementary fluorophore (red) is conjugated to an unpaired cysteine residue within the same streptavidin subunit and used to identify platform-bound fluorophores of interest, while distinguishing them from background localizations. Figure adapted from [63].

We characterized the blinking behavior of four fluorescent labels: the photoswitchable fluorophores PS-CFP2 and mEOS3.2, and the photoactivatable organic dyes Abberior CAGE635 (CAGE635) and Janelia Fluor 549 (PA-JF549). To label the platform itself we used Alexa Fluor 488 (AF488; for characterization of CAGE635) or Abberior STAR635 P (STAR635; for the characterization of PS-CFP2, mEOS3.2 and PA-JF549), which were site-specifically conjugated to the biotin-binding subunit of mSAv*-3cHis₆. These platform-fluorophores are spectrally distinct to the respective fluorophores of interest. Imaging of the platform-fluorophores allowed to determine the platform positions. Subsequently, a density filter was applied to the platform data; platform positions with a neighbor in a vicinity of 500 nm were discarded. This density filtering allowed to omit fluorophores with overlapping point spread functions. The fluorophore of interest was imaged in a separate color channel. The two color channels for the platform and blinking data were corrected for chromatic aberration via an affine transformation matrix, which was determined by imaging of multi-spectral beads.

Subsequently, the recorded localizations of the fluorophore of interest were grouped into localization clusters arising from individual fluorophores via hierarchical agglomerative clustering as described in Fig. 4.2. Of note, other methods may be used as alternative for this task, e.g. clustering can also be performed via a tracking algorithm. Finally, a colocalization analysis between the centers of the localization clusters and the platform signals was performed (Fig. 4.2c). This ensured that any background signals were discarded, which would distort the blinking statistics.

Subsequently, a characterization of fluorophore blinking was performed based on the remaining localization data. In Fig. 4.3, representative intensity traces of two recorded individual fluorophore molecules are shown. Via an intensity threshold, these traces were converted into a binary sequence of on- and off-states. The estimated positions of fluorophores in the on-state are given by the corresponding localization map. A simplified blinking trace is depicted in Fig. 4.4. The blinking sequence can be characterized by several parameters. For a comprehen-

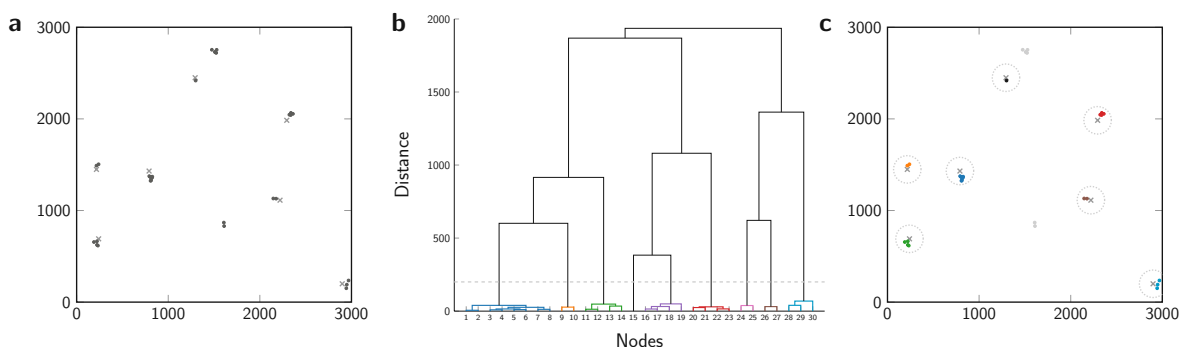


Figure 4.2.: Grouping of localizations and colocalization with platform data. Panel (a) shows an illustrative localization map including the platform signals (gray crosses) and the localization data of the fluorophore of interest (black dots). Localizations arising from individual fluorophores are grouped via hierarchical clustering using the Euclidean distance metric. Unweighted average distance (UPGMA) was selected as linkage criterion. The resulting dendrogram (b) was cut at 200 nm (dashed line) to obtain individual clusters indicated by color-code in panel (c). Localizations are considered colocalized with a platform if a platform signal is located within a radius r_{coloc} from the localization cluster center. Colocalized localization clusters are kept for further analysis, all other localizations are discarded.

sive characterization of fluorophore blinking, we determined the number N of total detections of a single fluorophore, the numbers of consecutive frames t_{on} and t_{off} a fluorophore is in its on- or off-state, respectively, the number of gaps g in the blinking trace (i.e. the number of switches between the on- and off-state), and the frame number f_{start} of the first appearance. The values of these parameters are different for each recorded single fluorophore and thus, yield a probability distribution. Optionally, the resulting distributions may be filtered for outliers. Here, we discarded labels detected more often than a specified threshold value (see *Methods*, section 4.4) and removed these outliers from the blinking distributions. Of note, many methods for the detection of true molecular clustering only take into account the mean number of detections \bar{N} of a single fluorophore, reducing the whole distribution of N to a single number. This approach may be sufficient if the standard deviation of the distribution is low. In case of a broad distribution with heavy tails, however, outliers will confound the analysis.

Fig. 4.5 shows the resulting blinking statistics recorded for the four investigated fluorophores PS-CFP2, mEOS3.2, PA-JF549 and CAGE635. The figure includes histograms for the total number of detections N , the number of gaps g , as well as on- and off-times t_{on} and t_{off} , respectively. Notably, nearly all obtained distributions exhibit heavy tails. In principle, high values of N , g and t_{on} can be accounted for by simple merging of localizations as proposed by Annibale et al. [3, 5]. However, high values of t_{off} impede this analysis, as repeated detections of the same fluorophore cannot be distinguished from a newly appearing fluorophore. As we observed, a considerable percentage of t_{off} values exceeds a value of 200 frames for the recorded data (Fig. 4.5), which is higher than typical threshold values chosen for merging of localizations.

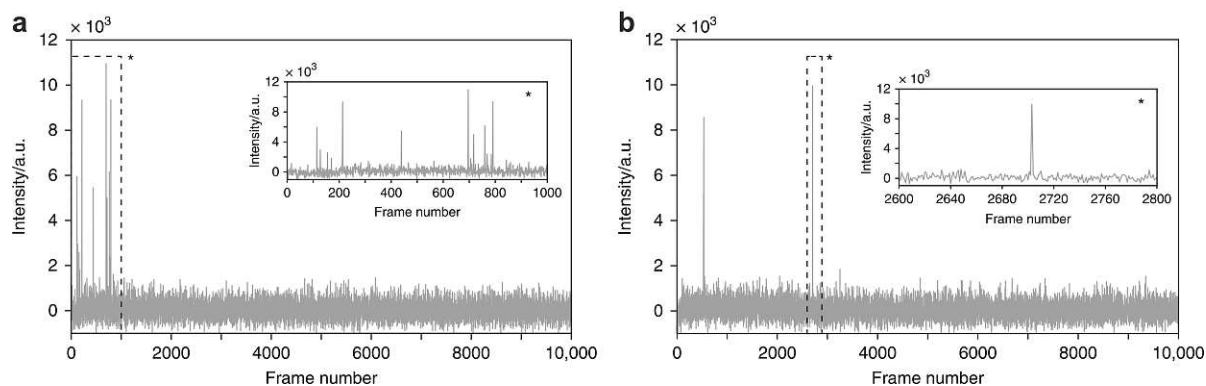


Figure 4.3.: Representative intensity traces of PS-CFP2 molecules. Intensity traces of single PS-CFP2 molecules (a,b) were recorded over 10 000 frames. Both molecules exhibited multiple bursts of detections. Insets show enlarged views of the indicated regions. Figure adapted from [63].

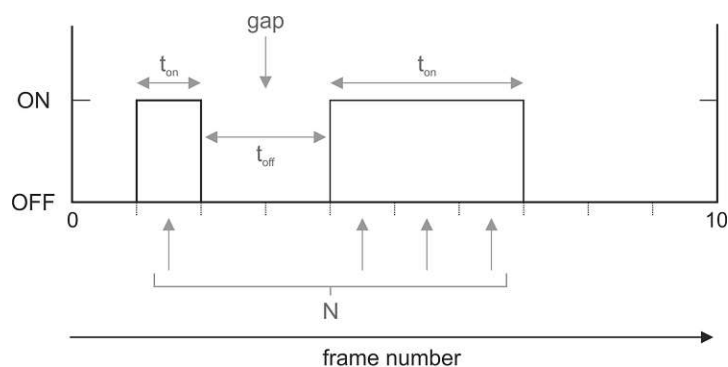


Figure 4.4.: Blinking statistic parameters. The state of a fluorophore is shown over the time given in frame numbers. A fluorophore can switch between its bright on-state and its dark off-state. The blinking trace can be characterized by the total number of detections of the fluorophore N , the duration of on- and off-states t_{on} and t_{off} , respectively, and the number of switches between the on- and off-state, which is described by the number of gaps. Figure recreated and adapted from [63].

4. Monte Carlo simulations based on blinking statistics

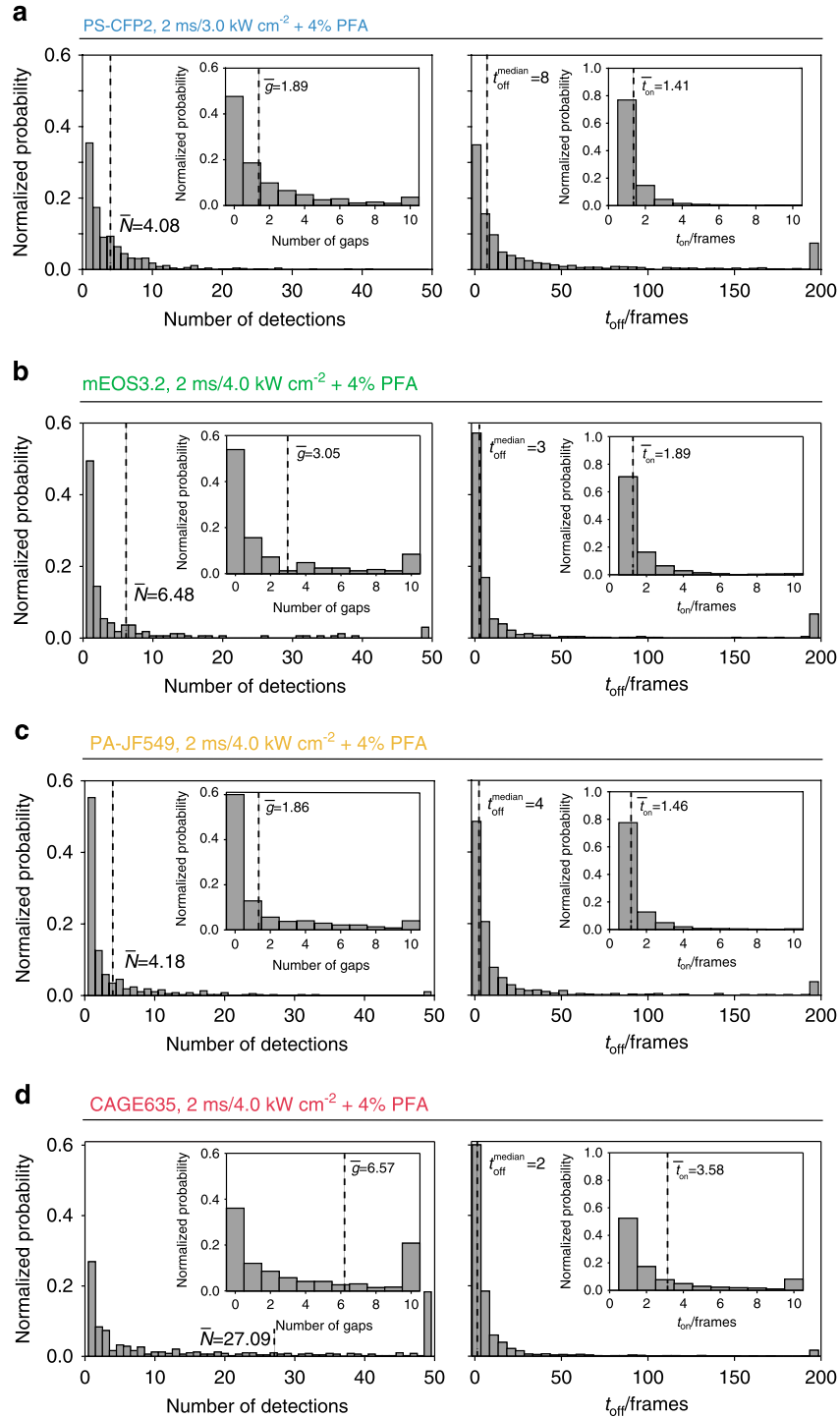


Figure 4.5.: Experimentally recorded blinking statistics. The four panels show the blinking statistics for the fluorescent proteins PS-CFP2 (a) and mEOS3.2 (b), and the organic dyes PA-JF549 (c) and CAGE635 (d). Imaging was performed at 2 ms illumination and 3 or 4 kW/cm², respectively, in the presence of 4 % paraformaldehyde (PFA). Histograms show the distribution of the total number of detections N , the number of gaps g , and the on- and off-times t_{on} and t_{off} , respectively. Vertical dashed lines indicate the mean for N , g and t_{on} , and the median for t_{off} . Figure adapted from [63].

4.2.2. Cluster analysis via simulation envelopes

Fluorophore blinking prohibits adequate cluster analysis via methods that do not account for the blinking behavior, as for example analysis via Ripley's H function. This can be easily seen via simulations: For Fig. 4.6a, we simulated a random distribution of molecules (left column). For the corresponding localization maps (Fig. 4.6b), we included multiple detections of each label. The assigned number of detections for each biomolecule was chosen randomly based on the experimentally determined blinking statistics of PS-CFP2, mEOS3.2, PA-JF549 and CAGE635. Subsequently, the resulting localization maps were analyzed via Ripley's analysis. As described in section 3.1.2, in case of complete spatial randomness Ripley's H function is equal to 0 at all scales, i.e. $H(r) = 0$ for all $r \in \mathbb{R}^+$. Fluorophore blinking, however, leads to localization clusters which cannot be distinguished from true molecular clustering. The resulting Ripley's H functions show a clear deviation from 0 (Fig. 4.6c). Therefore, a simple analysis based on deviations of Ripley's H function from 0 leads to misleading results and is not adequate in the presence of overcounting.

Spatial point patterns of localizations arising from complex blinking statistics lead to a form of the Ripley's function that cannot easily be described theoretically. Hence, comparing an obtained curve to the form of Ripley's function under a random distribution is not straightforward. Nevertheless, if a comprehensive characterization of fluorophore blinking properties is available, true molecular clustering may be discriminated from overcounting artifacts by means of Monte Carlo simulations [121, 140]: Simulations of randomly distributed molecules including experimentally recorded blinking statistics allow to estimate the form of Ripley's H function for random molecule distributions. In order to obtain reliable estimates, the number of simulations n should be high; here, we used $n = 99$.

A representative localization map for an underlying random distribution is shown in the top panel of Fig. 4.7a. For each simulated localization map, Ripley's H function was determined, yielding different realizations from the sampling distribution (Fig. 4.7b). From this set of curves, the pointwise mean $E(r)$ (black solid line), the standard deviation $V(r)$ (indicated by the dotted lines) and 95% confidence intervals (dashed lines) were calculated. Further, Ripley's H function was normalized by subtracting $E(r)$ (Fig. 4.7c). Thus, for a truly random distribution of underlying biomolecules, the function again follows the 0-line. For the analysis of a new data set (green lines), Ripley's H function $H(r)$ is determined from which $E(r)$ is subtracted. Now, deviations of the function $H(r) - E(r)$ from 0 indicate distributions that differ from the null hypothesis of an underlying random biomolecular distribution (Fig. 4.7c): Values greater than 0 indicate clustering, whereas values below 0 indicate dispersion [141, 142].

The top and bottom row in Fig. 4.7 show the analysis in case of a random and clustered biomolecular distribution. As can be seen in panel c, the obtained function $H(r) - E(r)$ for the simulated data shown in panel a (green line) follows the 0-line in case of a random distribution. In case of true biomolecular clustering, however, the green line shows a clear deviation from the confidence band at distances smaller than 200 nm, indicating nanoclustering.

Further, a significance test for the null hypothesis of a random biomolecular distribution can be conducted based on the simulated localization maps [120, 140]: Let T be a statistic describing the spatial distribution of a localization point pattern. As we are interested in nanoclustering,

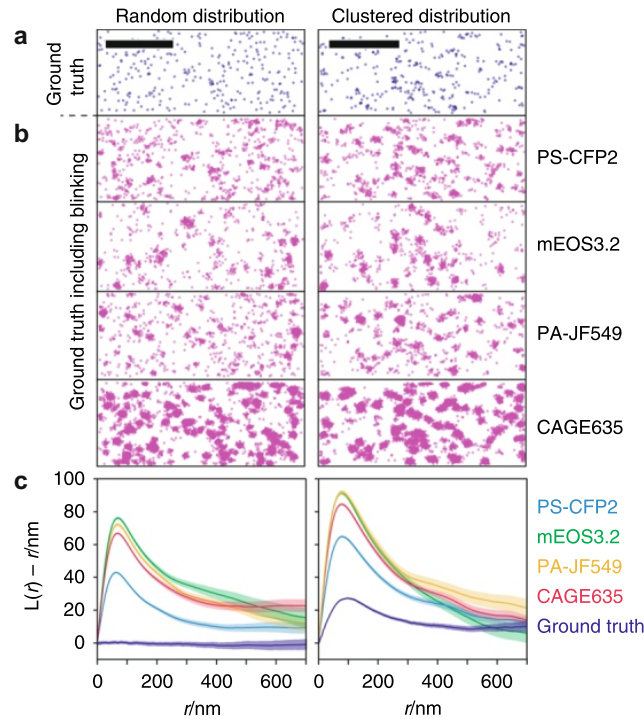


Figure 4.6.: Cluster analysis via Ripley's H function in the presence of overcounting. The left and right column show simulated point patterns for randomly distributed and clustered biomolecules, respectively, at a density of 70 molecules per μm^2 . For the clustering scenario, the cluster radius was set to 60 nm. The density of clusters was 20 clusters per μm^2 , with 80% of molecules inside clusters. The top panel (a) shows the ground truth distribution of molecules. The four panels below (b) show localization maps which include multiple detections of each biomolecule. The number of detections assigned to each biomolecule was chosen randomly based on experimentally determined blinking statistics of PS-CFP2, mEOS3.2, PA-JF549 and CAGE635 from Fig. 4.5. Scale bars: $1 \mu\text{m}$. (c) Resulting Ripley's H functions (mean \pm SD) from the analysis of 15 simulated point patterns as illustrated in panels a and b within an area of $15 \times 15 \mu\text{m}^2$. Notably, Ripley's H functions for the simulations of random molecular distributions which include overcounting well exceed values of 0 and thus, cannot be distinguished from clustered molecular distributions. Figure adapted from [63].

the value of the Ripley's function at $r = 50 \text{ nm}$ was taken as test statistic T for the analysis, in particular $T := H(50) - E(50)$. With t_0 we denote the value of the statistic for the data set of interest, and t_i for $i = 1, \dots, n$ denote the values obtained for a set of n Monte Carlo simulations under the null hypothesis, i.e. a random biomolecular distribution. Subsequently, the obtained set of values $\mathcal{T} := \{t_i \mid i = 0, \dots, n\}$ was ordered. Based on this order a rank was assigned to each value. The corresponding one-sided p-value for t_0 was calculated as

$$p = \frac{\text{rank}(t_0, \mathcal{T})}{n + 1}, \quad (4.1)$$

where $\text{rank}(t_0, \mathcal{T})$ denotes the rank of t_0 within the set \mathcal{T} in descending order, i.e. the maximum value has a rank of 1. Of note, this calculated p-value is limited to discrete numbers; the minimum p-value that can be obtained is given by $1/(n + 1)$. For hypothesis testing, the

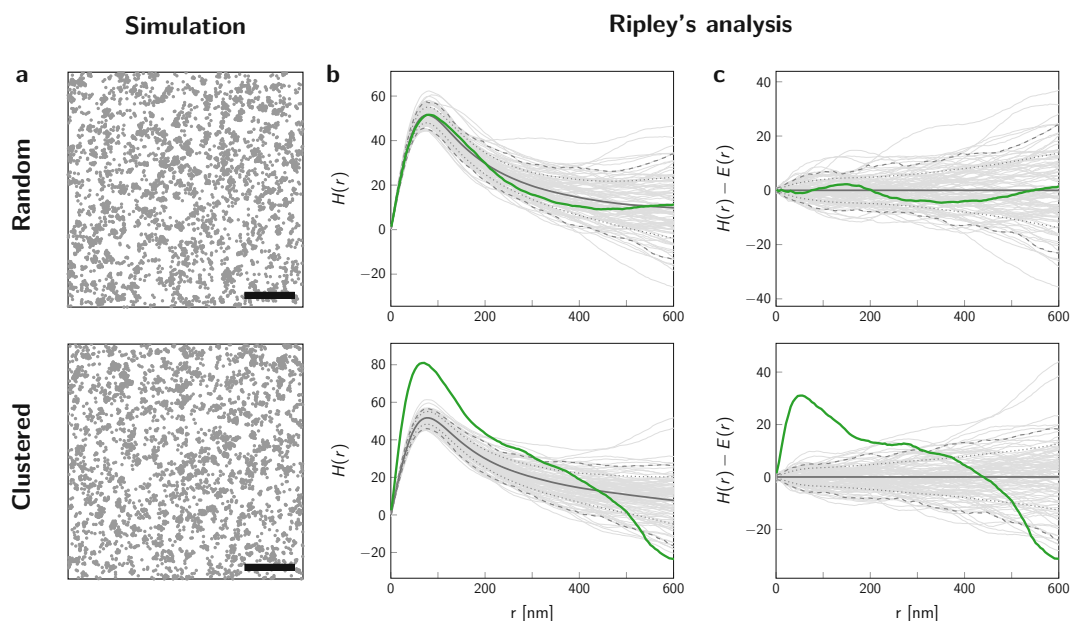


Figure 4.7.: Monte Carlo simulations and simulation envelopes. (a) Localization maps of a random (top) and clustered (bottom) biomolecular distribution were simulated with a density of 50 molecules/ μm^2 , including overcounting based on fluorophore blinking statistics of PS-CFP2. Parameters for clustered scenario: 10 clusters/ μm^2 , 60 nm cluster radius, 80% of molecules inside clusters. Scale bars: 1 μm . (b) In order to obtain an estimation of Ripley's H function under the null hypothesis, $n = 99$ simulation runs of randomly distributed molecules were performed. For each simulation, Ripley's H function $H(r)$ was calculated, creating a set of curves (gray lines) which constitute a simulation envelope. The pointwise mean $E(r)$ (black solid line), standard deviation $V(r)$ (indicated by the dotted lines) and 95% CI (dashed lines) are shown. The green curve was obtained for the localization data shown in panel a. (c) Deviations of $H(r) - E(r)$ from 0 indicate non-random molecule distributions. For the random biomolecular distribution (top), the green line lies well within the simulation envelope. The curve for the clustered biomolecular distribution (bottom) exhibits a clear peak which lies outside the simulation envelope. Investigating clustering at a range of $r = 50$ nm yielded p-values of $p = 0.64$ and $p = 0.01$ for the random and clustered scenario, respectively.

null hypothesis was rejected if the obtained p-value was smaller than the specified level of significance α , chosen as $\alpha = 0.05$. For the simulated data from Fig. 4.7, a p-value of $p = 0.64$ and $p = 0.01$ was obtained for the randomly and clustered scenario, respectively.

4.2.3. Analysis of experimental data

We applied our approach for investigating the spatial distribution of proteins in the T-cell, in particular the T-cell receptor (TCR) and the integrin LFA-1, which play important roles in T-cell activation [143, 144]. TCR-CD3 ζ was fused to PS-CFP2, and LFA-1 was labeled with a biotinylated antibody for detection via PS-CFP2. T-cells were chemically fixed and imaged using the same experimental settings as used for the characterization of the fluorophore blinking behavior (see *Methods*, section 4.4 for details).

In order to perform Monte Carlo simulations which correspond to the experimental data, one required parameter is the density of molecules. The simulated density needs to be similar to the density of molecules in the experiment which is to be evaluated. This density was estimated from the experimental data set by dividing the total number of localizations by the average number of detections \bar{N} derived from the recorded blinking statistics. For the simulations, a density of 86 molecules per μm^2 for TCR-CD3 ζ and 145 molecules per μm^2 for LFA-1 was used.

Fig. 4.8 shows the experimentally obtained localization maps (panel a) as well as a representative simulated localization map (panel b) for both TCR-CD3 ζ (top row) and LFA-1 (bottom row). In all cases, the localization maps exhibited obvious clustering. However, for TCR-CD3 ζ a comparison of Ripley's H function with the simulated data sets revealed no significant deviation from an underlying random distribution of biomolecules (Fig. 4.8c). The obtained p-value at a range of $r = 50$ nm was $p = 0.23$, which is in accordance with previous results on the distribution of TCR-CD3 ζ in non-activated T-cells [118, 145]. In contrast, LFA-1 showed a significant deviation from the random scenario with a p-value of 0.01. In this case, the observed localization clusters cannot be explained by mere overcounting, but true nanoclustering of LFA-1.

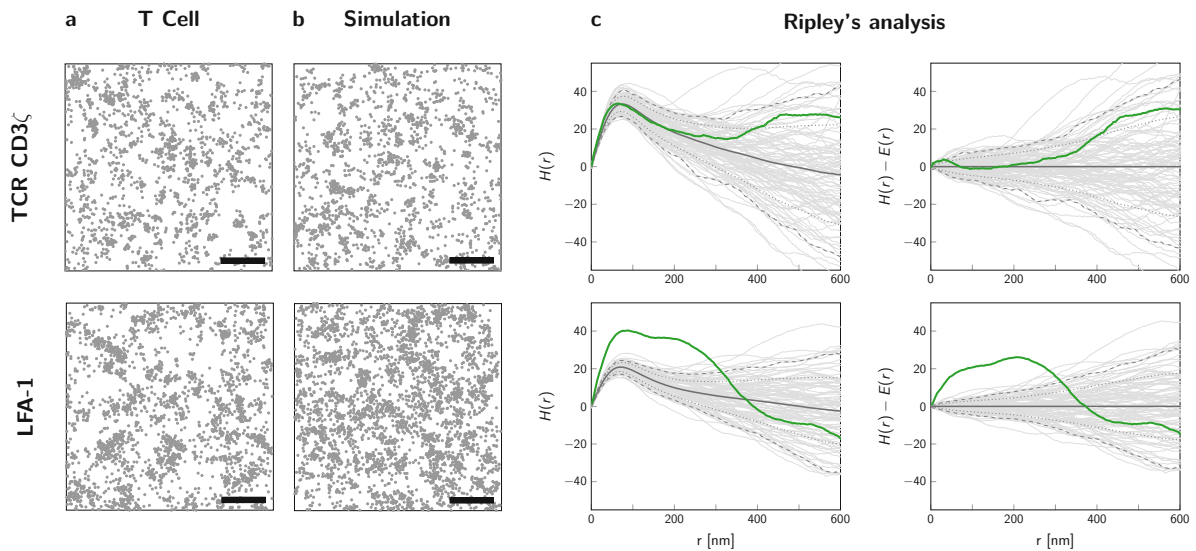


Figure 4.8.: Analysis of TCR-CD ζ and LFA-1 distributions in the T-cell. Localization maps for experimental data (a) and a representative simulation (b) for TCR-CD ζ (top row) and LFA-1 (bottom row). The simulated control data sets assumed a random distribution of molecules with a density of 86 molecules per μm^2 for TCR-CD3 ζ and 145 molecules per μm^2 for LFA-1. A number of $n = 99$ simulations was performed for each scenario. Scale bars: 500 nm. (c) For each localization map, Ripley's H function $H(r)$ was calculated (gray lines). The pointwise mean $E(r)$ (black solid line), standard deviation $V(r)$ (indicated by the dotted lines) and 95% CI (dashed lines) are shown. Ripley's H functions obtained for the experimental data are shown as green curves. The curve obtained for TCR-CD3 ζ could not be discriminated against a random scenario; in contrast, the curve for LFA-1 exhibited a clear deviation from the simulation envelope. Investigating the clustering at a range of $r = 50$ nm yielded p-values of $p = 0.23$ for TCR-CD3 ζ , and $p = 0.01$ for LFA-1.

4.3. Discussion

The results of cluster analysis methods are crucially affected by fluorophore blinking behavior. Simple approaches to account for overcounting artifacts are based on merging of localizations in spatial and temporal proximity [5]. However, such approaches are not suitable for complex blinking behavior, in particular long dark times, and fail to account for outliers exhibiting excessive blinking. Evidently, merging procedures cannot prohibit multiple detections of the same biomolecule in case of labeling strategies including multiple dyes per biomolecule of interest. Hence, merging approaches are not sufficient for reliable cluster assessment in case of antibody labeling, for example. Similarly, merging of localizations cannot account for multiple detections in case of PAINT imaging, as the time between multiple detections of the same biomolecule of interest is in principle unlimited.

Other cluster analysis approaches rely on a single number summarizing the blinking behavior, in particular the mean number of localizations [6, 7]. However, broad distributions of blinking parameters including heavy tails typically impede correct cluster assessment in this case. Consequently, not only the average number of detections of a fluorophore is important, but the overall shape of its blinking parameter distributions affects its suitability for accurate assessment of molecular clustering.

Organic dyes typically show extensive and complex blinking behavior [110–112]. Blinking of photoactivatable fluorescent proteins is less pronounced; nevertheless, also FPs may transition into prolonged dark states with a subsequent return into their bright state [3, 146, 147]. We showed that both PS-CFP2 and mEOS3.2 molecules may exhibit several cycles of emissive states on a timescale of several seconds to minutes. More than half of all molecules were detected at least twice. The maximum number of observations of a single molecule exceeded 20 and 50 detections for PS-CFP2 and mEOS3.2, respectively. Often, high excitation power is employed in a typical experiment, aiming to bleach the fluorophore after detection and thus suppress blinking. However, this approach does not solve the problem, as it causes a high number of unspecific background signals which cannot be distinguished from signals arising from molecules of interest [63]. In addition, fluorophores may be bleached before detection, which decreases the effective labeling efficiency [62].

For reliable cluster analysis results, the blinking behavior should be characterized under the same imaging conditions as the experiment which is supposed to be analyzed based on the recorded blinking statistics. This is important as blinking properties change with experimental conditions, including illumination protocols and the molecular nanoenvironment [8]. Interestingly, PFA-based fixation was shown to have no significant effect on the blinking behavior [63]. Further, changing the excitation power and illumination time while keeping the excitation energy per frame constant was shown to have only a minor effect on blinking statistics [63], although the effective labeling efficiency was reported to decrease for very high excitation intensities [62]. In contrast, varying the excitation intensity while keeping the exposure time constant affects the blinking statistics, in particular the observed on-times and number of localizations [62].

The presented approach for characterization of blinking statistics relies on a specially designed SLB-based experimental platform, which mimics experimental conditions. The colocalization

of blinking data with platform signals minimizes false positive detections arising from background signals. Blinking analysis without the platform data should only be performed if background signals are known to be negligible.

On the one hand, this platform-based approach allows to screen and identify suitable fluorophores and appropriate imaging conditions which minimize fluorophore blinking. On the other hand, the platform serves as an ideal tool for an exhaustive characterization of fluorophore blinking. Monte Carlo simulations based on the recorded blinking statistics offer a comprehensive way for analyzing localization maps and comparing them with various assumed models of biomolecular distributions, in particular, random distributions of underlying molecules of interest. Optionally, the presented assessment of clustering via Ripley's H function can be readily substituted with other cluster analysis tools, e.g. pair-correlation analysis, which offers the advantage of being non-cumulative. Further, a statistical significance test can be performed based on the obtained simulation envelopes. Of note, the presented approach assesses clustering at a single length scale only. If multiple length scales are tested at the same time, this should be accounted for in order to avoid an inflation of the type I error [124] (see also chapter 5.2.4 for a way to account for multiple tests). Moreover, the sensitivity of cluster detection will be affected by undercounting issues due to insufficient labeling or detection efficiency.

In conclusion, knowledge of fluorophore blinking statistics is crucial for accurate cluster analysis, in particular, if subtle differences in clustering behavior of individual samples are investigated. With conventional (1-color) SMLM imaging approaches, an assessment of clustering at or below the length scale of the localization error is impossible without correct knowledge about blinking behavior.

4.4. Methods

All details of the preparation of glass-supported lipid bilayers, protein expression, refolding and preparation of imaging tools as well as preparation of cell samples for microscopy are described in the *Methods* section of [63].

Platform design for recording of blinking statistics. The platform, consisting of monovalent and recombinant streptavidin (mSAv*-3cHis₆), was anchored to a glass-supported lipid bilayer (SLB) via three histidine tags. The fluorophore of interest (PS-CFP2, CAGE635, mEOS3.2, or PA-JF549) was site-specifically bound to the platform via a biotin-modification. A spectrally complementary fluorophore (AF488 for characterization of CAGE635; STAR635 for characterization of PS-CFP2, mEOS3.2 and PA-JF549) was conjugated to an unpaired cysteine residue within the same streptavidin subunit and used to identify platform-bound fluorophores of interest.

Microscopy. Objective-based TIRF microscopy was conducted using an inverted microscope (Axiovert 200, Zeiss) equipped with a chromatically corrected objective (100×, NA = 1.46, Plan-Apochromat, Zeiss) and 405 nm (photoswitching of PS-CFP2 and mEOS3.2 and photoactivation of CAGE635 and PA-JF549; iBeam smart, Toptica), 488 nm (imaging of AF488 and PS-CFP2; optically pumped semiconductor, Sapphire; Coherent), 532 nm (imaging of mEOS3.2 and PA-JF549; LCX532L with additional AOM, installed in L6Cc laser combiner, Oxxius), and 647 nm (imaging of STAR635 and CAGE635; iBeam smart, Toptica) laser sources. For rapid shuttering of the 488 nm laser illumination, an acousto-optical modulator was used (1205C, Isomet). Fluorescence emission was detected with a back-illuminated EMCCD camera (iXon Ultra 897, Andor). Timing protocols were generated by in-house developed programs implemented in LabVIEW (National Instruments) and executed by a built-in digital/analog IO-card (model PCI-6713, National Instruments). Single mSAv*-STAR635 (or mSAv*-AF488) molecules were imaged using 647 nm (or 488 nm) excitation with a 100 ms time lag for at least 50 frames and employing a power density of 1.5 kW cm^{-2} during the illumination time of 2 ms. For PS-CFP2 PALM measurements, 2 ms of illumination at 3 kW cm^{-2} were followed by a delay time of 4 ms, which was necessary to read out the cropped camera chip, yielding frames rates of 167 Hz. A total of 10 000 frames were recorded. For T-cell microscopy experiments, the T-cells were seeded on ICAM-1-His₁₂ coated glass slides and fixed with 4% PFA. The same microscopy setup, illumination scheme, and laser power was used as for recording of the blinking data of PS-CFP2. For CAGE635 PALM measurements, 10 000 frames were recorded with 2 ms of illumination at 4 kW cm^{-2} with a delay time of 4 ms (167 Hz frame rate). Excitation light was uncoupled from emission light with the use of a dichroic mirror (zt488/640rpc; Chroma). Emission was then split by a Dual View system (Photometrics) equipped with a 640dcxr dichroic mirror and HQ700/75 (both Chroma) and 525/45 (Semrock) emission filters. For mEOS3.2 and PA-JF549 PALM measurements, 10 000 frames were recorded with 2 ms of illumination at 4 kW cm^{-2} with a delay time of 4 ms (167 Hz frame rate). Excitation light was uncoupled from emission light with the use of a dichroic mirror (zt405/488/532/640rpc; Chroma). Emission was split by a Dual View system (Photometrics) equipped with a 640dcxr dichroic mirror and HQ700/75 and HQ585/40m (all three filters Chroma) emission filters.

Single-molecule blinking analysis. For both channels, single molecules were detected and localized by using a Maximum Likelihood Estimator implemented in the ThunderSTORM ImageJ plugin [89]. The position of mSAv*-STAR635 (or mSAv*-AF488) molecules was averaged over the imaging period by using the localization merging algorithm implemented in ThunderSTORM (parameter settings: maximum toff = 10 000 frames, maximum displacement = 1 pixel). This mean position was then employed for colocalization analysis. Determined positions of mSAv*-STAR635 (or mSAv*-AF488) were corrected for chromatic aberration by an affine transformation matrix, which was experimentally derived from imaging TetraSpeck beads (Thermo Fisher Scientific). Any mSAv*-STAR635 (or mSAv*-AF488) molecules with a nearest neighbor within a distance smaller than 500 nm were discarded. Fluorescent signals from individual labels (i.e. PS-CFP2, mEOS3.2, PA-JF549, or CAGE635 molecules) were grouped via hierarchical agglomerative clustering using the Euclidean distance metric. Unweighted average distance (UPGMA) was selected as linkage criterion. The resulting dendrogram was cut at 200 nm to obtain individual clusters. Localization clusters were regarded as colocalized if a platform signal was located within a radius of 500 nm from a cluster center. Only colocalized localization clusters were selected for further analysis. Localization clusters with a number of detections exceeding a certain threshold were discarded as outliers. This threshold was set to 150 (for mEOS3.2 and PA-JF549); less than three localization clusters were lost for each scenario. For the PS-CFP2 and CAGE635 data no filter was applied.

Simulations. A $15 \times 15 \mu\text{m}^2$ region of interest featuring molecules at specified densities was simulated as described previously [118]. Briefly, a probability mask was generated by placing centers of clusters randomly according to a uniform distribution, and distributing the positions of molecules within clusters based on a two-dimensional Gaussian distribution located at the cluster center and truncated at the cluster size, i.e. one time the standard deviation of the Gaussian. A given proportion of molecules was attributed to clusters (% of molecules in clusters). The remaining molecules were randomly added on areas outside the clusters. To include blinking, the number of detections per label was drawn from the experimentally derived probability distribution of N . Finally, a localization error was added by shifting the positions into a random direction by a distance drawn from a normal distribution with mean 0 and experimentally derived localization precision as standard deviation. For performing simulations used for comparison with cell-associated microscopy data, the approximate expression levels of CD3 ζ -PS-CFP2 and LFA-1 (stained with the mAb TS2/4-biotin and fluorophore-conjugated mSAv*) within a region of interest was determined by dividing the number of localizations with the mean number of detections per fluorescence molecule.

Calculation of p-values. For each experimentally acquired or simulated data set, the test statistic $T := H(r) - E(r)$ with $r = 50 \text{ nm}$ was calculated, where $H(r)$ denotes Ripley's H function and $E(r)$ is the pointwise mean of Ripley's H function over a set of $n = 99$ Monte Carlo simulations under the null hypothesis. With t_0 we denote the value of the statistic for the data set which is to be analyzed; t_i for $i = 1, \dots, n$ denote the values obtained for the simulations under the null hypothesis. The one-sided p-value was calculated as $p = \text{rank}(t_0, \mathcal{T}) / (n + 1)$, where $\text{rank}(t_0, \mathcal{T})$ denotes the rank of t_0 within the set $\mathcal{T} := \{t_i | i = 0, \dots, n\}$ in descending order. For hypothesis testing, the null hypothesis was rejected if the obtained p-value is smaller than or equal to the specified level of significance $\alpha = 0.05$.

5. 2-CLASTA

This chapter contains content from the following publication:

A. M. Arnold*, **M. C. Schneider***, C. Hüsön, R. Sablatnig, M. Brameshuber, F. Baumgart, G. J. Schütz. *Verifying molecular clusters by 2-color localization microscopy and significance testing*. Scientific Reports, 10, 2020. doi: 10.1038/s41598-020-60

Aim

SMLM localization maps and, in consequence, cluster analysis methods crucially depend on fluorophore blinking behavior. As fluorophore blinking statistics are subject to the local nanoenvironment of the chromophore and the applied imaging protocol, they need to be determined for every experimental condition individually. However, recording of reliable blinking statistics is challenging and time-consuming. Especially in cases of faint clustering, subtle differences in the blinking may lead to different results in the evaluation of clustering. Here, we aimed to develop an approach which is not affected by fluorophore blinking behavior and assesses biomolecular clustering in the framework of statistical significance testing.

Contribution

I first started to work on this project during my Master thesis [148], and further developed and extended work on this project during my time as PhD student. I developed the analytical method for p-value calculation for the null hypothesis of an underlying random distribution of biomolecules. Further, I developed a method which calculates a p-value for multiple experiments, i.e. which accounts for multiple testing. Together with Andreas Arnold, I developed code for simulations of SMLM localization maps. In addition, I developed code for our 2-CLASTA analysis method. Further, together with Christoph Hüsön, I conceived and developed an ImageJ plugin for 2-CLASTA analysis. I performed imaging experiments together with Andreas Arnold and Florian Baumgart. Together with Andreas Arnold and Mario Brameshuber, I analyzed the data.

Outcome

The developed 2-CLASTA method allows for identification of even faint biomolecular clustering completely independent of fluorophore blinking behavior. It is parameter-free and not susceptible to clustering artifacts due to overcounting. The method was extensively characterized via simulations of SMLM localization maps. A proof of concept was performed experimentally via SNAP-concatemers, which exhibit a defined oligomerization degree. The developed ImageJ plugin offers easy applicability of the method. In addition, I developed a method to correctly ascribe a p-value to a set of independent experiments, thereby avoiding the problem of fishing for p-values.

5.1. Introduction

The potential of SMLM to reliably detect molecular nanoclusters is impeded by overcounting artifacts. Multiple detections of the same biomolecule are caused by the presence of multiple dye molecules per molecule of interest, as well as stochastic blinking of dye molecules. Previous attempts to account for overcounting artifacts all pose assumptions on at least some characteristics of the blinking statistics of fluorophores [3–7]. These methods either require the choice of user-defined parameters [3, 5–7], which should be chosen in correspondence with fluorophore blinking, or incorporate a direct recording of fluorophore blinking statistics [4]. Without any knowledge of fluorophore blinking behavior, previous approaches may yield misleading results concerning true biomolecular clustering. Of note, fluorophore blinking statistics are also affected by the dye’s nanoenvironment and illumination protocols [8, 62, 63]. Hence, for reliable results, blinking statistics need to be recorded for each experimental condition separately. Taken together, a parameter-free method independent of any assumptions on blinking behavior would be of great advantage.

In this chapter, I present a method termed 2-Color Localization microscopy And Significance Testing Approach (2-CLASTA). The aim of the method is to determine the underlying distribution of biomolecules of interest rather than the mere observed localizations: It allows to assess whether biomolecules of interest show any significant difference from a completely random distribution. The major advantage of 2-CLASTA is its complete independence of any assumptions on fluorophore blinking behavior; especially, it does not require the recording of blinking statistics. Moreover, it can readily be applied to a single two-color localization map without the need of any additional experiments. In this approach, the same molecule of interest is targeted with two fluorescent labels of different color, which are imaged in two separate color channels. Nearest neighbor distances across the two channels are calculated and compared to nearest neighbor distances distributions for randomized data sets, which are calculated directly from the recorded data without the need for further experiments. The method was extensively validated via simulations. Additionally, experiments in cells expressing artificially clustered proteins showed that molecular nanoclustering down to only two molecules per cluster could be reliably detected.

5.2. Results

5.2.1. Testing the null hypothesis of a random biomolecular distribution

For 2-CLASTA, the biomolecules of interest are labeled competitively with fluorescent labels of two different colors. Importantly, a single biomolecule of interest must be labeled with one type of fluorophore only. Of note, a one-to-one label stoichiometry is not required for the method; a single biomolecule may carry multiple dyes as long as they are of the same type. In particular, this allows for the use of fluorescently labeled antibodies. The different fluorophore types can either be imaged alternately, or simultaneously on two separate regions of the camera chip. We assume in the following that fluorophores are imaged alternately in two separate color channels, a blue and a red one, respectively. Thereby, a two-color SMLM localization map is

obtained.

Fig. 5.1a depicts simulated localization maps of an underlying random (top) and clustered (bottom) biomolecular distribution. In both cases, localizations show clear clustering due to multiple observations of dyes belonging to the same biomolecule. As a crucial feature, all localizations belonging to a single biomolecule are of one color only, as the biomolecule carries only fluorophores of one type. When comparing the two-color localization maps arising from the underlying random and clustered biomolecular distribution, one can identify a characteristic difference between them: For an underlying random distribution of biomolecules, the two point patterns of all red and all blue localizations are independent of each other. For a clustered distribution, in contrast, the biomolecules are close to each other. Hence, localization clusters of different colors overlap and the two point patterns become correlated. This offers a basis for discriminating the two cases: The correlation between the two point patterns needs to be investigated, while the univariate clustering of localization in each color channels arising from overcounting artifacts should be neglected. As a quantitative measure of the correlation between the two point patterns, we used the cross-nearest neighbor distance r , which is the distance from all localizations in one color channel to their nearest neighbor in the other color channel. From all obtained distances r , we calculated their empirical cumulative distribution function (CDF), denoted as $\text{cdf}(r)$ in the following. Of note, it is difficult to derive the form of the CDF of cross-nearest neighbor distances theoretically. The CDF not only depends on the underlying distribution of biomolecules, but also on the number of dyes conjugated to a single biomolecule, as well as fluorophore blinking statistics. As these parameters are unknown or difficult to obtain, the exact form of the CDF is difficult to be derived. Consequently, it is also virtually impossible to conclude on the underlying distribution of biomolecules based only on the empirical CDF obtained from the recorded localization map.

In order to determine whether a recorded localization map arises from a random or clustered distribution, we compared the obtained CDF of cross-nearest neighbor distances with CDFs obtained for randomized data sets, for which the correlation between the two color channels was broken via toroidal shifts [150]. The principle of a toroidal shift is illustrated in Fig. 5.2. The randomized data was constructed directly from the original data. For this, all localizations of one color channel were shifted by a vector \vec{v} , considering periodic boundary conditions (Fig. 5.1b). Applying this toroidal shift to the localizations of one color channel breaks potential correlations between localizations of the two color channels while conserving the univariate characteristics of the individual point patterns, i.e. the patterns of the red and blue localizations, respectively. Notably, the obtained randomized data sets do not necessarily represent a complete randomization of underlying biomolecules. In case of true biomolecular clustering, biomolecules belonging to the same cluster and being labeled with the same fluorophore type will not be separated in the randomized data sets.

We calculated a set of $n = 99$ randomized data sets. For each data set, the shift vector \vec{v} was chosen randomly within the region of interest. As the randomized data sets are directly calculated from the experimental data of a single recorded localization map, the method requires neither additional experiments nor any prior information or assumptions on fluorophore blinking behavior.

For all obtained randomized data sets we calculated the CDFs of cross-nearest neighbor dis-

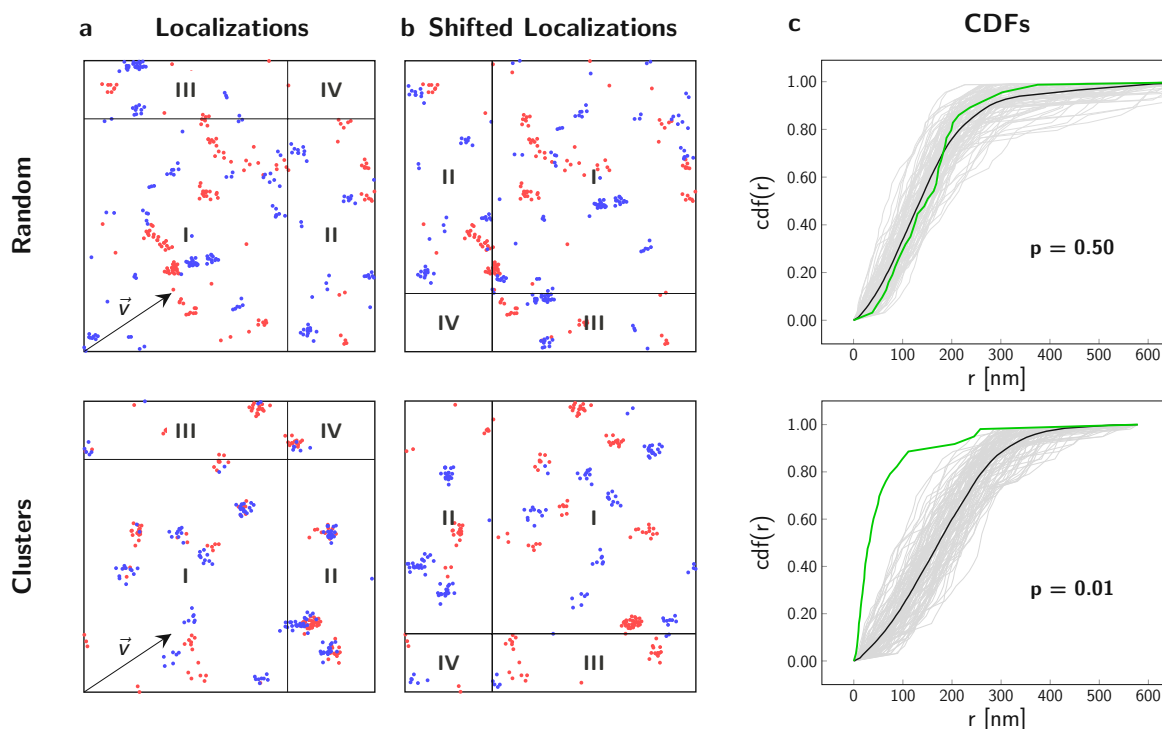


Figure 5.1.: Analysis of localization maps with 2-CLASTA. (a) Simulated two-color localization maps for a random (top) and a clustered (bottom) distribution of biomolecules. Images show a $2 \times 2 \mu\text{m}^2$ region. For the simulation of blinking we used experimental data obtained for SNAP-AF488 (blue channel) and SNAP-AF647 (red channel). (b) Shifting all localizations of the blue color channel by the shift vector \vec{v} breaks correlations between the two color channels. The principle of the toroidal shift is illustrated in Fig. 5.2. (c) The cumulative distribution function of nearest neighbor distances, r , between the two color channels is plotted in green for the localization data shown in panel a. The functions $\text{cdf}_{\text{rand}}(r)$ of $n = 99$ control curves, generated with randomly chosen toroidal shifts, are depicted in light gray. The mean of all control curves is shown in black. From the rank of the curves, we calculated a p-value $p = 0.50$ for the random case, and $p = 0.01$ for the clustered case. Figure adapted from [149].

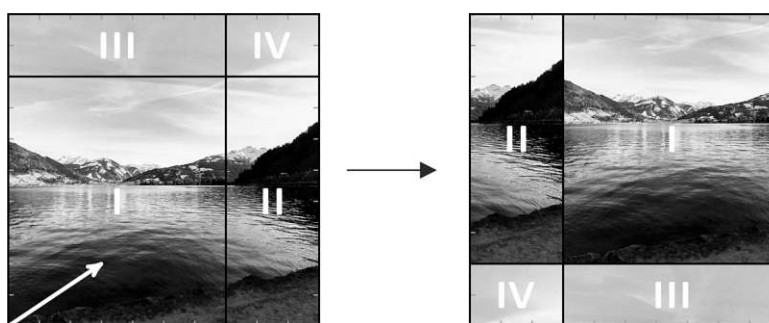


Figure 5.2.: Principle of a toroidal shift. The whole image is shifted by a vector (white arrow). Consequently, the areas indicated by II–IV lie outside the region of interest. Reassembling the image according to a toroidal geometry results in the image depicted on the right side.

tances, yielding a set of n CDFs, denoted as $\text{cdf}_{\text{rand},i}(r)$ for $i = 1, \dots, n$. These CDFs implicitly account for the correct blinking statistics and stoichiometry of labeling. Hence, they serve as a randomized control for uncorrelated two-color localization maps, irrespective of any univariate clustering, which arises from overcounting and is present in the individual color channels.

In case of a completely random distribution of biomolecules, the CDFs obtained for the original data set and the randomized controls are equal, except for variations due to sampling noise (Fig. 5.1c, top). For non-random distributions of biomolecules, however, the CDFs for the original and the randomized data differ from each other: Particularly, in case of clustered biomolecules the CDF for the original data will show a tendency towards shorter cross-nearest neighbor distances compared to the randomized controls (Fig. 5.1c, bottom).

Due to noise inherent in the sampling process, the empirical CDFs show variations; the more data points are available for the calculation of the CDFs, the less is the variation. In order to determine whether a CDF obtained from a sample can be expected from an underlying random distribution of biomolecules, we can select a test statistic and calculate a p-value. The p-value assesses whether the result of the test statistic obtained from the sample is more extreme than can be expected from random chance. Here, as a summary statistic T for the data we define the integral

$$t = \int_0^{r_{\max}} \text{cdf}(r) dr. \quad (5.1)$$

The parameter r_{\max} determines the length scale over which clustering is considered. If prior knowledge on cluster sizes is available, the analysis can be restricted to shorter distances by setting r_{\max} according to the expected cluster size and localization precision. Otherwise, r_{\max} is set to the maximum occurring distance in the analysis, in which case the method is completely independent of any user-defined parameters. The influence of setting a threshold for r_{\max} will be discussed later (see Fig. 5.8).

The summary statistic T defined in Eq. (5.1) is calculated for the CDF of the original data, yielding a value t_0 , as well as for all randomized controls, yielding a set of values t_i with $i = 1, \dots, n$. Subsequently, all values of the set $\mathcal{T} := \{t_i \mid i = 0, \dots, n\}$ are sorted in descending order and a rank is assigned to each value according to its position in the ordered sequence: A value t_i has the rank j if it is the j th largest element; consequently, the largest value of the set has rank 1.

Since we want to test the null hypothesis of a random distribution against the alternative hypothesis of nanoclustering, we are interested whether the original data show a tendency towards shorter nearest neighbor distances. Deviations towards larger distances are not considered of importance here. Hence, we calculate a one-sided p-value according to

$$p = \frac{\text{rank}(t_0, \mathcal{T})}{n+1}, \quad (5.2)$$

where $\text{rank}(t_0, \mathcal{T})$ denotes the descending rank of t_0 within the set \mathcal{T} . The approach for determining the p-value is analogous to a p-value based on Monte Carlo simulations (compare section 4.2.2 and [120, 140]). The p-value shows a discrete uniform distribution on $S = \{i/(n+1) \mid i = 1, \dots, n+1\}$ under the null hypothesis of randomly distributed biomolecules (Fig. 5.3).

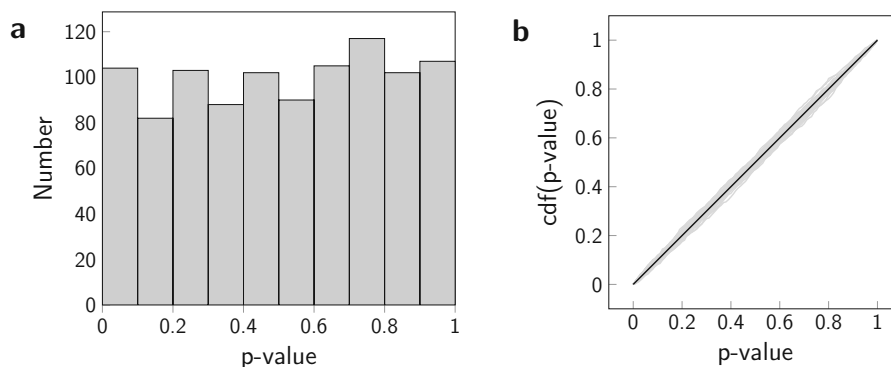


Figure 5.3.: Distribution of the p-value under the null hypothesis. Realizations of the null hypothesis of randomly distributed biomolecules were simulated and tested with 2-CLASTA. We simulated 36 different parameter sets, varying the number of molecules (50; 75; 100 molecules per μm^2), the labeling efficiency (40%, 60%, 80% and 100%) and the labeling ratio (3:7, 2:3, 1:1). All other simulation parameters were held constant. (a) Histogram of the p-values obtained for one exemplary parameter set. (b) Cumulative distribution functions of p-values for various parameter settings are shown in light gray. The ideal uniform distribution is indicated by the solid black line, as comparison. For each parameter set we performed 1000 independent simulations. Figure from [149].

Based on the p-value from Eq. (5.2) and a chosen level of significance α , we can construct a significance test for the null hypothesis of a random distribution of biomolecules against the alternative hypothesis of a clustered biomolecular distribution: The null hypothesis is rejected, if the obtained p-value is smaller than or equal to α , and kept otherwise. This is an exact, one-sided test of size α [140]. The performance of the test can be described by its sensitivity (= true positive rate, TPR) and specificity (= true negative rate, TNR), which are calculated as

$$\text{TPR} = \frac{\text{TP}}{\text{TP} + \text{FN}} \quad \text{and} \quad \text{TNR} = \frac{\text{TN}}{\text{TN} + \text{FP}}, \quad (5.3)$$

where TP denotes the number of true positives (i.e. cases of correctly detected clustering), FN the number of false negatives (i.e. cases of erroneously missed clustering), TN the number of true negatives (i.e. correctly identified random distributions), and FP the number of false positives (i.e. cases of erroneously detected clustering).

The specificity of the test is directly determined by the chosen significance level α , and is calculated as $1 - \alpha$. The significance level itself is equal to the probability of falsely rejecting the null hypothesis, i.e. the erroneous detection of molecular clustering in case of an underlying random distribution of biomolecules. Especially, for low values of α the 2-CLASTA method is hardly susceptible to misinterpretation of overcounting-induced localization clusters as biomolecular nanoclusters. Of note, setting α to a low value will decrease the number of false positives at the cost of the sensitivity. High sensitivity is crucial for the performance of the test and will be extensively assessed in the following sections.

5.2.2. Simulations

We assessed the performance of 2-CLASTA, in particular its sensitivity, via extensive simulations of various clustering scenarios. Two different types of biomolecular clustering were considered: (i) oligomerization into dimers, trimers, or tetramers, (ii) spatially extended clusters of varying size and occupancy.

The spatial distribution of the biomolecules and the corresponding two-color localization maps were generated via Monte Carlo simulations. In particular, positions of biomolecules on a region of $10 \times 10 \mu\text{m}^2$ were simulated according to the specified distribution of biomolecules. Two different types of labels (referred to as red and blue in the following) were assigned randomly and competitively to the simulated biomolecules according to the labeling ratio and overall labeling efficiency. Localizations were simulated using the respective blinking statistics of the labels and normally distributed localization errors. If not specified otherwise, experimentally derived blinking statistics for SNAP-AF488 and SNAP-AF647 were used for the simulations. The details for recording of the blinking statistics are given in the *Methods*, section 5.4.2. The histograms of the resulting number of detections of SNAP-AF488 and SNAP-AF647 are shown in Fig. 5.4.

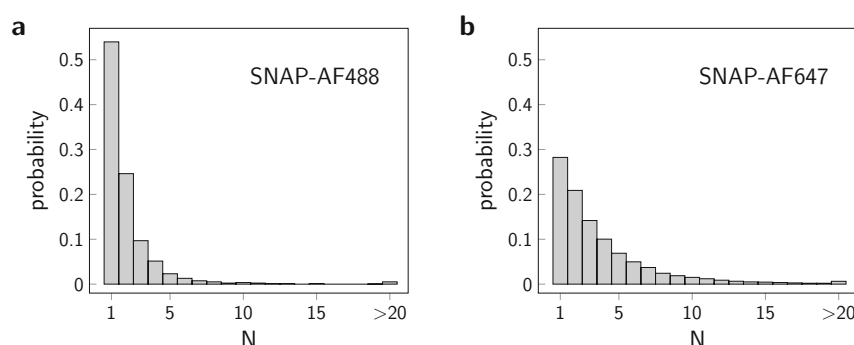


Figure 5.4.: Single molecule blinking statistics for SNAP-labels. Blinking statistics of individual SNAP-AF488 (a) and SNAP-AF647 molecules (b) were recorded on fixed HeLa cells expressing monomeric SNAP-GPI protein construct. Cells were labeled at sufficiently low concentrations of the SNAP-ligand so that well-separated single molecule signals could be observed. Histograms show the probability of a single label to result in N localizations. Figure adapted from [149].

The obtained two-color localization maps were tested for the null hypothesis of an underlying random distribution of biomolecules via the 2-CLASTA method. For generation of the randomized data sets, toroidal shifts were applied to the localizations of the red color channel. For calculation of the CDF of cross-nearest neighbor distances, we calculated the distances from each red localization to the nearest blue localization. If not specified otherwise, the upper limit r_{max} for the calculation of the summary statistic T , Eq. (5.1), was set to the maximum occurring value during the analysis. The level of significance was set to $\alpha = 0.05$. For each parameter set, 1000 simulation runs were performed. For each run, 2-CLASTA yielded a p-value and the respective test decision. The number of correctly detected clustering cases was taken as an estimate for the sensitivity of the method.

In the following, we assessed the performance of 2-CLASTA for both an ideal and a realistic scenario. If not specified otherwise, the parameters for the two scenarios were set as follows: For the *ideal scenario*, we assumed an overall labeling efficiency of 100% (i.e. every molecule was detected at least once), balanced labeling ratio for the two different label types, and the absence of any unspecific signals. In a realistic scenario, however, not every biomolecule of interest carries a detectable label. For this reason we additionally assessed the method performance for a *realistic scenario* with a reduced overall labeling efficiency of 40% (i.e. only 40% of molecules were detected at least once). Further, localizations arising from unspecifically bound labels or background signals may be present in a real-life experiment, which affect the localization maps. Therefore, for the realistic scenario we added 5 unspecifically bound labels per μm^2 per color channel. In addition, we simulated 1 or 2 unspecific background sources per μm^2 in each color channel, respectively. The blinking statistics for the background were determined experimentally in unlabeled cells. Further details of the simulations and all simulation parameters are described in the *Methods*, section 5.4.1.

Sensitivity to detect biomolecular oligomerization

In the following, we investigated the performance of 2-CLASTA in case of biomolecular oligomerization. In particular, we determined its sensitivity for dimers, trimers and tetramers. Notably, dimers consist of two biomolecules only and thus constitute the smallest possible cluster of biomolecules.

In order to obtain statistical significant results, the size of the sample needs to be large enough. Hence, sensitivity depends on the number of observations. Therefore, we assessed the sensitivity of the method as a function of the total number of biomolecules present in the region of interest (Fig. 5.5a). Results are shown both for the ideal (solid line) and realistic (dashed line) scenario. Already low numbers of biomolecules of approximately 1000 molecules per region of interest, corresponding to 10 molecules per μm^2 in the simulations, allowed for sensitive detection of oligomerization. It can be seen that the sensitivity decreased with lower degree of oligomerization. Further, the sensitivity was reduced for the realistic scenario. This is expected, as the method relies on the presence of two different types of labels in close proximity. For dimers, the fraction of oligomers that carries two labels of different type is small, especially in case of low overall labeling efficiency for the realistic scenario. For all following simulations, we fixed the number of molecules to 7500, corresponding to 75 molecules/ μm^2 on a $10 \times 10 \mu\text{m}^2$ region of interest.

As aforementioned, the method relies on the presence of two different types of labels within one biomolecular cluster. The probability for this and thus the method's sensitivity is directly influenced by the overall labeling efficiency (Fig. 5.5b) as well as the labeling ratio of the two different types of labels (Fig. 5.5c). For labeling efficiencies down to around 20%, the method was highly robust. For even lower labeling efficiencies, the sensitivity dropped rapidly. In an experiment, two different types of labels may show different binding affinities for the target molecules, leading to unbalanced labeling. This can be compensated for by adjusting the concentration of the two labels in the experiment. However, also in case of unbalanced label ratios sensitivity remained high (Fig. 5.5c).

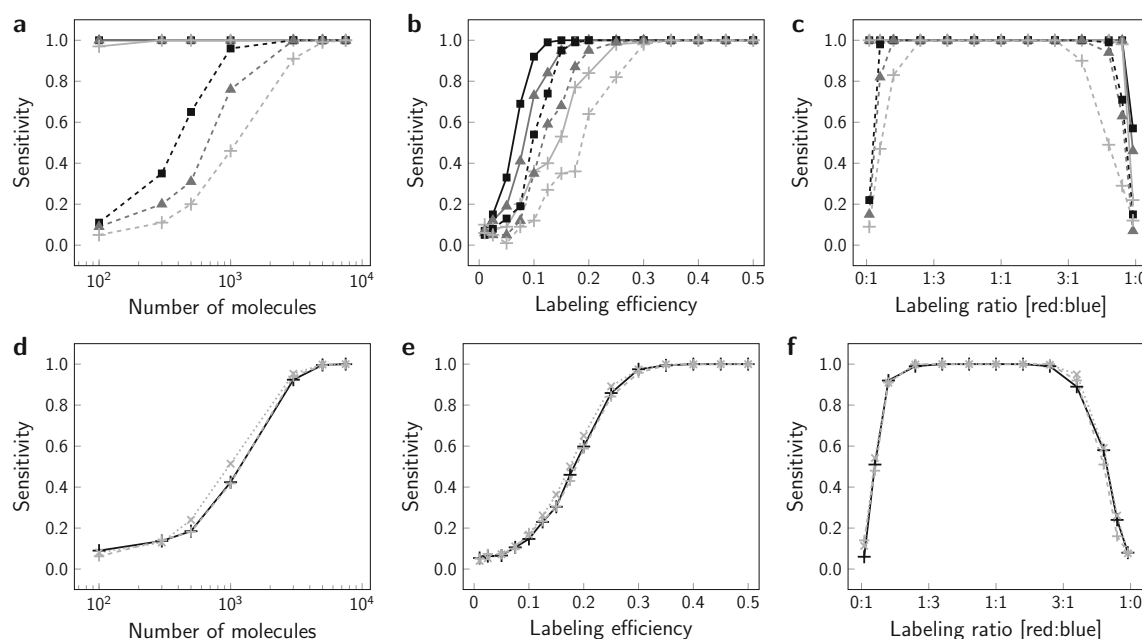


Figure 5.5.: Robustness of 2-CLASTA. To assess the influence of individual parameters we determined the sensitivity as a function of the number of molecules (**a,d**), the labeling efficiency (**b,e**) and the labeling ratio (**c,f**). In panels **a-c** results are shown for simulations of dimers (+), trimers (▲) and tetramers (■), both for the ideal (solid lines) and the realistic scenario (dashed lines). Panels **d-f** show the influence of different fluorescent labels on 2-CLASTA sensitivity for simulations of dimers, assuming the realistic scenario. Included are experimentally derived blinking statistics for SNAP-AF488 and SNAP-AF647 (+, black solid lines), and for KT3-AF647 and PS-CFP2 (+, gray dashed lines), as well as analytical blinking statistics assuming a log-normal distribution of the number of blinks (x, gray dotted lines). Log-normal distributions were simulated with a mean of 2.54 and 25.4 localizations per biomolecule for the red and blue color channel, respectively; standard deviations were adjusted to 2 and 20 localizations, respectively. If not varied in the respective subpanel, parameters in all simulations were set to a molecular density of 75 molecules/ μm^2 , a labeling efficiency of 40% for the realistic case and 100% for the ideal case and a labeling ratio of 1:1. Each data point corresponds to 100 independent simulations. Figure adapted from [149].

Additionally, we assessed the influence of the blinking statistics on the performance of the method (Fig. 5.5d-f). We performed simulations of the realistic scenario with the following pairs of blinking statistic for the two different label types (assumed blue and red color channel, respectively): SNAP-AF499 and SNAP-AF647; photoactivatable protein PS-CFP2 and KT3 antibody conjugated with multiple AF647 fluorophores (KT3-AF647) [118]. These blinking statistics were obtained from experiments performed at low labeling concentrations in cells. Therefore, they accurately reflect the variability in the blinking present in experimental conditions. We also simulated a scenario using artificial blinking statistics with a log-normally distributed number of detections for each label. Here, we assumed a rather extreme difference in the blinking behavior of the two labels with a ten-fold difference in the mean number of detections per biomolecule. As expected, the resulting sensitivity curves for all different blinking scenarios were virtually identical, because the 2-CLASTA method is independent of the

blinking statistics.

Furthermore, we were interested in the influence of experimental errors on the sensitivity of our method. First, we studied the influence of unspecifically bound labels, which were randomly distributed over the region of interest (Fig. 5.6a). As these labels were randomly distributed, localizations arising from them were not correlated in the two color channels. Hence, a slight decrease of sensitivity could be expected. Still, even high numbers of unspecific labels yielded only minor influence on the sensitivity.

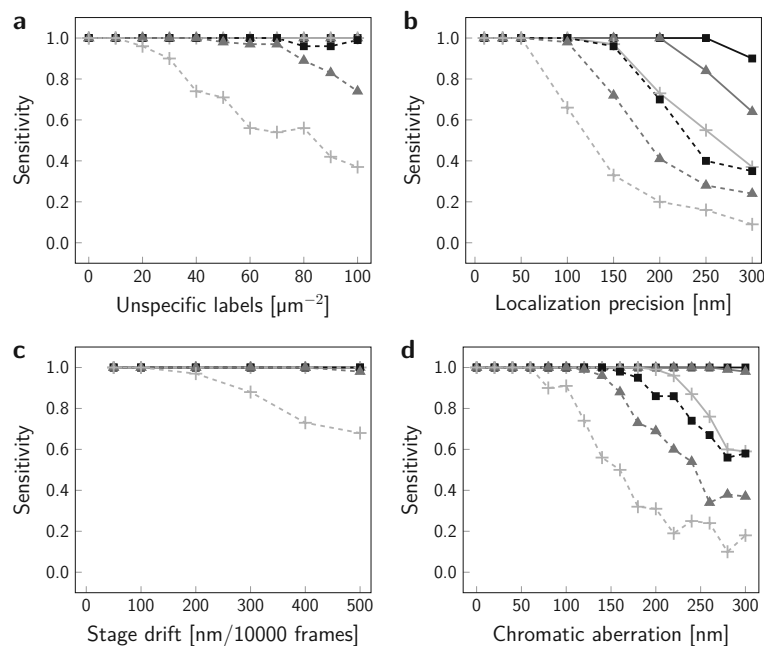


Figure 5.6.: Influence of experimental errors on the sensitivity. The sensitivity of 2-CLASTA was determined as a function of unspecifically bound labels (a), localization precision (b), stage drift (c) and lateral chromatic aberration (d). For chromatic aberration, the values on the x-axis denote the mean displacement over the whole region of interest. We simulated dimers (+), trimers (▲) and tetramers (■), both for the ideal (solid lines) and the realistic scenario (dashed lines). Each data point corresponds to 100 independent simulations. For panel c, virtually all simulated scenarios yielded a sensitivity of 1. Figure adapted from [149].

Second, we investigated the influence of localization precision (Fig. 5.6b). Due to localization errors, the localization of a molecule is displaced from its true position. Consequently, molecules which belong to the same biomolecular cluster may appear further apart in the localization map. Nevertheless, localizations are spread around the true positions and thus, the correlation between the two color channels is in general not lost in case of sufficient localization precision. Only in case of very large localization errors exceeding the distance between different clusters, we could observe that the correlation was broken and the sensitivity decreased. Typically, a localization precision below 30 nm can be achieved for SMLM experiments. In this length range, the sensitivity of the method was hardly affected. Of note, the sensitivity drastically decreased only beyond 200 nm, which corresponds to the diffraction limit and thus, is unrealistic for an SMLM experiment.

Similarly, simulated stage drift during image acquisition of a velocity up to 500 nm over 10000 frames barely had an influence on the sensitivity results (Fig. 5.6c). Again, as alternating laser excitation was assumed, correlations between localizations which occurred not only in spatial but also temporal proximity were kept and detected by the method. Note that possible correlations are broken if the two different label types are imaged consecutively, as in Exchange-PAINT, and the results of Fig. 5.6c are not valid in this case. Of note, stage drift can be corrected for using fiducial markers or image cross correlation [99–101, 151].

Next, we assessed the influence of lateral chromatic aberrations (Fig. 5.6d). Likewise, for moderate aberrations the effect on sensitivity was negligible, as correlations between the two color channels were preserved around the optical axis. The simulated vector field of displacements is described in detail in the *Methods*, section 5.4.1. Notably, this type of experimental error is only present if the two labels are distinguished based on different emission spectra. If another property is exploited for the discrimination, chromatic aberrations will not be present. In case of spectrally distinct labels, lateral chromatic aberrations may also be corrected for based on recordings of multi-spectral beads.

Eventually, we investigated how the choice of the summary statistic influenced the test results. For this, we first evaluated simulations of dimers using the k -nearest neighbor statistics for $k = 1, 3, 5, 10$, and the L_{cross} statistics [152]. In case of the k -nearest neighbor statistics, the CDF of the mean distance of the k cross-nearest neighbors was taken in Eq. (5.1). In case of the L_{cross} statistics, the CDFs of $L = L_{\text{cross}}(r^*)$ with a radius $r^* = 50$ nm were generated. The integral of the CDF in Eq. (5.1) was then taken over L . Since high values of L_{cross} indicate clustering, the rank in Eq. (5.2) was determined in ascending order. Notably, L_{cross} requires the setting of the radius r^* and thus, is not parameter-free. Importantly, using other summary statistics than the cross-nearest neighbor distance did not improve the sensitivity of the test, as can be seen in Fig. 5.7.

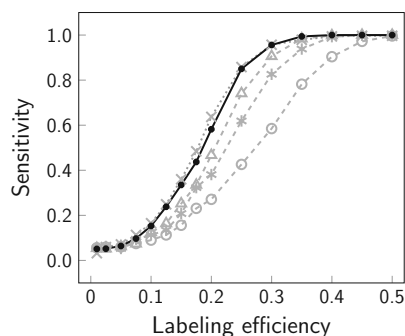


Figure 5.7.: Influence of different summary statistics on 2-CLASTA sensitivity. Dimers were simulated under the realistic scenario with varying labeling efficiency and analyzed with 2-CLASTA based on the distances to 1 (●), 3 (△), 5 (*) or 10 cross-nearest neighbors (○), as well as values of L_{cross} at a radius of 50 nm (×) as a summary statistic. Each data point corresponds to 1000 independent simulations. Figure from [149].

Further, the summary statistics is influenced by the choice of r_{max} in Eq. (5.1). Without prior knowledge on the length range of clustering, r_{max} can be set to the maximum occurring value during the analysis. In this case, the 2-CLASTA method is completely parameter-free. If

prior knowledge is available, r_{\max} may be set in accordance with the assumed cluster size and localization precision. However, restricting the analysis to shorter distances had only minor effects on sensitivity (Fig. 5.8). Effects were most pronounced for simulations of dimers, but negligible for extended clusters.

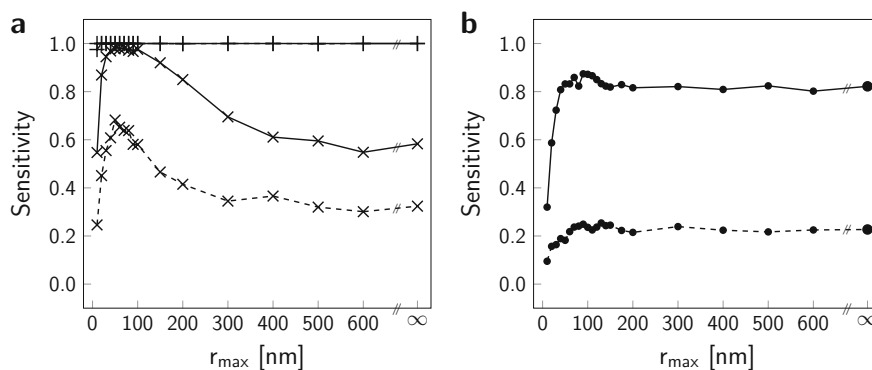


Figure 5.8.: Influence of r_{\max} on 2-CLASTA sensitivity. (a) Influence of the analysis parameter r_{\max} on 2-CLASTA sensitivity for the detection of biomolecular dimers, both for the ideal (solid line, +) and realistic scenario (dashed line, +). Note that virtually all simulated scenarios yielded a sensitivity of 1. Hence, we also included simulations for cases with reduced labeling efficiency of only 15%, while keeping all other parameters as before (x). (b) Influence of the analysis parameter r_{\max} on 2-CLASTA sensitivity for the detection of circular nanodomains of 100 nm radius, 3 clusters per μm^2 and 20% of molecules inside the nanodomains, both for the ideal (solid line, ●) and the realistic scenario (dashed line, ●). The symbol ∞ denotes the maximum cross-nearest neighbor distance occurring in the analysis. Each data point corresponds to 1000 independent simulations. Figure from [149].

Sensitivity to detect areas of enrichment or depletion of biomolecules

As a second type of biomolecular clustering we studied spatially extended clusters. For this, we simulated circular domains, the centers of which were randomly distributed over the region of interest. We varied the radius of domains from 20 nm to 150 nm, and the number of domains from 3 to 20 domains per μm^2 . The fraction of molecules inside the domains was varied between 20% and 100%, leading to different densities of molecules inside and outside the domains, while the average density across the whole image was kept constant at 75 molecules per μm^2 . In case of overlapping domains, the density in the intersection area was adjusted to the density of a single domain. Depending on the respective densities in and outside of the domains, domains represented either areas of enrichment or depletion. Of note, depletion inside the domains corresponded to clustering outside the domains. Examples of domains, respective distributions of biomolecules and corresponding localization maps are depicted in Fig. 5.9.

We performed simulations of spatially extended clusters both for the ideal and realistic scenario and determined the sensitivity for each parameter set (Fig. 5.10). Each table shows the results for a specific domain size. The top right corner of each table corresponds to scenarios in which molecules are enriched within the domains, the bottom left corner corresponds to scenarios in which molecules are enriched outside of the domains. The gray-scale indicates the sensitivity for a particular parameter set. All scenarios showing substantial relative enrichment of molecules

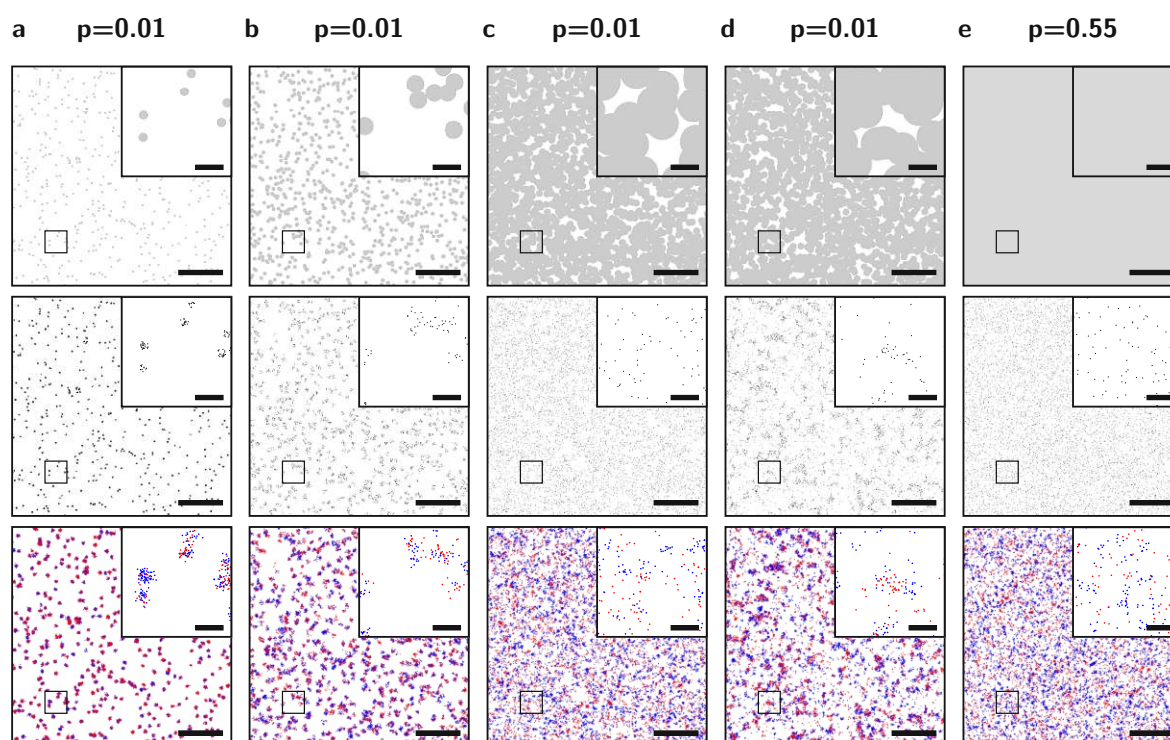


Figure 5.9.: Examples of simulated nanodomains. The underlying simulated nanodomains (top row), the positions of simulated biomolecules (middle row), and the resulting localization maps (bottom row) under the ideal scenario are shown for rare small clusters (**a**), medium clusters (**b**), frequent large clusters (**c**), exclusion areas (**d**), and a random distribution of biomolecules (**e**). The resulting p-value for each scenario is indicated on top. Scale bars 250 nm (inset) and 2 μ m. Figure adapted from [149].

either inside or outside the domains could reliably be detected. The realistic scenario yielded similar results as the ideal scenario, with a slightly reduced sensitivity. Notably, the 2-CLASTA method was more sensitive than the previously published approach from our group based on label titration, as can be seen by comparing Fig. 5.10 with Supplementary Figure 5 and 6 from [118].

Importantly, some parameter combinations yielded a relative enrichment of molecules inside the nanodomains of around 1, corresponding to a random distribution of molecules over the whole image. Rejecting the null hypothesis in this case would lead to false positive results. Consistently, for such scenarios we indeed observed sensitivity values close to the chosen level of significance of 0.05.

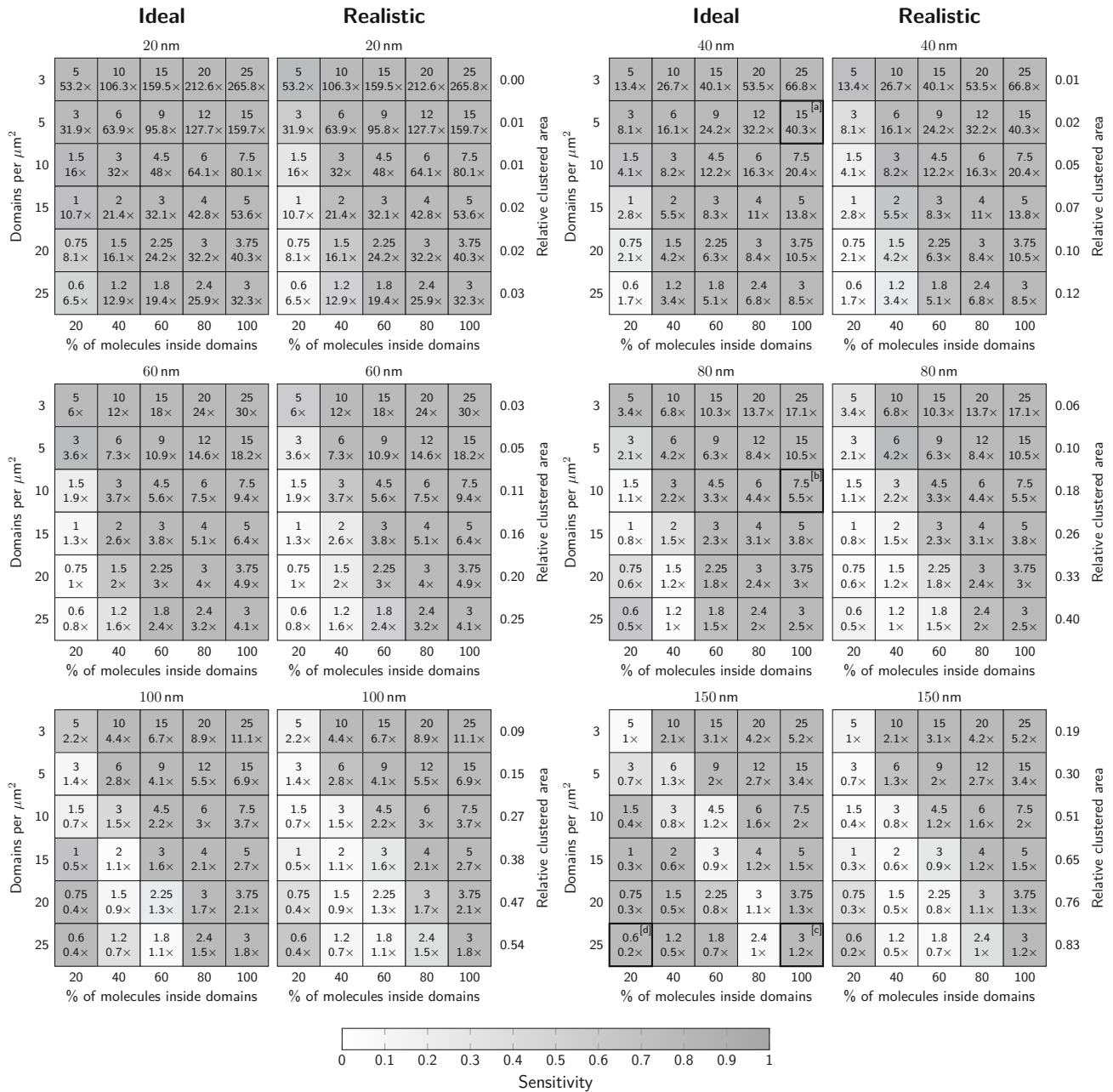


Figure 5.10.: Sensitivity of 2-CLASTA to detect spatially extended clusters. We determined the sensitivity of 2-CLASTA for varying densities of circular domains and percentage of molecules inside the domains. Simulations were performed for circular nanodomains with radii of 20, 40, 60, 80, 100 and 150 nm for both the ideal and realistic scenario. The number of domains per μm^2 was varied between 3 and 25, and the percentage of molecules inside the domains between 20% and 100%. The numbers in individual fields indicate the average number of molecules per domain, and the relative enrichment or depletion of molecules compared to a random distribution with identical average density. The gray scale indicates the fraction of scenarios with a p-value below the significance level $\alpha = 0.05$, reflecting the sensitivity. Each field corresponds to 100 independent simulations. The bold black boxes indicate the scenarios depicted in Fig. 5.9, letters indicate the respective subpanels. Figure adapted from [149].

In addition, we repeated the simulations for domains of 100 nm radius with the blinking statistics of PS-CFP2 and KT3-AF647 [118]. As was the case for oligomerization, also for spatially extended clusters the blinking statistics did not have any impact on the sensitivity results (Fig. 5.11).

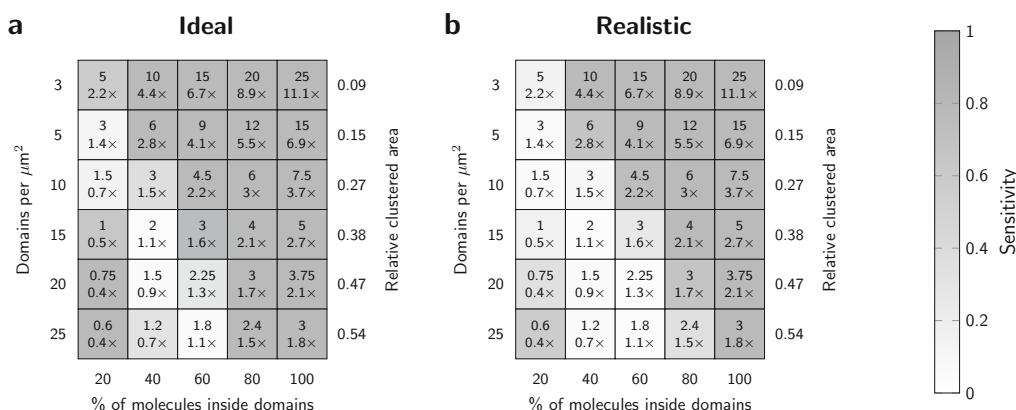


Figure 5.11.: Sensitivity results for different fluorescent labels. We determined the sensitivity of 2-CLASTA for varying densities of circular domains and percentage of molecules inside the domains, assuming the blinking statistics of PS-CFP2 and KT3-AF647. Data are shown for a cluster radius of 100 nm for the ideal (a) and the realistic scenario (b). The numbers in individual fields indicate the average number of molecules per domain, and the relative enrichment or depletion of molecules compared to a random distribution with identical average density. The gray scale indicates the fraction of scenarios with a p-value below the significance level $\alpha = 0.05$, reflecting the sensitivity. Each field corresponds to 100 independent simulations. Figure from [149].

Moreover, we assessed whether localization errors had any influence on the results for spatially extended clusters (Fig. 5.12). For this, we simulated circular domains of 60 nm radius with a localization precision of 30 and 70 nm, respectively. We could observe a slight decrease in sensitivity for high localization errors. However, a localization precision well above 30 nm is unrealistic for SMLM experiments. Localization errors for a precision below 30 nm showed only negligible influence on the sensitivity of the method.

Finally, we investigated the influence of the shape of the nanodomains on the sensitivity of 2-CLASTA. For this, we simulated clusters with a rectangular shape of $80 \times 400 \text{ nm}^2$ (Fig. 5.13). As the method does not require any assumptions about the shape of clusters, results should be independent of the cluster shape. Indeed, results agreed very well with those obtained for circular clusters of 100 nm radius, which show an approximately identical cluster area.

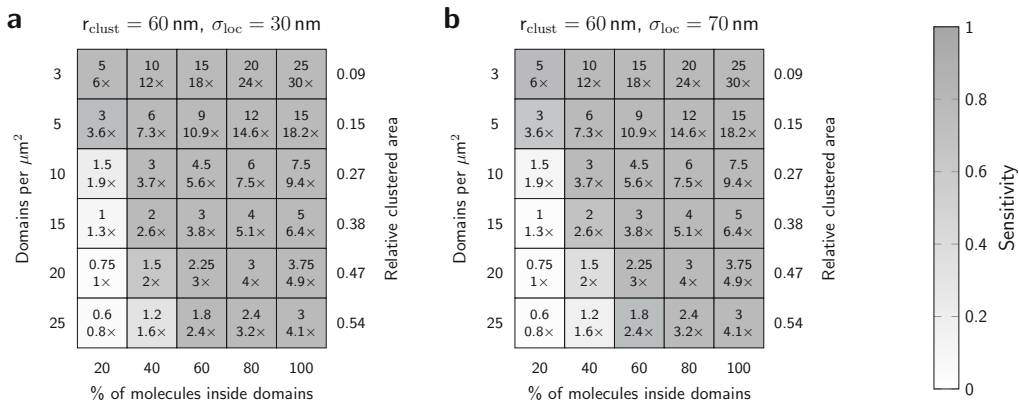


Figure 5.12.: Influence of localization precision on the sensitivity of 2-CLASTA for spatially extended clusters. We determined the sensitivity of 2-CLASTA for varying densities of circular domains and percentage of molecules inside the domains, assuming a localization precision of 30 nm (a) and 70 nm (b). Data are shown for a cluster radius of 60 nm for the ideal scenario. The numbers in individual fields indicate the average number of molecules per domain, and the relative enrichment or depletion of molecules compared to a random distribution with identical average density. The gray scale indicates the fraction of scenarios with a p-value below the significance level $\alpha = 0.05$, reflecting the sensitivity. Each field corresponds to 100 independent simulations. Figure adapted from [149].

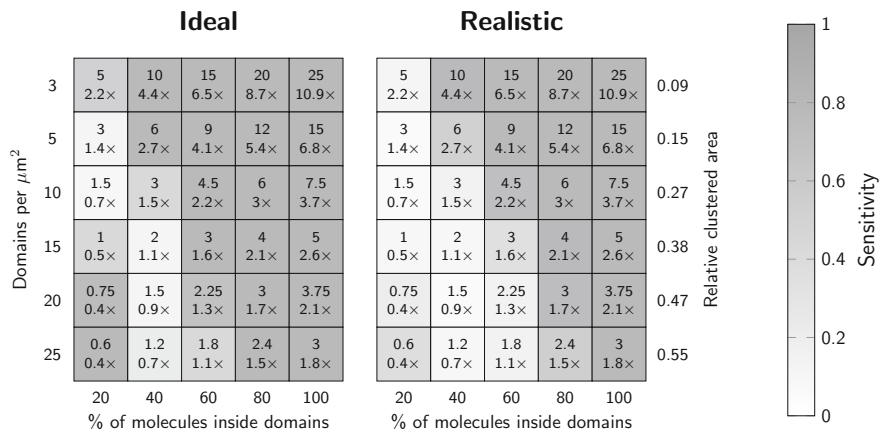


Figure 5.13.: Influence of cluster shape on the sensitivity of 2-CLASTA. The sensitivity for the detection of rectangular clusters with a size of $80 \times 400 \text{ nm}^2$ is shown both for the ideal and realistic scenario. The numbers in individual fields indicate the average number of molecules per domain, and the relative enrichment or depletion of molecules compared to a random distribution with identical average density. The gray scale indicates the fraction of scenarios with a p-value below the significance level $\alpha = 0.05$, reflecting the sensitivity. Each field corresponds to 100 independent simulations. Figure adapted from [149].

5.2.3. Experimental validation

In order to validate the 2-CLASTA method experimentally, we engineered protein constructs mimicking either monomers or oligomers. For this, we concatenated one to four SNAP-tag proteins, representing monomers (1-SNAP), dimers (2-SNAP), trimers (3-SNAP) and tetramers (4-SNAP), respectively. The protein constructs were expressed in HeLa cells and anchored in the cell membrane via a glycosyl-phosphatidylinositol (GPI) anchor. Of note, GPI-anchored proteins are assumed to be distributed randomly within the cell membrane, and oligomerization of the GPI-anchor itself is not expected [4]. Hence, the 1-SNAP construct yielded randomly distributed proteins in the plasma cell membrane.

The SNAP-tag proteins were labeled competitively with SNAP-Surface Alexa Fluor 488 (SNAP-AF488) and SNAP-Surface Alexa Fluor 647 (SNAP-AF647). The concentrations of the dyes were adjusted in order to yield a balanced labeling ratio of the two colors. We performed dSTORM experiments with alternating excitation at 640 nm and 488 nm, and split the signals from the two labels into two separate color channels, yielding two-color localization maps (Fig. 5.14a).

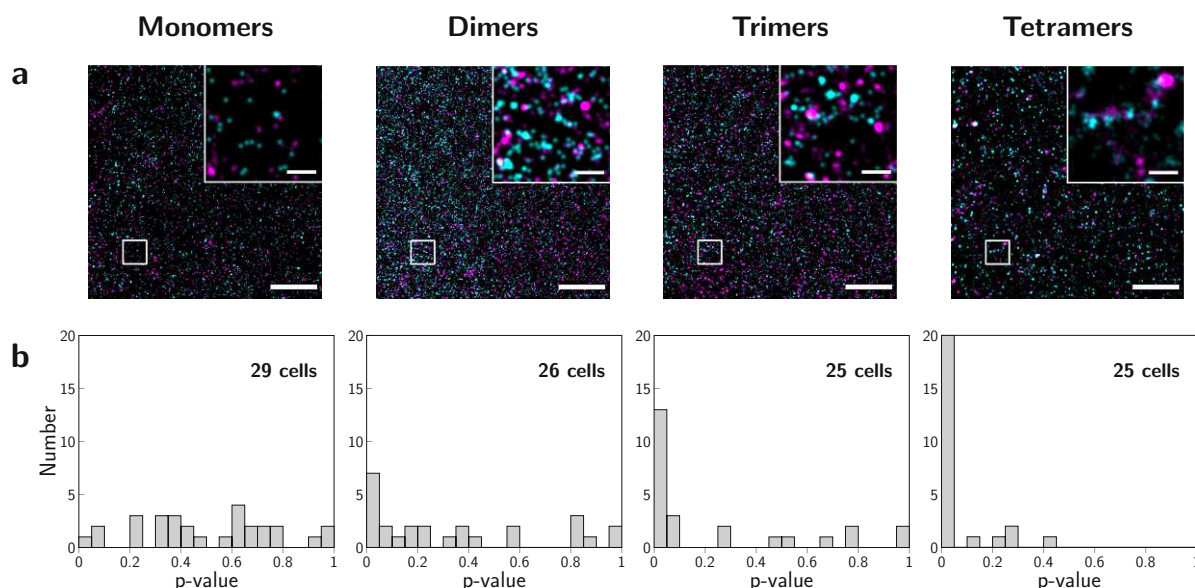


Figure 5.14.: 2-CLASTA analysis of experimental data. We analyzed GPI-anchored concatemers of SNAP-tags with one to four subunits expressed in HeLa cells, mimicking monomers, dimers, trimers and tetramers. For dSTORM experiments, cells were labeled with SNAP-AF488 and SNAP-AF647. Panels (a) show two-color localization maps for representative cells, and panels (b) histograms of p-values obtained from at least four independent experiments per SNAP construct. Scale bars: 250 nm (inset) and 2 μ m. Figure adapted from [149].

For each SNAP-construct we imaged at least 25 cells and analyzed each two-color localization map with the 2-CLASTA method. For each cell, we thus obtained a p-value for the null hypothesis of an underlying random distribution of proteins. A histogram of the resulting p-values for each SNAP-construct is shown in Fig. 5.14b. For the 1-SNAP construct, p-values are uniformly distributed between 0 and 1, thereby showing no indication for clustering of proteins.

For the oligomeric SNAP constructs, in contrast, the distribution of p-values exhibits a peak at low p-values below 0.05, as is expected for an underlying clustered distribution of proteins. The peak is less pronounced for dimers, but increases for trimers and tetramers, according to the higher sensitivity of the method to detect higher degrees of oligomerization. Also for oligomeric constructs, some cells yielded p-values above 0.05, the chosen level of significance. Hence, these were false negative cases. The sensitivity may have been reduced in these cases by low labeling efficiency of the SNAP-tag [69, 109], unspecifically bound labels or autofluorescence from the cell. In addition, protein expression levels and the size of the analyzed region of interest vary from cell to cell. Thus, also the number of proteins within the region of interest varies. If only 1000 or less proteins are present, the sensitivity of the method is decreased, as was shown in Fig. 5.5a. This relationship was also discernible for the experimental data (Fig. 5.15). Overall, the 2-CLASTA method could reliably detect true molecular clustering in experiments for even low degrees of oligomerization, while avoiding the misinterpretation of overcounting artifacts as biomolecular clustering.

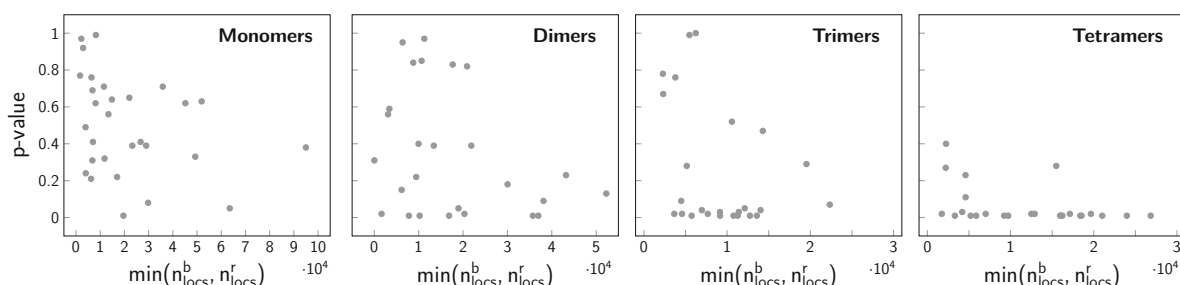


Figure 5.15.: Obtained p-value versus number of analyzed localizations. For each analyzed region of interest (data from Fig. 5.14), the obtained p-value is plotted versus the minimum of the number of localizations $n_{\text{locs}}^b, n_{\text{locs}}^r$ recorded in the blue and red color channel, respectively. Results for monomers, dimers, trimers, and tetramers are shown from left to right. Figure adapted from [149].

5.2.4. Multiple experiments

In practice, a single experiment often is repeated. This is reasonable, for example, if a single cell provides a small region of interest only. In this case, the included number of molecules may be too low for a detection of clustering with high sensitivity. In addition, an assessment based on a single experiment might not be robust, as the particular experimental conditions for this experiment (e.g. the labeling efficiency) might decrease the sensitivity. If the same experiment is performed multiple times, a different p-value will be obtained for each individual experiment. In order to assess the overall outcome of all experiments in a joint statistical analysis, one straightforward option seems to be taking the minimum of all observed p-values as overall p-value and reject the null hypothesis if this minimum p-value is significant. However, this procedure is not valid as it drastically increases the type I error rate, i.e. the false positive rate. This can be seen as follows: If only one test is performed, the false positive rate equals the chosen level of significance α . Under the null hypothesis, the probability of observing no significant p-value for one test is $1 - \alpha$. For m independent experiments, the probability that none of the p-values is significant can be calculated as $(1 - \alpha)^m$. In turn, the probability

that at least one of the m p-values is significant is given by $1 - (1 - \alpha)^m$. For example, if $m = 100$ independent tests are performed with a significance level of $\alpha = 0.05$, the expected number of significant p-values is 5, and the probability to obtain at least one significant p-value is $1 - (1 - 0.05)^{100} = 0.994$. Hence, the false positive rate increases drastically with the number of experiments m . This is also evident from the probability distribution of the minimum p-value. In case of a continuous p-value, the distribution of the minimum of m uniformly distributed values $p_{\min} = \min(p_1, \dots, p_m)$ is not uniform but follows the probability density function

$$f(p_{\min}) = m \cdot (1 - p_{\min})^{m-1}. \quad (5.4)$$

In order to obtain a valid p-value, we need to adjust the overall p-value for multiple experiments for the number m of performed tests. This can be achieved by the following transformation function [153]:

$$p_{\text{corr}} = 1 - (1 - p_{\min})^m, \quad (5.5)$$

yielding a uniform distribution of p_{corr} on the interval $[0, 1]$.

In case of a p-value estimated from Monte Carlo simulations, the p-value is not continuously distributed, but can only take on discrete values $i/(n+1)$ for $i = 1, \dots, n+1$, where n is the number of simulated controls. Hence, p_{\min} is bounded by $1/(n+1)$, and p_{corr} is bounded by $1 - (1 - \frac{1}{n+1})^m = 1 - (\frac{n}{n+1})^m$. However,

$$1 - \left(\frac{n}{n+1}\right)^m \rightarrow 1 \quad \text{for } m \rightarrow \infty, \quad (5.6)$$

which means that for a large number of experiments m the null hypothesis would never be rejected. Therefore, in case of discrete p-values a different method for adjusting the p-value for multiple experiments is required, which will be presented in the following.

Method for discrete p-values

In case of discrete p-values, the p-value for a single experiment under the null hypothesis shows a discrete uniform distribution, i.e.

$$\mathbb{P}\left(P = \frac{i}{n+1}\right) = \frac{1}{n+1} \quad \text{for } i = 1, \dots, n+1, \quad (5.7)$$

where n is the number of simulated controls. In order to combine the p-values obtained from multiple experiments, we can determine whether the number of observed p-values falling below a certain threshold p_0 can be expected from a discrete uniform distribution or not. Of note, p_0 needs to be selected from the set $\{i/(n+1) \mid i = 1, \dots, n+1\}$. Under the null hypothesis, the probability for obtaining a p-value with $p \leq p_0$ for a single experiment is given as $\mathbb{P}(P \leq p_0) = p_0$. Hence, the probability to obtain a p-value below or equal to the threshold p_0 in exactly k out of m experiments can be described by a Binomial distribution $B(k \mid p_0, m)$. In contrast, in case of true molecular clustering the histogram of p-values obtained from multiple experiments will show a peak at low p-values. Thus, the number of p-values below the threshold p_0 will be higher than expected under the null hypothesis.

In general, the obtained number k of p-values below the threshold p_0 can be described by a Binomial distribution with $B(k | q, m)$, where $q \in [0, 1]$, describes the probability for a single experiment. In case of the null hypothesis of a random biomolecular distribution it holds that $q = p_0$; in case of biomolecular clustering a peak at small p-values is expected, and hence, $q > p_0$. Therefore, we can perform a Binomial test in order to determine whether the p-values obtained from multiple experiments are in correspondence with a uniform distribution and thus, also with the null hypothesis of a random biomolecular distribution. Particularly, we performed a right-sided Binomial test of the null hypothesis $q \leq p_0$ against the alternative hypothesis $q > p_0$, corresponding to a clustered biomolecular distribution. The overall p-value p^* for multiple experiments is calculated as

$$p^* = \mathbb{P}(X \geq k) = \sum_{i=k}^m B(i | p_0, m) = \sum_{i=k}^m \binom{m}{i} p_0^i (1-p_0)^{m-i} = 1 - \sum_{i=1}^{k-1} \binom{m}{i} p_0^i (1-p_0)^{m-i}, \quad (5.8)$$

where k is the number of observed p-values below the chosen threshold p_0 and m the number of performed experiments. If p^* is smaller than the chosen level of significance α^* for the joint analysis of experiments, the null hypothesis was rejected and we assumed that the molecular distribution is clustered.

The increase in sensitivity for the joint analysis of multiple experiments compared to a single experiment is shown in Fig. 5.16a. For this, dimers were simulated under the realistic scenario with varying labeling efficiency. A joint analysis of 20 or 50 simulated experiments yielded a drastic increase of the sensitivity compared to the analysis of a single experiment only. Interestingly, the method is very robust with regard to the chosen threshold p_0 (Fig. 5.16b). As expected, the higher the number of analyzed experiments, the higher is the sensitivity of the method. The proposed joint analysis of multiple experiments was also applied to the results of the SNAP constructs from Fig. 5.14. The calculated overall p-values for multiple experiments are shown in Fig. 5.17. As anticipated, the null hypothesis of a random protein distribution was kept for the monomeric 1-SNAP construct. For all the oligomeric constructs representing dimers, trimers and tetramers, the null hypothesis was rejected and the biomolecular distribution was correctly identified as clustered.

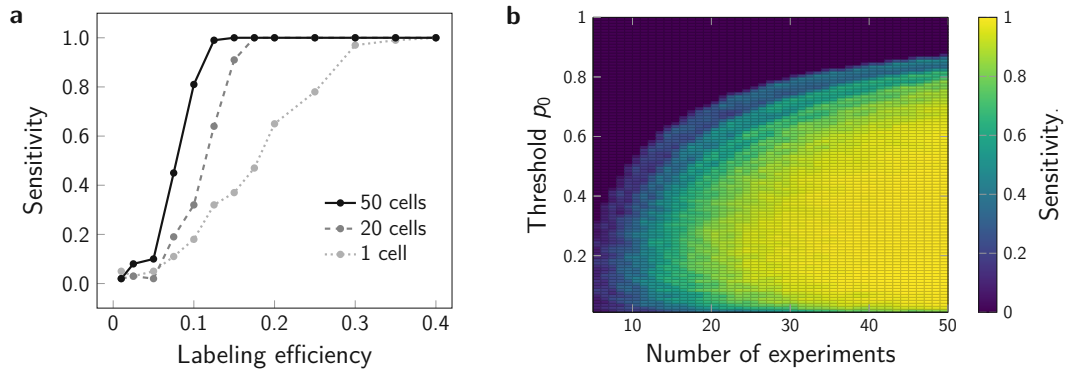


Figure 5.16.: Sensitivity for joint analysis of multiple experiments. Dimers were simulated under the realistic scenario and analyzed with 2-CLASTA. Each data point corresponds to 100 simulation runs. (a) Sensitivity for varying labeling efficiency. The sensitivity for analysis of a single experiment is shown by the dotted line. The sensitivity in case of joint analysis of 20 and 50 cells is shown by the dashed and solid line, respectively; a threshold of $p_0 = 0.05$ was chosen. For calculation of the sensitivity, the level of significance was set to $\alpha^* = 0.05$. (b) Influence of the threshold p_0 and the number of experiments on the sensitivity. Here, the labeling efficiency was set to 15%. The obtained sensitivity is indicated by color; a significance level of $\alpha^* = 0.001$ was chosen for calculating the sensitivity.

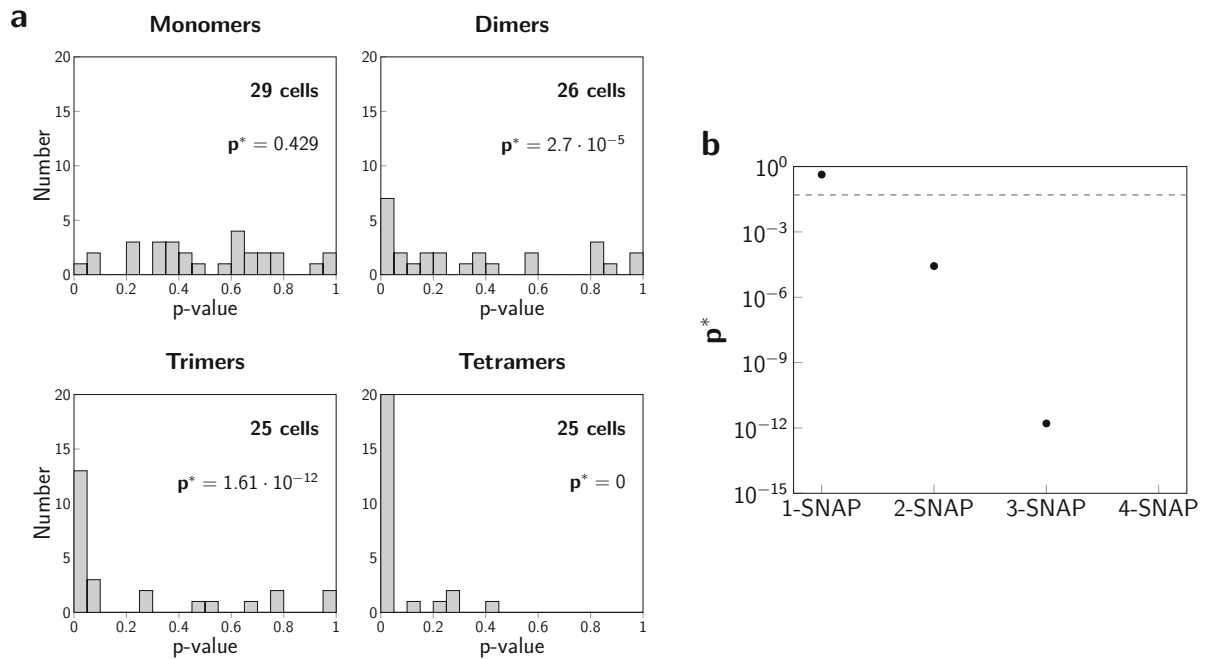


Figure 5.17.: Overall p-value for multiple experiments. (a) Histograms of p-values as shown in Fig. 5.14. For each SNAP construct, the corresponding overall p-value p^* for multiple experiments is indicated. The threshold p_0 was set to 0.05. (b) Logarithmic plot of the values of p^* obtained from panel a. The horizontal dashed line indicates a significance level of $\alpha^* = 0.05$. Note that $p^* = 0$ for the 4-SNAP construct.

5.3. Discussion

The presented 2-CLASTA approach offers a parameter-free method for statistical assessment of molecular clustering based on a single recorded two-color localization map. The method is ideally suited for a global assessment whether true molecular clustering is present at all, before a detailed characterization of clustering is performed via other methods. As a note of caution, clustering methods such as DBSCAN [125] may detect local features arising from purely random variations or overcounting artifacts, thus leading to misleading results if no previous global assessment is performed.

While other methods for a global assessment of clustering exist [4, 6, 63], all previous methods rely on at least some assumption or knowledge about fluorophore blinking statistics. The blinking behavior, however, is dependent on experimental conditions [8, 62, 63] and the recording of reliable blinking statistics is challenging and laborious. Crucially, deviations in fluorophore blinking may impede correct assessment of the clustering behavior of biomolecules, in particular, in cases of faint clustering. Hence, one key advantage of 2-CLASTA is its complete independence of blinking statistics. The method performs well in detecting clustering even in the case of dimers, which represent the smallest possible clusters.

Merging procedures aim at generating an image corrected for overcounting based on averaging of localizations in temporal and spatial proximity [5, 135], which subsequently can be analyzed for clustering by conventional cluster analysis methods. Those merging approaches rely on the assumption that the signal obtained from a single biomolecule is confined to a certain time interval much shorter than the image acquisition time. However, this assumption is not valid in case of PAINT imaging, where fresh probes may consistently bind to the same target over the whole image acquisition time. The same holds true if the same biomolecule of interest is labeled with multiple dyes, as given for example in case of antibody labeling: One of the dyes may be activated right at the beginning of the image acquisition, while another dye belonging to the same label may be activated towards the end only. Further, also in case of PALM or STORM in combination with a one-to-one label stoichiometry, prolonged dark states will impede the accuracy of merging approaches [63]. Hence, merging procedures are not appropriate in these cases. In contrast, 2-CLASTA is completely independent of blinking behavior. Although it does not yield a corrected image, 2-CLASTA accurately assesses biomolecular clustering even in case of PAINT imaging approaches, labeling with multiple dyes per molecule of interest, or in the presence of long-lived dark states.

Additionally, 2-CLASTA is independent of cluster characteristics. It does not require any assumptions on cluster parameters such as cluster size, cluster shape or occupancy, and will correctly identify molecular clustering for any clustering scenario. This is an advantage compared to Bayesian approaches, which require a model of clustering—often, circular clusters with Gaussian-shaped molecular distributions are assumed [128]. Subsequently, different models or model parameters are compared to each other and the model or parameter maximizing the likelihood is selected. However, the best selected model does not necessarily need to give a valid description of clustering if all of the provided models were inappropriate in the first place.

The 2-CLASTA method calculates a p-value for the null hypothesis of an underlying random

biomolecular distribution and thus, provides the basis for a statistical significance test. The performance of the test is described by its specificity and sensitivity. The specificity can be directly set via the chosen level of significance; the sensitivity was extensively investigated via simulations. Overall, the 2-CLASTA method was found to be robust against experimental errors. First, the sensitivity is virtually unaffected by localization errors in the range typically achieved in SMLM. Localization errors only spread the localizations belonging to a single molecule, but preserve the correlation of the two color channels. Similarly, errors in two-color image registration or drift correction have only marginal impact on the performance. As long as the errors are small compared to the cross-correlation distances of the two color channels, the sensitivity of the method is hardly affected. Further, the method is stable with regard to experimental challenges, including non-specific localizations, insufficient degree of labeling or unbalanced labeling ratios of the two different labels. If prior knowledge about cluster size is available, the sensitivity of the test can be further increased by restricting the analysis to certain ranges defined by a chosen value for r_{\max} .

In practice, certain experimental conditions may lead to decreased sensitivity, e.g. low labeling or detection efficiency, a small region of interest with a low number of molecules, or a large number of unspecifically bound labels. Hence, it often is reasonable to repeat an experiment under different, improved experimental conditions. In order to avoid fishing for p-values, it is crucial to account for multiple performed experiments. An approach for this was presented in section 5.2.4. This combined approach increases the resulting sensitivity without inflating the type I error rate.

As a key feature, 2-CLASTA requires the competitive labeling of the biomolecule of interest with two distinguishable labels. For this work, fluorophores were distinguished based on their emission spectra, and imaged alternately in two separate color channels. Notably, the label types may be distinguished based on other fluorophore characteristics (e.g. excitation spectra, fluorescence lifetime), or via complementary docking strands in Exchange-PAINT [106]. Crucially, the two labels need to be well distinguishable. A label of one type must not be detected erroneously as a label of the other type; any overlap between the two channels must be prohibited, including crosstalk between channels or photobleaching of dyes [154]. Otherwise, spurious clustering will be detected. Similarly, a single biomolecule of interest must carry one label type only; otherwise, clustering will be detected also in case of random biomolecular distributions. A one-to-one label stoichiometry is not required for the method; a single biomolecule may carry multiple dyes as long as they are of the same type. 2-CLASTA is compatible with many fluorescence labeling techniques, including protein tags, nanobodies, antibodies, or low affinity binders. The different fluorophore types can either be imaged alternately, or simultaneously on two separate regions of the camera chip. The label types may also be imaged consecutively, as required for Exchange-PAINT. Notably, the choice of the labeling and imaging technique slightly influences the properties of the method. In Fig. 5.6c we showed that moderate stage drift hardly affects the sensitivity of 2-CLASTA as correlations between localizations in spatial and temporal proximity are not broken. However, possible correlations will be broken if the two different label types are imaged consecutively, as required for Exchange-PAINT; in this case, the results of Fig. 5.6c are not valid. Nevertheless, stage drift can be corrected for via fiducial markers or image cross correlation [99–101, 151]. Further, chromatic aberrations as shown in Fig. 5.6d are only present if the two labels are distinguished based on different emis-

sion spectra. If another property is exploited for the discrimination, chromatic aberrations will not be present.

In the presented version of the 2-CLASTA method, the test statistic for quantifying the correlation is based on cross-nearest neighbor distances between localizations of the two color channels. As an alternative, other metrics may be employed (see Fig. 5.7), e.g. metrics based on the first k -nearest neighbors with $k > 1$, Ripley's covariate analysis [152] or pair cross-correlation analysis [6, 155]. However, these statistics may again be confounded by overcounting, as only the first localization of a different color definitely arises from a new molecule. In addition, for faint clustering in combination with little overcounting the sensitivity will decrease if more than the first nearest neighbor is taken into account. This can be understood by means of the following example: For a dimer with a single localization per molecule, only the first nearest localization of different color will be in close vicinity.

A few points have to be considered when applying the 2-CLASTA method: First, the null hypothesis assumes a completely random distribution of biomolecules on the plasma membrane, which is described by a two-dimensional surface parallel to the focal plane. A different topography of the sample may affect the results. If molecules are distributed randomly on an arbitrary two-dimensional manifold, the projection of this distribution onto a two-dimensional plane may lead to virtual clustering. For example, membrane invaginations or elevations of the membrane at the cell borders will lead to accumulation of localizations in the projection of the 2D SMLM localization map [22, 156]. These clusters caused by projection will lead to a rejection of the null hypothesis even if the molecules are distributed randomly on the surface. Consequently, the region of interest for the 2-CLASTA analysis should be selected carefully. An appropriate region is central in the cell, avoiding the cell edges and any apparent vesicular structures. In principle, the region of interest can be further restricted in order to investigate specific subcellular structures (e.g. synapses). However, for small regions the number of imaged molecules is reduced, which in turn reduces the sensitivity of the test. Further, SMLM experiments should be performed in fixed cells, as molecular diffusion during image acquisition will lead to distortions of the localization map and also break potential correlations between the two color channels.

The presented version of 2-CLASTA investigates clustering of one type of biomolecule on a flat 2D plasma membrane. Several extensions of the 2-CLASTA method are feasible: The method can easily be extended to 3D, i.e. biomolecules which are distributed within the cell interior rather than in the plasma membrane. This requires the recording of 3D SMLM data and the incorporation of the z -coordinate in the analysis. For this, the toroidal shift is simply extended to a cuboid and distances are calculated as Euclidean distances in 3D space. Notably, 2-CLASTA can be adapted for other cases of interest. Biomolecular repulsion can be assessed by determining the rank in ascending order instead of descending order. Moreover, not only clustering or repulsion of the same type of molecule, but also co-localization or repulsion between different types of molecules may be investigated. In this case, the two different labels do not target the same molecule type, but each targets a different molecule type.

In conclusion, 2-CLASTA offers a parameter-free and versatile tool for qualitative assessment of spatial biomolecular distributions, while being completely independent of blinking statistics and cluster characteristics. The method can be readily applied to a single recorded SMLM

localization map without the need for additional calibration or control experiments, thereby reducing experimental efforts. 2-CLASTA allows for reliable detection of even faint biomolecular clustering, while preventing the wrong interpretation of overcounting artifacts as true biomolecular clusters. Thus, it is ideally suited as a first step in the assessment of clustering, before other methods may be applied for quantitative characterization of cluster parameters [59, 104].

5.4. Methods

5.4.1. Simulations

Conceptually, simulations were performed as described previously [118]. All simulations were carried out in MATLAB (R2019b, The MathWorks Inc., Natick, MA) on a standard personal computer.

First, we simulated the underlying protein distributions for regions of $10 \times 10 \mu\text{m}^2$, reflecting approximately the size of a typical cell. For all simulations we used 75 molecules per μm^2 , if not mentioned otherwise.

Simulation of oligomers: We distributed oligomers randomly within the region of interest, and assigned a number of s biomolecules to each oligomer position ($s = 1$ to 4). A random distribution of biomolecules is naturally reflected by the case of $s = 1$.

Simulation of areas of enrichment or depletion of biomolecules: Circular domains with a radius of 20, 40, 60, 80, 100 or 150 nm were distributed randomly on the region of interest with adjustable number of domains per μm^2 (3, 5, 10, 15, 20 and 25). The number of biomolecules per domain was calculated from the total number of simulated molecules (here 7500), the fraction of molecules inside domains (20, 40, 60, 80, 100%), and the number of simulated domains, assuming a Poisson distribution. Biomolecules were distributed randomly within the domains. In case of overlapping domains, the density in the intersection area was adjusted to the density of a single domain. The remaining molecules were distributed randomly in the areas outside of the domains.

Second, two different types of labels, corresponding to the two colors, were assigned randomly to the molecules according to the specified labeling ratio, assuming Binomial statistics.

Third, to simulate blinking, we assigned a certain number of detections to each label following the blinking statistics determined for SNAP-AF488 and SNAP-AF647 (Fig. 5.4). For the simulations shown in Fig. 5.5d-f and Fig. 5.11, we used blinking statistics of PS-CFP2 and KT3-AF647 determined previously [118], or artificial blinking statistics following a log-normal distribution. Localization errors were simulated by spreading these detections using a Gaussian profile centered on the molecule position with a width of 30 nm, which corresponds to a typical localization precision achieved in SMLM experiments. We assumed identical localization precision for the two color channels.

Fourth, to account for experimental errors in the realistic scenarios, we included unspecifically bound labels with a mean density of 5 labels/ μm^2 for each color channel, assuming the blinking statistics determined for SNAP-AF488 and SNAP-AF647. We finally considered also false positive localizations by adding a background of 1 (2) signals/ μm^2 for the red (blue) color channel, with experimentally determined blinking statistics obtained from unlabeled cells.

Fifth, to account for stage drift in Fig. 5.6c we assumed alternating laser excitation and hence added a global drift vector \vec{d} to the localizations of both color channels obtained at time t according to $\vec{x} \rightarrow \vec{x} + \vec{d} \cdot t$.

Sixth, to account for residual chromatic aberrations in Fig. 5.6d, we displaced every localization

of the red color channel by a vector which was characterized by the vector field $(x', y') = c \cdot (x - x_0, y - y_0)$; we set $x_0 = y_0 = 2.5 \mu\text{m}$. The parameter c was varied between 0 and 0.06. An illustration of the vector field is shown in Fig. 5.18.

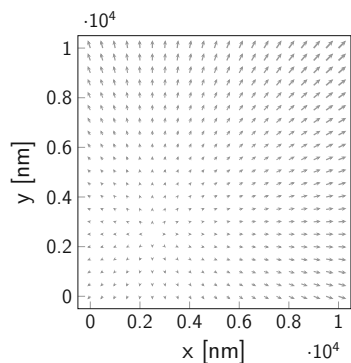


Figure 5.18: Displacement vector field for chromatic aberration. For the simulation of chromatic aberration, every localization of the red color channel was displaced according to the vector field described by $(x', y') = c \cdot (x - x_0, y - y_0)$. For the illustrated vector field, the parameters were set to $(x_0, y_0) = (2500, 2500)$ and $c = 0.04$. Figure adapted from [149].

If not mentioned otherwise, we used the following set of parameters: $10 \times 10 \mu\text{m}^2$ region of interest, 75 molecules per μm^2 , a balanced labeling ratio between the two color channels, no stage drift, 30 nm localization precision, and the blinking statistics of SNAP-AF488 and SNAP-AF647 for the two color channels. For the *ideal* scenario we simulated 100% labeling efficiency, no unspecifically bound labels and no unspecific background signals. For the *realistic* scenario we simulated 40% labeling efficiency, 5 unspecifically bound labels per μm^2 and color channel, and 1 or 2 unspecific background signals per μm^2 in the red and blue color channel, respectively.

5.4.2. Experiments

Quantitative analysis of single label blinking. We quantified single label blinking on HeLa cells expressing GPI-anchored SNAP-monomers, using the identical illumination protocol as for two-color dSTORM recordings. To assure sufficient separation between individual label molecules, dSTORM experiments were performed at low labeling concentrations of either SNAP-AF647 or SNAP-AF488. To statistically quantify the blinking of SNAP-AF647 and SNAP-AF488, localizations from individual label molecules were grouped and quantified in MATLAB (R2019b, The MathWorks Inc., Natick, MA). We determined the first frame of appearance, the total number of detections per label (N) (Fig. 5.4), the time a label was detectable in consecutive frames (t_{on}) and the time a label was not detectable (t_{off}).

Cell culture, DNA constructs, and reagents. All chemicals and cell culture supplies were from Sigma if not noted otherwise. All reagents for molecular cloning were from New England Biolabs. HeLa cells were purchased from DSMZ (ACC 57 Lot 23) and cultured in DMEM high glucose medium (D6439) supplemented with 10% fetal bovine serum (F7524) and 1 kU/ml Penicillin-Streptomycin (P4333). All cells were grown in a humidified atmosphere at 37°C and 5% CO_2 .

For transient transfection of HeLa cells with GPI-anchored SNAP concatemers, we fused one or

multiple copies of the SNAPf sequence to the N-terminus of the GPI-anchor signal of the human folate receptor. To this end, we carried out PCR to amplify the SNAPN9183S sequence from pSNAPf (N9183S) with > 15 nt overhangs complementary to adjacent regions of the following SNAPf copy. We then used the Gibson assembly Master Mix (E2611) following the supplier's instructions to iteratively insert multiple consecutive copies of the SNAPf sequence in frame with the GPI anchor. The resulting colonies were screened by site specific restriction digest using HindIII (R3104) to verify the number of inserted copies.

SNAP-Surface Alexa Fluor 488 (SNAP-AF488) and SNAP-Surface Alexa Fluor 647 (SNAP-AF647) were from New England BioLabs. Both labels were reconstituted in water-free DMSO (276855) at 10 mg/ml, aliquoted and stored at -20°C until used. The dSTORM blinking buffer consisted of PBS, 50 mM β -Mercaptoethylamine (30070), 3% (v/v) OxyFluor (Oxyrase Inc., Mansfield, Ohio, U.S.A.), and 20% (v/v) sodium DL-lactate (L1375) [74]. The pH was adjusted to 8-8.5 using 1 M NaOH.

Sample preparation. Cells were transfected by reverse transfection using Turbofect (ThermoFisher, R0531) according to the supplier's instructions with Opti-MEM (Gibco, 31985062) as serum-free growth medium. Briefly, cells were detached from tissue culture flasks using Accutase (A6964). Subsequently, approximately 50 000 cells were mixed with Turbofect-DNA complexes and seeded on fibronectin-coated (F1141) LabTek chambers (Nunc) and incubated overnight. The following day, cells were labeled for 30-45 min in the incubator with 50 nM SNAP-AF488 and 1 μM SNAP-AF647 diluted in cell culture medium. After labeling, cells were extensively washed with HBSS, and fixed with 4% formaldehyde (Thermo Scientific, R28908) and 0.2% glutaraldehyde (GA) for 30 min at room temperature. After another series of two washing steps, we added 450 μl freshly prepared dSTORM buffer immediately prior to imaging.

Superresolution microscopy and image reconstruction. A Zeiss Axiovert 200 microscope equipped with a 100x Plan-Apochromat ($\text{NA} = 1.46$) objective (Zeiss) was used for imaging samples in objective-based total internal reflection (TIR) configuration. TIR illumination was achieved by shifting the excitation beam parallel to the optical axis with a mirror mounted on a motorized table. The setup was further equipped with a 640 nm diode laser (Obis640, Coherent), a 405 nm diode laser (iBeam smart 405, Toptica) and a 488 nm diode laser (iBeam smart 488, Toptica). Laser lines were overlaid with an OBIS Galaxy beam combiner (Coherent). Laser intensity and timings were modulated using in-house developed LabVIEW software (National Instruments). To separate emission from excitation light, we used a dichroic mirror (Z488 647 RPC, Chroma). Images were split chromatically into two emission channels using an Optosplit2 (Cairn Research) with a dichroic mirror (DD640-FDi01-25x36, Semrock) and additional emission filters for each color channel (690/70H and FF01-550/88-25, Chroma). All data was recorded on a back-illuminated EMCCD camera (Andor iXon DU897-DV).

Typically, we recorded sequences of 20 000 frames in alternating excitation mode. Samples were illuminated repeatedly at 640 nm, 405 nm, and 488 nm with $2\text{--}3\text{ kW/cm}^2$ intensity (640 nm and 488 nm) and $3\text{--}5\text{ W/cm}^2$ (405 nm); intensities were measured in epi-configuration. We selected the illumination times in ranges of 3–10 ms (640 nm), 3–30 ms (488 nm), and 6 ms (405 nm).

Time delays between consecutive illuminations were below 6 ms. The camera was read out after the 640 nm and after the 488 nm illumination, yielding 10 000 frames in each color channel. Thus, the total recording time for a full data set ranged from 3 to 7 minutes. Only data from those frames were included in the analysis, in which well-separated single molecule signals were observable.

We recorded calibration images of immobilized fluorescent beads after each experiment (Tetra-Speck Fluorescent Microspheres, life technologies, T14792) and registered the images as described previously [157]. Single molecule localization and image reconstruction was performed using the open-source ThunderSTORM ImageJ plugin [89].

5.4.3. Calculation of p-value

Single experiment. We tested the null hypothesis of a random biomolecular distribution against the alternative hypothesis of nanoclustering. As a summary statistic T for the data we calculated the integral $t = \int_0^{r_{\max}} \text{cdf}(r) dr$, where $\text{cdf}(r)$ denotes the cumulative distribution function of nearest neighbor distances from each red localization to the nearest blue localization. If no value for r_{\max} was explicitly chosen, r_{\max} was set to the maximum occurring distance in the analysis. For generating the randomized control data sets, a toroidal shift was applied to the original localization data: The localizations from the red color channel were displaced by a shift vector, i.e. $(\tilde{x}_{\text{red}}, \tilde{y}_{\text{red}}) = (x_{\text{red}}, y_{\text{red}}) + (x_{\text{shift}}, y_{\text{shift}})$, with periodic boundary conditions set by the region of interest. The shift vectors $\vec{v}_i = (x_{\text{shift},i}, y_{\text{shift},i})$ with $i = 1, \dots, n$ were chosen uniformly within the region of interest, where n denotes the number of generated control data sets. The value of the test statistic T was calculated for the CDF of the original data, yielding a value t_0 , as well as for all randomized controls, yielding a set of values t_i with $i = 1, \dots, n$. The p-value was calculated as $p = \text{rank}(t_0, \mathcal{T}) / (n + 1)$, where $\text{rank}(t_0, \mathcal{T})$ denotes the rank of t_0 within the set $\mathcal{T} := \{t_i \mid i = 0, \dots, n\}$ in descending order. If not stated otherwise, the level of significance was set to $\alpha = 0.05$.

Multiple experiments. The overall p-value p^* for multiple experiments was calculated as $p^* = 1 - \sum_{i=1}^{k-1} \binom{m}{i} p_0^i (1 - p_0)^{m-i}$, where m is the number of performed experiments, k the number of observed p-values smaller or equal to the threshold p_0 and $\binom{m}{i}$ denotes the Binomial coefficient. If not stated otherwise, the level of significance for the joint analysis of p-values was set to $\alpha^* = 0.05$.

Part II.

Particle averaging in cryo-SMLM

6. Introduction

Chapters 4 and 5 of this thesis dealt with the overall distribution of biomolecules of interest in the cell, in particular the cellular plasma membrane. These chapters proposed methods in order to distinguish a purely random distribution of biomolecules of interest from clustered biomolecular distributions. In case that the distribution of molecules is indeed clustered, the arrangement of the molecules may be further scrutinized. On the one hand, biomolecules may form loosely arranged clusters of various spacial extent and occupation density. On the other hand, a specific number of individual biomolecules can arrange into distinct spatial structures, thus forming an oligomer.

The degree of oligomers and their spatial structure is typically determined via purification and crystallization of proteins, and subsequent structure determination via X-ray crystallography or, more recently, cryo-electron microscopy [158–161]. However, some proteins—especially membrane proteins—are hard to crystallize [162]. Furthermore, the structure of the purified protein may be altered during the purification and crystallization process, in particular in the presence of detergents [163]. Therefore, it is of great interest to determine the arrangement of proteins directly within the cellular plasma membrane. This possibility to study the protein structure in their native environment is offered by SMLM techniques.

SMLM requires the recording of thousands of frames and thus, the image acquisition may last minutes up to hours. Hence, thorough sample fixation is crucial. Conventional fixation methods based on chemical fixatives may still allow for residual protein mobility, leading to distortions of the obtained localization maps [9]. Moreover, they may affect the sample morphology [10]. Preservation of the biological ultrastructure, however, is a crucial prerequisite for performing structural biology at the nanoscale. Cryo-fixation currently represents the gold standard for preserving the biological ultrastructure [11]. At the same time, it prevents any residual mobility and is compatible with SMLM imaging approaches [75, 90, 164, 165]. In addition, the photostability of fluorophores is increased at cryogenic temperature. Thus, more photons per individual fluorophore can be collected, which in turn improves the localization precision [75, 87].

Performing SMLM under cryogenic temperatures, however, is more complicated compared to experiments performed at room temperature (compare section 2.3.4). First, the optical setup requires a larger working distance due to the included vacuum chamber, thus, limiting the possible numerical aperture to low values of typically 0.7–0.8. Secondly, the localization procedure becomes more difficult. At room temperature, fluorophore dipoles can freely rotate and the resulting PSF can be well approximated by a Gaussian function [41, 55]. At cryogenic temperature, however, fluorophore dipoles are fixed. A tilt of the PSF with respect to the optical axis leads to a distorted PSF, which complicates the localization procedure as a simple Gauss fit in general leads to biased estimates of the fluorophore position [12, 13].

Notably, SMLM comes with several challenges, which hamper a direct determination of the biological structure of a particle of interest from the obtained localization maps. These challenges include insufficient labeling efficiency and overcounting in combination with localization

uncertainties. In order to overcome these challenges, hundreds to thousands of copies of the same particle need to be imaged and averaged for reconstruction of the underlying particle structure.

In the following part of this thesis, I will describe new methods for the determination of oligomeric structures from SMLM experiments performed under cryogenic temperatures. This part comprises two aspects: First, the bias-free localization of fixed dipole emitters, and second, the reconstruction of the oligomer structure from thousands of identical copies of the same particle. In the next two sections, I will give an overview of available methods concerning these two topics.

6.1. PSF for fixed dipole emitters

The emission properties of a dye molecule can be well described by the model of an oscillating electric dipole (Fig. 6.1a). If the fluorophore molecule can freely rotate in all dimensions, the photon emission is isotropic. The resulting PSF—an Airy pattern—can be well approximated by a Gaussian function. This is mainly due to the centrosymmetry of both the Gaussian and Airy function. In addition, the side maxima of the Airy function are typically obscured by noise. Thus, the Gaussian function yields excellent estimates for the lateral position of a fluorophore: Fitting the PSF image of a freely rotating fluorophore by a Gaussian via maximum likelihood estimation was shown to achieve theoretically optimum localization results while at the same time being computationally very efficient [166]. If the rotational mobility of a fluorophore molecule is restricted, however, the emission becomes anisotropic. In particular for SMLM recordings under cryogenic temperatures, the orientation of each fluorophore’s dipole transition moment is fixed. If the dipole orientation is tilted with respect to the optical axis, the PSF becomes distorted (Fig. 6.1b,c), which easily leads to substantial deviations between the estimated and actual fluorophore position when fitting with a simple Gaussian function [41, 167].

Enderlein et al. studied the localization bias in the position estimate for in-focus, fixed fluorophores [12]. For objectives with a high numerical aperture of $NA = 1.4$, the intensity maximum of the PSF may deviate by more than 100 nm from the actual position of the emitter [12]. The center position of the fitted Gaussian shows smaller deviations, but a bias of up to 10 nm may remain, especially for intermediate dipole orientation angles characterized by an elevation angle between $\theta = \pi/6$ and $\theta = \pi/3$. For lower numerical aperture of $NA = 1.2$, this bias reduces to less than 2.5 nm. It has to be kept in mind, though, that a lower NA reduces the light collection efficiency and thus, negatively affects the achievable localization precision. Stallinga et al. extended their analysis to fluorophores which are positioned out of the focal plane [41]. Crucially, they pointed out that the localization bias worsens with increasing amount of defocus, also in the case of low NA. This was further demonstrated in experiments, which yielded a bias of over 100 nm for out-of focus fluorophore molecules [13]. Of note, the size and direction of the lateral shift in the PSF depends on the fluorophore dipole orientation and the amount of defocus. Therefore, the shift is different for every observed fluorophore molecule and thus, cannot easily be corrected, and even less so, if the dipole orientation and defocus are unknown.

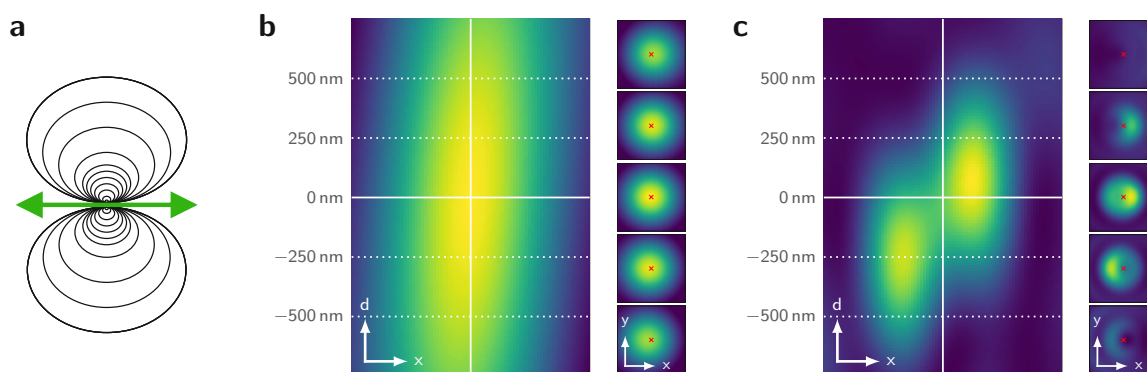


Figure 6.1.: PSFs for fixed fluorophore dipole orientations. The emission characteristics of a fluorophore molecule can be modeled by an ideal oscillating electric dipole (a). The fluorophore’s dipole orientation is indicated by the green arrow. If the dipole orientation is tilted with respect to the optical axis, the PSF becomes distorted. The resulting theoretical PSF for a dipole with azimuthal angle $\phi = 0$ and elevation angle $\theta = \pi/2$ imaged with a 0.7 NA/60x and 1.45 NA/100x objective is depicted in panels b and c, respectively. In each panel, the left plot shows a cross-section of the PSF for varying defocus; the plots on the right side show xy -sections of the PSF for defocus values of $d = -500$ nm to 500 nm in steps of 250 nm (as indicated by the horizontal white lines). The color indicates intensity and was normalized to the maximum intensity occurring in each panel. The lateral shift of the PSF increases with increasing amount of defocus.

In summary, in case of fixed fluorophore dipoles a simple Gaussian approximation of the PSF leads to a substantial localization bias. In order to avoid this bias, more sophisticated imaging and analysis approaches are required. An overview of current methods will be given in the following section.

6.1.1. PSF modeling

Several approaches have been developed which rely on a more elaborate PSF model based on the laws of optics in order to fit the experimentally recorded PSF. A full theoretical model of the PSF as it is obtained from a single dipole emitter point source can be derived based on vectorial diffraction theory [42, 43].

Mortensen et al. fitted the PSF of in-focus, fixed dipole emitters via maximum likelihood estimation (MLE) and thus, simultaneously obtained estimates for the lateral position, fluorophore orientation, number of detected photons and background signal [85]. The maximum likelihood method is an unbiased estimator which achieves the Cramér–Rao bound (CRB, see chapter 2.3.5) and thus, yields optimum precision [93, 96]; no other unbiased estimator will yield a better precision. However, MLE fitting is computationally demanding, as time for generating the PSF and calculating the log-likelihood is required in every iteration of the fit.

A computationally more efficient approach was proposed by Zhang et al. [168], who relied on the same PSF model but generated simulated PSFs in order to train an artificial neural network. Via this neural network they could not only estimate the position and orientation

of a fluorophore, but also potential rotational mobility. In addition, this work extended the analysis to out-of focus emitters. In case of defocus, the localization bias could be drastically reduced, but a bias of up to 20 nm for ± 300 nm defocus remained.

Alternatively, the image formation of a fixed dipole emitter can be reformulated: The diffraction pattern can be modeled as a linear combination of six template patterns (Fig. 6.2), as shown by Aguet et al. [169]. The weighting coefficients can be expressed as trigonometric functions which depend on the dipole orientation. Thus, an estimate for the position and orientation of a fluorophore is obtained.

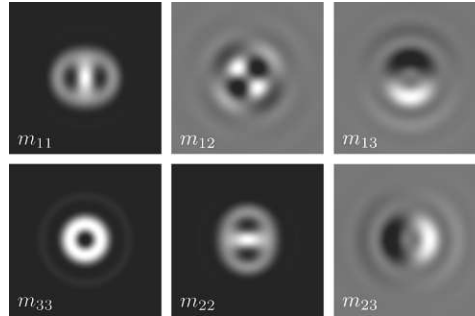


Figure 6.2.: Template basis patterns. A simplified model of the PSF describes the PSF as a linear combination of six basic template patterns. The coefficients of the linear combination are directly linked to fluorophore orientation. Figure adapted from [169].

In theory, the full PSF model based on diffraction theory describes the obtained PSF of a single emitter best. In practice, however, the full theoretical model is computationally expensive. Furthermore, more delicate shape characteristics of the PSF are often obscured by various sources of noise. Therefore, Stallinga et al. developed a simplified model, which still captures all relevant shape characteristics required for correct estimation of the fluorophore position, while being computationally efficient [170]. For this, the emission was split into four polarization channels and the images were fit by a modified Gaussian function, which was multiplied by a weighted combination of Hermite polynomials. This approach allowed to reduce the localization bias both for in- and off-focus emitters to less than 5 nm.

Another point to take into account are imperfections of the optical system leading to aberrations of the PSF. Common aberration errors include spherical aberrations, coma, and astigmatism. Although optical systems are typically corrected for (undesired) aberrations, slight imperfections may be left, which may vary over the field of view. These aberrations will have an impact on the achieved localization precision and accuracy if disregarded by the localization procedure [171]. Coma, in particular, produces asymmetries in the PSF which lead to biased position estimates. Of note, model-based localization procedures can in principle account for residual aberrations by including a calibrated aberration map in the PSF model [172].

6.1.2. Back focal plane manipulation

Further approaches trying to reduce the localization bias in case of fixed dipole emitters rely on manipulation of the back focal plane (BFP). Backlund et al. used a phase mask for engineering a

double-helix PSF (Fig. 6.3a) and split the emission into orthogonal polarization channels [173]. Fitting the two lobes of the obtained PSFs with a sum of two Gaussian functions allows to determine the z -position as well as the linear dichroism and lobe asymmetry. Comparing the obtained images together with the estimated parameters to simulations yields an estimate for the dipole orientation. Subsequently, the characteristic bias for a set of parameters can be determined from simulations. Finally, this bias can be subtracted from the apparent lateral position obtained from the simple Gauss fit.

A conceptually similar method was used by Zhang et al., but with a Tri-spot phase mask [174]. The Tri-spot PSF (Fig. 6.3b) together with polarization information allows to estimate a fluorophore's orientation. Subsequently, the localization bias for the standard PSF is obtained from this orientation estimate based on simulations. Finally, the bias is subtracted from the localizations obtained from the standard PSF. Thus, the bias was shown to be reduced to around 7 nm for a defocus range within ± 200 nm.

A different approach is based on azimuthal polarization filtering in the back focal plane (Fig. 6.3c). This approach was first conceived theoretically by Lew et al. [175] and later demonstrated experimentally by Backlund et al. [176]. Simulations showed that in principle, this strategy allows to completely abolish the localization bias for any dipole orientation and amount of defocus. In practice, however, the implementation of this phase mask is experimentally challenging and a slight bias of around 5 nm remained for defocus values of ± 200 nm. Moreover, the phase mask reduces the photon collection efficiency, leading to a reduction of localization precision of 30–75% depending on the specific dipole orientation [175].

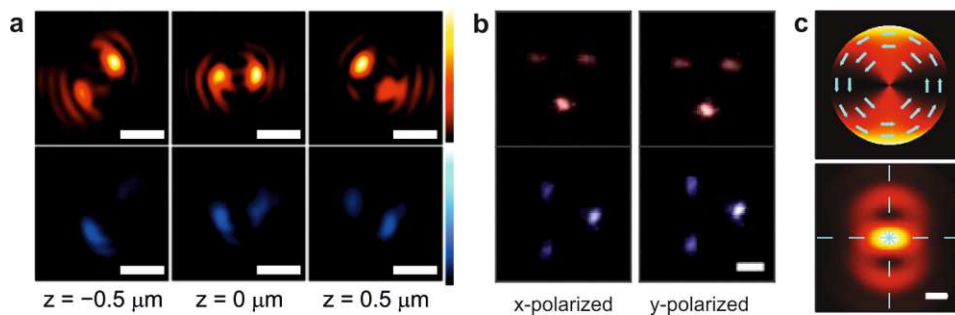


Figure 6.3.: Manipulation of the back focal plane. The localization bias for fixed dipole emitters can be greatly reduced by altering the electric field in the back focal plane via a phase mask. (a) Double-helix PSF. The parallel and perpendicular polarization channel are shown in red and blue color, respectively. Scale bars: $1 \mu\text{m}$. (b) Tri-spot PSF. Scale bar: $1 \mu\text{m}$. (c) Azimuthal filtering of the back focal plane. The top panel shows the electric field at the BFP with arrows indicating the azimuthal filtering. The bottom panel shows the resulting PSF. Scale bar: 200 nm . Figures adapted from [173, 174, 176].

6.1.3. Polarization

A different approach recently suggested by Nevskyi et al. is based on polarization filtering in the emission path [177]: Two images with orthogonal polarization are recorded simultaneously (Fig. 6.4). Interestingly, the x -polarized image does not seem to show any bias with regard to

the y -coordinate and vice versa. Thus, a simple Gaussian fit of the x - and y -polarized images yields a virtually bias-free estimate of the y and x position, respectively. It has to be noted, though, that a slight bias for larger defocus values remains, which is also dependent on the dipole orientation; in particular for specific dipole orientations and large defocus the bias is substantial. Although the method does not discard any emission light, the emission is split into two channels and thus, not all obtained photons are used for estimating each of the two lateral directions. Of note, depending on the dipole orientation, the splitting may be rather unbalanced and one of the channels may appear dark, leading to unsatisfactory localization precision for the respective coordinate.

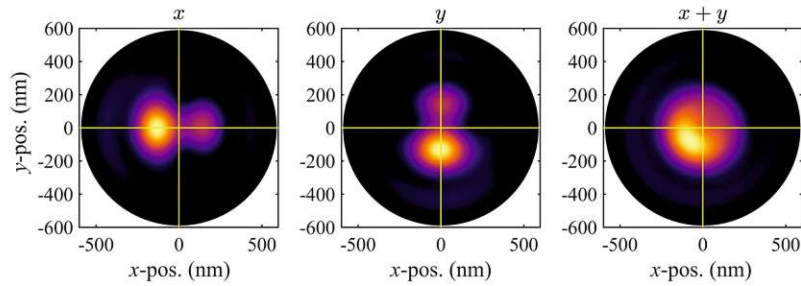


Figure 6.4.: Polarization splitting approach. The emission light is split into an x - and y -polarized channel, shown in the first two images. The true emitter position at $(0,0)$ is indicated by the yellow cross. The x -polarized image shows no bias in the y -coordinate of the emitter, while the y -polarized image shows no bias in the x -coordinate. Therefore, a simple Gaussian fit can be employed for each of the two images in order to determine the y - and x -coordinate, respectively. For comparison, the unpolarized image is shown in the third image. Fitting this PSF with a Gaussian function would lead to a considerable bias in the position estimate. Figure adapted from [177].

6.2. Particle averaging

An SMLM experiment yields a list of localization coordinates. A direct inference of the biological ultrastructure of a particle of interest, however, is hampered by two aspects inherent to SMLM [178]: On the one hand, insufficient labeling efficiency leads to undercounting. This problem is further increased by insufficient detection efficiency; fluorophores may bleach before they are detected or rest in the dark state during the whole image acquisition. On the other hand, multiple detections of individual molecules results in overcounting. While multiple detections in consecutive frames or close spatial and temporal proximity may be corrected for [5], complex blinking behavior of fluorophores or the presence of multiple dye molecules per biomolecule of interest impede such a correction. In consequence, the imaged particle appears distorted; some parts of the bimolecular structure may not be visible at all, while others are heavily overrepresented as depicted in Fig. 6.5.

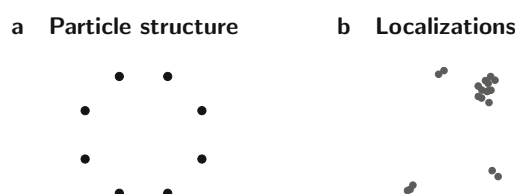


Figure 6.5.: Effect of under- and overcounting. The structure of the particle of interest (a), and an illustrative corresponding localization map (b) are shown. Due to insufficient labeling and/or detection efficiency some parts of the structure are not visible, while multiple detections of the same molecule lead to overrepresentation of other parts.

As under- and overcounting are based on stochastic processes, each individual imaged particle will yield a slightly different localization map. Particle averaging approaches combine the information obtained from thousands of identical copies of a particle, thus aiming to circumvent statistical noise present in single observations [104, 179]. In the following sections, I will give a short overview of currently existing methods for particle averaging.

6.2.1. Sum images

In a pioneering study, Szymborska et al. performed particle averaging on recorded data of the nuclear pore complex (NPC) [44]. For this, SMLM images obtained from individual NPC particles were aligned and summed up (Fig. 6.6a). Assuming a circular arrangement of molecules in the NPC, the resulting image subsequently was rotationally averaged. A fit of the radial profile (Fig. 6.6b) yielded an estimate for the NPC radius with a precision of 0.1 nm. By labeling different sites of the NPC and estimating the corresponding radius for each site, the orientation of the Y-shaped Nup107-160 subunit within the NPC could be determined (Fig. 6.6c).

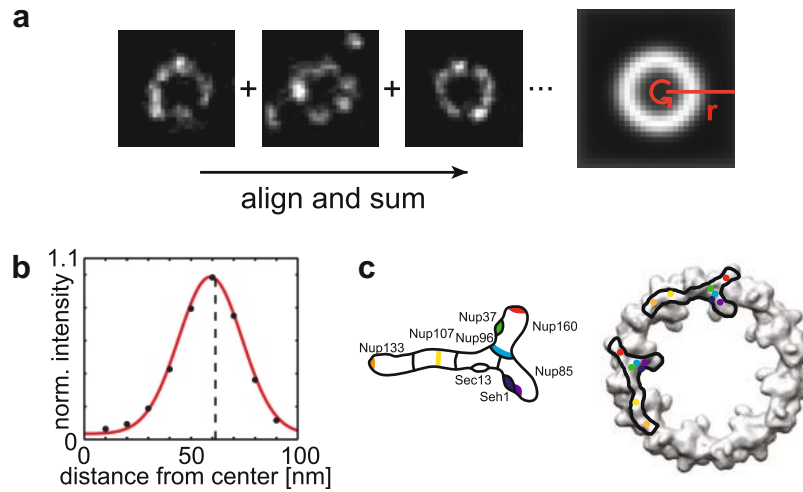


Figure 6.6.: Radius determination from sum images. Images obtained from individual particles are aligned, summed up and rotationally averaged (**a**). Fitting of the resulting radial profile (indicated by the red line in panel **a**) yields an estimate for the particle radius (**b**, dashed line). Labeling various sites on the Nup107-160 subunit, its orientation within the NPC can be derived (**c**). Figure adapted from [44].

6.2.2. Adapted EM-algorithms

The concept of particle averaging is well-known and established in the field of cryo-electron microscopy (EM) [160]. Several studies hence tried to adapt algorithms developed for cryo-EM data for the use with SMLM data [90, 180]. For this, the localization maps obtained from SMLM first need to be converted to pixel-based images since EM-algorithms expect intensity distributions rather than a list of coordinates. Previously, this was performed by either calculating the probability density of localizations [180], or by representing each localization as a Gaussian with a width corresponding to the respective localization uncertainty [90]. Salas et al. [180] demonstrated successful 3D reconstruction of larger particles of around 100 nm to 200 nm in size (Fig. 6.7a). Weisenburger et al. [90] performed SMLM imaging under cryogenic temperatures and thereby could reconstruct the GtCitA PASc domain dimer and the streptavidin homo-tetramer with a remarkable resolution at the Ångström scale (Fig. 6.7a). Moreover, Sieben et al. presented an analysis approach which allows for multicolor 3D reconstruction of several particles simultaneously [181].

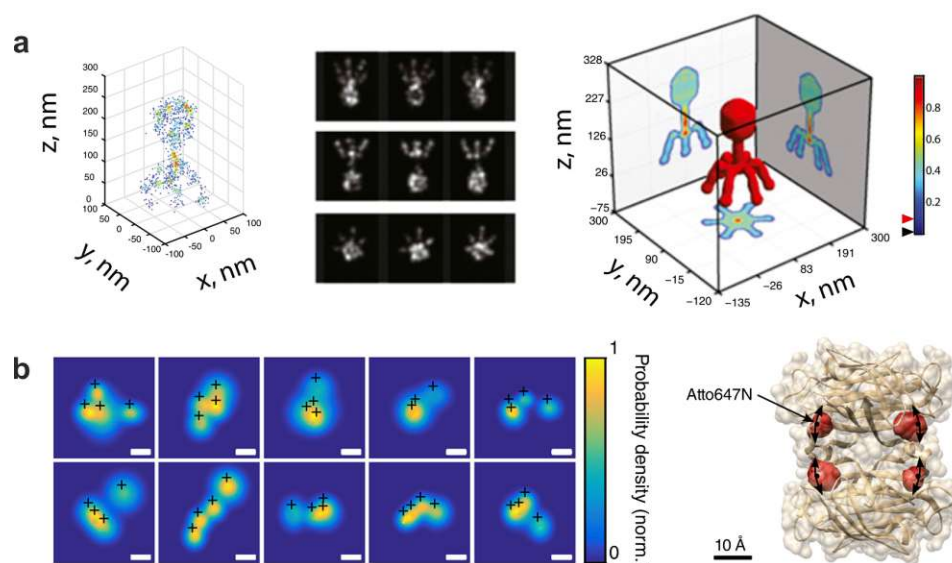


Figure 6.7.: Particle reconstruction based on EM-algorithms. 3D reconstruction from two-dimensional SMLM projection images are possible with algorithms adapted from cryo-EM. **(a)** Reconstruction of a virus (T4 bacteriophage) by Salas et al. The left image shows the 3D localization map obtained from SMLM recordings, the middle image shows projection images based on localization densities. The right image depicts the resulting reconstructed model of the virus. Figure adapted from [180]. **(b)** Reconstruction of the streptavidin homo-tetramer by Weisenburger et al. with imaging performed under cryogenic temperatures. On the left, obtained localizations from individual particles are shown. The corresponding images were created with Gaussian functions centered at the localization position with a width corresponding to the localization precision. In the image on the right, the reconstructed positions of the ATTO 647N dye molecules are illustrated in red, the crystal structure is shown in brown. Figure adapted from [90].

6.2.3. Coordinate-based reconstruction methods

One has to be aware that the imaging modalities of EM and SMLM differ quite substantially and thus, reconstruction algorithms adapted from EM will not fully account for the specific characteristics of SMLM imaging. Most evidently, the SMLM data consists of a list of localization coordinates, which is fundamentally different from the continuous intensity data obtained in EM. Therefore, various approaches have been developed which directly use the localization coordinates for particle reconstruction and address issues specific to SMLM, including localization precision and overcounting.

Registration methods

The localization point clouds obtained from individual particles, e.g. oligomeric protein complexes, may be registered and superimposed in order to yield a single *super*-particle. Methods for registration can roughly be distinguished into template and template-free registration methods. Using template-based as well as template-free registration methods various studies successfully reconstructed the structure of the nuclear pore complex and revealed its structural

details [109, 182–184].

For template registration [182], the localizations of each individual recorded particle are registered onto a predefined template structure (Fig. 6.8a). This *a priori* knowledge about the structure can be retrieved from EM studies or inferred from the localization maps. If no prior knowledge about the particle structure is available, template-free registration methods have to be employed. In pyramid registration, particles are registered pairwise to each other and merged in consecutive steps [182], until only one *super*-particle is left (Fig. 6.8b). In the all-to-all registration approach [183, 184], all particles are registered to all other particles simultaneously (Fig. 6.8b). Also in case of template-free registration, any knowledge or assumption on the particle structure, in particular particle symmetry, may be included in order to increase the quality of the reconstruction [183, 184].

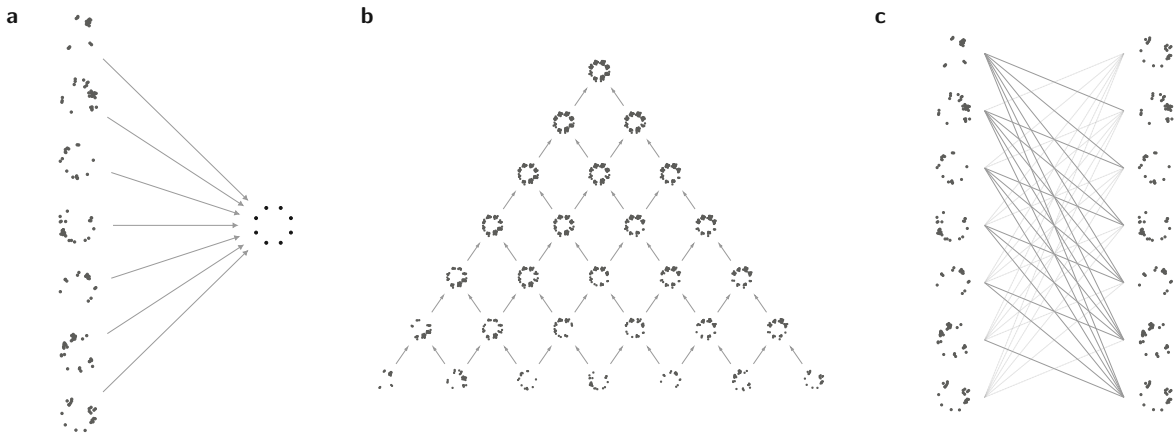


Figure 6.8.: Particle registration methods. (a) Template registration. For each individual particle shown on the left side, the localizations are registered to a predefined template depicted on the right. (b) Pyramid registration. The scheme shows the registration procedure from bottom to top. In each step, particles are registered pairwise to each other and subsequently combined. For each layer of the pyramid scheme, the procedure is repeated until a single *super*-particle is left. (c) All-to-all registration. All particles are registered pairwise to each other simultaneously. The light, dotted lines depict redundant registrations.

The registration procedure aims at minimizing the distances between localizations of the particles supposed to be registered. As the distance measure, the Bhattacharyya distance can be applied, yielding the following cost function [182, 183]:

$$D = \sum_{i=1}^{n_t} \sum_{j=1}^{n_m} \exp \left(- \left(\vec{x}_{t,i} - (R\vec{x}_{m,j} + \vec{s}) \right)^T \left(\Sigma_{t,i} + R \Sigma_{m,j} R^T \right)^{-1} \left(\vec{x}_{t,i} - (R\vec{x}_{m,j} + \vec{s}) \right) \right), \quad (6.1)$$

where \vec{x}_t, \vec{x}_m are the coordinate positions of the registered particles, n_t, n_m the corresponding number of localizations for each particle, R the rotation matrix and \vec{s} the translation vector. The covariance matrices Σ_t, Σ_m reflect the localization uncertainties in different directions and are given as $\Sigma = \text{diag}(\sigma_x^2, \sigma_y^2, \sigma_z^2)$. Via the covariance matrices, anisotropic localization precision in the different directions can be accounted for. In addition, the distance measure

penalizes large distances, leading to proper registration results also in case of missing labels. Further, the registration process can be adapted in order to allow for deformations of the particles [185], which may occur for example due to a 2D-projection of the structure.

Regarding the runtime, template-based registration methods are most efficient, as each particle is registered to the template individually and thus, the runtime scales linearly with the number of particles. In comparison, pyramid and all-to-all registration scale quadratically with the number of particles [182, 183]: For n recorded particles, a number of $n(n - 1)/2$ pairwise registrations have to be performed.

Reconstruction from relative positions

Curd et al. recently proposed an approach termed PERPL (pattern extraction from relative positions of localizations) for extracting the underlying structure of a particle from the distribution of the distances between its localizations [186]. For this, an experimental relative position distribution (RPD) is obtained by calculating all relative distances between localizations. As a next step, several candidate models for the structure are chosen based on prior knowledge or structural details discernible from the localization map. For each model, the relative distances between its position coordinates are calculated (Fig. 6.9a). Next, based on these discrete distances a distribution of distances is determined according to the localization precision (Fig. 6.9b). In addition, a term accounting for distances between localizations arising from the same molecule of interest (solid black line) as well as a background term (dashed black line) are included. Combining all the contributions yields a total model RPD (red line). This model RPD can be compared to the experimental RPD (Fig. 6.9c). Finally, the model which represents the experimental RPD best is selected.

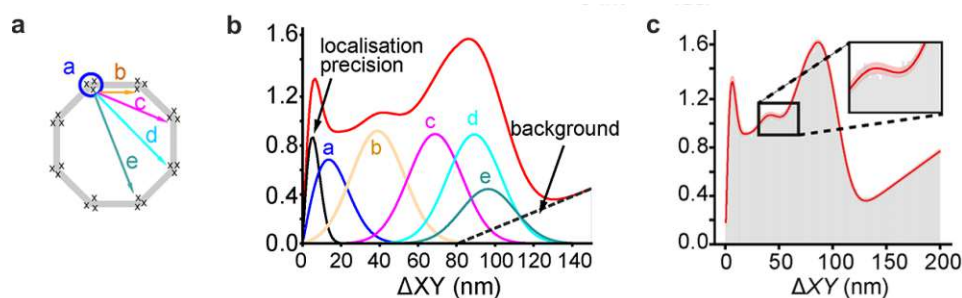


Figure 6.9.: Pattern extraction from relative positions of localizations (PERPL). The PERPL approach determines the underlying particle structure from the distribution of relative distances between all obtained localizations of a particle. For a chosen model, all relative distances between its positions are calculated (a). These discrete distances are then converted into distance distributions based on the localization precision (b). In addition, a term accounting for multiple detections of the same molecule (solid black line) and a background term (dashed black line) are included. Combining all contributions yields the total model RPD (red line). Finally, the obtained model RPD (red line) is compared to the experimental RPD represented by the histogram shown in gray (c). Figure adapted from [186].

7. Localization of fixed dipole emitters

This chapter contains data and figures from the following preprint:

F. Hinterer*, **M. C. Schneider***, S. Hubmer, M. López-Martinez, P. Zelger, A. Jesacher, R. Ramlau, G. J. Schütz. *Robust and bias-free localization of individual fixed dipole emitters achieving the Cramér Rao bound*. arXiv, 2021.

arXiv-ID: 2104.02449

Aim

The fixed orientation of fluorophore dipoles in cryo-SMLM leads to complex and asymmetric PSF shapes. Simple fitting of the obtained PSF images with a Gaussian function may cause a considerable localization bias, in particular for tilted dipoles and imperfect focusing. Here, we aimed at developing a bias-free localization procedure for fixed dipole emitters under low NA conditions as given for the considered cryo-SMLM setup.

Contribution

This study was performed in cooperation with Fabian Hinterer, Simon Hubmer and Ronny Ramlau from the Johannes Kepler Universität (JKU) Linz and the Johann Radon Institute (RICAM) Linz, as well as Philipp Zelger and Alexander Jesacher from the Medical University of Innsbruck. I conceived the method for localization analysis in cooperation with Fabian Hinterer and Gerhard Schütz. Together with Philipp Zelger, Alexander Jesacher and Fabian Hinterer, I developed a software package for simulation and analysis of PSF images for fixed dipole emitters.

Outcome

We established an approach for precise and accurate localization of fixed dipole emitters under a low NA setting. The method is based on maximum-likelihood estimation of the emitter position using the complete theoretical point-spread function model. A straightforward astigmatic imaging approach encodes additional information about the axial position of the emitter. Based on simulations of PSF images we showed that this approach allows for unbiased localization estimates even under defocused imaging conditions, while achieving the best possible localization precision at the Cramér–Rao bound.

7.1. Introduction

Cryogenic temperatures promise superior fixation for SMLM applications, as the sample's ultrastructure is conserved and residual diffusion of molecules is minimized [9, 11]. However, performing SMLM imaging at cryogenic temperatures leads to fixed dipole orientations of dye molecules characterized by the azimuthal angle ϕ and elevation angle θ (Fig. 7.1). In consequence, if the fluorophore is not positioned exactly in the focal plane the peak of the PSF will be shifted laterally. Therefore, a simple Gaussian fit of the PSF image or centroid calculation leads to a bias in the position estimate [12, 13]. In chapter 6, I presented an overview of methods which allow to circumvent this issue and yield virtually bias-free localizations. In many of the previous studies, imaging with a high-NA objective was assumed [85, 175–177]. Here, we consider a setup for performing SMLM at cryogenic temperatures (compare section 2.3.4). Due to the vacuum chamber required for thermal isolation of the sample, a large working distance is required and one is typically restricted to an air-objective with a limited NA of 0.7–0.8 [75].

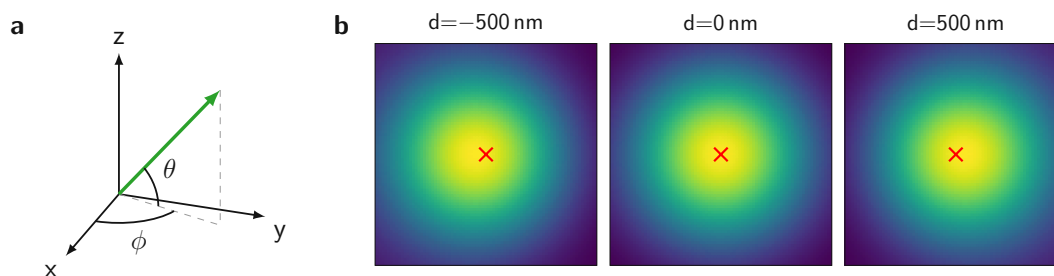


Figure 7.1.: Coordinate system and fluorophore dipole orientation. Panel **a** depicts an illustrative dipole orientation (green arrow) characterized by its elevation angle θ and azimuthal angle ϕ . The optical axis is assumed to be parallel to the z -axis. Panel **b** shows normalized xy -cross sections of the PSF for an emitter with dipole orientation $(\theta, \phi) = (\pi/4, 0)$ for defocus values of $d = -500$ nm (left), $d = 0$ nm (middle) and $d = 500$ nm (right). Each plot shows a quadratic region of interest with $0.81 \mu\text{m}$ side length. The red cross indicates the true position of the emitter. Although the shapes of the PSF cross sections are virtually identical, a vertical shift of the PSF along the x -axis is discernible.

For low-NA objectives, the PSF of a defocused fixed dipole can, in practice, hardly be distinguished from a defocused PSF arising from a dipole with a laterally shifted true position (Fig. 7.1b). Hence, obtaining unbiased position estimates is challenging even when applying a maximum-likelihood fit with the full vectorial PSF model for fixed dipole emitters. The assumed PSF model is described in detail in the *Methods*, section 7.4.1. Fig. 7.2 shows a quantification of the localization errors for simulated PSF images, assuming fixed dipole emitters with elevation angles $\theta = 0, \pi/6, \pi/3, \pi/2$ and azimuthal angle $\phi = \pi/4$. We assumed an emission wavelength of $\lambda = 680$ nm. The number of detected photons was set to $N = 5 \cdot 10^5$ with a background noise of $b = 100$ (Fig. 7.2a) and $b = 300$ (Fig. 7.2b), corresponding to a signal-to-noise ratio of 5000 and 1666, respectively, and a signal-to-background ratio of 50 and 5.55, respectively. Indeed, values above 10^6 for the number of obtained photons per fluorophore were reported previously for experiments performed under cryogenic conditions with decelerated photophysics [75, 87]. A comparison of representative PSF images with and with-

out background noise is shown in Fig. 7.3. The theoretical PSF model (see *Methods*, section 7.4.1) was fitted to each simulated PSF image via maximum likelihood estimation (MLE) (see *Methods*, section 7.4.4), yielding parameter estimates $(\hat{x}, \hat{y}, \hat{d})$ for the lateral position of the emitter and the amount of defocus. In principle, a maximum likelihood fit of the PSF using the exact PSF model should yield bias-free results. However, the presence of background noise hampers the fitting procedure as faint differences in the shape of the PSF are obscured by background fluctuations and the fit algorithm may be trapped in local minima. Thus, the fit results become unstable and strongly depend on the choice of the starting values.

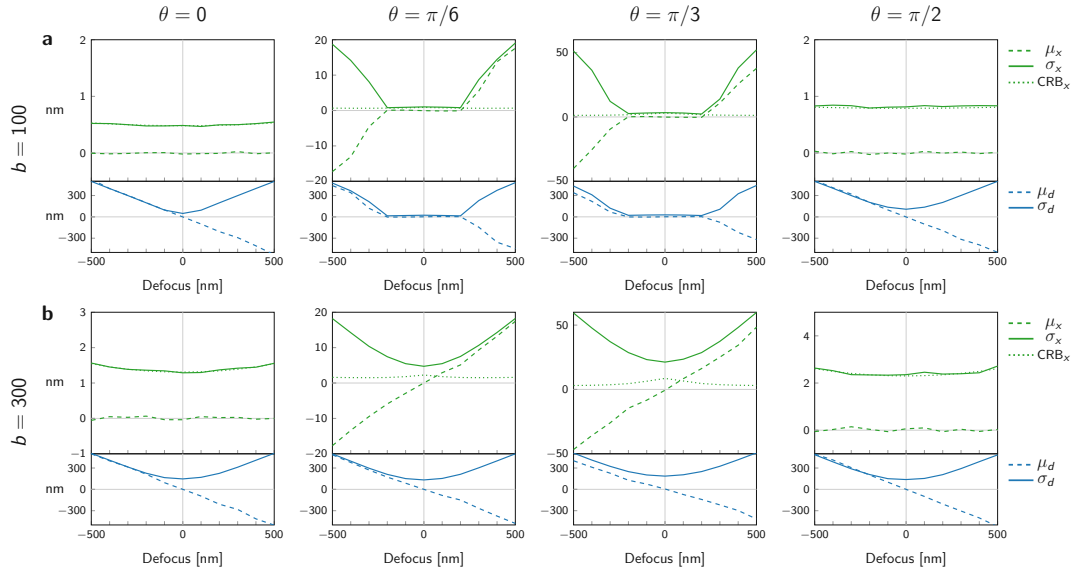


Figure 7.2.: Localization errors for fixed dipole emitters. Simulations of the PSFs were performed assuming a standard optical setup and cryogenic imaging conditions. We simulated PSFs for different dipole orientations with elevation angle $\theta = 0, \pi/6, \pi/3, \pi/2$. The azimuthal angle was set to $\phi = \pi/4$. For each simulated PSF image, we fitted the position and defocus (x, y, d) with the full vectorial PSF model via maximum-likelihood estimation, while the dipole orientation (θ, ϕ) was assumed to be known exactly. Shown are the resulting bias μ_x, μ_d (dashed lines) and localization precision σ_x, σ_d (solid lines) for the x -position (green) and defocus values d (blue), respectively. Note that for symmetry reasons, the bias and localization precision for the x - and y -position are identical. The CRB for the localization precision of the x -coordinate is indicated by the dotted green line. The number of photons was set to $N = 5 \cdot 10^5$, the background noise to $b = 100$ (a) and $b = 300$ (b). The amount of defocus was varied from -500 nm to 500 nm in steps of 100 nm. Each data point represents 1000 simulations. Figure adapted from [187].

For the lower noise level of $b = 100$ (Fig. 7.2a), we still obtained satisfactory results for the lateral position estimate in case of slight defocus within 200 nm of the focal plane. For larger amounts of defocus, however, the localization bias increased up to 50 nm. For an elevated noise level of $b = 300$ (Fig. 7.2b), the fitting results became increasingly unstable and it was virtually impossible to estimate the correct fluorophore position. For $d = 0$, i.e. perfect focusing, the localization bias seemingly vanished. This can be explained by the starting values chosen for the fitting procedure, which were distributed symmetrically in this case; thus, positive and negative errors could compensate. Nevertheless, these errors still affected the obtained

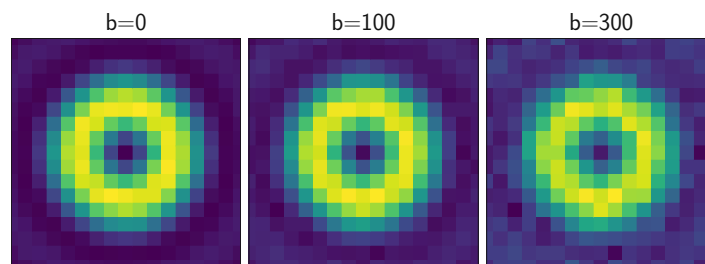


Figure 7.3.: Comparison of PSF images for different noise levels. The plots depict simulated PSF images for a fluorophore with elevation angle $\theta = \pi/2$. A signal of $N = 5 \cdot 10^5$ photons was simulated with background noise of $b = 0$ (left), $b = 100$ (middle) and $b = 300$ (right), assuming a perfect focus ($d = 0$). Each plot shows a 17×17 pixel region with a pixel size of 108 nm.

localization precision, which could not attain the CRB (dotted line).

Interestingly, the main difficulty was to extract the correct defocus value from the PSF images (Fig. 7.2, blue lines), which in turn affected the estimation of the lateral fluorophore position, especially for low signal-to-noise ratios. Notably, the PSFs for $\theta = 0$ and $\theta = \pi/2$ are always symmetric, also in the case of defocusing (see Fig. 7.4). On the one hand, this symmetry impeded a correct estimation of the defocus, which consistently exhibited a substantial bias (Fig. 7.2, dashed blue lines). On the other hand, for $\theta = 0$ and $\theta = \pi/2$ the PSF is not tilted and thus, no localization bias in the estimation of the lateral position (x, y) could be observed, even for large defocus values (Fig. 7.2, dashed green lines).

In this chapter, I show how additional information on the defocus can improve the stability of the localization procedure for non-rotating single dipole emitters. Information on the defocus can directly be encoded in the PSF by inserting a weak cylindrical lens into the optical path. This induces astigmatism, which leads to elliptical distortions of the PSF above and below the focal plane, as can be seen in Fig. 7.4b,d. Astigmatism-based imaging is a well-established method, which has previously been applied for estimating the z -position of isotropic emitters [188–191]. For the localization procedure, we fitted the PSF image with the full vectorial PSF model via the maximum likelihood method, yielding an estimate for the lateral position (x, y) of a fluorophore as well as the amount of defocus d . We extensively investigated the performance of the method based on simulations, which allowed to directly compare the obtained fitting results to the ground truth fluorophore positions. Our method provided bias-free localization results for fixed dipole emitters. In addition, the obtained precision attained the Cramér–Rao bound (CRB) (see *Methods*, section 7.4.3). The proposed approach is directly applicable to SMLM recordings under cryogenic conditions.

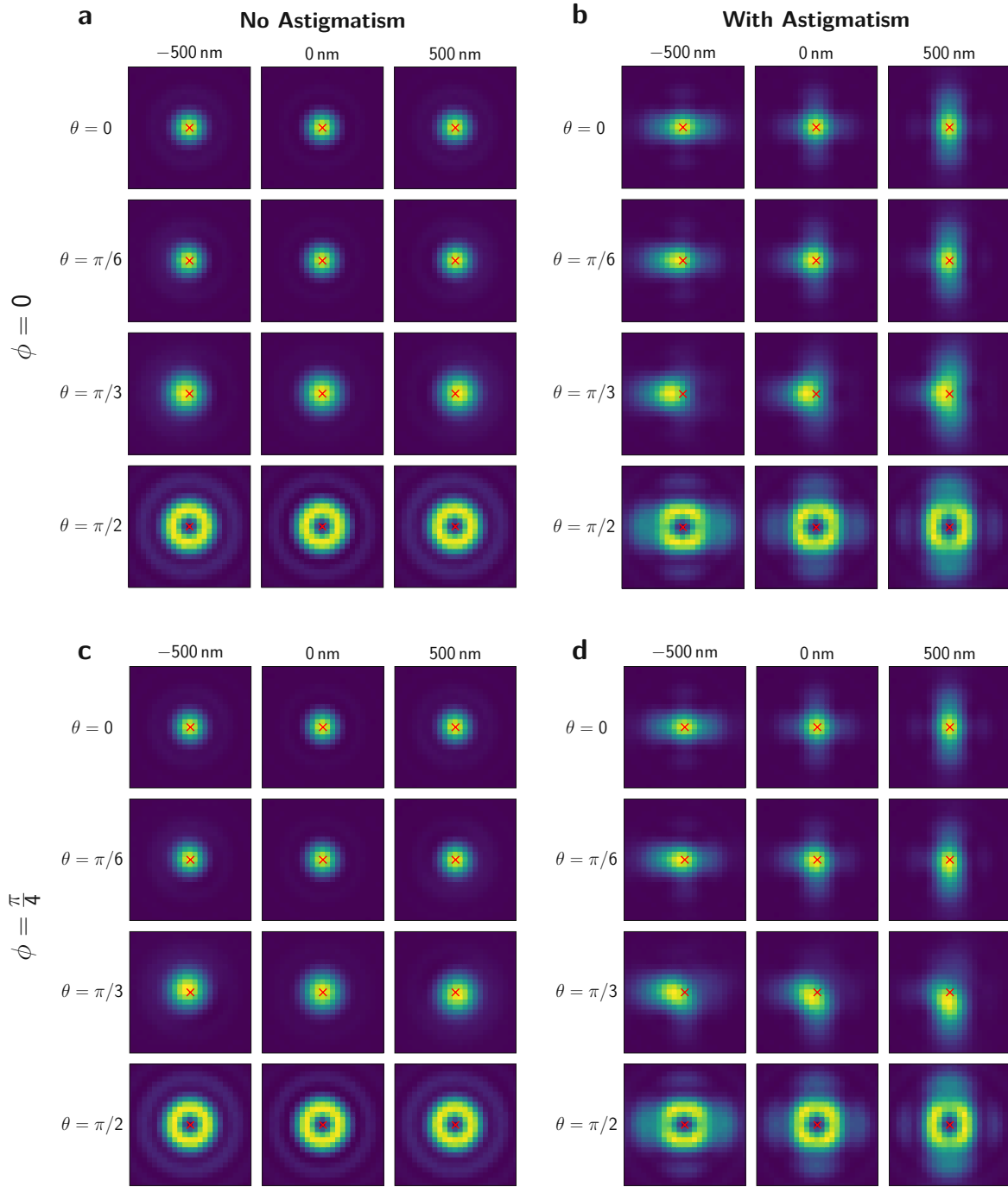


Figure 7.4.: Point spread functions for different dipole orientations. Simulated PSF intensity patterns in the case of no astigmatism (**a,c**) and 75 nm RMS vertical astigmatism (**b,d**). The elevation angle was set to $\theta = 0, \pi/6, \pi/3, \pi/2$, the azimuthal angle was set to $\phi = 0$ (**a,b**) or $\phi = \pi/4$ (**c,d**). Each PSF plot depicts a 25×25 pixelated image with a pixel size of 108 nm. The red crosses indicate the actual position of the dipole emitter in the center of the image. Figure adapted from [187].

7.2. Results

In order to encode information about the defocus in the PSF image, we considered an astigmatic imaging approach. For this, we assumed a weak astigmatism with 75 nm RMS vertical astigmatism, corresponding to a shift between the x - and y -focal plane of approximately 1.4 μm . We simulated PSF images for various dipole orientations and defocus values ranging from -500 nm to 500 nm. A comparison of the obtained PSF shapes with and without astigmatic distortions is depicted in Fig. 7.4. Simulated PSF images were fitted with a maximum likelihood approach, yielding estimates for the lateral position (x, y) and the amount of defocus d .

First, we were interested whether the introduced astigmatism offers enough information in order to not only estimate (x, y, d) , but to leave the dipole orientation (θ, ϕ) as a free parameter of the fit as well (Fig. 7.5a). While the obtained results for both the lateral position and the defocus showed no substantial bias, the fit nevertheless was unstable and yielded poor values for the localization precision up to 40 nm for (x, y) and 100 nm for d . In order to increase the stability of the fit, we assumed the azimuthal angle ϕ to be known and left only the elevation angle θ as a free parameter of the fit (Fig. 7.5b). Indeed, the estimation of the lateral position (x, y) could be improved. Nevertheless, the obtained localization precision of around 20 nm is still insufficient for resolving structures at the nanometer scale. In addition, the localization precision for the defocus hardly improved. Hence, we concluded that a simultaneous fitting and estimation of the lateral position (x, y) , defocus d and dipole orientation (θ, ϕ) is not feasible in order to achieve satisfactory results.

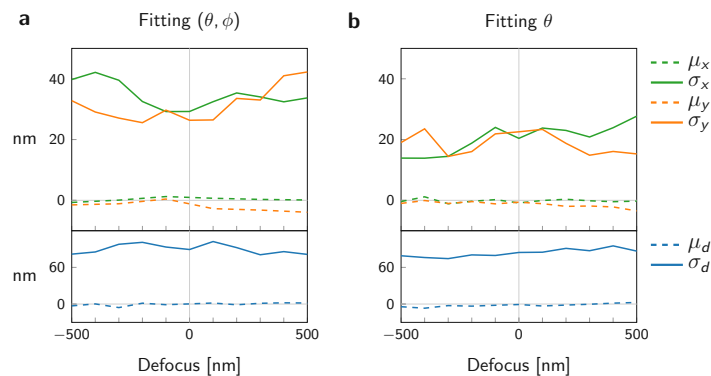


Figure 7.5.: Fitting the dipole orientation in the presence of astigmatism. PSF images with $N = 5 \cdot 10^5$ photons and background noise $b = 0$ were simulated. For each simulation, the ground truth dipole orientation was chosen randomly. We fitted the lateral position (x, y) , defocus d and dipole orientation in the presence of astigmatism with the full vectorial PSF model via MLE. In panel **a** we fitted both the elevation and azimuthal angles (θ, ϕ) . In panel **b** we assumed the azimuthal angle ϕ to be known and fitted the elevation angle θ only. Shown are the resulting bias μ_x, μ_y, μ_d (dashed lines) and localization precision $\sigma_x, \sigma_y, \sigma_d$ (solid lines) for the x -position (green), y -position (orange) and defocus values d (blue), respectively. Each data point represents 5000 simulations. A list of all simulation parameters is given in Table 7.1 in the Appendix. Figure adapted from [187].

Consequently, in the following we assumed that knowledge about the dipole orientation is available. This assumption is justified, as various approaches for determining the dipole orientation

of a fluorophore are available, which are also applicable for low-NA objectives as considered here [192–196]. Henceforth, we left only the lateral position and defocus as free parameters of the fit (Fig. 7.6). Here, we simulated PSF images for four different dipole orientations with $\theta = 0, \pi/6, \pi/3, \pi/2$ and $\phi = \pi/4$. The number of photons per PSF was set to $N = 5 \cdot 10^5$ while background noise was not considered ($b = 0$), i.e. the only noise source was assumed to be photon shot noise. Fig. 7.6 shows the obtained values for the bias (dashed lines) and the localization precision (solid lines) for the estimation of x , y and d . For comparison, the CRB for x and y is indicated as dotted lines. As expected, our method yielded bias-free results. Moreover, including knowledge about the dipole orientation greatly enhanced the localization precision, which achieved the CRB over the whole range of defocusing values. The introduced astigmatism causes a shift of the focal planes for the x - and y -direction and thus, the x - and y -localization precision show opposing trends for negative and positive values of the defocus. Per definition, a defocus value of 0 corresponds to the position in the middle of the x - and y -focal planes.

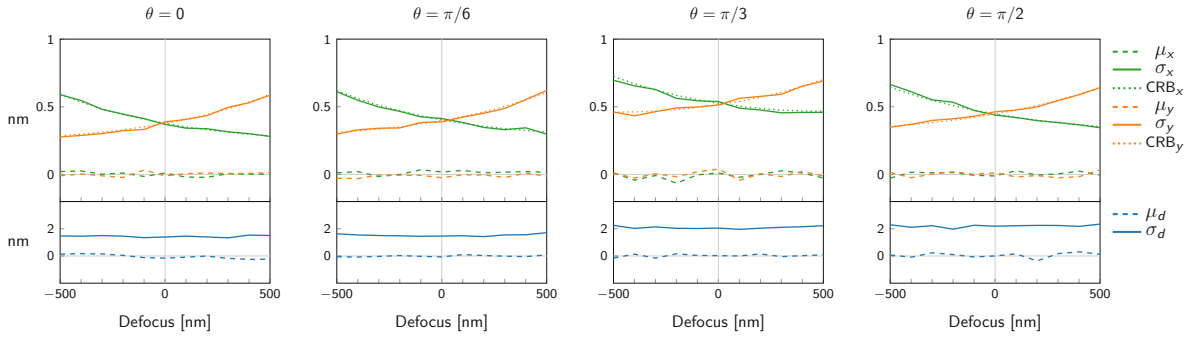


Figure 7.6.: Localization errors in the presence of astigmatism. PSFs were simulated for different dipole orientations with elevation angle $\theta = 0, \pi/6, \pi/3, \pi/2$ and azimuthal angle $\phi = \pi/4$. The number of photons was set to $N = 5 \cdot 10^5$ and the background noise to $b = 0$. We fitted the full vectorial PSF model via MLE to obtain estimates for the position and defocus (x, y, d); the dipole orientation (θ, ϕ) was assumed to be known exactly. Shown are the resulting bias μ_x, μ_y, μ_d (dashed lines) and localization precision $\sigma_x, \sigma_y, \sigma_d$ (solid lines) for the x -position (green), y -position (orange) and defocus values d (blue), respectively. The CRB for the estimation of the x - and y -position are indicated by the dotted lines. Each data point represents 1000 simulations. A list of all simulation parameters is given in Table 7.1 in the Appendix. Figure adapted from [187].

As can be seen in Fig. 7.4, the position of the intensity maximum of the PSF depends on the azimuthal angle ϕ . Therefore, we repeated the simulations from the previous figure, but changed the azimuthal angle from $\phi = \pi/4$ to $\phi = 0$. Changing the azimuthal angle yielded similar results both for the bias and localization precision (Fig. 7.7). As the influence of the azimuthal angle on the obtained results was found to be negligible, we kept the azimuthal angle at $\phi = \pi/4$ for all following simulations. Next, we reduced the simulated number of photons obtained for each PSF (Fig. 7.8). As expected, the localization errors increased for a reduced number of photons. Importantly, the method still did not exhibit any bias; the trends for the localization precision remained the same. In addition, we were interested in the influence of the camera pixel size. For this, we increased the pixel size by two, i.e. we simulated PSF images with a pixel size of 216 nm. The increase in the pixel size hardly affected the obtained results

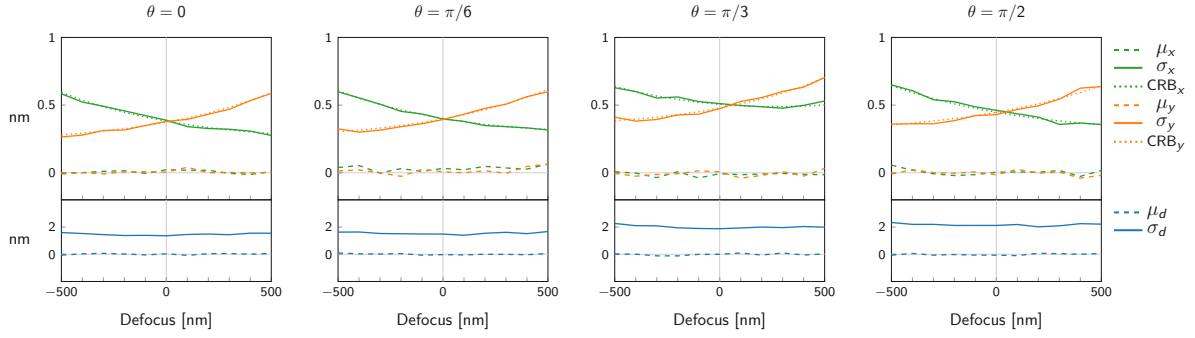


Figure 7.7.: Influence of the azimuthal angle. All simulation parameters and the fitting procedure were identical to Fig. 7.6, except for the azimuthal angle, which was set to $\phi = 0$. A list of all simulation parameters is given in Table 7.1 in the Appendix. Figure adapted from [187].

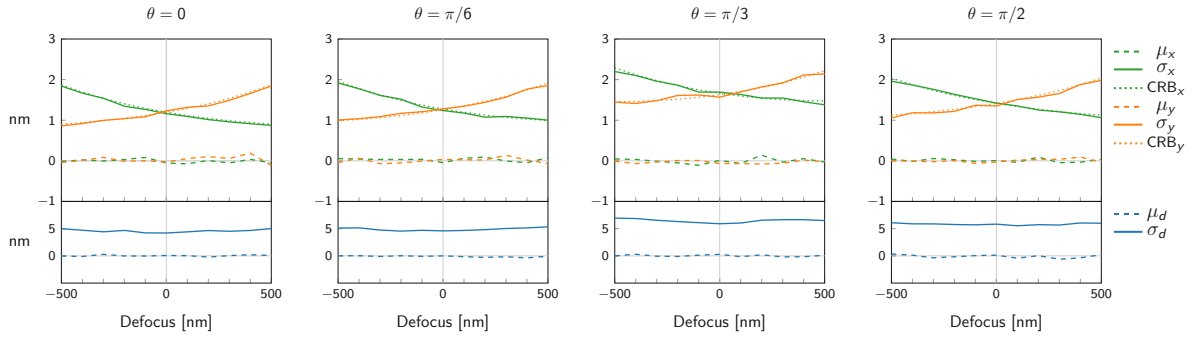


Figure 7.8.: Influence of number of photons. All simulation parameters and the fitting procedure were identical to Fig. 7.6, except for the photon number, which was reduced to $N = 5 \cdot 10^4$. A list of all simulation parameters is given in Table 7.1 in the Appendix. Figure adapted from [187].

for the bias and localization precision (Fig. 7.9).

In an SMLM experiment, the obtained signal is impaired by background noise arising among others from camera noise, other emitters in the same field of view, or scattering. In order to consider noise sources in our simulations, we added homogeneous Poisson-distributed background noise to each pixel. We simulated background noise with a magnitude of both $b = 100$ (Fig. 7.10a) and $b = 300$ (Fig. 7.10b). In all scenarios, the obtained localization precision for the x - and y -position (solid lines) followed the CRB (dotted lines) extremely well. Overall, the localization precision for the x and y -position was below 2 nm and 5 nm for background noise with $b = 100$ and $b = 300$, respectively. Of note, the precision for the estimation of the defocus was worse, with σ_d up to 7 nm and 20 nm for $b = 100$ and $b = 300$, respectively.

Further, we investigated the influence of the number of pixels which were taken into account for the fitting procedure. For this, we varied the size of the analyzed region of interest (ROI) from 3×3 pixels up to 41×41 pixels (Fig. 7.11). For small ROIs below 10×10 pixels the calculated CRB increased rapidly, as large parts of the signal are cut off, leading to loss of information. As expected, the localization precision was poor for small ROIs. In this regime, the obtained localization precision deviated from the CRB. This can be explained by the fact

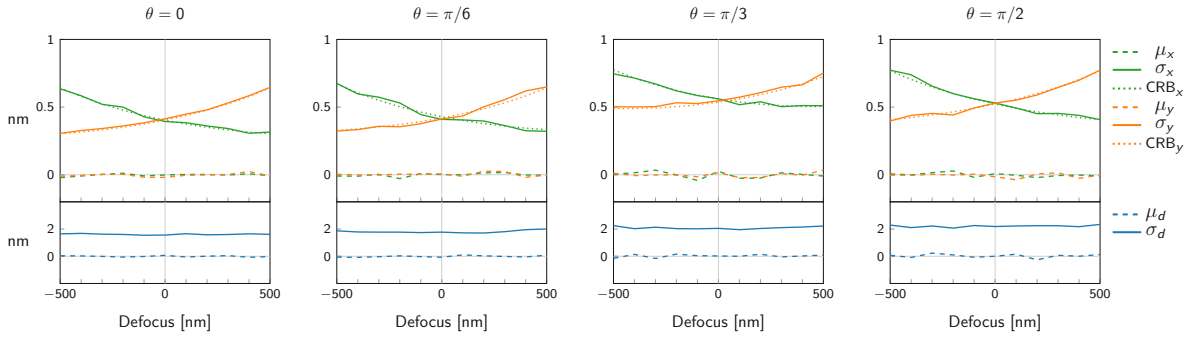


Figure 7.9.: Influence of pixel size. All simulation parameters and the fitting procedure were identical to Fig. 7.6, except for the simulated pixel size, which was set to 216 nm. A list of all simulation parameters is given in Table 7.1 in the Appendix. Figure adapted from [187].

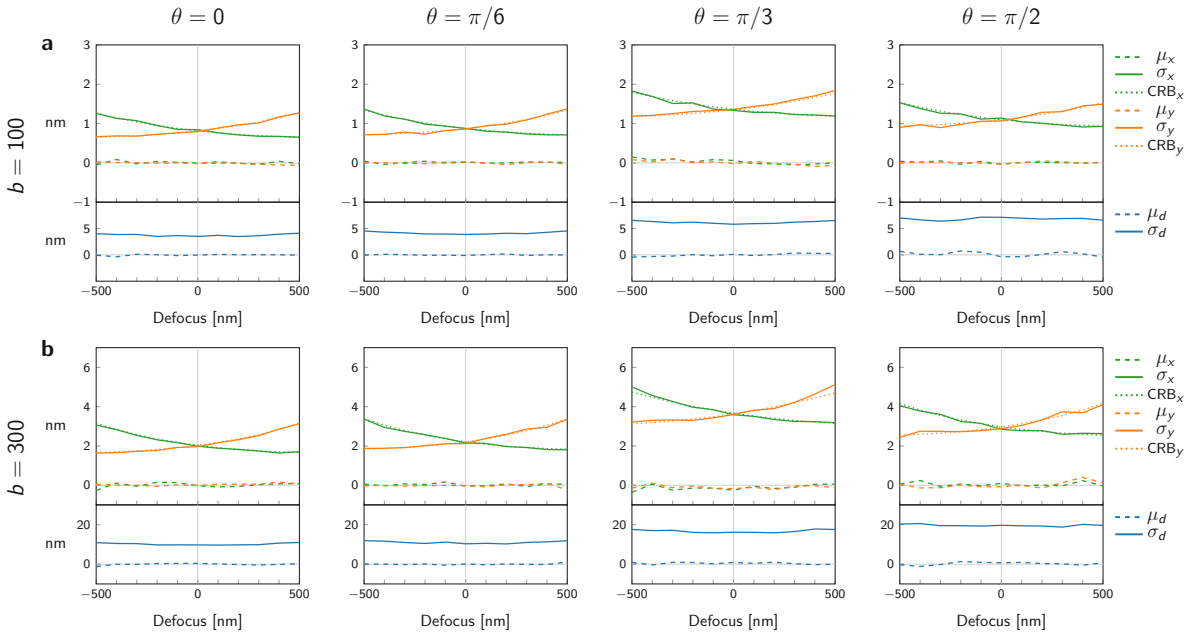


Figure 7.10.: Influence of background noise. Simulations and fitting procedure were analogous to Fig. 7.6, except for adding background noise, which was set to $b = 100$ (a) and $b = 300$ (b). A list of all simulation parameters is given in Table 7.1 in the Appendix. Figure adapted from [187].

that the ground truth position of the emitter was varied for the simulations, while the CRB was calculated for the center position; for very small ROIs the fitting procedure was exceedingly sensitive to slight changes in the subpixel position of the emitter. For ROIs larger than 10×10 pixels, the obtained values for the localization precision were almost constant. Without any background noise, a larger ROI always led to improved results. In the presence of background noise, however, the localization precision showed a minimum at around 13×13 pixels. The obtained results confirm our choice of a fitting region of 17×17 pixels, yielding good localization precision and high fitting stability.

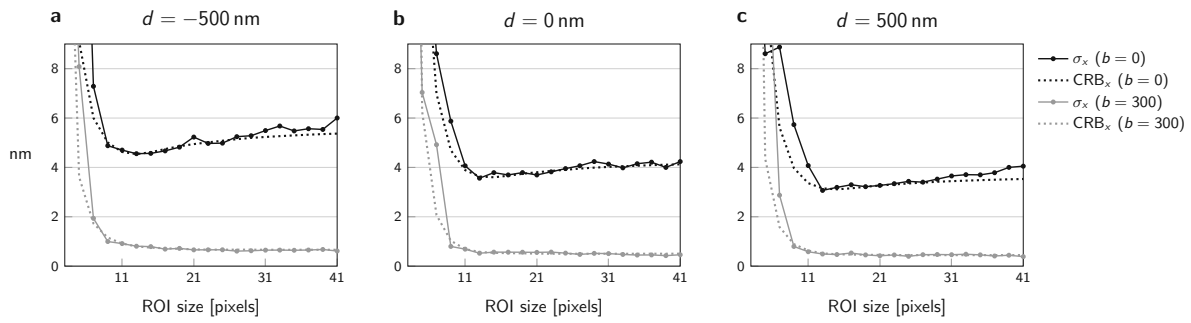


Figure 7.11.: Influence of the size of the fitted region. Localization precision (solid lines) and the CRB (dotted lines) are shown for fitted regions of interest ranging from 3×3 pixels to 41×41 pixels. For all simulations, the fluorophore dipole orientation was chosen as $(\theta, \phi) = (\pi/6, \pi/4)$. Three different defocus values were simulated: $d = -500$ nm (a), $d = 0$ nm (b), $d = 500$ nm (c). The background noise was set to $b = 0$ (gray lines) and $b = 300$ (black lines). Each data point represents 1000 simulations. A list of all simulation parameters is given in Table 7.1 in the Appendix. Figure adapted from [187].

In practice, the fluorophore dipole orientation has to be estimated and thus, perfect knowledge about the orientation is unrealistic [192–196]. Therefore, we investigated the influence of errors in the assumed dipole orientation on the localization procedure. For this, we added errors to the dipole orientation, following two different distributions: (i) Errors were distributed normally with a mean of 0 and a standard deviation of 2° for both the elevation angle θ and azimuthal angle ϕ . (ii) Errors were distributed normally with a mean of 0 and a standard deviation of 4° and 2° for θ and ϕ , respectively. The increased standard deviation for θ was selected to represent the higher difficulty in the estimation of the elevation angle. Of note, the chosen values correspond to standard deviations in the angle estimation reported previously [167]. The results for case (i) and (ii) are shown in Fig. 7.12a,b and Fig. 7.12c,d, respectively. Imperfect knowledge about the fluorophore dipole orientation did not lead to any bias in the estimation of the lateral position or the defocus (dashed lines). Regarding the precision, similar trends as for the previous simulations with exact knowledge about the dipole orientation (Fig. 7.6) could be observed. Overall, uncertainties in the dipole orientation deteriorated the localization precision. Notably, the results for $\theta = \pi/6$ and $\theta = \pi/3$ were affected more strongly—in particular for large defocusing—as for these angles the shape of the PSF is more sensitive to slight changes in the dipole orientation.

In all previous simulations, we assumed an equal number of photons for each fluorophore, which was subjected to photon shot noise only. In practice, however, the photon yield is directly dependent on the fluorophore dipole orientation: The excitation probability for a fluorophore is proportional to $\cos^2(\beta)$, where β is the angle between the fluorophore dipole orientation and the electric field vector of the excitation light. Assuming circularly polarized excitation light, the number of obtained photons can be calculated as $N_{\text{eff}} = N \cos^2(\theta)$, where θ is the elevation angle of the dipole orientation of the emitter. Thus, the photon yield is reduced for dipoles which are not parallel to the focal plane, but tilted with respect to the focal plane. Notably, the photon yield of fluorophores with a dipole orientation almost parallel to the optical axis will be close to zero. In Fig. 7.13 we examined the influence of reduced excitation on the localization precision for tilted dipoles. The simulations and fitting procedure

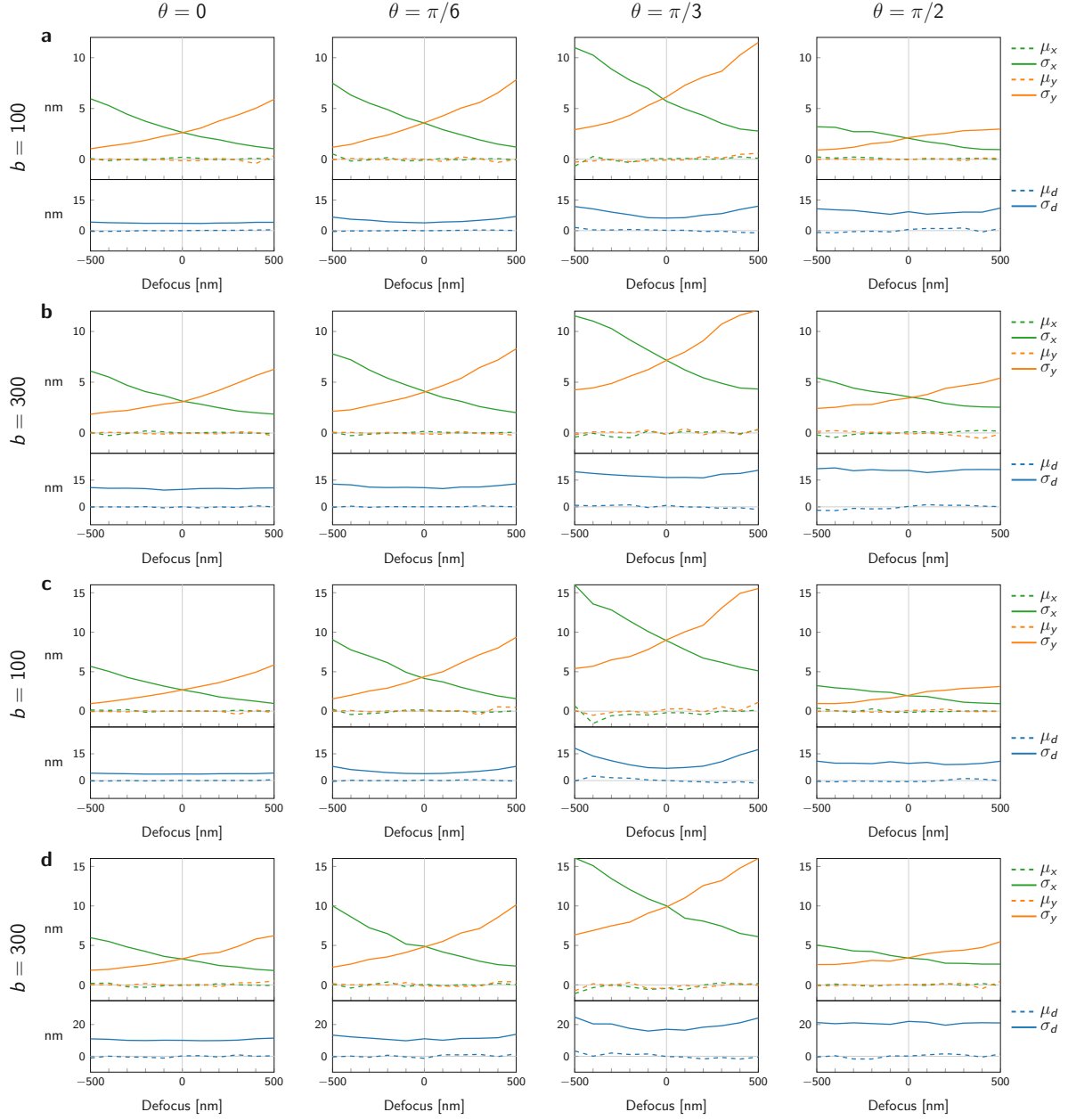


Figure 7.12.: Influence of uncertainties in dipole orientation. Simulations and fitting procedure were analogous to Fig. 7.6, except that the dipole orientation was not assumed to be known exactly, but determined with errors. The errors for the dipole orientation were distributed normally with standard deviation of 2° for both θ and ϕ (a,b), or standard deviation of 4° in θ and 2° in ϕ (c,d). Background noise was set to $b = 100$ (a,c) and $b = 300$ (b,d). A list of all simulation parameters is given in Table 7.1 in the Appendix. Figure adapted from [187].

were carried out analogously as for Fig. 7.6 (in particular, exact knowledge about the dipole orientation was assumed), except that the obtained number of photons was adjusted according

to the fluorophore dipole orientation. Note that for a fluorophore with an elevation angle of $\theta = \pi/2$, i.e. an orientation parallel to the optical axis, the excitation probability is always zero; therefore, this case was omitted in the figure. As expected, the results for $\theta = 0$ were identical to those from Fig. 7.6, as the dipole orientation is parallel to the focal plane in this case and thus, $N_{\text{eff}} = N$. For the tilted dipoles characterized by $\theta = \pi/6$ and $\theta = \pi/3$, however, the number of photons was reduced and thus, the localization precision deteriorated. Remarkably, in all cases the obtained localization precision could still attain the CRB (dotted lines).

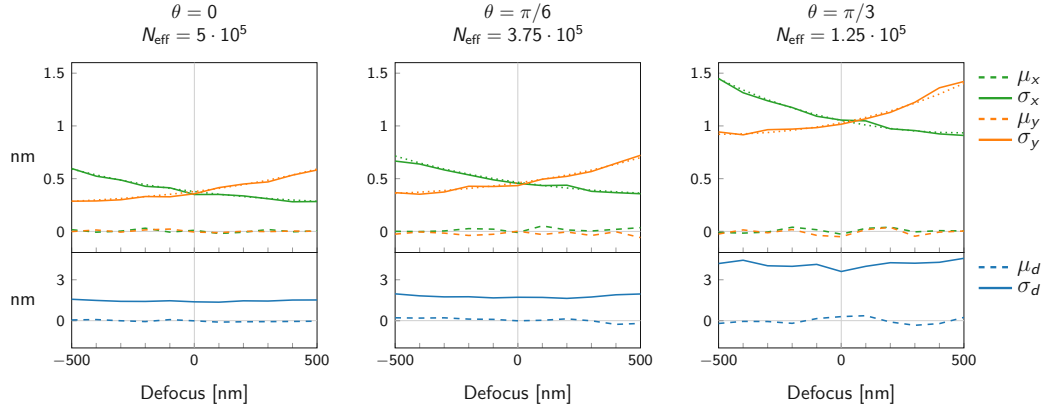


Figure 7.13.: Influence of reduced excitation probability for tilted dipoles. The photon yield for each simulated fluorophore was adjusted according to its dipole orientation, with a maximum photon number of $N = 5 \cdot 10^5$. The effective number of photons $N_{\text{eff}} = N \cos^2(\theta)$ is indicated at the top of each plot. The remaining parameters and fitting procedure are identical to Fig. 7.6, of note background noise was set to $b = 0$ and exact knowledge about the dipole orientation was assumed. A list of all simulation parameters is given in Table 7.1 in the Appendix. Figure adapted from [187].

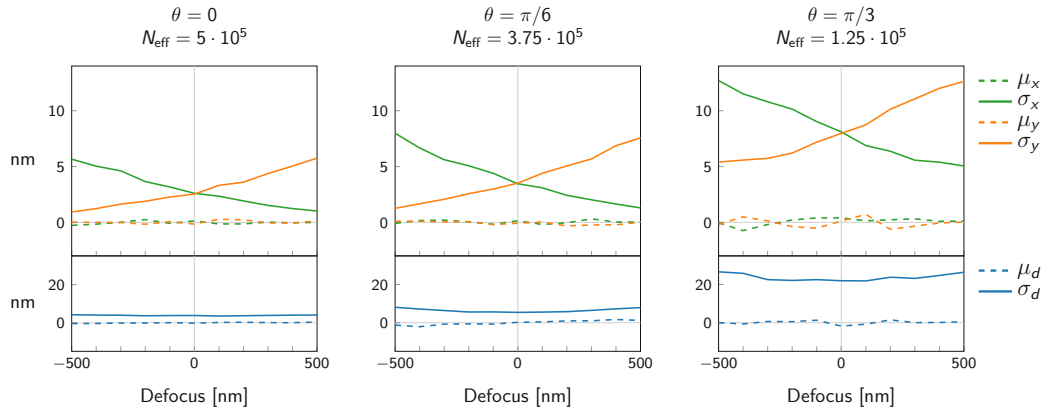


Figure 7.14.: Combined effect of reduced excitation probability for tilted dipoles and uncertainties in dipole orientation. The figure shows the results for localization bias and precision when including both a reduced excitation probability for tilted dipoles, as well as errors in the determination of the dipole orientation. Again, we assumed the errors in the dipole orientation to follow a normal distribution with a standard deviation of 2° for both θ and ϕ , as in Fig. 7.12a,b. A list of all simulation parameters is given in Table 7.1 in the Appendix. Figure adapted from [187].

Finally, Fig. 7.14 shows the combined effect of the reduced excitation for tilted dipoles and imperfect knowledge about the dipole orientation. Here, we assumed the errors in the dipole orientation to be distributed normally with a standard deviation of 2° for both θ and ϕ , as in Fig. 7.12a,b. Again, for $\theta = 0$ the number of obtained photons was not reduced and the best localization precision could be achieved. For tilted fluorophores with $\theta = \pi/6$ and $\theta = \pi/3$, the obtained localization precision deteriorated as the errors due to both the reduced photon numbers and the uncertainty in the dipole orientation accumulated.

7.3. Discussion

Precise and accurate localization of emitters in SMLM is prerequisite for resolving biomolecular structures at the nanoscale. At cryogenic temperature, the reduced photobleaching leads to high photon yields per fluorophore—average values of more than 10^6 photons were reported in previous experiments [75, 87]. Thus, a localization with a remarkable precision below one nanometer can be achieved [75, 87, 90].

One challenge of cryo-SMLM is the anisotropic emission of fixed dipole emitters, causing a bias in the estimation of the fluorophore position for standard localization procedures that rely on Gaussian fitting or centroid calculation [12, 13]. The presence of localization biases of tens of nanometers thwarts the gain in localization precision for cryo-SMLM. Several methods aim at avoiding a localization bias in case of fixed dipole emitters [85, 172, 175–177]. Notably, these studies assumed high-NA conditions; in this case high angular components of the emission are captured, leading to more distinct PSF shapes than in a low-NA setting as given for the considered cryo-setup. An interesting approach to collect high angular components in combination with large working distances is the implementation of a super-hemispherical solid immersion lens [76]. For a low-NA setting, in contrast, the problem of localization biases is inherently less severe, in particular for perfect focusing [12]. In case of defocus, however, a tilt of the PSF still leads to considerable lateral shifts of the intensity peak [41]. The presented astigmatic imaging approach considers cryo-SMLM with low NA and yields bias-free localization results over a large range of defocus values of ± 500 nm. Additionally, the introduced astigmatism allows for an estimate of the axial position, albeit with smaller precision compared to the lateral precision.

For achieving stable fit results, knowledge of the dipole orientation of fluorophores is required (compare Fig. 7.5 and Fig. 7.6). Various approaches exist for estimating the orientation of the dipole: Methods based on spot shape analysis deduce the dipole orientation directly from the PSF shape [167]. However, they require the use of a high-NA objective in order to capture faint differences in the PSF. For a low-NA setting, other methods may be employed, which rely on polarization effects in the absorption or emission of fluorophores; the number of obtained photons for different polarization angles allows to infer the fluorophore's dipole orientation [192, 196]. In practice, this can be achieved, for example, by alternating excitation with linearly polarized light of two orthogonal polarization directions, yielding two different intensity values. The azimuthal angle ϕ can be inferred from the ratio of the obtained intensity values; the elevation angle θ can be inferred from the sum of the intensities relative to the maximum occurring single molecule intensity. Alternatively, the fluorophore emission can be used to

determine the dipole orientation by splitting the emitted photons in different polarization channels [193–195]. Further, the method assumes *a priori* knowledge on the amount of spatially homogeneous background noise. An estimate for the background noise can be obtained from regions in the field of view which are devoid of any specific signal. Notably, a recent preprint presented an approach for simultaneous estimation of emitter position, number of photons, background counts, and dipole orientation based on a Vortex PSF [172], assuming a high NA of 1.49—whether the method performance is transferable to a low-NA setting remains to be investigated.

The following aspects should be considered in order to obtain optimal results for our localization method and to interpret the resulting data correctly:

- Each fitted signal should arise from a single dye emitter only. In its current form, the method does not support multi-emitter fitting. Of note, under cryogenic temperatures the photophysics of fluorophores are decelerated [75, 197], resulting in the presence of overlapping signals. This issue can be circumvented by scrutinizing the intensity traces of a signal and selecting only those frames in which the signal is of single-emitter origin [90].
- In our simulations, we considered spatially homogeneous background only. In reality, spatially varying background may arise due to other fluorophores in close proximity, unspecific background signal or cellular autofluorescence. Contributions from other fluorophores can be avoided by analyzing only those frames in which all perturbing fluorophores are in the dark state. In general, other background signal typically shows less fluctuations in time and thus, can be subtracted, e.g. by filtering the signal in the time domain [198, 199].
- The analyzed pixel region should be large enough in order to contain the whole signal. As confirmed by Fig. 7.11, a rather small region of 13×13 pixels is sufficient, which corresponds to a side length of the region of approximately 2λ . However, the true fluorophore position is unknown *a priori*; selecting a ROI which is not centered at the true fluorophore position may lead to additional fitting instabilities, which can be avoided by selecting a slightly larger pixel region for the analysis. A choice of larger fitting regions requires a larger separation between fluorophores in the bright state, i.e. a lower density of active emitters. In addition, the presence of background signal may degrade the fit for very large ROIs.
- For the fitting procedure, the amount of astigmatism is assumed to be known. In addition, not only astigmatic distortion may affect the signal, but other aberrations due to imperfections in the optical setup may be present as well. Wavefront aberrations present in the optical system can be assessed by determining the 3D PSF of an isotropic single molecule emitter, either by recording the PSF of a freely rotating emitter at room temperature or merging the signals from multiple fixed emitters of different dipole orientations. Subsequently, Zernike polynomials can be fitted to the obtained PSF (Eq. (7.2) in *Methods*, section 7.4.1), yielding the astigmatism and any potential additional aberrations present in a particular setup. In principle, the possibility to include custom aberration maps is an advantage of any localization procedure which is based on fitting of an exact PSF model.

- Notably, fluorophore molecules with a dipole orientation close to the optical axis cannot be detected in case of usual excitation schemes, as their excitation probability is almost zero. This slightly reduces the detection efficiency in cryo-SMLM and should be considered when further analyzing and interpreting the obtained localization maps.

Taken together, a simple astigmatic imaging approach in combination with knowledge about the fluorophore dipole orientation allows to avoid localization biases in low-NA microscopy over a wide range of defocusing. In addition, the approach was shown to achieve optimal precision in the estimation of the lateral position as it attains the CRB. A precise and accurate localization of fluorophores provides the basis for reconstructing oligomeric structures of a few nanometers in size, as will be discussed in chapter 8 of this thesis.

7.4. Methods

7.4.1. Point spread function model

The PSF model used in this work is the full vectorial PSF model as described previously [43, 85, 169]. It comprises the electric field originating from a dipole emitter, the propagation through the layers of the optical system and the resulting intensity distribution at the image plane. We additionally introduced vertical astigmatism into the optical system, which breaks the symmetry of the PSF above and below the focal plane and thus, allows to estimate the amount of defocus.

We assumed a standard optical setup consisting of a sample layer with refractive index $n_1 = 1.33$ and an immersion layer with refractive index $n_2 = 1$, reflecting the situation of an air-objective corrected for the presence of a cryostat window. We chose a coordinate system in the canonic way, i.e. such that the z -axis coincides with the optical axis and the xy -plane coincides with the focal plane. A fluorophore situated in the focal plane can be described by a dipole point source with lateral position (x, y) and orientation (θ, ϕ) , where θ and ϕ denote the elevation and azimuthal angle, respectively (see Fig. 7.1a).

The starting point for our model is the electric field vector E_{BFP} (in Cartesian coordinates) in the back focal plane given by Eq. (18) in [43]. The electric field vector E_f in the image plane is then given by the Fourier transform (Eq. (5-14) in [42])

$$E_f(x_f, y_f) = \frac{1}{i\lambda f} e^{i\frac{\pi}{\lambda f}(x_f^2 + y_f^2)} \iint E_{\text{BFP}}(x, y) e^{i\frac{2\pi}{\lambda}W(x, y)} e^{-i\frac{2\pi}{\lambda f}(x_f x + y_f y)} dx dy, \quad (7.1)$$

where f denotes the focal length of the tube lens, λ the emission wavelength, and integration happens over the circular pupil area. The aberration term $W(x, y)$ introduces wavefront aberrations (Eq. (6-33) in [42]), which can be expanded into a linear combination of orthonormal Zernike polynomials

$$W(x, y) = \sum w_i Z_i(x, y), \quad (7.2)$$

where Z_i denotes the i -th Zernike polynomial (using Noll's indices) and w_i is the corresponding Zernike coefficient. For the calculation of the Zernike polynomials we used [200]. The normalized intensity distribution is then given by

$$I(x_f, y_f) = |E_f(x_f, y_f)|^2 \cdot \left(\iint |E_f(x_f, y_f)|^2 dx_f dy_f \right)^{-1}. \quad (7.3)$$

7.4.2. Simulations

Simulations were carried out in MATLAB using implementations of the above equations on a discrete grid. For a given dipole emitter with position (x, y) and orientation (θ, ϕ) we calculated the intensity distribution (Eq. (7.3)) within a region of interest (ROI) of size 17×17 pixels. Calculating the intensity values only at the discrete positions of the camera pixels may lead to inaccuracies. We therefore computed the values on a finer grid. The values of the smaller pixels were summed up to obtain the model value for each camera pixel. For the PSF simulations,

we chose an oversampling factor of 9. Further refinement of the discretization did not yield any measurable improvements (Fig. 7.15).

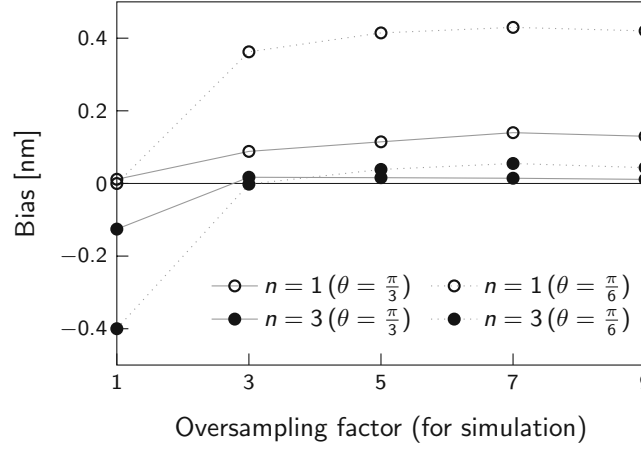


Figure 7.15.: Discretization of the PSF. The plot shows the localization bias arising from the choice of the oversampling factor in the calculation of the PSF. The x -axis shows the oversampling factor used for the simulation of the PSF. An oversampling factor of 1 corresponds to the PSF being evaluated at the discrete positions of the camera pixels. For larger oversampling factors, the PSF was evaluated on a finer grid, and resulting subpixel values were subsequently summed up. For the fitting, we used a PSF model calculated with an oversampling factor of n ($n = 1$ open symbols, $n = 3$ filled symbols). The defocus was set to $d = -500$ nm. Each data point represents 1500 simulations. A list of the remaining simulation parameters is given in Table 7.1 in the Appendix. Figure adapted from [187].

For each simulation the position (x, y) was chosen randomly in an area of 216×216 nm, typically corresponding to 2×2 pixels, in the center of the ROI.

In Eq. (7.2), we only considered nonzero coefficients w_4 and w_6 corresponding to defocus and vertical astigmatism, respectively. For the coefficient w_6 , we chose a value of $w_6 = 0.11\lambda$, corresponding to a RMS wavefront error of approximately 75 nm.

Unless specified otherwise, for our simulations we assumed the air-objective ($n_2 = 1$) LUC-PLFLN60X (Olympus), which has a magnification of 60x, a numerical aperture $NA = 0.7$ and a focal length of 3 mm. The focal length of the tube lens was set to $f = 180$ mm. For the sample we assumed dyes with an emission in the red region of the spectrum ($\lambda = 680$ nm) for staining the biological sample. For the sample, a refractive index of water ($n_1 = 1.33$) was assumed. As detector we assumed a sCMOS camera with a pixel size of $6.5 \mu\text{m}$, corresponding to 108 nm in the object space.

Simulations were performed for defocus values ranging from -500 nm to 500 nm in steps of 100 nm. For the dipole orientation, we considered combinations of the values $\phi \in \{0, \frac{\pi}{4}\}$ and $\theta \in \{0, \frac{\pi}{6}, \frac{\pi}{3}, \frac{\pi}{2}\}$. If not mentioned otherwise, a number of $N = 5 \cdot 10^5$ photons was assumed for each fluorophore. In practice, the absorption probability of a fluorophore depends on its dipole orientation. Thus, for Fig. 7.13 and 7.14, the obtained numbers of emitted photons N_{eff} was reduced accordingly and calculated as

$$N_{\text{eff}} = N \cos^2(\theta), \quad (7.4)$$

where θ is the elevation angle of the fluorophore dipole orientation. For all simulations, the obtained photon numbers for each pixel were subjected to Poissonian shot noise. Additionally, for some simulations a Poissonian background noise with standard deviation b was considered.

7.4.3. Cramér–Rao bound

The Cramér–Rao Bound (CRB) represents a lower bound on the variance of any unbiased estimator $\hat{\xi}$ for a parameter vector ξ [201]. The variance of the estimator $\hat{\xi}$ is bounded by

$$\text{Var}(\hat{\xi}_k) \geq (\mathcal{I}^{-1}(\xi))_{kk}, \quad (7.5)$$

where $(\mathcal{I}^{-1}(\xi))_{kk}$ are the diagonal elements of the inverse of the Fisher information matrix $\mathcal{I}(\xi)$ of the underlying stochastic process defined by

$$\mathcal{I}(\xi) := \mathbb{E} \left[\left(\frac{\partial}{\partial \xi} \ln f_{\xi}(z) \right)^T \left(\frac{\partial}{\partial \xi} \ln f_{\xi}(z) \right) \right], \quad (7.6)$$

with f_{ξ} being the probability distribution function of the data generation process. Note that ξ is assumed to be given as row vector. An estimator which attains the CRB is said to be efficient, i.e. it fully utilizes the information which is contained in the data and its precision cannot be further improved. The maximum likelihood estimator can attain the CRB and thus, is efficient [96]; no other estimator will yield a better precision.

If not stated otherwise, the parameter vector ξ which we estimated is given by the lateral position (x, y) of the dye molecule and the defocus value d , i.e. $\xi := (x, y, d)$. In order to calculate the CRB, one first needs to choose an appropriate model which describes the image data. A Poissonian model has been demonstrated to be a reasonable approximation for photon shot noise [202]. The photon count z_k in the k th pixel is modeled as the realization of a Poissonian random variable with mean $\nu_{\xi,k}$ and the probability distribution

$$f_{\xi,k}(z_k) = \frac{\nu_{\xi,k}^{z_k} e^{-\nu_{\xi,k}}}{z_k!}. \quad (7.7)$$

The probability distribution f_{ξ} for the whole image is then given by the product

$$f_{\xi}(z) = \prod_{k=1}^K f_{\xi,k}(z_k). \quad (7.8)$$

Combining Eq. (7.7) and (7.8) yields

$$\ln f_{\xi}(z) = \sum_{k=1}^K [z_k \ln(\nu_{\xi,k}) - \nu_{\xi,k} - \ln(z_k!)]. \quad (7.9)$$

The resulting Fisher information matrix is then given by

$$\mathcal{I}(\xi) = \sum_{k=1}^K \left(\frac{\partial \nu_{\xi,k}}{\partial \xi} \right)^T \left(\frac{\partial \nu_{\xi,k}}{\partial \xi} \right) \frac{1}{\nu_{\xi,k}}, \quad (7.10)$$

where we refer to [202] for a detailed calculation. Finally, the CRB is obtained by taking the inverse of the Fisher information matrix $\mathcal{I}(\xi)$. Since analytical computation of the partial derivatives in Eq. (7.10) is infeasible, we approximated them by numerically computing difference quotients.

7.4.4. Fitting procedure

First, as an *a priori* estimate for the mean background signal b^2 we calculated the mean signal of an image without fluorophore signal. Next, we determined an estimate for the total number of detected photons N_{total} per molecule by summing over all noise-corrected pixels. If not stated otherwise, we estimated the free parameters $\xi := (x, y, d)$. For this, we used a maximum likelihood estimator, since in this case the localization precision can attain the CRB [96]. Fitting was performed on normalized images. If not mentioned otherwise, the whole 17×17 region of interest was used for fitting. The log-likelihood function is identical to Eq. (7.9); here z_k denotes the photon number of the k th pixel of the normalized image. For the fit function $\nu_{\xi,k}$, we first determined the normalized PSF via Eq. (7.3): The PSF model for fitting was calculated on a discrete grid using an oversampling factor of 3, representing a good compromise between accuracy and computational speed of the fitting procedure (compare Fig. 7.15). Further, the obtained PSF was multiplied by N_{total} , and the mean of the background signal b^2 was added to each pixel. Finally, this function was normalized by the total sum of detected photons. The negative log-likelihood function was then minimized using the MATLAB function `fminunc`, yielding an estimate $\hat{\xi} := (\hat{x}, \hat{y}, \hat{d})$. It turned out to be important to select appropriate starting values, in order to avoid that the maximum likelihood estimator is trapped in local minima. Hence, we implemented a non-linear least squares fit, the outcome of which was used as the starting value for the maximum likelihood fit. The (x, y) starting values for the non-linear least squares fit were chosen randomly within a 2×2 pixel region around the center of the image. The starting value for the defocus d was chosen randomly between -500 nm and 500 nm.

In case of astigmatic imaging, we assumed the astigmatism to be known for the fitting procedure. If not stated otherwise, we also assumed that an estimate $(\hat{\theta}, \hat{\phi})$ is available for the fluorophore dipole orientation. We considered three different cases for the errors $\hat{\theta} - \theta$ and $\hat{\phi} - \phi$: (i) no errors, (ii) both errors in θ and ϕ are distributed normally with mean 0 and variance 2° , (iii) the errors in θ and ϕ are distributed normally with mean 0 and variance 4° or 2° , respectively.

For each parameter set, we simulated $n = 1000$ individual PSF images. The accuracy, i.e. the bias of the localization procedure, was calculated as $\mu_x = \bar{x} - x_0$ with $\bar{x} = \frac{1}{n} \sum_{i=1}^n \hat{x}_i$ and $n = 1000$, where \hat{x}_i denotes the estimate for the x -position obtained from image i . In addition, we calculated the precision σ_x of the fitting procedure as the standard deviation, i.e. $\sigma_x = \sqrt{\frac{1}{n-1} \sum_{i=1}^n (\hat{x}_i - \bar{x})^2}$ with $n = 1000$. The corresponding biases μ_y, μ_d and precisions σ_y, σ_d for the y -position and defocus, respectively, were calculated analogously.

7.5. Appendix

Fig.	ϕ	Astigm.	N	Red. exc.	b	Err. θ	Err. ϕ	Pixel size	ROI
7.2a	$\pi/4$	no	$5 \cdot 10^5$	no	100	0°	0°	108 nm	17×17
7.2b	$\pi/4$	no	$5 \cdot 10^5$	no	300	0°	0°	108 nm	17×17
7.4a,b	0	no	$5 \cdot 10^5$	no	0	—	—	108 nm	25×25
7.4c,d	$\pi/4$	no	$5 \cdot 10^5$	no	0	—	—	108 nm	25×25
7.5	random	yes	$5 \cdot 10^5$	no	100	—	—	108 nm	17×17
7.6	$\pi/4$	yes	$5 \cdot 10^5$	no	0	0°	0°	108 nm	17×17
7.7	0	yes	$5 \cdot 10^5$	no	0	0°	0°	108 nm	17×17
7.8	$\pi/4$	yes	$5 \cdot 10^4$	no	0	0°	0°	108 nm	17×17
7.9	$\pi/4$	yes	$5 \cdot 10^5$	no	0	0°	0°	216 nm	17×17
7.10a	$\pi/4$	yes	$5 \cdot 10^5$	no	100	0°	0°	108 nm	17×17
7.10b	$\pi/4$	yes	$5 \cdot 10^5$	no	300	0°	0°	108 nm	17×17
7.11	$\pi/4$	yes	$5 \cdot 10^5$	no	0, 300	0°	0°	108 nm	various
7.12a	$\pi/4$	yes	$5 \cdot 10^5$	no	100	2°	2°	108 nm	17×17
7.12b	$\pi/4$	yes	$5 \cdot 10^5$	no	300	2°	2°	108 nm	17×17
7.12c	$\pi/4$	yes	$5 \cdot 10^5$	no	100	4°	2°	108 nm	17×17
7.12d	$\pi/4$	yes	$5 \cdot 10^5$	no	300	4°	2°	108 nm	17×17
7.13	$\pi/4$	yes	$5 \cdot 10^5$	yes	0	0°	0°	108 nm	17×17
7.14	$\pi/4$	yes	$5 \cdot 10^5$	yes	100	2°	2°	108 nm	17×17
7.15	$\pi/4$	yes	$5 \cdot 10^5$	no	0	0°	0°	108 nm	17×17

Table 7.1.: **Table of simulation parameters.** If not mentioned otherwise, the elevation angle was set to $\theta = 0, \pi/6, \pi/3, \pi/2$ and 1000 simulations per data point were performed. Columns: Figure number, azimuthal angle (ϕ), astigmatism, number of photons (N), reduced excitation, background noise (b), standard deviation of estimation of θ , standard deviation of estimation of ϕ , pixel size, region of interest (ROI) in pixel.

8. Sizing of oligomers via cryo-SMLM

This chapter contains content from the following publication:

M. C. Schneider*, R. Telschow*, G. Mercier, M. López-Martinez, O. Scherzer, G. J. Schütz.
A workflow for sizing oligomeric biomolecules based on cryo single molecule localization microscopy. PLoS One, 16(1), 2021.

doi: 10.1371/journal.pone.0245693

Aim

Protein function is often tightly connected to its arrangement within oligomeric complexes. A localization precision of around 10 nm achieved at room temperature is sufficient to resolve and reconstruct larger structures such as the nuclear pore complex with a diameter of around 100 nm; other proteins, including ion channels in the plasma membrane, have a size of a few nanometers only and thus, cannot be resolved with conventional SMLM techniques. Here, we aimed to develop a workflow for sizing oligomeric structures at the nanoscale tailored for SMLM performed at cryogenic temperatures.

Contribution

This work was performed in collaboration with Roger Telschow, Gwenael Mercier and Otmar Scherzer from the Faculty of Mathematics of the University of Vienna. Together with all co-authors, I designed the workflow and conceived the analysis method. Further, I developed code for the simulation of SMLM localization maps of oligomeric structures assuming cryogenic conditions. In addition, I implemented code for the analysis of localization maps together with Roger Telschow and Gwenael Mercier. I performed simulations, analyzed and interpreted the resulting data.

Outcome

We developed a workflow for precise sizing of regular oligomeric structures under cryogenic conditions. The fixed orientation of fluorophores in cryo-SMLM was used as additional information in the analysis in order to assign localizations to individual fluorophores with high reliability. The performance of our method for sizing oligomeric structures was extensively characterized based on simulations of SMLM localization maps. Oligomer side lengths could be determined with a relative error of less than 1% for tetramers with a nominal side length of 5 nm, even if the assumed localization precision for an individual signal was more than 2 nm.

8.1. Introduction

The exact structural arrangement of proteins is crucial for their function. As a common feature in biology, the function of proteins is often established and affected by the association of several polypeptide chains into an oligomer. In particular, an oligomer is a protein composed of several subunits; if all structural subunits are identical, the protein complex is a homo-oligomer, otherwise a hetero-oligomer. A structural subunit of an oligomer—composed either of a single or multiple polypeptide chains—is referred to as protomer. Oligomers can be comprised of different numbers of subunits; for example, a dimer, trimer or tetramer is an assembly of two, three or four subunits, respectively. The number of subunits is also referred to as the degree of oligomerization. Most oligomers in the human proteome form dimers (two subunits) to hexamers (six subunits) and exhibit a symmetric structure [203]. Common examples for oligomers in the plasma membrane are ion channels [24], which regulate the transport of ions across the plasma membrane and are highly selective. Typically, they have a size of 2–10 nm with pore diameters below 1 nm. As example, the tetrameric structure of the potassium/sodium channel HCN1 is depicted in Fig. 8.1.



Figure 8.1.: Oligomer structure. The figure depicts the structure of the voltage-gated potassium/sodium channel HCN1 in an *en face* view [204]. This ion channel is a homo-tetrameric protein composed of four identical subunits, referred to as protomers. Scale bar: 1 nm. Figure adapted from [24].

Although many protein structures have been determined via cryo-EM, their exact size and arrangement in the plasma membrane often remains unknown. While larger protein complexes such as the NPC can be imaged in their native environment via SMLM, the resolution of conventional SMLM techniques is not sufficient to resolve small oligomers of less than 5 nm in size. The problem is illustrated in Fig. 8.2: Overcounting in combination with insufficient localization precision compared to oligomer size hampers a correct identification of the oligomer structure; apparently, there is no realistic chance to identify any structural organization of the oligomer. In addition, the oligomer size is substantially overestimated by a circle fit of the localizations (dashed lines).

SMLM performed at cryogenic temperature promises to yield superior localization precision [75, 90, 164, 165]. First, cryo-fixation approaches offer supreme fixation by prohibiting residual diffusion and conserving the sample's ultrastructure [11]. Second, due to the decelerated photobleaching rates of fluorophores at cryogenic temperatures, a higher photon yield per

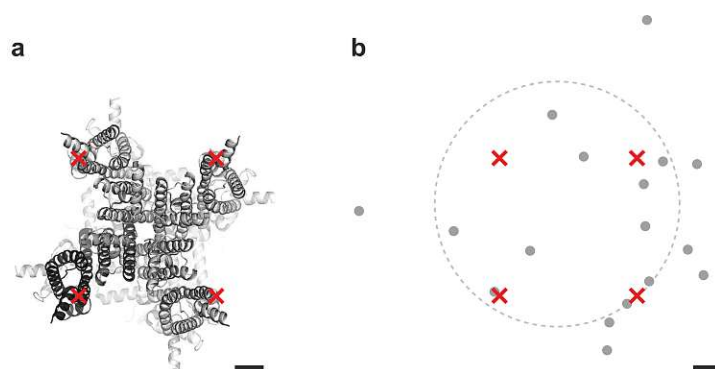


Figure 8.2.: SMLM imaging of small oligomeric structures. (a) Protein structure of the ion channel HCN1 [204]. Red crosses illustrate the assumed positions of dye molecules for SMLM imaging. Figure adapted from [24]. (b) SMLM localization map. The actual positions of the dye molecules—arranged in a square with a side length of 5 nm—are shown as red crosses. The gray dots represent the obtained localization map from a simulated SMLM experiment. The mean localization precision was 1.8 nm. Performing a circle fit of the localizations substantially overestimated the oligomer size (dashed line). Scale bars: 1 nm.

fluorophore can be achieved [75,87]. Still, a direct interpretation of SMLM localization maps is impeded by two factors: Due to inefficient labeling or detection efficiency, some parts of a biomolecular structure may not be visible at all, while others may be heavily overrepresented due to overcounting. Particle averaging approaches aim to circumvent this issue by combining the information obtained from thousands of identical copies of a particle [44,182–184].

In the following, we assumed a tetrameric protein within the plasma membrane with a side length of 5 nm (as in Fig. 8.2). We simulated corresponding localization maps for SMLM performed under cryogenic conditions. Each protomer was assumed to be labeled with one dye molecule only, which can be achieved experimentally for example via protein tags or unnatural amino acids [69,205]. For simulating fluorophore blinking, we used a log-normal distribution for the number of localizations per molecule (see *Methods*, section 8.4.1). Of note, at cryogenic temperature fluorophore dipole orientations are fixed; therefore, a random dipole orientation was assigned to each fluorophore and the number of photons for each signal was calculated dependent on this orientation. The maximum photon number that can be obtained for a dipole orientation parallel to the excitation polarization is denoted as N_{\max} in the following.

First, we analyzed the simulated localization data obtained for a set of 1000 simulated tetramers with a template-free approach published by Heydarian et al. [183], which allows to reconstruct oligomers of unknown structures. For high single molecule localization precision achieved with $N_{\max} = 10^5$ photons, the method indeed yielded satisfactory results and clearly revealed the tetrameric arrangement of the individual dye molecules (Fig. 8.3d). However, a decrease in the photon number leads to increased localization errors and the analysis of the localization maps becomes more difficult. Eventually, for $N_{\max} = 10^4$ photons per dye molecule no oligomeric substructure could be identified (Fig. 8.3a). Notably, the possibility to reliably assign localizations to individual biomolecules of interest would greatly facilitate and improve particle reconstruction.

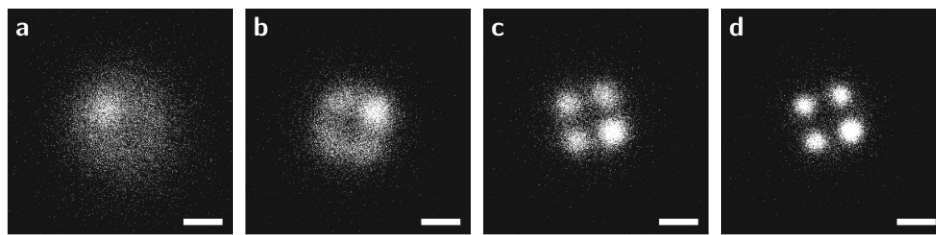


Figure 8.3.: Reconstruction with a template-free method. Localization maps of tetramers recorded under cryogenic conditions were simulated and analyzed via a template-free all-to-all registration method published by Heydarian et al. [183]. For each panel, 1000 tetramers with a side length of 5 nm were simulated, assuming $N_{\max} = 10^4$ (a), $N_{\max} = 3 \cdot 10^4$ (b), $N_{\max} = 5 \cdot 10^4$ (c) and $N_{\max} = 10^5$ photons (d). Scale bars: 5 nm. Figure from [206].

In this chapter, I present a new workflow for the analysis of SMLM localization maps obtained from oligomeric protein complexes recorded under cryogenic conditions. The presented approach is template-based and aims at the precise determination of oligomer size via assignment of localizations to individual dye molecules. Particularly, in cryo-SMLM rotational diffusion of the fluorophores' dipole orientation is prevented at least over the time scale of hours [90]. The dipole orientation, fixed at the time point of freezing, constitutes a unique characteristic for each dye molecule, which can be exploited in order to distinguish localizations arising from different fluorophores. This can be achieved via exciting the sample alternately with linearly polarized light of orthogonal polarization direction. The assignment of localizations to individual molecules substantially improved oligomer reconstruction. The performance of the proposed approach was validated and characterized by determining the size of regular oligomeric structures in 2D based on the analysis of simulated SMLM localizations obtained from thousands of oligomers.

8.2. Results

8.2.1. Sizing oligomers assuming cryogenic imaging conditions

In the following, we assumed a tetrameric protein structure with a side length of 5 nm as in Fig. 8.2 and Fig. 8.3. In order to facilitate the analysis of oligomeric structures, one may opt for a template-based approach and include prior knowledge. Here, we assumed that the oligomer can be represented by a regular polygonal structure, i.e. a square in the case of a tetramer. Each protomer was assumed to be labeled with exactly one dye molecule. Hence, the dyes representing the protomers were assumed to lie on the perimeter of a circle. As illustrative example, we considered a tetramer which yields the same localization map as depicted in Fig. 8.2b, but assumed cryogenic imaging conditions (Fig. 8.4).

A key feature of the proposed method is the grouping of localizations belonging to the same dye molecule. At cryogenic temperatures, rotational diffusion of the dye molecules is severely restricted and thus, the fluorophores' dipole orientations appear virtually fixed over time-scales of hours [90]. Fig. 8.4a shows the assumed fluorophore dipole orientations for our representative

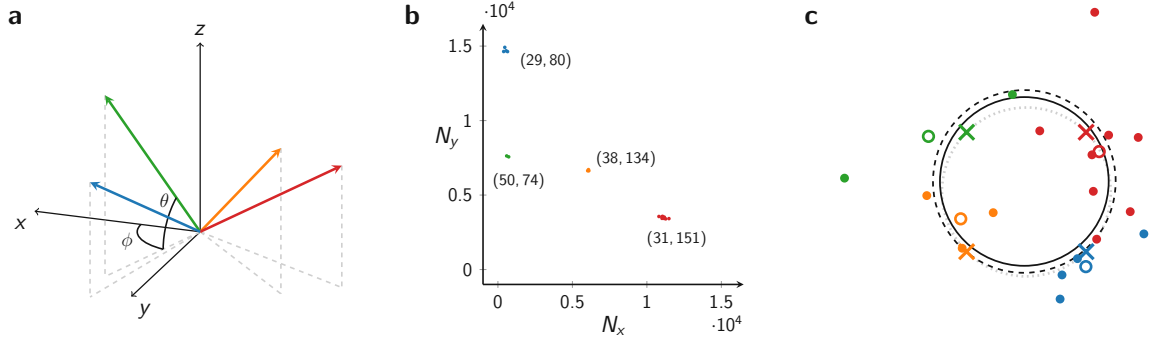


Figure 8.4.: Schematic representation of the method. We assumed a tetramer being labeled with four dye molecules, i.e. each protomer was assumed to carry exactly one fluorophore. A random but fixed dipole orientation was assigned to each fluorophore as indicated by the colored arrows in panel **a**. The optical axis was assumed to be parallel to the z -axis; the dipole orientations were defined by the azimuthal angle ϕ and the elevation angle θ . Subsequently, the fluorophores were assumed to be excited alternately with linearly polarized light of polarization direction along the x - and y -axis, respectively. The obtained signal brightness values N_x and N_y for x - and y -polarized excitation light, respectively, are shown in panel **b**. The color code corresponds to panel **a** and indicates the fluorophore from which each localization was obtained. Annotated numbers indicate the respective dipole orientation (θ, ϕ) of the fluorophore in degrees. N_{\max} was set to $2 \cdot 10^4$ photons. Based on the intensity values N_x, N_y , the localizations could be divided easily into four groups. This grouping of localizations was applied to the localization map obtained from the oligomer (**c**). The average position of each localization group is plotted as open dot. These positions were used to estimate the oligomer size via a circle fit. The dashed and solid lines show the uncorrected and bias-corrected fitting results. Figure modified from [206].

simulated tetramer. If a fixed fluorophore is excited with linearly polarized light, the absorption probability directly depends on the scalar product between the fluorophore's dipole orientation and the vector describing the polarization of the excitation light. The dipole orientation of a fluorophore can be described by the vector (θ, ϕ) , where θ is the elevation angle and ϕ the azimuthal angle (Fig. 8.4a). For our method, we assumed the fluorophores to be excited consecutively with light of orthogonal polarization directions \vec{p}_1 and \vec{p}_2 , which are parallel to the imaging plane and orthogonal to each other. Without loss of generality, we set the Cartesian coordinate system such that the z -axis corresponds to the optical axis, and the x, y -axes are aligned with \vec{p}_1 and \vec{p}_2 , respectively. Then, the obtained effective number of photons N_x and N_y for excitation with \vec{p}_1 - and \vec{p}_2 -polarized light, respectively, can be calculated as

$$N_x = N_{\max} \cos^2(\theta) \cos^2(\phi), \quad (8.1)$$

$$N_y = N_{\max} \cos^2(\theta) \sin^2(\phi). \quad (8.2)$$

where N_{\max} denotes the maximum number of photons per single molecule signal obtained in case that the fluorophore's dipole orientation is parallel to the excitation polarization. The obtained brightness values for the dipole orientations from Fig. 8.4a are shown in panel b. Provided that the dipole orientations are distributed randomly in space, the values (N_x, N_y) can in principle cover the whole region confined by $N_x > 0, N_y > 0$ and $N_x + N_y < N_{\max}$, with a slightly reduced probability density in the center of the region (Fig. 8.5a).

For our method, we assumed the following experimental procedure: The sample is excited

consecutively with \vec{p}_1 - and \vec{p}_2 -polarized light, leading to signals of brightness (N_x, N_y) according to Eq. (8.1) and (8.2), which are imaged on the same region of the camera chip. Subsequently, the two images are added up, yielding a total number of photons $N_{\text{total}} = N_x + N_y$ for a single molecule signal. The localization procedure is performed on the sum image. Considering fixed dipole moments, a certain fraction of the fluorophores will show dipoles with an elevation angle close to 90° , i.e. almost parallel to the optical axis. These fluorophores will yield rather faint signals characterized by high localization errors. Consequently, a rather broad distribution of localization errors can be expected. If faint signals are taken into account, this will also cause a lot of undesired background localizations in an experiment. We hence restricted the analysis to sufficiently bright signals with $N_x + N_y > N_{\text{min}}$ (Fig. 8.5b). Signals with $N_x + N_y < N_{\text{min}}$ were rejected, corresponding to a threshold for the localization precision σ_{loc}^* set to 10 nm.

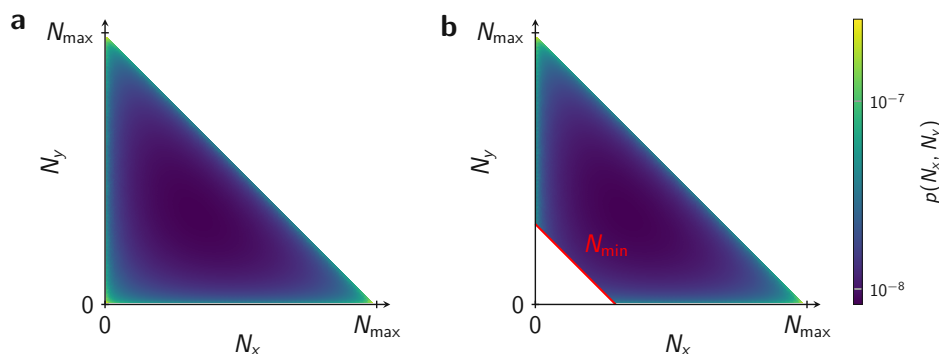


Figure 8.5.: Probability density for brightness values. Fluorophore dipole orientations were assumed to be distributed uniformly on a sphere. Naturally, the brightness values (N_x, N_y) are confined to the region defined by $N_x > 0$, $N_y > 0$ and $N_x + N_y < N_{\text{max}}$. (a) Full probability distribution according to Eq. (8.6) from the *Methods*, section 8.4.1. (b) Truncated distribution, which accounts for the user-defined detection threshold N_{min} . For the calculation of panel b we assumed $N_{\text{max}} = 10^4$ photons, background noise $b = 300$, and a threshold for the localization precision $\sigma_{\text{loc}}^* = 10$ nm, corresponding to $N_{\text{min}} = 2960$. Figure adapted from [206].

In Fig. 8.4b each data point represents one localization. In this representation of the data it is straightforward to group all the localizations into four groups. The localizations of each group belong to one of the four simulated fluorophore molecules; the grouping is indicated by color. Note that for the simulations the obtained numbers of photons (N_x, N_y) for each single molecule signal was subjected to photon shot noise. Hence, the point clouds corresponding to each fluorophore can be elliptically distorted according to different amounts of Poisson noise for N_x and N_y .

The assignment of localizations to individual fluorophores substantially improved the oligomer analysis as can be seen in Fig. 8.4c. In this case, all localizations assigned to the same dye molecule—as indicated by the color code—were averaged (open dots). Performing a circle fit of these averaged positions yielded a resulting circle (dashed line) which was fairly close to the ground truth (dotted line). Interestingly, a circle fit exhibits an inherent bias towards larger circle radii [207]. This can be intuitively understood as on average more data points lie outside the circle, which thus contribute with overall higher statistical weight. Correcting for this bias yielded an improved fit result, as shown by the solid line in Fig. 8.4c. The formula for the bias

and the details of the bias correction can be found in the *Methods* (section 8.4.2, Eq. (8.14) and (8.19)).

In order to obtain a robust estimation of the oligomer size, a large number of identical oligomers can be recorded and analyzed. For this, we assumed the oligomers to be sufficiently separated from each other so that localizations belonging to individual oligomers can be reliably grouped by a standard 2D clustering method [59, 116]. If not mentioned otherwise, we assumed that every protomer was labeled with exactly one dye molecule. For each oligomer, the corresponding localizations were further subdivided into localization groups representing individual fluorophores. This assignment was based on the detected intensities (N_x, N_y) for each localization. Next, all oligomers yielding n distinct groups of localizations were regarded as eligible and taken for further analysis, where n corresponds to the assumed oligomer degree. In particular, this eligibility criterion rejects scenarios in which groups of localizations overlap and thus, would be interpreted as one spurious position at the average of these localizations.

All oligomers which qualified as eligible were further analyzed as described above. In short, for each oligomer the individual localization groups were averaged and a circle fit was performed while accounting for the bias. Of note, each oligomer was analyzed separately. The obtained radii estimates \hat{R} were transformed into side length estimates via $\hat{l} = 2\hat{R}\sin(\pi/n)$, where n denotes the oligomer degree. Fig. 8.6 shows a histogram of the resulting estimated side lengths for $5 \cdot 10^5$ simulated tetramers with a nominal side length of 5 nm. In order to obtain a single overall value as side length estimate for the underlying oligomer structure, a summary statistic of all estimated side lengths can be calculated, e.g. the mean (blue line) or the median (green

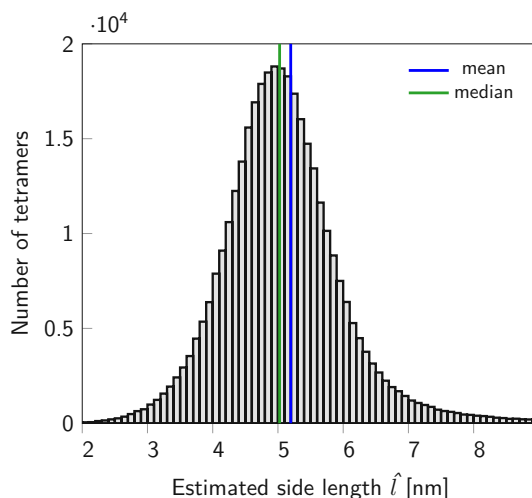


Figure 8.6.: Estimating oligomer side length from a set of oligomers. The histogram shows the estimated tetramer side length for a data set of $5 \cdot 10^5$ tetramers with nominal side length of 5 nm. After localization assignment to individual dye molecules, a total number of approximately $3.67 \cdot 10^5$ tetramers were eligible for further analysis. For the side length estimation, a circle fit was performed for each oligomer by minimizing the term from Eq. (8.10) while accounting for the bias according to Eq. (8.19) from the *Methods* (section 8.4.2). Analysis of the histogram yields a mean of 5.1959 nm (blue line) and a median of 5.0256 nm (green line). Values larger than 9 nm were cut off for display only. Figure adapted from [206].

line). Note that the histogram in Fig. 8.6 shows a distribution which exhibits a slight positive skew. As expected, the median of the simulation results shown in the histogram was closer to the ground truth value of 5 nm than the mean, and hence, was taken in the following as an overall estimator for the oligomer size.

8.2.2. Characterization of the method

We investigated the performance of the proposed method via extensive simulations. Fig. 8.7 shows a characterization of the localization assignment process (gray solid line) and the resulting eligibility of oligomers (black solid line) for varying levels of single molecule brightness N_{\max} . The fraction of tetramers for which all localizations were assigned to individual fluorophores correctly increases for higher number of photons and approaches a value of 1. This can be explained by the fact that the relative spread of the point clouds (N_x, N_y) representing the localizations of a single fluorophore shrinks with increasing N_{\max} . Hence, the results of the applied clustering algorithm improved. The improved assignment of localizations in turn increased the number of eligible oligomers and thus, the curve for the fraction of eligible oligomers followed a similar trend. However, this fraction was slightly lower because fluorophores with a dipole orientation almost parallel to the optical axis could not be detected. Therefore, some oligomers yielded less than n localization groups and thus, did not qualify as eligible. For very high values of N_{\max} an increased number of fluorophores exceeded the detection threshold and its impact decreased. The dashed line in Fig. 8.7 shows the fraction of eligible oligomers with incorrectly assigned localizations, the contribution of which was found to be negligible.

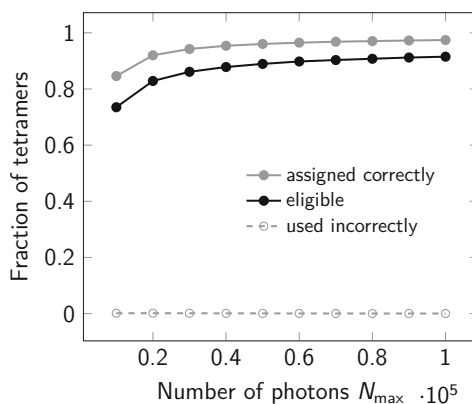


Figure 8.7.: Assignment of localizations and eligibility of oligomers. The maximum number of photons N_{\max} emitted from a fluorophore was varied from 10^4 to 10^5 . The gray line indicates the fraction of tetramers, for which all localizations were assigned to the correct dye molecule. A tetramer was considered eligible for further analysis, if its localizations were assigned to $n=4$ groups. The black line shows the fraction of eligible tetramers. The fraction of oligomers which contained incorrectly assigned localizations, but were regarded as eligible was negligible (gray dashed line). For each data point a set of $5 \cdot 10^5$ tetramers with a side length 5 nm was simulated. Figure adapted from [206].

In the following, we characterized the performance of the method regarding the estimation of oligomer side length. For this, we determined the relative error ε_l of the side length estimate

as

$$\varepsilon_l = \frac{\hat{l} - l}{l}, \quad (8.3)$$

where \hat{l} and l denote the estimated and ground truth side length, respectively. First, we analyzed the dependence of ε_l on the obtained number of photons by varying N_{\max} from 10^4 to 10^5 (Fig. 8.8a). Note that the plot shows a symmetric logarithmic y-axis. Positive and negative values on the y-axis correspond to positive and negative relative errors, respectively. Relative errors with absolute values $|\varepsilon_l|$ smaller than 10^{-3} are shown on a linear scale. The plot shows results both for taking the mean (filled symbols) and median (open symbols) of all individual estimated side lengths as a summary statistics for the whole data set of oligomers. The comparison revealed a superior performance of the median, which was hence used for all subsequent figures. For all considered values of N_{\max} , the median yielded highly precise results with ε_l below 0.5 %, corresponding to 0.025 nm. For N_{\max} above $2 \cdot 10^4$ photons the side length was slightly underestimated. Notably, the average localization precision $\bar{\sigma}_{\text{loc}}$ was given by 2.30 nm and 0.78 nm for $N_{\max} = 10^4$ and $N_{\max} = 10^5$, respectively, which exceeded the achieved precision of the side length estimate by several orders of magnitude.

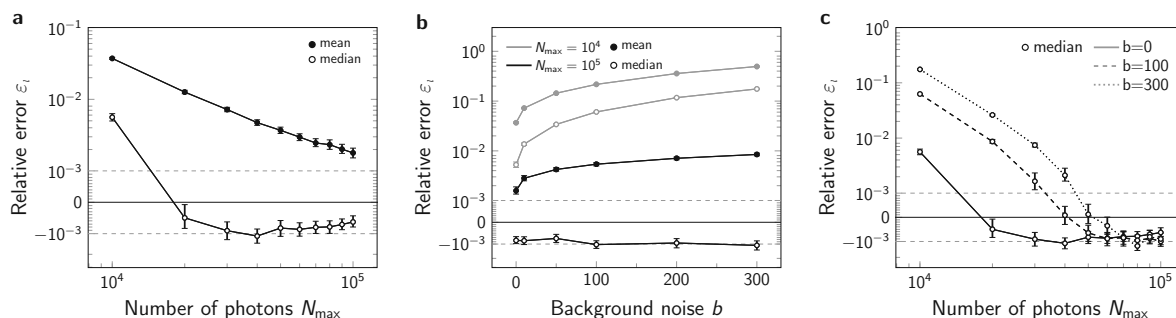


Figure 8.8.: Influence of signal brightness and noise. Relative errors ε_l for the estimation of tetramer side length are shown for varying number of photons N_{\max} (a) and background noise (b). In both panels we compared the performance of the mean (full symbols) and median (open symbols) as a summary statistic. For a, we assumed zero background noise b . For panel b, we considered $N_{\max} = 10^4$ photons (gray lines) and $N_{\max} = 10^5$ (black lines). Panel c shows the influence of signal brightness for different levels of background noise including $b = 0$ (solid line), $b = 100$ (dashed line) and $b = 300$ (dotted line). Note that the data for $b = 0$ is identical to the data for the median from panel a. All panels show symmetric logarithmic plots, where positive and negative relative errors represent overestimation and underestimation, respectively. For each data point $5 \cdot 10^5$ tetramers with a side length of 5 nm were simulated. Error bars indicate the 95% confidence intervals. Figure adapted from [206].

In the previous simulations, we did not consider any background noise, which inevitably occurs in a real experiment. Contributions to this noise may arise both from camera noise and sample background. The main consequence of background noise in the simulations is an increase in the localization errors. In Fig. 8.8b we explored the impact of background noise on the estimation of oligomer side length by increasing the standard deviation of simulated background counts per pixel up to $b = 300$; this corresponds to a signal-to-noise ratio of 33 and 333 for $N_{\max} = 10^4$ photons and $N_{\max} = 10^5$ photons, respectively, in the best case of fluorophore dipole orientations being parallel to the focal plane. Results are shown both for photon numbers

$N_{\max} = 10^4$ and 10^5 . For low photon numbers with $N_{\max} = 10^4$, the relative contribution of background noise was higher and the side length estimation slightly deteriorated with increasing background noise. For high photon numbers, the influence of background noise was found to be negligible. Fig. 8.8c shows a combined plot of the influence of photon numbers and background noise. In case that photon numbers were high relative to the background noise, the method yielded highly precise estimation of the oligomer side length.

Further, we were interested in the number of recorded oligomers required for achieving a reliable estimation of oligomer side length. Fig. 8.9a shows the resulting relative errors for both $N_{\max} = 10^4$ (gray) and $N_{\max} = 10^5$ (black) photons. Our method yielded robust results, which were independent of the number of analyzed oligomers. For $N_{\max} = 10^4$ and 10^5 photons a marginal bias towards over- and underestimation of oligomer size, respectively, was observed. As expected, the relative standard error of the median decreased with the number of oligomers available for the analysis (Fig. 8.9b). In all further simulations, we assumed a total number of $N_{\text{oligo}} = 5 \cdot 10^5$ oligomers.

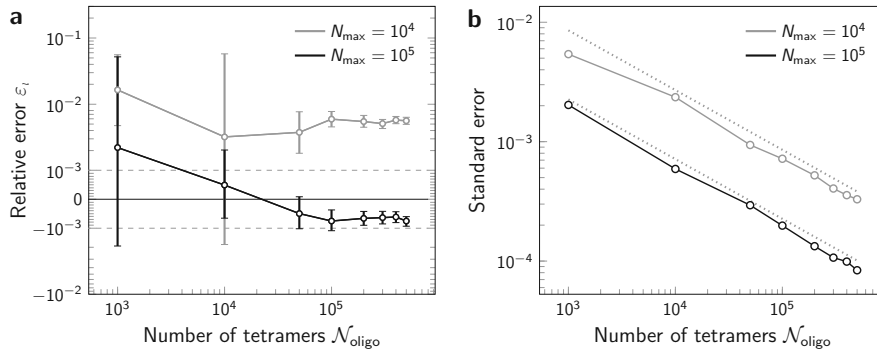


Figure 8.9.: Influence of the number of available oligomers. The panels show the effect of varying numbers of simulated tetramers N_{oligo} on the relative error ε_l (a) and its standard error (b), both for a maximum photon number $N_{\max} = 10^4$ (gray) and $N_{\max} = 10^5$ (black). Positive and negative relative errors in panel a represent overestimation and underestimation, respectively. Error bars indicate the 95% confidence intervals. The dashed lines in panel b are shown as a reference and depict $N_{\text{oligo}}^{-1/2}$. Figure adapted from [206].

An important aspect in fluorescence microscopy is labeling efficiency. In an SMLM experiment, a certain fraction of protomers will never be detected. This may be due to incomplete maturation of fluorescent proteins or prebleaching of dye molecules, for example. In Fig. 8.10 we investigated the impact of incomplete labeling on our method. The probability that an individual oligomer is labeled with exactly n dye molecules is given by η^n , where η denotes the labeling efficiency. For example, with $n=4$ and $\eta=0.3$, the probability that a tetramer is fully labeled calculates to 0.0081. Of note, this probability further reduces when considering that fluorophores with a dipole orientation close to the optical axis cannot be detected. As expected, the fraction of eligible tetramers decreased drastically with decreasing labeling efficiency (Fig. 8.10a). In general, incomplete labeling impairs the results of oligomer reconstruction. For our method, however, the effect of decreased labeling efficiency was only marginal as can be seen in Fig. 8.10b. This can be explained by the fact that data was filtered according to the eligibility criterion: Any oligomers which yielded less than n localization groups

and thus would have distorted the analysis were rejected. Of note, this approach requires an assumption about the oligomer degree. The effect of decreased labeling efficiency (Fig. 8.10) was comparable with the influence of a lower number of recorded oligomers. In both cases, the number of eligible tetramers for further analysis reduced (Fig. 8.10a). While correct side length estimation was hardly impeded, the standard error of the estimates increased for decreasing labeling efficiency (Fig. 8.10b,c).

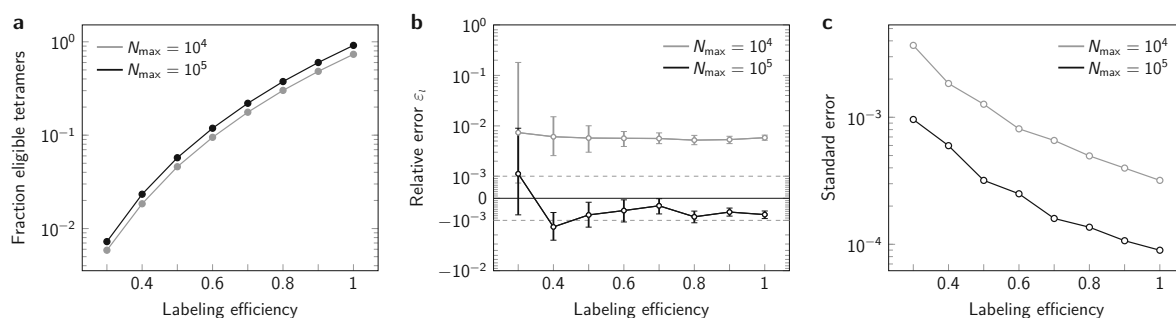


Figure 8.10.: Influence of labeling efficiency. (a) Fraction of eligible tetramers for varying labeling efficiency. (b) Relative error ε_l of the side length estimation. Positive and negative relative errors represent overestimation and underestimation, respectively. Error bars indicate the 95% confidence intervals. (c) Relative standard error of the median for varying labeling efficiency. For each data point $5 \cdot 10^5$ tetramers with a side length of 5 nm were simulated. Assumed photon numbers were $N_{\max} = 10^4$ (gray) and 10^5 (black). Figure adapted from [206].

Next, we investigated the performance of the method for extremely small oligomers. For this, we simulated oligomers with side lengths of 10 nm down to 1 nm (Fig. 8.11). The resulting relative errors were found to be negligible for side lengths above 5 nm and 2 nm for $N_{\max} = 10^4$ and 10^5 photons, respectively. For even shorter side lengths, relative errors strongly increased and an overestimation of oligomer side length up to a factor of 2 could be observed. This can be explained by increasingly unstable fit results in case that localization errors are high compared to the oligomer side length. Overall, relative errors in side length estimation of less than 1 % could be achieved if the ratio of the average localization precision $\bar{\sigma}_{\text{loc}}$ and the ground truth side length l was smaller than 0.5.

Further, we were interested in the performance of our method for different oligomer degrees. For this, we applied the method to simulations of tri-, tetra-, penta- and hexamers, i.e. oligomers consisting of $n = 3, 4, 5, 6$ protomers (Fig. 8.12). The shape of each oligomer type was assumed to be a regular polygon with n vertices and a circumradius of 4 nm. Note that this yielded a different ground truth side length l for each oligomer type, as indicated in Fig. 8.12. With an increasing number n of protomers, the fraction of eligible oligomers decreased slightly (Fig. 8.12a). This can be explained by the increased probability of at least one protomer carrying a fluorophore with a dipole orientation close to the optical axis, thus falling below the detection threshold. In addition, for a higher number of protomers per oligomer the localization assignment becomes increasingly difficult; wrong assignments further reduce the number of eligible oligomers. The relative errors in side length estimation obtained for different oligomer degrees are shown in Fig. 8.12b. For both $N_{\max} = 10^4$ and 10^5 photons we observed a slightly better performance of our method for higher oligomer degrees. This can be explained by the

increased number of localizations available for higher oligomer degrees n , which enhances the quality of the circle fit. Importantly, for all simulated scenarios the resulting relative errors were well below 1 %.

In an experiment, it can be difficult to ensure that the orientation of oligomers is exactly parallel to the focal plane. Hence, the localizations arising from an oligomer with a shape of a regular polygon may appear slightly elliptically distorted. Therefore, we were interested to what extent a tilt out of the focal plane influences the results (Fig. 8.13). Evidently, a decrease

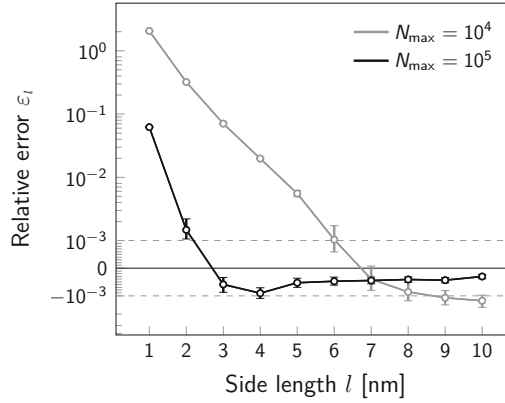


Figure 8.11.: Influence of oligomer side length. The relative error ε_l for the estimation of tetramer side length upon variation of the nominal side length l is shown both for a maximum number of photons $N_{\max} = 10^4$ (gray) and 10^5 (black), corresponding to an average localization precision of $\bar{\sigma}_{\text{loc}} = 2.3$ nm and 0.78 nm, respectively. Positive and negative relative errors represent overestimation and underestimation, respectively. For each data point a set of $5 \cdot 10^5$ tetramers was simulated. Error bars indicate the 95% confidence intervals. Figure adapted from [206].

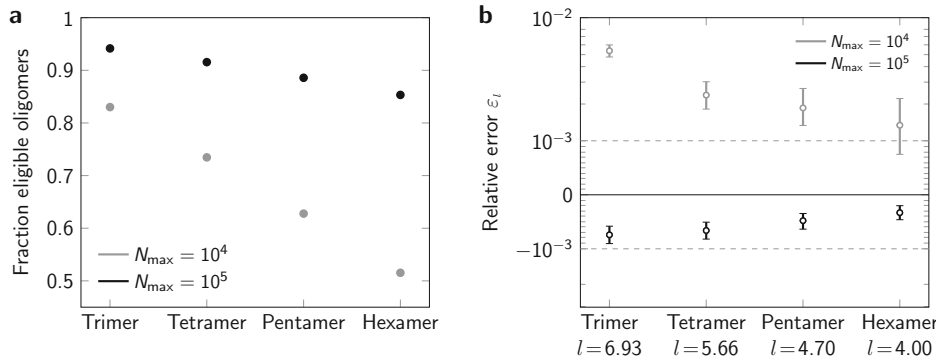


Figure 8.12.: Degree of oligomerization. Oligomers consisting of $n = 3, 4, 5, 6$ protomers were simulated, representing tri-, tetra-, penta- and hexamers. The radius of the circumscribed circle of each oligomer was set to 4 nm, yielding a side length of $l = 6.93$ nm, 5.66 nm, 4.70 nm and 4.00 nm for the respective oligomer types. (a) Percentage of eligible oligomers for varying degree of oligomerization. (b) Relative error ε_l for varying degree of oligomerization shown in a symmetric logarithmic plot. Positive and negative relative errors represent overestimation and underestimation, respectively. Error bars indicate the 95% confidence intervals. Assumed photon numbers were $N_{\max} = 10^4$ (gray) and 10^5 (black). For each data point $5 \cdot 10^5$ oligomers were simulated. Figure adapted from [206].

in the tilt angle led to shorter side length estimates. For tilts below a value of 10 degrees, the relative errors for side length estimation remained below 1 %. Surprisingly, even for substantial tilts up to 40 degrees, relative errors below 10 % could be achieved.

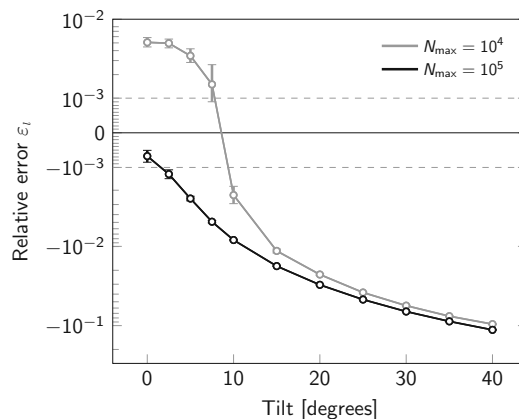


Figure 8.13.: Influence of a tilt of oligomers. The relative error ε_l is shown for varying degrees of tilt of the oligomers with respect to the focal plane. Overestimation of oligomer sizes is indicated by positive relative errors, underestimation by negative relative errors. The assumed maximum number of photons was set to $N_{\max} = 10^4$ (gray) and 10^5 (black). For each data point $5 \cdot 10^5$ tetramers with a side length of 5 nm were simulated. Error bars indicate the 95% confidence intervals. Figure from [206].

Finally, we were interested in the performance of our method regarding runtime. Fig. 8.14 shows the runtime for the analysis of data sets containing varying numbers of simulated tetramers. The input for the analysis were the localization coordinates for each simulated oligomer. The given runtime comprises the localization assignment to individual fluorophores and the circle fit. The runtime of our analysis for a set of $5 \cdot 10^5$ tetramers, as used in all previous figures, amounted to approximately 3 min. As each oligomer was analyzed separately, the runtime scaled linearly with the number of oligomers $\mathcal{N}_{\text{oligo}}$. Notably, linear time complexity is a great advantage especially for the analysis of large data sets.

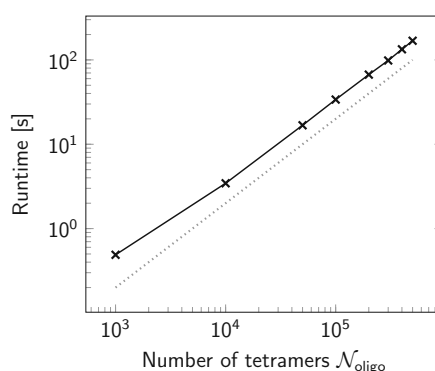


Figure 8.14.: Runtime scaling. Analysis of runtime for varying number $\mathcal{N}_{\text{oligo}}$ of simulated tetramers, assuming $N_{\max} = 10^5$ photons. The dashed line is shown as a reference and indicates linear complexity. Figure from adapted from [206].

8.3. Discussion

The presented approach provides quantitative analysis of regular oligomeric structures via cryo-SMLM, yielding precise size estimates. Cryo-fixation preserves the sample's ultrastructure [11] and prohibits residual diffusion of molecules during image acquisition, thus allowing to resolve structures at the nanometer length scale. Moreover, fluorophore dipole orientations are virtually fixed under cryogenic temperatures. This feature can be exploited by polarized excitation: Based on characteristic brightness changes, localizations can be assigned to individual fluorophores, which substantially improves the further analysis.

For optimal application of the approach, a few considerations have to be taken into account. First, the method is template-based: The structure of the analyzed oligomers is assumed to be known and to follow a regular polygon. In particular, the number of protomers which constitute a single oligomer needs to be known. For many proteins in the cellular plasma membrane, a template is provided by their crystal structure obtained from EM experiments. If the degree of oligomerization is unknown, the number of protomers n may be obtained from the maximum number of localization groups which occurs during the localization assignment. Of note, for some oligomers errors may occur in the grouping of the localizations and thus, the maximum number of groups may be higher than the number of protomers n . Importantly, the investigated sample should be homogeneous. Reconstructing a sample containing oligomers of different oligomerization degrees or structures is challenging for any particle averaging approach. Applying our method to a mixed sample would yield a size estimate for the highest oligomerization degree, while rejecting all other oligomers as non-eligible during the analysis.

Concerning the labeling procedure, the size of the labels and particularly the linkage error should be small compared to the size of the oligomer structure of interest. In addition, each target site must be labeled with one dye molecule only. Of note, antibodies do not fulfill these requirements. Appropriate alternative labeling strategies include small tags [69] and unnatural amino acids [205]. The labeling efficiency typically is a crucial parameter for achieving valid reconstruction results as incompletely labeled oligomers distort the results. Notably, our method is not severely affected by low labeling efficiencies: Oligomers which are not fully labeled are rejected for further analysis by the eligibility criterion and thus, a possible bias in the size estimation is prevented. Ideally, the labeling efficiency should be close to one in order to ensure that a large fraction of imaged oligomers is eligible for the analysis. However, a lower labeling efficiency can be compensated by recording a larger number of oligomers.

Ideally, the fluorophore dipole orientations should be distributed randomly in space. Otherwise, the assignment of localizations to individual dye molecules may become complicated: If fluorophores had the same or a similar dipole orientation, their localizations would be grouped into one cluster; averaging of these localizations would lead to a spurious localization. Although the eligibility criterion avoids these cases, the analysis would be impeded if no eligible oligomers are left.

A few requirements regarding the imaging procedure need to be fulfilled for appropriate application of the method:

- The distance between individual oligomers should be large enough in order to ensure that

localizations belonging to different oligomers do not overlap. In particular, the mutual distance d between oligomers should exceed the oligomer radius while accounting for the localization errors, i.e. $d \gg R + \sigma_{\text{loc}}$. This ensures that localizations from each oligomer can be analyzed separately. If necessary, this can be achieved by reducing the protein expression levels of the cell.

- The oligomers should be aligned parallel to the focal plane. If the plasma membrane is not perfectly flat, the oligomers may be tilted. In this case, the recorded 2D image will be a projection of the actual structure and the localizations will be distorted. For tilt angles below 10 degrees, our method yields satisfactory results with relative errors below 1 nm (Fig. 8.13). For higher tilt angles, the analysis should be adapted in order to achieve optimal results. For example, oligomers with localizations that highly deviate from a regular polygon structure may be discarded. Further, including a deformation matrix in the model would allow to account for slightly distorted structures [185]. For molecules within the cell interior, oligomerization may not only occur in two but also in three dimensions. In its current form, our method does not incorporate these cases. Alternatives for reconstruction in 3D are provided by tomographic approaches [90].
- Imaging under cryogenic temperatures leads to fixed dipole orientations of fluorophores. If a fluorophore is shifted from the focal plane, the peak of its point spread function will shift laterally. This issue has to be considered in the localization process since simple fitting of a Gaussian function will lead to a bias [167]. Possible solutions are provided by azimuthal filtering [175, 176], polarization-resolved imaging [177] or astigmatic imaging [187] as proposed in chapter 7.
- The signals of individual fluorophores are required to be non-overlapping. For this, individual fluorophores need to be mutually independent. Chromophores in close proximity of a few nanometers may exhibit coupling via singlet-triplet energy transfers [208], affecting the dyes' blinking behavior. Of note, these effects were not observed in a previous study by Weisenburger et al. in which oligomeric structures at the nanometer scale were reconstructed under cryogenic conditions [90]. Further, cryogenic temperatures slow down fluorophore photophysics. On the one hand, reduced photobleaching kinetics lead to a higher number of localizations per molecule and thus to even more precise estimates of oligomer size. On the other hand, signals of different fluorophores are likely to partially overlap in case of low blinking rates, which impedes the analysis. Nevertheless, frames with overlapping signals could be detected based on the obtained brightness values (N_x, N_y) and filtered out.

The proposed method consists of two main parts: First, the assignment of localizations to individual fluorophores via excitation with polarized light and second, the determination of oligomer size via a circle fit. In principle, the localization assignment may be used in combination with any other particle averaging approach in order to improve the reconstruction results [182, 183]. The estimation of side lengths can be applied to investigate the exact arrangement of proteins and the orientation of protomers within an oligomeric structure. For this, specific sites within a protein can be targeted by the chosen label. Similar approaches were applied successfully for the analysis of larger structures, including endocytic sites [209] and nuclear pore complexes [44]. In conclusion, the presented approach takes advantage of the

specific conditions of SMLM under cryogenic temperatures and thus allows to substantially improve the analysis of oligomers in order to answer questions of structural biology.

8.4. Methods

8.4.1. Simulations

First, we simulated the positions of the protomers. For this, n protomers were assigned to each n -mer ($n = 3, 4, 5, 6$). Individual protomers belonging to one oligomer were arranged around the oligomer's center position in the shape of a regular polygon with fixed side length, but random in-plane orientation. If not specified otherwise, we simulated $\mathcal{N}_{\text{oligo}} = 5 \cdot 10^5$ oligomers for each analyzed data set.

Second, each protomer was assumed to be labeled with exactly one dye molecule. For Fig. 8.10 the labeling efficiency was adjusted accordingly. In order to account for recordings at cryogenic conditions, a random but fixed dipole orientation was assigned to each dye molecule. The inherent brightness N_{max} was considered to be the same for all dye molecules.

To simulate blinking, we assigned a random number of detections to each dye molecule, which was drawn from an artificial blinking statistics following a log-normal distribution. The mean of the log-normal distribution was set to 6.4 localizations and the standard deviation to 5 localizations. These values correspond to previously reported blinking characteristics of fluorescent probes under realistic experimental conditions, albeit recorded at room temperature (compare [118]).

Fluorophores were simulated to be excited alternately with polarized excitation light of polarization directions \vec{p}_1, \vec{p}_2 , which are orthogonal to each other as well as orthogonal to the optical axis. The xy -axes of the coordinate system were chosen to be aligned with the polarization directions \vec{p}_1, \vec{p}_2 , and the z -axis with the optical axis. The absorption probability of a fluorophore depends on the angle between its dipole orientation and the polarization of the excitation light. Hence, without loss of generality, the effective number of photons (N_x, N_y) for the two polarizations of excitation light can be calculated as

$$N_x = N_{\text{max}} \cos^2(\theta) \cos^2(\phi), \quad (8.4)$$

$$N_y = N_{\text{max}} \cos^2(\theta) \sin^2(\phi), \quad (8.5)$$

where θ and ϕ are the elevation and azimuthal angle of the fluorophore's dipole orientation relative to the x -axis, respectively (see Fig. 8.4a), and N_{max} the number of photons emitted if the dipole orientation is parallel to the excitation polarization. For all simulations, we assumed random distributions of θ and ϕ on a sphere. The resulting probability density for detecting (N_x, N_y) photons is given by (see *Appendix*, section 8.5, for a derivation)

$$\rho_{\text{phot.}}(N_x, N_y) = \begin{cases} \frac{1}{2\pi} \left(N_{\text{max}} N_x N_y (N_{\text{max}} - N_x - N_y) \right)^{-\frac{1}{2}} & \text{for } N_x, N_y \geq 0, \\ & N_x + N_y \leq N_{\text{max}}, \\ 0 & \text{otherwise.} \end{cases} \quad (8.6)$$

Photon shot noise was included by drawing the observed number of photons from Poisson distributions with mean N_x and N_y , respectively.

The error in the intensity estimation was distributed according to a normal distribution with mean 0 and variance $(\Delta N)^2$. The variance $(\Delta N)^2$ was set to [97]:

$$\langle (\Delta N)^2 \rangle = N \left(1 + 4\tau + \sqrt{\frac{\tau}{14(1+2\tau)}} \right), \quad \text{with } \tau = \frac{2\pi b (\sigma_{\text{PSF}}^2 + a^2/12)}{Na^2}, \quad (8.7)$$

where a is the pixel size, b the background noise, N the signal photon count (i.e. N_x , N_y) and σ_{PSF} the standard deviation of the PSF. If not mentioned otherwise, the background noise was set to $b = 0$. We assumed a pixel size of 100 nm and a standard deviation of the PSF of 160 nm.

Determination of the single molecule positions was assumed to be performed based on the combined images acquired by excitation with differently polarized light. The total intensity was calculated as $N_{\text{total}} = N_x + N_y = N_{\text{max}} \cos^2(\theta)$. Hence, the uncertainty of the localization procedure was set to [97]

$$\sigma_{\text{loc}}^2 = \frac{\sigma_{\text{PSF}}^2 + a^2/12}{N_{\text{total}}} \left(1 + 4\tau + \sqrt{\frac{2\tau}{1+4\tau}} \right). \quad (8.8)$$

As the background noise of the two individual frames combines, b was replaced by $\sqrt{2}b$ in the calculation of τ for Eq. 8.8. Localization coordinates were displaced from the true protomer position by adding a random localization error according to the localization precision σ_{loc} . Any detections with a localization precision below 10 nm were discarded. Together with given values of background noise b , pixel size a and the standard deviation of the PSF σ_{PSF} this defines a minimum number of required photons to detect a single molecule signal N_{min} . In order to simulate tilted tetramers, without loss of generality we assumed a tilt around the x -axis. To this end, we transformed the y -coordinates of the single molecule positions according to $y' = y \cdot \cos(\alpha)$, where α denotes the tilt angle of the oligomerization plane with respect to the focal plane.

8.4.2. Mathematical analysis

Identification of individual oligomeric structures

For our method, we assumed that the individual oligomers as well as the corresponding localizations are well separated from each other. In that case, the localizations can be clustered spatially in order to group localizations belonging to individual oligomers. This can be done effectively with standard two dimensional clustering techniques [59, 116]. For the simulations, we used ground truth in order to analyze each oligomer separately.

Assignment of localizations to individual fluorophores

The localizations of an oligomer are assigned to individual fluorophores based on their dipole orientation. The fluorophores are excited consecutively with light of orthogonal polarization directions, yielding characteristic intensities N_x and N_y . Given that the dipole orientations of all fluorophores within an oligomer are sufficiently distinct, we can cluster the localizations

based on the intensity values N_x and N_y (see Fig. 8.4b). For clustering, we grouped localizations based on differences in both N_x and N_y values according to a specified threshold δ_p . Clusters of a single localization only were discarded. Empirical tests suggest $\delta_p = 300 + N_{\max}/100$ to be a feasible choice in order to separate localizations from individual fluorophores. We considered an oligomer eligible for further analysis, if the corresponding localizations were clustered into exactly n groups.

Estimation of distance between single protomers

Given the localization data of one individual oligomer, we were interested in the distance l between the individual protomers. We assumed the oligomeric structure to be a regular polygon. Hence, the structure is equilateral. The radius R and the side length l , i.e. the distance between adjacent protomers, are directly related via $l = 2R \sin(\pi/n)$, where n is the number of polygon vertices.

In order to find an estimation \hat{l} for the side length, we used a geometric circle fit. For a simple circle fit of all localizations, one can minimize the mean square distance between the localizations and the fitted circle:

$$\min_{\substack{a, b \in \mathbb{R} \\ R \geq 0}} \sum_{i=1}^n \sum_{j=1}^{m_i} \left(\sqrt{(x_j^{(i)} - a)^2 + (y_j^{(i)} - b)^2} - R \right)^2, \quad (8.9)$$

where (a, b) are the coordinates of the circle center, R the circle radius, and $(x_j^{(i)}, y_j^{(i)})$ with $j = 1, \dots, m_i$ the localizations belonging to oligomer i . However, this approach overestimates the true oligomer size, as shown in Fig. 8.2b.

We can improve the circle fit by assigning the localizations to individual fluorophores as described above. The assignment of localizations to individual fluorophores allows to average all localizations that arise from the same fluorophore and thus, obtain a more precise estimate of the fluorophore's position. For the circle fit, we hence minimize the term

$$\min_{\substack{a, b \in \mathbb{R} \\ R \geq 0}} \sum_{i=1}^n \left(\sqrt{(\bar{x}_i - a)^2 + (\bar{y}_i - b)^2} - R \right)^2, \quad (8.10)$$

where (\bar{x}_i, \bar{y}_i) denote the mean x - and y -position of all localizations belonging to the fluorophore bound to protomer i , which are given by

$$\bar{x}_i = \frac{1}{m_i} \sum_{j=1}^{m_i} x_j^{(i)}, \quad \bar{y}_i = \frac{1}{m_i} \sum_{j=1}^{m_i} y_j^{(i)}, \quad i = 1, \dots, n, \quad (8.11)$$

where m_i denotes the number of localizations belonging to protomer i . The assignment of the localizations to their respective fluorophores improves both the estimation of the circle center as well as the estimation of the radius, as can be seen in Fig. 8.4c.

We minimized the terms in (8.9) and (8.10) based on the Levenberg-Marquardt algorithm, a robust iterative optimization algorithm for solving non-linear least square problems [210, 211].

As start parameters we used the average position of all fitted coordinates for the center (a_0, b_0) , and a value R_0 for the radius, which was sufficiently small such that $R_0 < R_{\text{truth}}$. Of note, the resulting estimate for the circle radius R shows a certain bias (compare [207, 212, 213]), which will be determined in the following section.

Identification of the bias

Suppose that the localizations belonging to a single protomer are identically and independently distributed normal random variables with mean zero (i.e. centered around the true protomer position) and constant variance σ^2 , where σ corresponds to the localization precision. Fitting a circle to all localizations arising from an oligomer by minimizing the term in (8.10) yields an estimate \hat{r} of the true oligomer radius R . As described in [207], the bias of this estimator is essentially given by

$$\mathbb{E}(\hat{r} - R) \simeq \frac{\sigma^2}{2R}. \quad (8.12)$$

Under cryogenic conditions, however, the fluorophores' dipole orientations are fixed and the number of emitted photons is determined by the angle between the dipole orientation and the polarization direction of the excitation light. Hence, the localization precision is not constant but a different localization precision σ_i will be observed for each protomer $i = 1, \dots, n$.

For each localization j of protomer i we denote by $s_j^{(i)}$ with $j = 1, \dots, m_i$ a given estimate of its localization precision in x as well as in y -direction. Hence, the localization precision after merging all the localizations belonging to protomer i can be estimated by

$$\hat{z}_i = \frac{1}{m} \sqrt{\sum_{j=1}^{m_i} (s_j^{(i)})^2}, \quad i = 1, \dots, n. \quad (8.13)$$

Due to the fact that the merged localization precision is different for every protomer, the bias cannot simply be calculated by Eq. (8.12). In this case, the bias is given by

$$\mathbb{E}(\hat{r} - R) = \frac{1}{R} \left(\frac{1}{2} \frac{\sum_{i=1}^n \hat{z}_i^2}{n} + \frac{1}{n} \frac{\sum_{i=1}^n \hat{z}_i^2}{n} \right) = \frac{1}{R} \left(\frac{1}{2n} \sum_{i=1}^n \hat{z}_i^2 + \frac{1}{n^2} \sum_{i=1}^n \hat{z}_i^2 \right). \quad (8.14)$$

For a detailed derivation of this equation, refer to [206]. Note that the used notation slightly differs from [206]. If the merged localization precision \hat{z}_i is the same for every protomer, i.e. $\hat{z}_i = z$ for all $i = 1, \dots, n$, Eq. (8.14) reduces again to

$$\mathbb{E}(\hat{r} - R) = \frac{1}{R} \left(\frac{nz^2}{2n} + \frac{nz^2}{n^2} \right) = \frac{z^2}{2R} + \frac{z^2}{Rn}, \quad (8.15)$$

which is consistent with Eq. (8.12). Note that the second summand was neglected in Eq. (8.12) since it vanishes asymptotically for n tending to infinity. The first summand, which does not depend on n , is the so-called essential bias. In our case, however, the second summand in Eq. (8.14) and (8.15) must not be neglected since n is small for the considered oligomers ($n = 3, 4, 5, 6$). Importantly, the merged localization precision \hat{z}_i in Eq. (8.14) becomes smaller

the higher the number m_i of localizations that are available for each protomer i . The entire bias tends to zero for m_i tending to infinity.

Considering $\mathbb{E}(\hat{r} - R) = \mathbb{E}(\hat{r}) - R$ in Eq. (8.14), the bias $\mathbb{E}(\hat{r})$ of the estimator \hat{r} can be calculated as

$$\mathbb{E}(\hat{r}) = R + \frac{\sum_{i=1}^n \hat{z}_i^2}{R} \left(\frac{1}{2n} + \frac{1}{n^2} \right). \quad (8.16)$$

The true radius R can hence be deduced from

$$R_{1,2} = \frac{\mathbb{E}(\hat{r})}{2} \pm \sqrt{\left(\frac{\mathbb{E}(\hat{r})}{2} \right)^2 - \left(\frac{1}{2n} + \frac{1}{n^2} \right) \sum_{i=1}^n \hat{z}_i^2}. \quad (8.17)$$

In case of $R > \frac{\sum_{i=1}^n \hat{z}_i^2}{R} \left(\frac{1}{2n} + \frac{1}{n^2} \right)$, the correct solution is given by

$$R = \frac{\mathbb{E}(\hat{r})}{2} + \sqrt{\left(\frac{\mathbb{E}(\hat{r})}{2} \right)^2 - \left(\frac{1}{2n} + \frac{1}{n^2} \right) \sum_{i=1}^n \hat{z}_i^2}. \quad (8.18)$$

Since $\mathbb{E}(\hat{r})$ is experimentally not accessible, we can replace it by the random variable \hat{r} . Hence, the bias-corrected estimator \hat{r}_{corr} for the oligomer radius is given by

$$\hat{r}_{\text{corr}} = \frac{\hat{r}}{2} + \sqrt{\left(\frac{\hat{r}}{2} \right)^2 - \left(\frac{1}{2n} + \frac{1}{n^2} \right) \sum_{i=1}^n \hat{z}_i^2}. \quad (8.19)$$

An estimator of the radius based on the analysis of a set of oligomers is obtain via $\hat{R} = \mathbb{E}(\hat{r}_{\text{corr}})$ or $\hat{R} = \text{median}(\hat{r}_{\text{corr}})$, respectively. If not indicated otherwise, the median was taken in the analysis.

Calculation of error bars

All error bars were calculated based on 1000 bootstrap samples, which were drawn from the individual data sets. The error bars represent the 95% confidence intervals of the mean (or median).

Runtime analysis

The runtime shown in Fig. 8.14 was determined on a standard personal computer model XPS 15 9570 with an Intel Core i7-8750H processor.

8.5. Appendix

Probability density of (N_x, N_y)

In the following, the probability density for detecting (N_x, N_y) photons is calculated. The fluorophore dipole moments are assumed to be distributed randomly on a sphere. In order to ensure a bijective functional relationship between (N_x, N_y) and (θ, ϕ) as specified by Eq. (8.4) and (8.5) in the *Methods* (section 8.4.1), the analysis is confined to the octant defined by (θ, ϕ) in the intervals $[0, \frac{\pi}{2}] \times [0, \frac{\pi}{2}]$. The probability densities for θ and ϕ are given by

$$\rho_{\text{az.}}(\theta) = \begin{cases} \cos(\theta) & \text{for } \theta \in [0, \frac{\pi}{2}], \\ 0 & \text{otherwise,} \end{cases}$$

$$\rho_{\text{el.}}(\phi) = \begin{cases} \frac{2}{\pi} & \text{for } \phi \in [0, \frac{\pi}{2}], \\ 0 & \text{otherwise.} \end{cases}$$

The joint probability density for (θ, ϕ) is given by

$$\rho_{\text{dipole}}(\theta, \phi) = \begin{cases} \frac{2}{\pi} \cos(\theta) & \text{for } \theta \in [0, \frac{\pi}{2}], \phi \in [0, \frac{\pi}{2}], \\ 0 & \text{otherwise.} \end{cases}$$

Inverting Eq. (8.4) and (8.5) from the *Methods* (section 8.4.1) yields

$$\theta = \arccos\left(\sqrt{\frac{N_x + N_y}{N_{\text{max}}}}\right), \quad \phi = \arccos\left(\sqrt{\frac{N_x}{N_x + N_y}}\right)$$

and for the joint probability density of the detected number of photons

$$\begin{aligned} \rho_{\text{phot.}}(N_x, N_y) &= \rho_{\text{dipole}}\left(\arccos\left(\sqrt{\frac{N_x + N_y}{N_{\text{max}}}}\right), \arccos\left(\sqrt{\frac{N_x}{N_x + N_y}}\right)\right) \cdot \left|\frac{\partial(\theta, \phi)}{\partial(N_x, N_y)}\right| \\ &= \frac{2}{\pi} \sqrt{\frac{N_x + N_y}{N_{\text{max}}}} \cdot \left|\frac{\partial(\theta, \phi)}{\partial(N_x, N_y)}\right|. \end{aligned} \quad (8.20)$$

The Jacobian yields

$$\begin{aligned} \left|\frac{\partial(\theta, \phi)}{\partial(N_x, N_y)}\right| &= \left| \begin{bmatrix} -\frac{1}{2} \left((N_x + N_y)(N_{\text{max}} - N_x - N_y) \right)^{-\frac{1}{2}} & -\frac{1}{2} \left((N_x + N_y)(N_{\text{max}} - N_x - N_y) \right)^{-\frac{1}{2}} \\ -\frac{1}{2} \frac{1}{N_x + N_y} \sqrt{\frac{N_y}{N_x}} & \frac{1}{2} \frac{1}{N_x + N_y} \sqrt{\frac{N_x}{N_y}} \end{bmatrix} \right| \\ &= \frac{1}{4} \left(N_x N_y (N_x + N_y) (N_{\text{max}} - N_x - N_y) \right)^{-\frac{1}{2}}. \end{aligned}$$

Inserting this into Eq. (8.20) finally yields

$$\rho_{\text{phot.}}(N_x, N_y) = \begin{cases} \frac{1}{2\pi} \left(N_{\text{max}} N_x N_y (N_{\text{max}} - N_x - N_y) \right)^{-\frac{1}{2}} & \text{for } N_x, N_y \geq 0, N_x + N_y \leq N_{\text{max}}, \\ 0 & \text{otherwise.} \end{cases}$$

9. Conclusion and outlook

The structural arrangement of proteins in the cell plasma membrane is directly connected to their function. Clustering and oligomerization of membrane proteins are crucial to many biological mechanisms: As important examples, T-cell receptor clustering is key in T-cell activation [214], and defined oligomerization states are a prerequisite for correct pore formation and, thus, the selectivity of ion channels [24]. In contrast, changes in oligomerization states have been associated with many diseases, including Parkinson's disease [32] and cancer [33]. Taken together, knowledge about subcellular organization, in particular the plasma membrane, is key to understanding biological processes as well as identifying the causes of disease.

Single molecule localization microscopy has offered the possibility to circumvent the diffraction limit and enabled the visualization of cellular structures within their native environment at a level of detail which has previously been thought to be beyond reach [16]. However, SMLM techniques are sensitive to experimental imperfections, including incomplete labeling or background localizations, and prone to artifacts [133]. Most remarkably, overcounting artifacts led to the notion of protein nanoclustering being a prevalent feature of plasma membrane organization [1].

For a meaningful analysis of localization maps, it is important to realize that it is the distribution of the underlying biomolecules of interest which is of biological relevance, not the mere distribution of localizations themselves. First of all, a localization map should be assessed globally before studying local features in greater detail: Due to random chance alone, some biomolecules in a small local environment will show alleged clustering, even in the case of complete spatial randomness. In addition, stochastic effects in the blinking behavior lead to statistical variations in overcounting and thus obscure the reliability of a local analysis. Notably, any factors possibly distorting the localization map, such as membrane undulations or vesicles, should be avoided for a correct assessment of biomolecular distributions in the plasma membrane. In this thesis, I present two methods to overcome the issue of overcounting artifacts in a global analysis: (i) 2-CLASTA allows to distinguish overcounting clusters from true biomolecular nanoclustering; remarkably, it is the first method which achieves this completely independent of any knowledge or assumption about blinking behavior. (ii) Monte Carlo simulations based on a reliable characterization of blinking statistics offer a comprehensive tool for comparing experimental data to various spatial distributions. Both methods are compatible with any current labeling and SMLM technique. Moreover, both methods allow for the calculation of a p-value, which provides a good indication whether an observed distribution of localizations might be due to pure random chance or whether it supports the alternative hypothesis of true biomolecular clustering. Performing multiple experiments increases the amount of available data, thus increasing the sensitivity of the analysis; here, I present an approach which prevents the problem of fishing for p-values in this case. Nevertheless, a scientific conclusion should never be drawn on the sole basis of a single p-value without any other scientific reasoning. In the case of protein clusters in the cell plasma membrane, for example, one should rather pose additional questions: What are the forces that keep the molecules together? Is there any functional purpose of this arrangement of molecules? Complementary methods

may be employed in order to answer these questions and gain a comprehensive understanding of biological processes.

With SMLM, only structures at a scale above the localization precision can be resolved directly; for smaller structures, advanced analysis methods are required in order to circumvent overcounting artifacts. In turn, however, overcounting issues would become negligible if the localization precision would reach a scale below the size of a single biomolecule of interest. Cryo-SMLM promises to push the spatial resolution of SMLM even further, ultimately approaching the size of single molecules themselves at the Ångström scale. Cryo-fixation preserves the sample's ultrastructure [11], and prohibits any residual diffusion. Thin cell sections of interest can be sliced by ion beam milling [77], thus removing any perturbing background. Notably, not only single cells adhering to a coverslip might be processed this way, but also investigating the interface between cell complexes—in particular, cell synapses—or even thin sections of tissue becomes feasible. Thus, cryo-SMLM paves the way for studying cellular behavior within the cell's native environment in nanoscopic detail. One feature of SMLM performed at cryogenic temperature is the fixed orientation of fluorophore dipoles. In this thesis, I suggest an astigmatic imaging approach which allows to avoid localization bias for fixed dipole emitters in a low-NA setting. Interestingly, cryo-SMLM offers a direct way of circumventing the problem of overcounting: As presented in this thesis, the fixed orientations of fluorophore dipoles provide valuable information for assigning localizations to individual molecules. Thus, the results of particle averaging and reconstruction approaches can be greatly improved which makes cryo-SMLM an ideal tool for detailed local analysis, particularly for a determination of the exact structure of oligomers. Temporal information about cellular processes can be recovered in cryo-SMLM by fixing cells at different time points [209].

Ultimately, the automatization of data acquisition will lead to huge amounts of data which cannot be processed manually anymore. Hence, the development of algorithms and analysis approaches specific to the needs of SMLM are indispensable. The synergy of complementary imaging and analysis methods allows for a comprehensive characterization and validation of biomolecular structures in their native environment and, hence, a better understanding of cellular processes in the plasma membrane.

References

- [1] M. F. Garcia-Parajo, *et al.* “Nanoclustering as a dominant feature of plasma membrane organization”. *J Cell Sci*, 127(23):4995–5005, 2014, doi:[10.1242/jcs.146340](https://doi.org/10.1242/jcs.146340).
- [2] S. K. Saka, *et al.* “Multi-protein assemblies underlie the mesoscale organization of the plasma membrane”. *Nat Commun*, 5:1–14, 2014, doi:[10.1038/ncomms5509](https://doi.org/10.1038/ncomms5509).
- [3] P. Annibale, *et al.* “Identification of clustering artifacts in photoactivated localization microscopy”. *Nat Methods*, 8(7):527–8, 2011, doi:[10.1038/nmeth.1627](https://doi.org/10.1038/nmeth.1627).
- [4] F. Baumgart, *et al.* “Varying label density allows artifact-free analysis of membrane-protein nanoclusters”. *Nat Methods*, 13(8):661–664, 2016, doi:[10.1038/nmeth.3897](https://doi.org/10.1038/nmeth.3897).
- [5] P. Annibale, *et al.* “Quantitative photo activated localization microscopy: Unraveling the effects of photoblinking”. *PLoS One*, 6(7):e22678, 2011, doi:[10.1371/journal.pone.0022678](https://doi.org/10.1371/journal.pone.0022678).
- [6] P. Sengupta, *et al.* “Probing protein heterogeneity in the plasma membrane using PALM and pair correlation analysis”. *Nat Methods*, 8(11):969–975, 2011, doi:[10.1038/nmeth.1704](https://doi.org/10.1038/nmeth.1704).
- [7] C. Spahn, *et al.* “Temporal accumulation analysis provides simplified artifact-free analysis of membrane-protein nanoclusters”. *Nat Methods*, 13(12):963–964, 2016, doi:[10.1038/nmeth.4065](https://doi.org/10.1038/nmeth.4065).
- [8] M. Levitus and S. Ranjit. “Cyanine dyes in biophysical research: The photophysics of polymethine fluorescent dyes in biomolecular environments”. *Q Rev Biophys*, 44(1):123–151, 2011, doi:[10.1017/S0033583510000247](https://doi.org/10.1017/S0033583510000247).
- [9] K. A. Tanaka, *et al.* “Membrane molecules mobile even after chemical fixation”. *Nat Methods*, 7(11):865–866, 2010, doi:[10.1038/nmeth.f.314](https://doi.org/10.1038/nmeth.f.314).
- [10] E. Kellenberger, *et al.* “Artefacts and morphological changes during chemical fixation”. *J Microsc*, 168(2):181–201, 1992, doi:[10.1111/j.1365-2818.1992.tb03260.x](https://doi.org/10.1111/j.1365-2818.1992.tb03260.x).
- [11] T. K. Tsang, *et al.* “High-quality ultrastructural preservation using cryofixation for 3D electron microscopy of genetically labeled tissues”. *Elife*, 7, 2018, doi:[10.7554/eLife.35524](https://doi.org/10.7554/eLife.35524).
- [12] J. Enderlein, *et al.* “Polarization effect on position accuracy of fluorophore localization”. *Opt Express*, 14(18):8111–8120, 2006.
- [13] J. Engelhardt, *et al.* “Molecular orientation affects localization accuracy in superresolution far-field fluorescence microscopy”. *Nano Lett*, 11(1):209–13, 2011, doi:[10.1021/nl103472b](https://doi.org/10.1021/nl103472b).
- [14] R. Hooke, “Micrographia: Or some physiological descriptions of minute bodies made by magnifying glasses”. London: Royal Society, 1665.
- [15] Y. M. Sigal, *et al.* “Visualizing and discovering cellular structures with super-resolution microscopy”. *Science*, 361:880–887, 2018.
- [16] M. Lelek, *et al.* “Single-molecule localization microscopy”. *Nat Rev Methods Primers*, 1(1), 2021, doi:[10.1038/s43586-021-00038-x](https://doi.org/10.1038/s43586-021-00038-x).

- [17] B. Alberts, *et al.*, “Molecular biology of the cell”. Garland Science, 6th ed., 2015.
- [18] M. S. Almen, *et al.* “Mapping the human membrane proteome: A majority of the human membrane proteins can be classified according to function and evolutionary origin”. *BMC Biol*, 7:50, 2009, doi:[10.1186/1741-7007-7-50](https://doi.org/10.1186/1741-7007-7-50).
- [19] S. J. Singer and G. L. Nicolson. “The fluid mosaic model of the structure of cell membranes”. *Science*, 175, 1972.
- [20] D. M. Engelman. “Membranes are more mosaic than fluid”. *Nature*, 438(7068):578–80, 2005, doi:[10.1038/nature04394](https://doi.org/10.1038/nature04394).
- [21] J. D. Robertson. “Membrane structure”. *J Cell Biol*, 91(3), 1981.
- [22] R. Orbach and X. Su. “Surfing on membrane waves: Microvilli, curved membranes, and immune signaling”. *Frontiers in Immunology*, 11, 2020, doi:[10.3389/fimmu.2020.02187](https://doi.org/10.3389/fimmu.2020.02187).
- [23] D. Leyton-Puig, *et al.* “PFA fixation enables artifact-free super-resolution imaging of the actin cytoskeleton and associated proteins”. *Biol Open*, 5(7):1001–9, 2016, doi:[10.1242/bio.019570](https://doi.org/10.1242/bio.019570).
- [24] X. C. Zhang, *et al.* “Thermodynamics of voltage-gated ion channels”. *Biophys Rep*, 4(6):300–319, 2018, doi:[10.1007/s41048-018-0074-y](https://doi.org/10.1007/s41048-018-0074-y).
- [25] D. A. Doyle, *et al.* “The structure of the potassium channel: Molecular basis of K⁺ conduction and selectivity”. *Science*, 280(5360):69–77, 1998.
- [26] “Amino acid.” URL: https://en.wikipedia.org/wiki/Amino_acid. (Last accessed: June 2021).
- [27] “Protein structure.” URL: https://en.wikipedia.org/wiki/Protein_structure. (Last accessed: June 2021).
- [28] H. M. Berman, *et al.* “The Protein Data Bank”. *Nucleic Acids Research*, 28(1):235–242, 2000, doi:[10.1093/nar/28.1.235](https://doi.org/10.1093/nar/28.1.235).
- [29] D. Sehnal, *et al.* “Mol* Viewer: Modern web app for 3D visualization and analysis of large biomolecular structures”. *Nucleic Acids Res*, 2021, doi:[10.1093/nar/gkab314](https://doi.org/10.1093/nar/gkab314).
- [30] N. Gregersen, *et al.* “Protein misfolding and human disease”. *Annu Rev Genomics Hum Genet*, 7:103–24, 2006, doi:[10.1146/annurev.genom.7.080505.115737](https://doi.org/10.1146/annurev.genom.7.080505.115737).
- [31] D. P. Ryan and J. M. Matthews. “Protein-protein interactions in human disease”. *Curr Opin Struct Biol*, 15(4):441–6, 2005, doi:[10.1016/j.sbi.2005.06.001](https://doi.org/10.1016/j.sbi.2005.06.001).
- [32] X. Y. Du, *et al.* “The role of alpha-synuclein oligomers in Parkinson’s disease”. *Int J Mol Sci*, 21(22), 2020, doi:[10.3390/ijms21228645](https://doi.org/10.3390/ijms21228645).
- [33] A. Appert-Collin, *et al.* “Role of ErbB receptors in cancer cell migration and invasion”. *Front Pharmacol*, 6:283, 2015, doi:[10.3389/fphar.2015.00283](https://doi.org/10.3389/fphar.2015.00283).
- [34] K. Feher, *et al.* “Can single molecule localization microscopy detect nanoclusters in T cells?”. *Curr Opin Chem Biol*, 51:130–137, 2019, doi:[10.1016/j.cbpa.2019.05.019](https://doi.org/10.1016/j.cbpa.2019.05.019).
- [35] U. Kubitscheck, “Fluorescence microscopy”. Weinheim: Wiley-VCH, 2nd ed., 2017.
- [36] “Fluorescence spectraviewer.” URL: <https://www.thermofisher.com/order/fluorescence-spectraviewer>. (Last accessed: June 2021).

- [37] M. Born and E. Wolf, “Principles of optics: Electromagnetic theory of propagation, interference and diffraction of light”. Cambridge University Press, 7th ed., 1999.
- [38] E. Abbe. “Beiträge zur Theorie des Mikroskops und der mikroskopischen Wahrnehmung”. *Archiv für mikroskopische Anatomie*, 9(1):413–468, 1873.
- [39] “Airy disk.” URL: https://en.wikipedia.org/wiki/Airy_disk. (Last accessed: June 2021).
- [40] “Angular resolution.” URL: https://en.wikipedia.org/wiki/Angular_resolution. (Last accessed: June 2021).
- [41] S. Stallinga and B. Rieger. “Accuracy of the Gaussian point spread function model in 2D localization microscopy”. *Opt Express*, 18(24), 2010.
- [42] J. W. Goodman, “Introduction to Fourier optics”. McGraw-Hill series in electrical and computer engineering, McGraw-Hill, 2nd ed., 1996.
- [43] D. Axelrod. “Fluorescence excitation and imaging of single molecules near dielectric-coated and bare surfaces: A theoretical study”. *J Microsc*, 247(2):147–60, 2012, doi:10.1111/j.1365-2818.2012.03625.x.
- [44] A. Szymborska, *et al.* “Nuclear pore scaffold structure analyzed by super-resolution microscopy and particle averaging”. *Science*, 341, 2013.
- [45] D. Axelrod, *et al.* “Total internal reflection fluorescence”. *Ann Rev Biophys Bioeng*, 13:47–68, 1984.
- [46] D. Axelrod. “Cell-substrate contacts illuminated by total internal reflection fluorescence”. *Journal of Cell Biology*, 89(1):141–145, 1981.
- [47] M. Bramehuber and G. J. Schütz, “Single molecule measurements in membranes”, In: *Comprehensive biophysics*, 5:337–365, Elsevier, 2012. doi:10.1016/b978-0-12-374920-8.00527-0.
- [48] S. W. Hell and J. Wichmann. “Breaking the diffraction resolution limit by stimulated emission: Stimulated-emission-depletion fluorescence microscopy”. *Optics Letters*, 19(11):780–782, 1994.
- [49] E. Betzig, *et al.* “Imaging intracellular fluorescent proteins at nanometer resolution”. *Science*, 313:1642–1645, 2006.
- [50] S. T. Hess, *et al.* “Ultra-high resolution imaging by fluorescence photoactivation localization microscopy”. *Biophys J*, 91(11):4258–72, 2006, doi:10.1529/biophysj.106.091116.
- [51] M. J. Rust, *et al.* “Sub-diffraction-limit imaging by stochastic optical reconstruction microscopy (STORM)”. *Nat Methods*, 3(10):793–5, 2006, doi:10.1038/nmeth929.
- [52] M. Heilemann, *et al.* “Subdiffraction-resolution fluorescence imaging with conventional fluorescent probes”. *Angew Chem Int Ed Engl*, 47(33):6172–6, 2008, doi:10.1002/anie.200802376.
- [53] A. Sharonov and R. Hochstrasser. “Wide-field subdiffraction imaging by accumulated binding of diffusing probes”. *Proc Natl Acad Sci USA*, 2006.
- [54] R. Jungmann, *et al.* “Single-molecule kinetics and super-resolution microscopy by fluorescence imaging of transient binding on DNA origami”. *Nano Lett*, 10(11):4756–61, 2010, doi:10.1021/nl103427w.

- [55] H. Deschout, *et al.* “Precisely and accurately localizing single emitters in fluorescence microscopy”. *Nat Methods*, 11(3):253–66, 2014, doi:[10.1038/nmeth.2843](https://doi.org/10.1038/nmeth.2843).
- [56] G. J. Schütz and M. C. Schneider, “Single molecule localization microscopy (SMLM)”, In: *Imaging modalities for biological and preclinical research: A compendium*, IOP Publishing, 2021. doi:[10.1088/978-0-7503-3059-6ch18](https://doi.org/10.1088/978-0-7503-3059-6ch18).
- [57] S. van de Linde, *et al.* “Live-cell super-resolution imaging with synthetic fluorophores”. *Annu Rev Phys Chem*, 63:519–40, 2012, doi:[10.1146/annurev-physchem-032811-112012](https://doi.org/10.1146/annurev-physchem-032811-112012).
- [58] A. Fürstenberg and M. Heilemann. “Single-molecule localization microscopy — near-molecular spatial resolution in light microscopy with photoswitchable fluorophores”. *Phys Chem Chem Phys*, 15(36):14919–30, 2013, doi:[10.1039/c3cp52289j](https://doi.org/10.1039/c3cp52289j).
- [59] F. Baumgart, *et al.* “What we talk about when we talk about nanoclusters”. *Methods Appl Fluoresc*, 7(1):013001, 2018, doi:[10.1088/2050-6120/aaed0f](https://doi.org/10.1088/2050-6120/aaed0f).
- [60] G. Giannone, *et al.* “Dynamic superresolution imaging of endogenous proteins on living cells at ultra-high density”. *Biophys J*, 99(4):1303–10, 2010, doi:[10.1016/j.bpj.2010.06.005](https://doi.org/10.1016/j.bpj.2010.06.005).
- [61] J. Schnitzbauer, *et al.* “Super-resolution microscopy with DNA-PAINT”. *Nat Protoc*, 12(6):1198–1228, 2017, doi:[10.1038/nprot.2017.024](https://doi.org/10.1038/nprot.2017.024).
- [62] R. Diekmann, *et al.* “Optimizing imaging speed and excitation intensity for single-molecule localization microscopy”. *Nat Methods*, 17(9):909–912, 2020, doi:[10.1038/s41592-020-0918-5](https://doi.org/10.1038/s41592-020-0918-5).
- [63] R. Platzter, *et al.* “Unscrambling fluorophore blinking for comprehensive cluster detection via photoactivated localization microscopy”. *Nat Commun*, 11(1):4993, 2020, doi:[10.1038/s41467-020-18726-9](https://doi.org/10.1038/s41467-020-18726-9).
- [64] K. M. Dean and A. E. Palmer. “Advances in fluorescence labeling strategies for dynamic cellular imaging”. *Nat Chem Biol*, 10(7):512–23, 2014, doi:[10.1038/nchembio.1556](https://doi.org/10.1038/nchembio.1556).
- [65] M. Sauer. “Localization microscopy coming of age: From concepts to biological impact”. *J Cell Sci*, 126(16):3505–13, 2013, doi:[10.1242/jcs.123612](https://doi.org/10.1242/jcs.123612).
- [66] “Alexa dyes.” URL: <https://www.atdbio.com/content/34/Alexa-dyes>. (Last accessed: June 2021).
- [67] O. Shimomura, *et al.* “Extraction, purification and properties of aequorin, a bioluminescent protein from the luminous hydromedusan, Aequorea”. *Journal of cellular and comparative physiology*, 59(3), 1962.
- [68] A. Gautier, *et al.* “An engineered protein tag for multiprotein labeling in living cells”. *Chem Biol*, 15(2):128–36, 2008, doi:[10.1016/j.chembiol.2008.01.007](https://doi.org/10.1016/j.chembiol.2008.01.007).
- [69] R. S. Erdmann, *et al.* “Labeling strategies matter for super-resolution microscopy: A comparison between HaloTags and SNAP-tags”. *Cell Chem Biol*, 26(4):584–592, 2019, doi:[10.1016/j.chembiol.2019.01.003](https://doi.org/10.1016/j.chembiol.2019.01.003).
- [70] K. Horisawa. “Specific and quantitative labeling of biomolecules using click chemistry”. *Front Physiol*, 5:457, 2014, doi:[10.3389/fphys.2014.00457](https://doi.org/10.3389/fphys.2014.00457).
- [71] P. Laxman, *et al.* “The benefits of unnatural amino acid incorporation as pro-

- tein labels for single molecule localization microscopy”. *Front Chem*, 9:641355, 2021, doi:10.3389/fchem.2021.641355.
- [72] S. van de Linde, *et al.* “Direct stochastic optical reconstruction microscopy with standard fluorescent probes”. *Nat Protoc*, 6(7):991–1009, 2011, doi:10.1038/nprot.2011.336.
- [73] F. Schueder, *et al.* “An order of magnitude faster DNA-PAINT imaging by optimized sequence design and buffer conditions”. *Nat Methods*, 2019, doi:10.1038/s41592-019-0584-7.
- [74] L. Nahidiazar, *et al.* “Optimizing imaging conditions for demanding multi-color super resolution localization microscopy”. *PLoS One*, 11(7):e0158884, 2016, doi:10.1371/journal.pone.0158884.
- [75] W. Li, *et al.* “Ultra-stable and versatile widefield cryo-fluorescence microscope for single-molecule localization with sub-nanometer accuracy”. *Opt Express*, 23(3):3770–83, 2015, doi:10.1364/OE.23.003770.
- [76] L. Wang, *et al.* “Solid immersion microscopy images cells under cryogenic conditions with 12 nm resolution”. *Commun Biol*, 2:74, 2019, doi:10.1038/s42003-019-0317-6.
- [77] E. Villa, *et al.* “Opening windows into the cell: Focused-ion-beam milling for cryo-electron tomography”. *Curr Opin Struct Biol*, 23(5):771–7, 2013, doi:10.1016/j.sbi.2013.08.006.
- [78] “APON100XHOTIRF, Olypmus.” URL: <https://www.olympus-lifescience.com/de/objectives/tirf-hr/>. (Last accessed: August 2021).
- [79] H. Toprak, Erdal Balci, *et al.* “Three-dimensional particle tracking via bifocal imaging”. *Nano Lett*, 7(7):2043–2045, 2007.
- [80] G. Shtengel, *et al.* “Interferometric fluorescent super-resolution microscopy resolves 3D cellular ultrastructure”. *Proc Natl Acad Sci USA*, 106(9):3125–30, 2009, doi:10.1073/pnas.0813131106.
- [81] D. Aquino, *et al.* “Two-color nanoscopy of three-dimensional volumes by 4Pi detection of stochastically switched fluorophores”. *Nat Methods*, 8(4):353–9, 2011, doi:10.1038/nmeth.1583.
- [82] N. Bourg, *et al.* “Direct optical nanoscopy with axially localized detection”. *Nat Photon*, 9(9):587–593, 2015, doi:10.1038/nphoton.2015.132.
- [83] M. Siemons, *et al.* “Comparing strategies for deep astigmatism-based single-molecule localization microscopy”. *Biomed Opt Express*, 11(2):735–751, 2020, doi:10.1364/BOE.382023.
- [84] S. R. P. Pavanaia, *et al.* “Three-dimensional, single-molecule fluorescence imaging beyond the diffraction limit by using a double-helix point spread function”. *PNAS*, 2009.
- [85] K. I. Mortensen, *et al.* “Optimized localization analysis for single-molecule tracking and superresolution microscopy”. *Nat Methods*, 2010.
- [86] Y. Li, *et al.* “Real-time 3D single-molecule localization using experimental point spread functions”. *Nat Methods*, 15(5):367–369, 2018, doi:10.1038/nmeth.4661.
- [87] S. Weisenburger, *et al.*, “Cryogenic localization of single molecules with Angstrom pre-

- cision" In: *Nanoimaging and Nanospectroscopy*, 8815:88150D, International Society for Optics and Photonics, 2013.
- [88] H. Babcock, *et al.* "A high-density 3D localization algorithm for stochastic optical reconstruction microscopy". *Opt Nanoscopy*, 1:1–10, 2012.
- [89] M. Ovesny, *et al.* "ThunderSTORM: A comprehensive ImageJ plug-in for PALM and STORM data analysis and super-resolution imaging". *Bioinformatics*, 30(16):2389–90, 2014, doi:[10.1093/bioinformatics/btu202](https://doi.org/10.1093/bioinformatics/btu202).
- [90] S. Weisenburger, *et al.* "Cryogenic optical localization provides 3D protein structure data with Angstrom resolution". *Nat Methods*, 14(2):141–144, 2017, doi:[10.1038/nmeth.4141](https://doi.org/10.1038/nmeth.4141).
- [91] D. Sage, *et al.* "Quantitative evaluation of software packages for single-molecule localization microscopy". *Nat Methods*, 12(8):717–24, 2015, doi:[10.1038/nmeth.3442](https://doi.org/10.1038/nmeth.3442).
- [92] D. Sage, *et al.* "Super-resolution fight club: Assessment of 2D and 3D single-molecule localization microscopy software". *Nat Methods*, 16(5):387–395, 2019, doi:[10.1038/s41592-019-0364-4](https://doi.org/10.1038/s41592-019-0364-4).
- [93] C. R. Rao, "Linear statistical inference and its applications", vol. 2. Wiley New York, 1973.
- [94] R. J. Ober, *et al.* "Localization accuracy in single-molecule microscopy". *Biophys J*, 86:1185–1200, 2004.
- [95] A. V. Abraham, *et al.* "Quantitative study of single molecule location estimation techniques". *Opt Express*, 17:23352 – 23373, 2009.
- [96] H. E. Daniels, "The asymptotic efficiency of a maximum likelihood estimator." In: *Fourth Berkeley Symposium on Mathematical Statistics and Probability*, 1:151–163, University of California Press Berkeley, 1961.
- [97] B. Rieger and S. Stallinga. "The lateral and axial localization uncertainty in super-resolution light microscopy". *Chemphyschem*, 15(4):664–70, 2014, doi:[10.1002/cphc.201300711](https://doi.org/10.1002/cphc.201300711).
- [98] R. Thompson, *et al.* "Precise nanometer localization analysis for individual fluorescent probes". *Biophys J*, 82:2775–2783, 2002.
- [99] S. H. Lee, *et al.* "Using fixed fiduciary markers for stage drift correction". *Opt Express*, 20(11):12177–12183, 2012.
- [100] W. Colomb, *et al.* "Estimation of microscope drift using fluorescent nanodiamonds as fiducial markers". *J Microsc*, 266(3):298–306, 2017, doi:[10.1111/jmi.12539](https://doi.org/10.1111/jmi.12539).
- [101] Y. Wang, *et al.* "Localization events-based sample drift correction for localization microscopy with redundant cross-correlation algorithm". *Opt Express*, 22(13):15982–91, 2014, doi:[10.1364/OE.22.015982](https://doi.org/10.1364/OE.22.015982).
- [102] M. Erdelyi, *et al.* "Correcting chromatic offset in multicolor super-resolution localization microscopy". *Opt Express*, 21(9):10978–88, 2013, doi:[10.1364/OE.21.010978](https://doi.org/10.1364/OE.21.010978).
- [103] N. Durisic, *et al.* "Quantitative super-resolution microscopy: Pitfalls and strategies for image analysis". *Curr Opin Chem Biol*, 20:22–8, 2014, doi:[10.1016/j.cbpa.2014.04.005](https://doi.org/10.1016/j.cbpa.2014.04.005).
- [104] Y. L. Wu, *et al.* "Quantitative data analysis in single-molecule localization microscopy". *Trends Cell Biol*, 30(11):837–851, 2020, doi:[10.1016/j.tcb.2020.07.005](https://doi.org/10.1016/j.tcb.2020.07.005).

- [105] R. P. Nieuwenhuizen, *et al.* “Measuring image resolution in optical nanoscopy”. *Nat Methods*, 10(6):557–62, 2013, doi:[10.1038/nmeth.2448](https://doi.org/10.1038/nmeth.2448).
- [106] R. Jungmann, *et al.* “Multiplexed 3D cellular super-resolution imaging with DNA-PAINT and Exchange-PAINT”. *Nat Methods*, 11(3):313–8, 2014, doi:[10.1038/nmeth.2835](https://doi.org/10.1038/nmeth.2835).
- [107] O. K. Wade, *et al.* “124-color super-resolution imaging by engineering DNA-PAINT blinking kinetics”. *Nano Lett*, 2019, doi:[10.1021/acs.nanolett.9b00508](https://doi.org/10.1021/acs.nanolett.9b00508).
- [108] P. R. Nicovich, *et al.* “Turning single-molecule localization microscopy into a quantitative bioanalytical tool”. *Nat Protoc*, 12(3):453–460, 2017, doi:[10.1038/nprot.2016.166](https://doi.org/10.1038/nprot.2016.166).
- [109] J. V. Thevathasan, *et al.* “Nuclear pores as versatile reference standards for quantitative superresolution microscopy”. *Nat Methods*, 16(10):1045–1053, 2019, doi:[10.1038/s41592-019-0574-9](https://doi.org/10.1038/s41592-019-0574-9).
- [110] J. Vogelsang, *et al.* “A reducing and oxidizing system minimizes photobleaching and blinking of fluorescent dyes”. *Angew Chem Int Ed Engl*, 47(29):5465–9, 2008, doi:[10.1002/anie.200801518](https://doi.org/10.1002/anie.200801518).
- [111] J. Widengren, *et al.* “Strategies to improve photostabilities in ultrasensitive fluorescence spectroscopy”. *J Phys Chem A*, 111:429–440, 2007.
- [112] E. Yeow, *et al.* “Characterizing the fluorescence intermittency and photobleaching kinetics of dye molecules immobilized on a glass surface”. *J Phys Chem A*, 110(5), 2006.
- [113] M. Mund and J. Ries. “How good are my data? Reference standards in superresolution microscopy”. *Mol Biol Cell*, 31(19):2093–2096, 2020, doi:[10.1091/mbc.E19-04-0189](https://doi.org/10.1091/mbc.E19-04-0189).
- [114] J. J. Schmied, *et al.* “Fluorescence and super-resolution standards based on DNA origami”. *Nat Methods*, 9(12):1133–4, 2012, doi:[10.1038/nmeth.2254](https://doi.org/10.1038/nmeth.2254).
- [115] S. Dey, *et al.* “DNA origami”. *Nat Rev Methods Primers*, 1(1), 2021, doi:[10.1038/s43586-020-00009-8](https://doi.org/10.1038/s43586-020-00009-8).
- [116] I. M. Khater, *et al.* “A review of super-resolution single-molecule localization microscopy cluster analysis and quantification methods”. *Patterns*, 1(3), 2020, doi:[10.1016/j.patter.2020.100038](https://doi.org/10.1016/j.patter.2020.100038).
- [117] D. J. Nieves and D. M. Owen. “Analysis methods for interrogating spatial organisation of single molecule localisation microscopy data”. *Int J Biochem Cell Biol*, 123:105749, 2020, doi:[10.1016/j.biocel.2020.105749](https://doi.org/10.1016/j.biocel.2020.105749).
- [118] B. Rossboth, *et al.* “TCRs are randomly distributed on the plasma membrane of resting antigen-experienced T cells”. *Nat Immunol*, 19(8):821–827, 2018, doi:[10.1038/s41590-018-0162-7](https://doi.org/10.1038/s41590-018-0162-7).
- [119] M. A. Thompson, *et al.* “Extending microscopic resolution with single-molecule imaging and active control”. *Annu Rev Biophys*, 41:321–42, 2012, doi:[10.1146/annurev-biophys-050511-102250](https://doi.org/10.1146/annurev-biophys-050511-102250).
- [120] Illian, “Statistical analysis and modelling of spatial point patterns”. John Wiley & Sons Ltd, 2008.
- [121] A. E. Gelfand, *et al.*, “Handbook of spatial statistics”. Chapman & Hall CRC, 2010.
- [122] D. Baddeley and J. Bewersdorf. “Biological insight from super-resolution microscopy:

- What we can learn from localization-based images”. *Annu Rev Biochem*, 87:965–989, 2018, doi:[10.1146/annurev-biochem-060815-014801](https://doi.org/10.1146/annurev-biochem-060815-014801).
- [123] B. Ripley. “Modelling spatial patterns”. *J R Stat Soc Series B Stat Methodol*, 39(2):172–212, 1977.
- [124] T. Wiegand and K. A. Moloney, “Handbook of spatial point-pattern analysis in ecology”. CRC Press, Taylor & Francis Group, 2014.
- [125] M. Ester, *et al.* “A density-based algorithm for discovering clusters in large spatial databases with noise”. *Kdd*, pages 226–231, 1996.
- [126] A. Mazouchi and J. N. Milstein. “Fast optimized cluster algorithm for localizations (FOCAL): A spatial cluster analysis for super-resolved microscopy”. *Bioinformatics*, 32(5):747–54, 2016, doi:[10.1093/bioinformatics/btv630](https://doi.org/10.1093/bioinformatics/btv630).
- [127] D. F. Nino, *et al.* “FOCAL3D: A 3-dimensional clustering package for single-molecule localization microscopy”. *PLoS Comput Biol*, 16(12):e1008479, 2020, doi:[10.1371/journal.pcbi.1008479](https://doi.org/10.1371/journal.pcbi.1008479).
- [128] P. Rubin-Delanchy, *et al.* “Bayesian cluster identification in single-molecule localization microscopy data”. *Nat Methods*, 12(11):1072–6, 2015, doi:[10.1038/nmeth.3612](https://doi.org/10.1038/nmeth.3612).
- [129] J. Griffie, *et al.* “A Bayesian cluster analysis method for single-molecule localization microscopy data”. *Nat Protoc*, 11(12):2499–2514, 2016, doi:[10.1038/nprot.2016.149](https://doi.org/10.1038/nprot.2016.149).
- [130] J. Griffie, *et al.* “3D Bayesian cluster analysis of super-resolution data reveals LAT recruitment to the T cell synapse”. *Sci Rep*, 7(1):4077, 2017, doi:[10.1038/s41598-017-04450-w](https://doi.org/10.1038/s41598-017-04450-w).
- [131] J. M. Scurll, *et al.* “StormGraph: A graph-based algorithm for quantitative clustering analysis of diverse single-molecule localization microscopy data”. *bioRxiv*, 2020, doi:[10.1101/515627](https://doi.org/10.1101/515627).
- [132] D. J. Williamson, *et al.* “Machine learning for cluster analysis of localization microscopy data”. *Nat Commun*, 11(1):1493, 2020, doi:[10.1038/s41467-020-15293-x](https://doi.org/10.1038/s41467-020-15293-x).
- [133] A. Burgert, *et al.* “Artifacts in single-molecule localization microscopy”. *Histochem Cell Biol*, 144(2):123–31, 2015, doi:[10.1007/s00418-015-1340-4](https://doi.org/10.1007/s00418-015-1340-4).
- [134] F. Baumgart, *et al.* “How T cells do the “search for the needle in the haystack””. *Front Phys*, 7, 2019, doi:[10.3389/fphy.2019.00011](https://doi.org/10.3389/fphy.2019.00011).
- [135] C. H. Bohrer, *et al.* “A pairwise distance distribution correction (DDC) algorithm to eliminate blinking-caused artifacts in SMLM”. *Nat Methods*, 2021, doi:[10.1038/s41592-021-01154-y](https://doi.org/10.1038/s41592-021-01154-y).
- [136] R. Jungmann, *et al.* “Quantitative super-resolution imaging with qPAINT”. *Nat Methods*, 13(5):439–42, 2016, doi:[10.1038/nmeth.3804](https://doi.org/10.1038/nmeth.3804).
- [137] G. Hummer, *et al.* “Model-independent counting of molecules in single-molecule localization microscopy”. *Mol Biol Cell*, 27(22):3637–3644, 2016, doi:[10.1091/mbc.E16-07-0525](https://doi.org/10.1091/mbc.E16-07-0525).
- [138] F. Fricke, *et al.* “One, two or three? Probing the stoichiometry of membrane proteins by single-molecule localization microscopy”. *Sci Rep*, 5:14072, 2015, doi:[10.1038/srep14072](https://doi.org/10.1038/srep14072).
- [139] R. L. Wasserstein and N. A. Lazar. “The ASA statement on p-values: Con-

- text, process, and purpose”. *The American Statistician*, 70(2):129–133, 2016, doi:[10.1080/00031305.2016.1154108](https://doi.org/10.1080/00031305.2016.1154108).
- [140] P. J. Diggle, “Statistical analysis of spatial and spatio-temporal point patterns”. CRC Press, Taylor & Francis Group, 2013.
 - [141] P. J. Diggle and A. G. Chetwynd. “Second-order analysis of spatial clustering for inhomogeneous populations”. *Biometrics*, 47(3):1155–1163, 1991.
 - [142] P. J. Diggle, *et al.* “Second-order analysis of inhomogeneous spatial point processes using case-control data”. *Biometrics*, 63(2):550–7, 2007, doi:[10.1111/j.1541-0420.2006.00683.x](https://doi.org/10.1111/j.1541-0420.2006.00683.x).
 - [143] J. Goyette, *et al.* “How does T cell receptor clustering impact on signal transduction?”. *J Cell Sci*, 132(4), 2019, doi:[10.1242/jcs.226423](https://doi.org/10.1242/jcs.226423).
 - [144] B. L. Walling and M. Kim. “LFA-1 in T cell migration and differentiation”. *Front Immunol*, 9:952, 2018, doi:[10.3389/fimmu.2018.00952](https://doi.org/10.3389/fimmu.2018.00952).
 - [145] M. Brameshuber, *et al.* “Monomeric TCRs drive T cell antigen recognition”. *Nat Immunol*, 19(5):487–496, 2018, doi:[10.1038/s41590-018-0092-4](https://doi.org/10.1038/s41590-018-0092-4).
 - [146] P. Annibale, *et al.* “Photoactivatable fluorescent protein mEos2 displays repeated photoactivation after a long-lived dark state in the red photoconverted form”. *The Journal of Physical Chemistry Letters*, 1(9):1506–1510, 2010, doi:[10.1021/jz1003523](https://doi.org/10.1021/jz1003523).
 - [147] S. Wang, *et al.* “Characterization and development of photoactivatable fluorescent proteins for single-molecule-based superresolution imaging”. *Proc Natl Acad Sci USA*, 111(23):8452–7, 2014, doi:[10.1073/pnas.1406593111](https://doi.org/10.1073/pnas.1406593111).
 - [148] M. Schneider, “Overcoming blinking artifacts in nanocluster detection using two-color single-molecule microscopy”. Diploma thesis, TU Wien, 2018.
 - [149] A. M. Arnold, *et al.* “Verifying molecular clusters by 2-color localization microscopy and significance testing”. *Sci Rep*, 10(1):4230, 2020, doi:[10.1038/s41598-020-60976-6](https://doi.org/10.1038/s41598-020-60976-6).
 - [150] H. Lotwick and B. Silverman. “Methods for analysing spatial processes of several types of points”. *J R Stat Soc Series B Stat Methodol*, 44(3):406–413, 1982.
 - [151] M. J. Mlodzianoski, *et al.* “Sample drift correction in 3D fluorescence photoactivation localization microscopy”. *Opt Express*, 19(16), 2011.
 - [152] J. Rossy, *et al.* “Method for co-cluster analysis in multichannel single-molecule localisation data”. *Histochem Cell Biol*, 141(6):605–12, 2014, doi:[10.1007/s00418-014-1208-z](https://doi.org/10.1007/s00418-014-1208-z).
 - [153] S. Wieser, *et al.* “Versatile analysis of single-molecule tracking data by comprehensive testing against Monte Carlo simulations”. *Biophys J*, 95(12):5988–6001, 2008, doi:[10.1529/biophysj.108.141655](https://doi.org/10.1529/biophysj.108.141655).
 - [154] D. A. Helmerich, *et al.* “Photobleaching of organic dyes can cause artifacts in super-resolution microscopy”. *Nat Methods*, 18(3):253–257, 2021, doi:[10.1038/s41592-021-01061-2](https://doi.org/10.1038/s41592-021-01061-2).
 - [155] J. Schnitzbauer, *et al.* “Correlation analysis framework for localization-based superresolution microscopy”. *Proc Natl Acad Sci USA*, 115(13):3219–3224, 2018, doi:[10.1073/pnas.1711314115](https://doi.org/10.1073/pnas.1711314115).
 - [156] J. Adler, *et al.* “Plasma membrane topography and interpretation of single-particle tracks”. *Nat Methods*, 7(3):170–1, 2010, doi:[10.1038/nmeth0310-170](https://doi.org/10.1038/nmeth0310-170).

- [157] V. Ruprecht, *et al.* “Two-color single molecule tracking combined with photobleaching for the detection of rare molecular interactions in fluid biomembranes”. *Soft Matter*, 6(3):568–581, 2010, doi:[10.1039/b916734j](https://doi.org/10.1039/b916734j).
- [158] M. C. Wiener. “A pedestrian guide to membrane protein crystallization”. *Methods*, 34(3):364–72, 2004, doi:[10.1016/j.ymeth.2004.03.025](https://doi.org/10.1016/j.ymeth.2004.03.025).
- [159] A. Ishchenko, *et al.*, “Crystallization of membrane proteins: An overview”, In: *Methods mol biol*, 1607:117–141, 2017. doi:[10.1007/978-1-4939-7000-1_5](https://doi.org/10.1007/978-1-4939-7000-1_5).
- [160] Y. Cheng, *et al.* “A primer to single-particle cryo-electron microscopy”. *Cell*, 161(3):438–449, 2015, doi:[10.1016/j.cell.2015.03.050](https://doi.org/10.1016/j.cell.2015.03.050).
- [161] L. A. Abriata and M. Dal Peraro. “Will cryo-electron microscopy shift the current paradigm in protein structure prediction?”. *J Chem Inf Model*, 2020, doi:[10.1021/acs.jcim.0c00177](https://doi.org/10.1021/acs.jcim.0c00177).
- [162] R. M. Garavito, *et al.* “Strategies for crystallizing membrane proteins”. *J Bioenerg Biomembr*, 28:13–27, 1996.
- [163] Y. Guo. “Be cautious with crystal structures of membrane proteins or complexes prepared in detergents”. *Crystals*, 10(2), 2020, doi:[10.3390/cryst10020086](https://doi.org/10.3390/cryst10020086).
- [164] R. Kaufmann, *et al.* “Super-resolution microscopy using standard fluorescent proteins in intact cells under cryo-conditions”. *Nano Lett*, 14(7):4171–5, 2014, doi:[10.1021/nl501870p](https://doi.org/10.1021/nl501870p).
- [165] M. W. Tuijtel, *et al.* “Correlative cryo super-resolution light and electron microscopy on mammalian cells using fluorescent proteins”. *Sci Rep*, 9(1):1369, 2019, doi:[10.1038/s41598-018-37728-8](https://doi.org/10.1038/s41598-018-37728-8).
- [166] C. S. Smith, *et al.* “Fast, single-molecule localization that achieves theoretically minimum uncertainty”. *Nat Methods*, 7(5):373–5, 2010, doi:[10.1038/nmeth.1449](https://doi.org/10.1038/nmeth.1449).
- [167] M. P. Backlund, *et al.* “The role of molecular dipole orientation in single-molecule fluorescence microscopy and implications for super-resolution imaging”. *Chemphyschem*, 15(4):587–99, 2014, doi:[10.1002/cphc.201300880](https://doi.org/10.1002/cphc.201300880).
- [168] Y. Zhang, *et al.* “Ultrafast, accurate, and robust localization of anisotropic dipoles”. *Protein Cell*, 4(8):598–606, 2013, doi:[10.1007/s13238-013-3904-1](https://doi.org/10.1007/s13238-013-3904-1).
- [169] F. Aguet, *et al.* “Super-resolution orientation estimation and localization of fluorescent dipoles using 3-D steerable filters”. *Opt Express*, 17(8), 2009.
- [170] S. Stallinga and B. Rieger. “Position and orientation estimation of fixed dipole emitters using an effective hermite point spread function model”. *Opt Express*, 20(6), 2012.
- [171] B. C. Coles, *et al.* “Characterisation of the effects of optical aberrations in single molecule techniques”. *Biomed Opt Express*, 7(5):1755–67, 2016, doi:[10.1364/BOE.7.001755](https://doi.org/10.1364/BOE.7.001755).
- [172] C. N. Hulleman, *et al.* “Simultaneous orientation and 3D localization microscopy with a Vortex point spread function”. *bioRxiv*, 2020, doi:[10.1101/2020.10.01.322834](https://doi.org/10.1101/2020.10.01.322834).
- [173] M. P. Backlund, *et al.* “Simultaneous, accurate measurement of the 3D position and orientation of single molecules”. *Proc Natl Acad Sci USA*, 109(47):19087–92, 2012, doi:[10.1073/pnas.1216687109](https://doi.org/10.1073/pnas.1216687109).

- [174] O. Zhang, *et al.* “Imaging the three-dimensional orientation and rotational mobility of fluorescent emitters using the Tri-spot point spread function”. *Appl Phys Lett*, 113(3):031103, 2018, doi:[10.1063/1.5031759](https://doi.org/10.1063/1.5031759).
- [175] M. D. Lew and W. E. Moerner. “Azimuthal polarization filtering for accurate, precise, and robust single-molecule localization microscopy”. *Nano Lett*, 14(11):6407–13, 2014, doi:[10.1021/nl502914k](https://doi.org/10.1021/nl502914k).
- [176] M. P. Backlund, *et al.* “Removing orientation-induced localization biases in single-molecule microscopy using a broadband metasurface mask”. *Nat Photonics*, 10:459–462, 2016, doi:[10.1038/nphoton.2016.93](https://doi.org/10.1038/nphoton.2016.93).
- [177] O. Nevskiy, *et al.* “Fluorescence polarization filtering for accurate single molecule localization”. *APL Photonics*, 5(6), 2020, doi:[10.1063/5.0009904](https://doi.org/10.1063/5.0009904).
- [178] H. Deschout, *et al.* “Progress in quantitative single-molecule localization microscopy”. *Histochem Cell Biol*, 142(1):5–17, 2014, doi:[10.1007/s00418-014-1217-y](https://doi.org/10.1007/s00418-014-1217-y).
- [179] C. Sieben, *et al.* “Super-resolution microscopy to decipher multi-molecular assemblies”. *Curr Opin Struct Biol*, 49:169–176, 2018, doi:[10.1016/j.sbi.2018.03.017](https://doi.org/10.1016/j.sbi.2018.03.017).
- [180] D. Salas, *et al.* “Angular reconstitution-based 3D reconstructions of nanomolecular structures from superresolution light-microscopy images”. *Proc Natl Acad Sci USA*, 114(35):9273–9278, 2017, doi:[10.1073/pnas.1704908114](https://doi.org/10.1073/pnas.1704908114).
- [181] C. Sieben, *et al.* “Multicolor single-particle reconstruction of protein complexes”. *Nat Methods*, 15(10):777–780, 2018, doi:[10.1038/s41592-018-0140-x](https://doi.org/10.1038/s41592-018-0140-x).
- [182] J. Broeken, *et al.* “Resolution improvement by 3D particle averaging in localization microscopy”. *Methods Appl Fluoresc*, 3(1):014003, 2015, doi:[10.1088/2050-6120/3/1/014003](https://doi.org/10.1088/2050-6120/3/1/014003).
- [183] H. Heydarian, *et al.* “Template-free 2D particle fusion in localization microscopy”. *Nat Methods*, 15(10):781–784, 2018, doi:[10.1038/s41592-018-0136-6](https://doi.org/10.1038/s41592-018-0136-6).
- [184] H. Heydarian, *et al.* “3D particle averaging and detection of macromolecular symmetry in localization microscopy”. *Nat Commun*, 12(1), 2021, doi:[10.1038/s41467-021-22006-5](https://doi.org/10.1038/s41467-021-22006-5).
- [185] X. Shi, *et al.* “Deformed alignment of super-resolution images for semi-flexible structures”. *PLoS One*, 14(3):e0212735, 2019, doi:[10.1371/journal.pone.0212735](https://doi.org/10.1371/journal.pone.0212735).
- [186] A. P. Curd, *et al.* “Nanoscale pattern extraction from relative positions of sparse 3D localizations”. *Nano Lett*, 21(3):1213–1220, 2021, doi:[10.1021/acs.nanolett.0c03332](https://doi.org/10.1021/acs.nanolett.0c03332).
- [187] F. Hinterer, *et al.* “Robust and bias-free localization of individual fixed dipole emitters achieving the Cramér Rao bound”. *arXiv*, 2021. arXiv-ID:2104.02449v1.
- [188] H. P. Kao and A. S. Verkman. “Tracking of single fluorescent particles in three dimensions: Use of cylindrical optics to encode particle position”. *Biophys J*, 67, 1994.
- [189] B. Huang and e. al. “Three-dimensional super-resolution imaging by stochastic optical reconstruction microscopy”. *Science*, 2008.
- [190] B. Hajj, *et al.* “Accessing the third dimension in localization-based super-resolution microscopy”. *Phys Chem Chem Phys*, 16(31):16340–8, 2014, doi:[10.1039/c4cp01380h](https://doi.org/10.1039/c4cp01380h).
- [191] P. Zelger, *et al.* “Three-dimensional single molecule localization close to the coverslip:

- A comparison of methods exploiting supercritical angle fluorescence". *Biomedical Optics Express*, 12(2), 2021, doi:[10.1364/boe.413018](https://doi.org/10.1364/boe.413018).
- [192] G. J. Schütz, *et al.* "Imaging single-molecule dichroism". *Optics Letters*, 22(9), 1997.
- [193] G. S. Harms, *et al.* "Single-molecule anisotropy imaging". *Biophys J*, 77:2864–2870, 1999.
- [194] J. T. Fourkas. "Rapid determination of the three-dimensional orientation of single molecules". *Optics Letters*, 26(4), 2001.
- [195] C. Lethiec, *et al.* "Measurement of three-dimensional dipole orientation of a single fluorescent nanoemitter by emission polarization analysis". *Physical Review X*, 4(2), 2014, doi:[10.1103/PhysRevX.4.021037](https://doi.org/10.1103/PhysRevX.4.021037).
- [196] K. Zhanghao, *et al.* "Super-resolution dipole orientation mapping via polarization demodulation". *Light Sci Appl*, 5(10):e16166, 2016, doi:[10.1038/lsa.2016.166](https://doi.org/10.1038/lsa.2016.166).
- [197] C. Schwartz, *et al.* "Cryo-fluorescence microscopy facilitates correlations between light and cryo-electron microscopy and reduces the rate of photobleaching". *J Microsc*, 227:98–109, 2007.
- [198] E. Hoogendoorn, *et al.* "The fidelity of stochastic single-molecule super-resolution reconstructions critically depends upon robust background estimation". *Sci Rep*, 4:3854, 2014, doi:[10.1038/srep03854](https://doi.org/10.1038/srep03854).
- [199] A. Reismann, *et al.* "Temporal filtering to improve single molecule identification in high background samples". *Molecules*, 23(12), 2018, doi:[10.3390/molecules23123338](https://doi.org/10.3390/molecules23123338).
- [200] R. Gray, "Zernikecalc." URL: <https://www.mathworks.com/matlabcentral/fileexchange/33330-zernikecalc>, 2013.
- [201] S. M. Kay, "Fundamentals of statistical signal processing". Prentice Hall PTR, 1993.
- [202] J. Chao, *et al.* "Fisher information theory for parameter estimation in single molecule microscopy: Tutorial". *J Opt Soc Am A Opt Image Sci Vis*, 33(7):B36–57, 2016, doi:[10.1364/JOSAA.33.000B36](https://doi.org/10.1364/JOSAA.33.000B36).
- [203] L. Danielli, *et al.* "Quantifying the distribution of protein oligomerization degree reflects cellular information capacity". *Sci Rep*, 10(1):17689, 2020, doi:[10.1038/s41598-020-74811-5](https://doi.org/10.1038/s41598-020-74811-5).
- [204] C. H. Lee and R. MacKinnon. "Structures of the human HCN1 hyperpolarization-activated channel". *Cell*, 168(1-2):111–120, 2017, doi:[10.1016/j.cell.2016.12.023](https://doi.org/10.1016/j.cell.2016.12.023).
- [205] L. Jakob, *et al.* "Evaluation and optimisation of unnatural amino acid incorporation and bioorthogonal bioconjugation for site-specific fluorescent labelling of proteins expressed in mammalian cells". *Biochem Biophys Rep*, 17:1–9, 2019, doi:[10.1016/j.bbrep.2018.10.011](https://doi.org/10.1016/j.bbrep.2018.10.011).
- [206] M. C. Schneider, *et al.* "A workflow for sizing oligomeric biomolecules based on cryo single molecule localization microscopy". *PLoS One*, 16(1):e0245693, 2021, doi:[10.1371/journal.pone.0245693](https://doi.org/10.1371/journal.pone.0245693).
- [207] A. Al-Sharadqah and N. Chernov. "Error analysis for circle fitting algorithms". *Electronic Journal of Statistics*, 3:886–911, 2009, doi:[10.1214/09-ejs419](https://doi.org/10.1214/09-ejs419).
- [208] P. Tinnefeld, *et al.* "Direct observation of collective blinking and energy transfer in a bichromophoric system". *J Phys Chem A*, 107(3), 2003.

-
- [209] M. Mund, *et al.* “Systematic nanoscale analysis of endocytosis links efficient vesicle formation to patterned actin nucleation”. *Cell*, 2018, doi:[10.1016/j.cell.2018.06.032](https://doi.org/10.1016/j.cell.2018.06.032).
- [210] K. Levenberg. “A method for the solution of certain non-linear problems in least squares”. *Quart Appl Math*, 2:164–168, 1944, doi:[10.1090/qam/10666](https://doi.org/10.1090/qam/10666).
- [211] D. W. Marquardt. “An algorithm for least-squares estimation of nonlinear parameters”. *SIAM Journal on Applied Mathematics*, 11(2):431–441, 1963, doi:[10.1137/0111030](https://doi.org/10.1137/0111030).
- [212] N. Chernov and C. Lesort. “Statistical efficiency of curve fitting algorithms”. *Comput Stat Data Anal*, 47(4):713–728, 2004, doi:[10.1016/j.csda.2003.11.008](https://doi.org/10.1016/j.csda.2003.11.008).
- [213] K. Kanatani, “Statistical optimization of geometric computation: Theory and practice”. Courier Corporation, 2005.
- [214] T. Yokosuka, *et al.* “Newly generated T cell receptor microclusters initiate and sustain T cell activation by recruitment of Zap70 and SLP-76”. *Nat Immunol*, 6(12):1253–62, 2005, doi:[10.1038/ni1272](https://doi.org/10.1038/ni1272).

List of Figures

2.1	The cell	5
2.2	Cellular plasma membrane	7
2.3	Protein structure	8
2.4	Fluorescence	11
2.5	Airy pattern and resolution	12
2.6	Illumination	14
2.7	Principle of single molecule localization microscopy (SMLM)	16
2.8	Methods for separating fluorescence signals in time	17
2.9	Structure and size of various labels	20
2.10	Schematic outline of microscope setups	22
2.11	Localization precision versus accuracy	27
2.12	Reasons for overcounting	30
2.13	Possible distortions of localization maps	31
3.1	Spatial distributions of point patterns	37
3.2	Ripley's function and pair-correlation analysis	38
3.3	DBSCAN	40
3.4	FOCAL	40
3.5	Image tessellation	41
3.6	Merging of localizations	42
3.7	Pair correlation analysis accounting for overcounting	44
3.8	Label titration method	45
3.9	Random spatial point pattern analyzed by DBSCAN	47
3.10	Population, sample and sampling distribution	49
3.11	The p-value	50
4.1	Platform design for recording of blinking statistics	57
4.2	Grouping of localizations and colocalization with platform data	58
4.3	Representative intensity traces of PS-CFP2 molecules	59
4.4	Blinking statistic parameters	59
4.5	Experimentally recorded blinking statistics	60
4.6	Cluster analysis via Ripley's H function in the presence of overcounting	62
4.7	Monte Carlo simulations and simulation envelopes	63
4.8	Analysis of TCR-CD ζ and LFA-1 distributions in the T-cell	64
5.1	Analysis of localization maps with 2-CLASTA	72
5.2	Principle of a toroidal shift	72

5.3	Distribution of the p-value under the null hypothesis	74
5.4	Single molecule blinking statistics for SNAP-labels	75
5.5	Robustness of 2-CLASTA	77
5.6	Influence of experimental errors on the sensitivity	78
5.7	Influence of different summary statistics on 2-CLASTA sensitivity	79
5.8	Influence of r_{\max} on 2-CLASTA sensitivity	80
5.9	Examples of simulated nanodomains	81
5.10	Sensitivity of 2-CLASTA to detect spatially extended clusters	82
5.11	Sensitivity results for different fluorescent labels	83
5.12	Influence of localization precision on the sensitivity of 2-CLASTA for spatially extended clusters	84
5.13	Influence of cluster shape on the sensitivity of 2-CLASTA	84
5.14	2-CLASTA analysis of experimental data	85
5.15	Obtained p-value versus number of analyzed localizations	86
5.16	Sensitivity for joint analysis of multiple experiments	89
5.17	Overall p-value for multiple experiments	89
5.18	Displacement vector field for chromatic aberration	95
6.1	PSFs for fixed fluorophore dipole orientations	103
6.2	Template basis patterns	104
6.3	Manipulation of the back focal plane	105
6.4	Polarization splitting approach	106
6.5	Effect of under- and overcounting	107
6.6	Radius determination from sum images	108
6.7	Particle reconstruction based on EM-algorithms	109
6.8	Particle registration methods	110
6.9	Pattern extraction from relative positions of localizations (PERPL)	111
7.1	Coordinate system and fluorophore dipole orientation	114
7.2	Localization errors for fixed dipole emitters	115
7.3	Comparison of PSF images for different noise levels	116
7.4	Point spread functions for different dipole orientations	117
7.5	Fitting the dipole orientation in the presence of astigmatism	118
7.6	Localization errors in the presence of astigmatism	119
7.7	Influence of the azimuthal angle	120
7.8	Influence of number of photons	120
7.9	Influence of pixel size	121
7.10	Influence of background noise	121
7.11	Influence of the size of the fitted region	122
7.12	Influence of uncertainties in dipole orientation	123
7.13	Influence of reduced excitation probability for tilted dipoles	124
7.14	Combined effect of reduced excitation probability for tilted dipoles and uncertainties in dipole orientation	124
7.15	Discretization of the PSF	129

8.1	Oligomer structure	134
8.2	SMLM imaging of small oligomeric structures	135
8.3	Reconstruction with a template-free method	136
8.4	Schematic representation of the method	137
8.5	Probability density for brightness values	138
8.6	Estimating oligomer side length from a set of oligomers	139
8.7	Assignment of localizations and eligibility of oligomers	140
8.8	Influence of signal brightness and noise	141
8.9	Influence of the number of available oligomers	142
8.10	Influence of labeling efficiency	143
8.11	Influence of oligomer side length	144
8.12	Degree of oligomerization	144
8.13	Influence of a tilt of oligomers	145
8.14	Runtime scaling	145

Curriculum Vitae

DI Magdalena Schneider, BSc

Date of birth: November 23, 1993
Citizenship: Austria
E-mail: schneider@iap.tuwien.ac.at
ORCID: 0000-0002-3771-8353

Education

- | | |
|-------------------|--|
| 05/2018 – Present | PhD studies in Technical Physics
TU Wien, Austria |
| 10/2015 – 04/2018 | MSc in Biomedical Engineering (with distinction)
Focus on Mathematical and Computational Biology
TU Wien, Austria |
| 02/2017 – 07/2017 | Swiss-European Mobility Programme (SEMP)
ETH Zurich, Switzerland |
| 10/2012 – 09/2015 | BSc in Technical Mathematics (with distinction)
TU Wien, Austria |

Research experience

- | | |
|-------------------|--|
| 05/2018 – Present | Project Assistant
Institute of Applied Physics, Biophysics
TU Wien, Austria |
| 09/2016 – 11/2016 | Research Assistant (FEMtech Internship)
Austrian Institute of Technology (AIT)
Center for Health & Bioresources, research field <i>Cardiovascular Diagnostics</i> |

Teaching experience

- | | |
|------------------------------|--|
| Summer 2016 &
Summer 2018 | Teaching assistant (TU Wien)
Mathematics for Technical Chemistry II, Exercises |
| Winter 2015 &
Winter 2017 | Teaching assistant (TU Wien)
Mathematics for Technical Chemistry I, Exercises |
| Winter 2017 | Teaching assistant (TU Wien)
Mathematics for Geodesy and Geoinformation I, Exercises |

Scholarships and Awards

- 2020 Christiana Hörbiger Award
- 2020 BPS Travel Award (Biophysical Society)
- 2019 Students' Award of the OePG (Austrian Physical Society)
Award for outstanding Master thesis in the field of physics.
- 2018 Best Student Talk Award (10th ÖGMBT Annual Meeting)
- 2018 Best Poster Prize (8th Single Molecule Localization Microscopy Symposium)
- 2017 Swiss-European Mobility Programme (SEMP) Scholarship
- 2016 FEMtech Scholarship (Austrian Ministry of Transport, Innovation and Technology)
- 2016 Performance Scholarship (Faculty of Physics, TU Wien)
- 2013 Performance Scholarship (Faculty of Mathematics and Geoinformation, TU Wien)

Scientific talks and poster presentations

- 07/2021 13th European Biophysics Conference (EBSA) (Vienna, Austria)
Poster: *Sizing oligomeric biomolecular structures with cryo-SMLM*
- 02/2021 65th Annual Meeting of the Biophysical Society (online)
Poster: *A workflow for determining and sizing oligomeric biomolecular structures with cryo single molecule localization microscopy*
- 02/2020 64th Annual Meeting of the Biophysical Society (San Diego, USA)
Talk: *2-Color Localization microscopy And Significance Testing Approach (2-CLASTA)*
- 09/2019 25th International Anniversary Workshop on "Single Molecule Spectroscopy and Super-resolution Microscopy in the Life Sciences" (Berlin, Germany)
Poster Flash Talk and Poster: *Overcoming Blinking Artifacts in Nanocluster Detection With Two-Color STORM*
- 02/2019 21st Annual Linz Winter Workshop (Linz, Austria)
Talk: *Overcoming Blinking Artifacts in Nanocluster Detection With Two-Color STORM*
- 01/2019 Quantitative Bioimaging (QBI) Conference (Rennes, France)
Talk: *Overcoming Blinking Artifacts in Nanocluster Detection With Two-Color STORM*
- 09/2018 10th ÖGMBT Annual Meeting (Vienna, Austria)
Talk: *Overcoming Blinking Artifacts in Nanocluster Detection With Two-Color STORM*
Selected for **Best Student Talk Award**
- 08/2018 8th Single Molecule Localization Microscopy Symposium (Berlin, Germany)
Poster: *Overcoming Blinking Artifacts in Nanocluster Detection With Two-Color STORM*
Selected for **Best Poster Prize**

Publications

- 2021 **Robust and bias-free localization of individual fixed dipole emitters achieving the Cramér Rao bound.** F. Hinterer*, M. C. Schneider*, S. Hubmer, M. López-Martinez, P. Zelger, A. Jesacher, R. Ramlau, G. J. Schütz. *arXiv*, ID: 2104.02449.
- 2021 **Strategies for the site-specific decoration of DNA origami nanostructures with functionally intact proteins.** J. Hellmeier, R. Platzer, V. Mühlgrabner, M. C. Schneider, E. Kurz, G. J. Schütz, J. B. Huppa, E. Sevcsik. *ACS Nano*, doi: 10.1021/acsnano.1c05411.
- 2021 **A workflow for sizing oligomeric biomolecules based on cryo single molecule localization microscopy.** M. C. Schneider*, R. Telschow*, G. Mercier, M. López-Martinez, O. Scherzer, G. J. Schütz. *PLoS One*, 16(1), doi: 10.1371/journal.pone.0245693.
- 2021 **DNA origami demonstrate the unique stimulatory power of single pMHCs as T-cell antigens.** J. Hellmeier, R. Platzer, A. S. Eklund, T. Schlichthaerle, A. Karner, V. Motsch, M. C. Schneider, E. Kurz, V. Bamieh, M. Brameshuber, J. Preiner, R. Jungmann, H. Stockinger, G. J. Schütz, J. B. Huppa, E. Sevcsik. *PNAS*, 2021. 118(4), doi: 10.1073/pnas.2016857118.
- 2021 **Single-Molecule Localization Microscopy (SMLM).** M. C. Schneider and G. J. Schütz. In: *Imaging modalities for biological and preclinical research: A compendium*. IOP Publishing, doi: 10.1088/978-0-7503-3059-6ch18.
- 2021 **Inverse Problems of Single Molecule Localization Microscopy.** M. López-Martinez, G. Mercier, K. Sadiq, O. Scherzer, M. Schneider, J. C. Schotland, G. J. Schütz, R. Telschow. In: *Time-dependent Problems in Imaging and Parameter Identification*. Springer International Publishing, doi: 10.1007/978-3-030-57784-1.
- 2020 **Unscrambling Fluorophore Blinking for Comprehensive Cluster Detection via PALM.** R. Platzer*, B. K. Rossboth*, M. C. Schneider, E. Sevcsik, F. Baumgart, H. Stockinger, G. J. Schütz, J. B. Huppa, M. Brameshuber. *Nature Communications*, 11, doi: 10.1038/s41467-020-18726-9.
- 2020 **Verifying molecular clusters by 2-color localization microscopy and significance testing.** A. M. Arnold*, M. C. Schneider*, C. Hüsön, R. Sablatnig, M. Brameshuber, F. Baumgart, G. J. Schütz. *Scientific Reports*, 10, doi: 10.1038/s41598-020-60.
- 2019 **Homo- and heteroassociations drive activation of ErbB3.** T. Váradi, M. Schneider, E. Sevcsik, D. Kiesenhofer, F. Baumgart, G. Batta, T. Kovács, R. Platzer, J. Huppa, J. Szöllösi, G. Schütz, M. Brameshuber, P. Nagy. *Biophysical Journal*, 117(10), doi: 10.1016/j.bpj.2019.10.001.
- 2019 **How T-cells do the “search for the needle in the haystack”.** F. Baumgart, M. Schneider, and G. J. Schütz. *Frontiers in Physics*, 7(11), doi: 10.3389/fphy.2019.00011.
- 2017 **Computational assessment of model-based wave separation using a database of virtual subjects.** B. Hametner, M. Schneider, S. Parragh, S. Wassertheurer. *Journal of Biomechanics*, 64, doi: 10.1016/j.jbiomech.2017.08.027.